UNIVERSITÉ DE STRASBOURG

ÉCOLE DOCTORALE MATHEMATIQUES, SCIENCES DE L'INFORMATION ET DE L'INGENIEUR

Institute of Solid and Fluid Mechanics, CNRS-FRE 3240

THÈSE

présentée par :

Wei WEN

soutenue le : **5th Mai 2013**

pour obtenir le grade de : **Docteur de l'université de Strasbourg**

Discipline/ Spécialité: **Mécanique des matériaux**

Simulation of large deformation response of polycrystals, deforming by slip and twinning, using the visco-plastic ϕ-model

THÈSE dirigée par :

Siham M'GUIL	MCF, HDR, Université de Strasbourg
Saïd AHZI	Professor, Université de Strasbourg

RAPPORTEURS :

Sébastien MERCIER	Professeur, Université de Lorraine, Metz
Akrum ABDUL-LATIF	Professeur, Université Paris 8

AUTRES MEMBRES DU JURY:

José GRACIO	Professeur, Université d'Aveiro, Portugal
Yves REMOND	Professeur, Université de Strasbourg

Acknowledgement

The work of this PhD dissertation was realized in ICube, department of mechanic (ex. Institute of fluid and solid mechanics, IMFS) and funded by Ministère de l'Enseignement Supérieur et de la Eecherche. I would like to thank Prof. Yves Rémond (ex-director of the IMFS) for welcoming me in this laboratory.

And then, I would like to express my sincere gratitude to my advisors, Prof. Saïd Ahzi and Prof. Siham M'Guil. They have introduced me into the research field of crystal plasticity and shared their wisdom and experience with me. During this work, they have contributed with excellent scientific support. All of the valuable ideas and suggestions are deeply grateful.

I would also like to thank Prof. Sébastien Mercier from University of Lorraine and Prof. Akrum Abdul-Latif from University Paris 8 for accepting to be the reporters of my thesis and for your excellent scientific suggestions.

A special thank goes to Prof. José Gracio from University of Aveiro for encouraging me to follow the academic research and for his excellent scientific help and suggestions. I would also like to thank Prof. Gabriela Vincze from University of Aveiro who helped me a lot in the experimental work. I am also grateful to Prof. Dongsheng Li from PNNL for the fruitful discussions about the numerical simulation and code writing.

I would like furthermore thank all my friends and colleagues that I have worked with. I had a great time during my PhD work and the memory working beside them is precious to me.

At the end, I am heartily thankful to my family. I am really grateful to my parents for their endless love and support. My greatest gratitude goes to my wife. She encourages me, supports me, loves me, gives me the reason to continue and is always there for me.

Content

Résumé

Les matériaux polycristallins sont constitués d'un grand nombre de monocristaux (appelés grains). Chaque grain montre un comportement anisotrope fort. Les comportements mécaniques macroscopiques des polycristaux dépendent fortement de la distribution des orientations des cristaux et du comportement du monocristal. Si les grains ont une distribution d'orientation aléatoire alors les propriétés mécaniques macroscopiques sont les mêmes dans toutes les directions et donc le matériau est isotrope. En revanche, si les grains sont de préférence orientés dans des directions cristallographiques données, le matériau est anisotrope. La distribution d'orientation cristallographique d'un échantillon polycristallin est définie comme la texture cristallographique.

Le calcul de la réponse macroscopique des agrégats polycristallins à partir des propriétés de leurs constituants (grains monocristallins) est considéré comme l'un des principaux problèmes de mécanique des matériaux. Lors de la déformation plastique, tous les grains de l'échantillon du matériau polycristallin sont réorientés. Une texture cristallographique peut alors se développer. Cette dernière est responsable de l'anisotropie du matériau, voir Fig. R-1 qui présente le schéma de l'évolution de l'orientation des grains lors des essais de laminage. Par conséquent, la modélisation de l'évolution de la texture dans les polycristaux est importante afin de prévoir les effets d'anisotropie présents dans de nombreux procédés industriels.

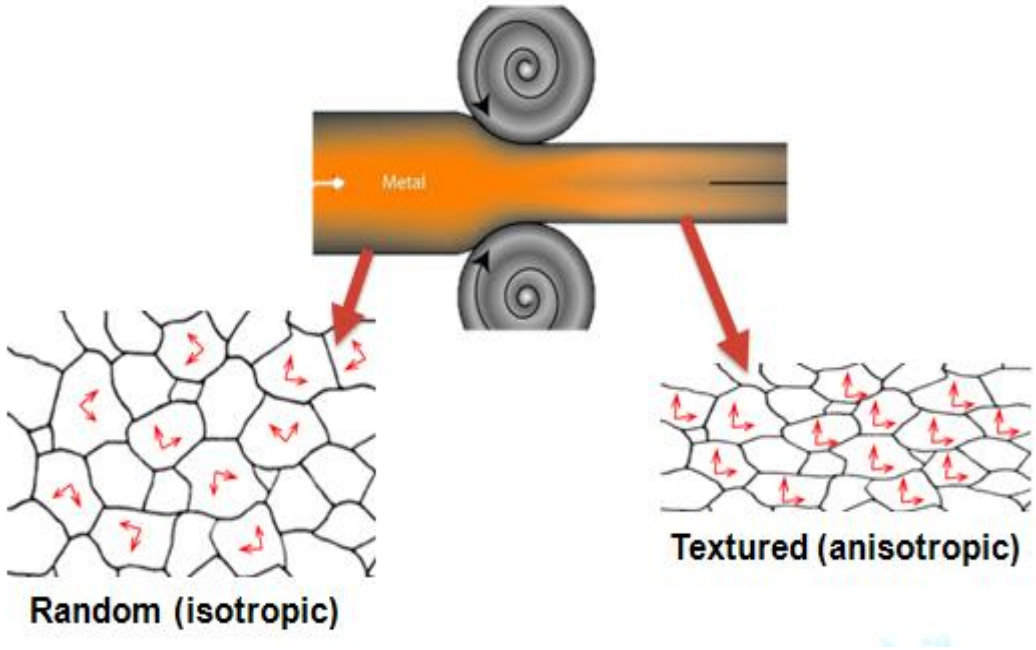

Fig. R-1. Schéma de l'évolution de l'orientation des grains lors des essais de laminage

La formulation de la plasticité des polycristaux métalliques a fait l'objet de nombreuses études et différentes approches d'homogénéisation ont été proposées. Ces techniques d'homogénéisation vont des limites classiques (Taylor et Sachs) à des approches auto-cohérente plus sophistiquées. L'insuffisance principale de la plupart des modèles existants de plasticité cristalline, c'est qu'ils sont incapables de prédire les résultats d'une interaction rigide à une interaction plus souple entre les grains. Cette insuffisance conduit à un manque de capacité de prévision des résultats à grande échelle. Par exemple, lors d'un essai de laminage, les métaux CFC développent généralement 2 types de texture: cuivre et laiton. Du point de vue de la simulation, les modèles de type Sachs ne peuvent pas prédire la texture de type cuivre. Les modèles de Taylor-type et le modèle visco-plastique auto-cohérent (VPSC) ne peuvent pas prédire la texture de type laiton à moins que le mécanisme de maclage soit pris en compte. Toutefois, certains matériaux, ayant des microstructures spécifiques ou pour des

conditions particulières de chargement, peuvent développer une texture de type cuivre même si le maclage n'ait pas été détecté. Ce manque de capacité des modèles existants à capturer correctement les transitions de texture pousse au développement de nouveaux modèles de plasticité cristalline.

Ahzi et M'Guil ont développé un nouveau modèle viscoplastique. Ce modèle-ϕ prend en compte les effets d'interaction entre les grains sans utiliser le problème de l'inclusion Eshelby. Ce modèle est formulé par la minimisation d'une fonction spécifique combinant les champs de déviations locaux (vitesse de déformation et de contrainte) aux champs macroscopiques. Cette fonction dépend également d'un paramètre de réglage, entre 0 et 1 qui permet à la force interaction du grain de varier d'une interaction rigide (petites valeurs de ϕ) à une interaction plus souple (valeurs élevées de ϕ). La loi d'interaction proposée permet de couvrir les résultats des modèles de la borne supérieure à la borne inférieure en variant un seul paramètre de force d'interaction ϕ, voir Fig. R-2. Ce modèle fournit la nouveauté sur la formulation et montre une bonne performance sur la prédiction des comportements de déformation plastique et des évolutions des textures cristallographiques des métaux au cours des procédés de mise en forme. Bien que l'avantage de ce modèle par rapport aux modèles existants soit significatif, il peut encore être modifié et complété. Par conséquent, l'objectif principal de ce travail est d'améliorer, d'étendre et d'appliquer ce modèle aux prévisions d'évolution de texture dans différents métaux au cours de la déformation plastique. Un tel travail répond au besoin d'une meilleure compréhension du comportement mécanique lors de la mise en forme des métaux par déformation plastique ; ce qui permettra d'optimiser les procédés industriels.

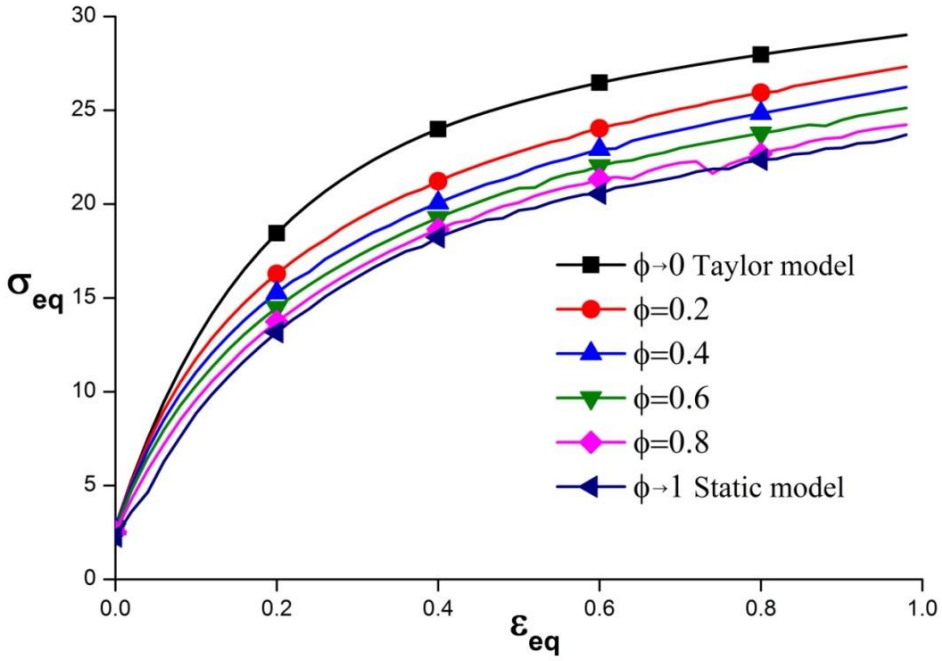

Fig. R-2. Courbes contrainte-déformation prédites pour différentes valeurs de ϕ lors d'un essai de traction dans les métaux CFC

Dans ce travail, le maclage mécanique, qui est l'un des mécanismes fondamentaux de la déformation plastique dans les matériaux polycrystallin, a été mis en œuvre dans le modèle. L'effet couplé du maclage mécanique et la force d'interaction entre les grains (contrôlée par le paramètre ϕ) sur l'évolution de la texture a été étudié pour les métaux CFC dans des conditions de chargement différents. La possibilité de la transition de texture de laminage du type cuivre au type laiton a été discutée. Le maclage mécanique permet également d'appliquer le modèle aux métaux HC. En outre, le modèle a été étendu aux métaux CC.

Le détail de chaque chapitre est présenté comme suit:

Chapitre I

Le chapitre I se compose d'une bibliographie sur la modélisation de la plasticité cristalline. Nous présentons brièvement la modélisation microscopique y compris le cadre constitutive des lois d'écrouissage des modèles. Ensuite, le concept de la texture dans les polycristaux et les principaux modèles d'homogénéisation existants sont résumés.

Chapitre II

Le nouveau modèle viscoplastique ϕ est présenté en détail dans ce chapitre. Après la présentation de la formulation de ce modèle, nous avons résumé les aspects numériques de la modélisation. En plus, nous proposons une étude des déviations de contrainte et vitesse de déformation normalisées. À la fin de ce chapitre, l'évolution du tenseur d'interaction est étudiée. Nous avons prédit l'évolution du tenseur d'interaction du modèle ϕ et comparé ces résultats avec ceux issus du modèle VPSC. Nous pouvons voir que les tenseurs d'interaction entre les deux modèles montrent différentes tendances d'évolution. Par ailleurs, nous avons analysé l'information contenue dans les tenseurs d'interaction de ces deux modèles. Celui du modèle VPSC peut prendre en compte l'effet de la forme des grains via le tenseur d'Eshelby. Toutefois, le tenseur d'interaction du modèle ϕ contient les informations de l'orientation cristallographique ce qui est absent dans le modèle VPSC

Chapitre III

Dans le chapitre III, la transition de la texture CFC de laminage du type-cuivre au type-laiton a été étudiée en utilisant le modèle-ϕ. Les exemples de textures type-cuivre et type-laiton sont présentés dans la Fig. R-3. La prédiction de l'évolution de la texture de laminage des métaux CFC est contrôlée par les lois d'interaction, les mécanismes de la déformation plastique ainsi que de la définition de la rotation du réseau. L'effet couplé de ces trois facteurs

sur l'évolution de la texture de laminage est analysé. Dans ce travail, deux définitions de la rotation du réseau, l'analyse mathématique (MA) et l'analyse en déformation plane (PSA), sont prises en compte dans le modèle. L'influence des définitions de MA et de PSA sur l'évolution de la CFC texture de laminage est analysée en détail en conjonction avec le maclage et la force d'interaction entre les grains. Une texture typique de type-laiton a été prédite, ce qui est généralement observé dans les métaux avec une énergie de défaut d'empilement (EDE) faible.

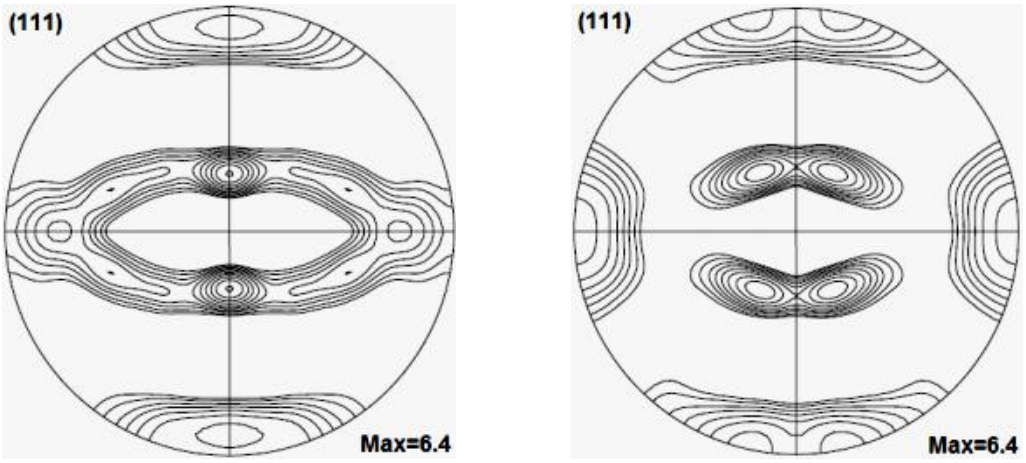

Texture type-cuivre Texture type-laiton

Fig. R-3. Exemples de texture de type-cuivre et type-laiton sous forme de (111) pole figure.

Chapitre IV

Dans ce chapitre, nous montrons que le modèle-ϕ peut-être utilisé pour calculer simplement la transition de texture cristallographique lors de l'essai de cisaillement des métaux CFC en grandes déformations. Les résultats prédits sont comparés aux textures expérimentales de cisaillement pour les métaux avec EDE haute/moyenne (i.e. cuivre) et EDE faible (i.e. argent). Nous montrons que le modèle est capable de prédire une transition de texture claire ce qui caractérise une gamme de métaux CFC ayant une EDE élevée/moyenne à faible. Le

mécanisme de maclage est pris en compte afin d'améliorer les textures de cisaillement prédites pour les métaux avec une EDE faible. L'effet du maclage sur les composantes idéales de texture de cisaillement est représenté et est comparé avec les résultats expérimentaux de la littérature. Nous avons montré que le mécanisme de maclage joue un rôle important dans la prédiction de la texture de cisaillement des métaux avec une EDE faible.

Chapitre V

Dans ce chapitre, les textures de laminage des métaux CC et les surfaces de charge correspondantes sont simulées en utilisant le modèle-ϕ. Nous comparons nos résultats à ceux prédits par le modèle viscoplastique auto-cohérent (VPSC). Les résultats sont comparés en termes d'activité de glissement, de l'évolution de la texture et de surface de charge. Nous présentons également une comparaison qualitative avec les textures expérimentales de laminage à froid issues de la littérature pour plusieurs métaux CC (voir Fig.R-4). Les liens possibles entre le paramètre de force d'interaction entre les grains et les caractéristiques microstructurales telles que la taille des grains sont brièvement mentionnés.

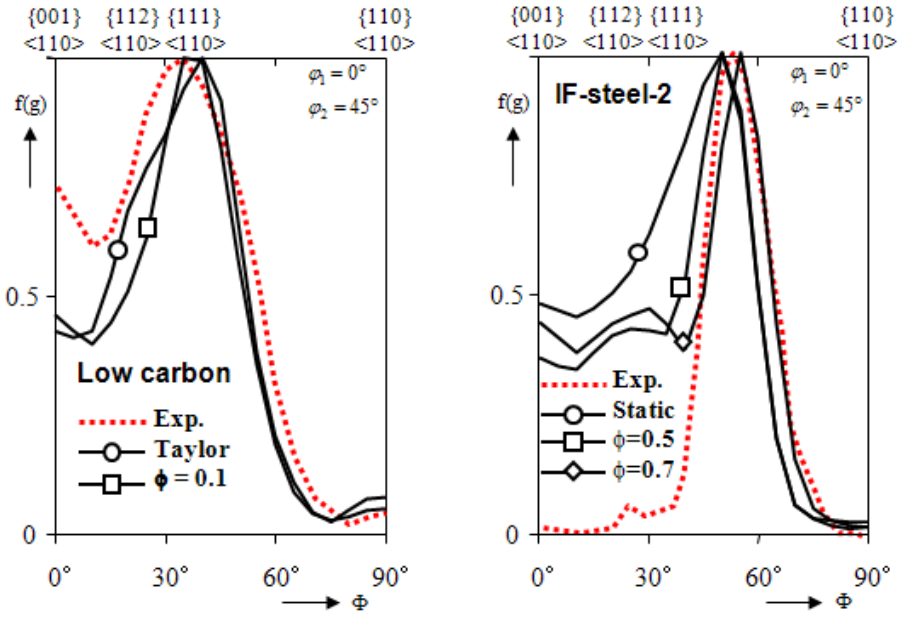

Fig. R-4. Textures prédites de laminage pour les métaux CC (fibre α) et comparaison avec les résultats expérimentaux (acier bas carbone et acier IF-2)

Chapitre VI

Le modèle ϕ a été étendu aux métaux HC. Dans la première partie de ce chapitre, le modèle-ϕ est utilisé pour prédire l'évolution de la texture de laminage dans les métaux HC, voir Fig.R-5. Les résultats sont comparés avec le modèle VPSC. L'effet du glissement pyramidal sur la texture de laminage est également étudié. Nous avons montré qu'une forte activité de glissement pyramidal conduit à une séparation du pole basale vers la direction de laminage.

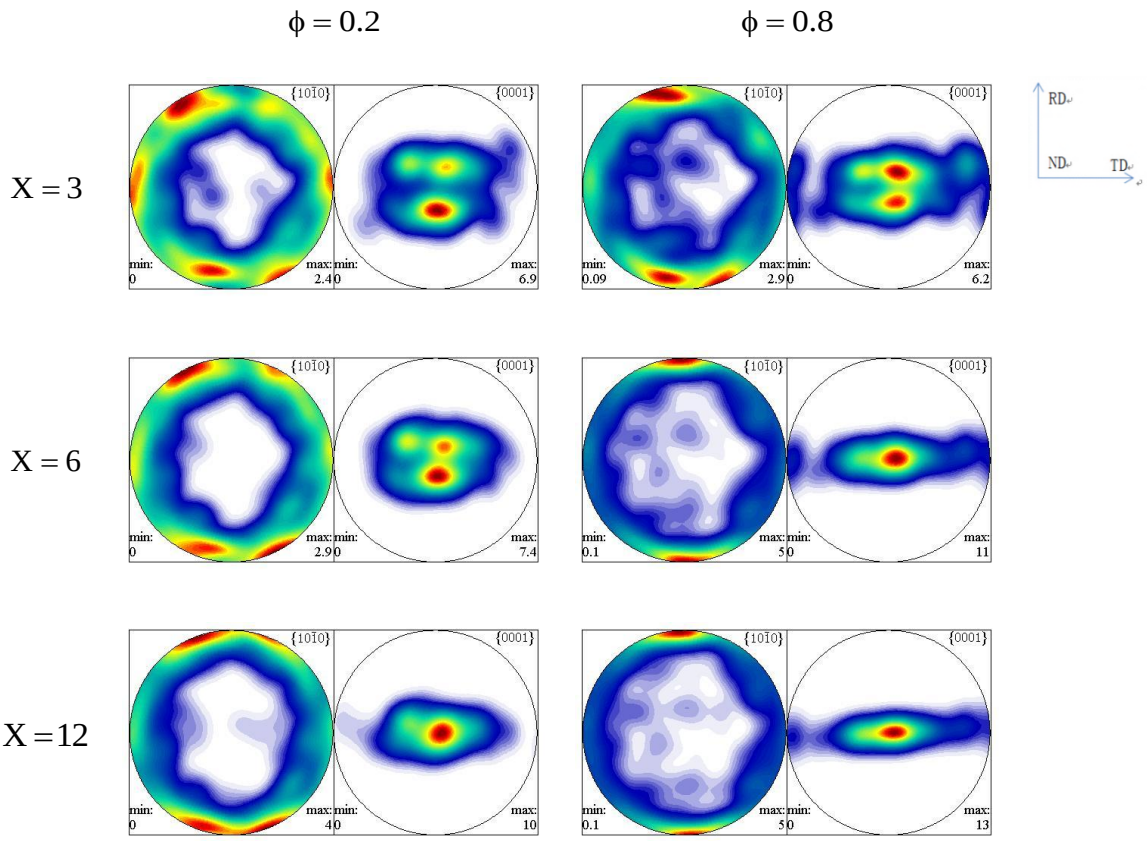

Fig. R-5. Effect du glissement pyramidal sur les textures de laminage pour les métaux HC métaux ($\tau_{basal} : \tau_{<c+a>} : \tau_{tw} = 1 : X : 2$) sous forme de (0002) and $(10\bar{1}0)$ pole figures , $\varepsilon_{eq} = 30\%$

Dans la deuxième partie, nous avons simulé le comportement mécanique du AZ31 qui est un alliage de magnésium. Nous avons considéré différentes forces d'interaction intergranulaire et comparé les résultats prédits avec les résultats expérimentaux tirés de la littérature. Les tests sont effectués pour le laminage (déformation en compression plane), ainsi que pour les tests de traction et de compression sur des feuilles laminées. Nous montrons que le modèle-ϕ avec de grandes valeurs de ϕ prédit des résultats en bon accord avec les textures expérimentales.

Mots-clé

Matériaux polycristallins, plasticité cristalline, texture cristallographique, visco-plasticité, modèle intermédiaire, maclage, interaction inter-granulaire, modèle-ϕ.

Abstract

The computation of the macroscopic response of polycrystalline aggregates from the properties of their constituent single-crystal grains is considered as one of the main problems in materials mechanics. During the mechanical deformation processing, all the grains in the polycrystalline material sample are reoriented. A crystallographic texture may thus be developed which is responsible for the material anisotropy. Therefore, the modeling of the texture evolution in polycrystals is important to predict the anisotropy effects that are present in many industrial processes.

The formulation of metallic polycrystals plasticity has been the subject of many studies and different approaches have been proposed. These homogenization techniques span from the classical bounds (Taylor and Sachs) to the more sophisticated self-consistent approaches. Ahzi and M'Guil developed a novel viscoplastic ϕ-model. This model takes into account the grains interaction effects without involving the Eshelby inclusion problems. The proposed interaction law allows spanning the results from the upper to the lower bound models by varying a single interaction strength parameter ϕ. This model provides the novelty on the formulation and shows a good performance on the prediction of plastic deformation behavior and texture evolution in metals during forming processes.

In this thesis, the ϕ-model was applied to different crystallographic structures and under different loading conditions. The mechanical twinning has been taken into account in the model. The FCC rolling texture transition from copper-type to brass-type texture is studied. In this part of the work, two definitions for the crystal lattice spin are considered: mathematical analysis (MA) and plane strain analysis (PSA). The influence of these two definitions, MA and PSA, on the rolling textures evolution in FCC metals is analyzed. In addition, the influence of twinning and the interaction strength between the grains (controlled by the parameter ϕ) is also analyzed.

The shear tests in FCC metals are also studied. The predicted results are compared with experimental shear textures for a range of metals having a high/medium stacking fault energy (SFE) to low SFE. We have shown that the ϕ-model is able to predict a transition from shear texture characterizing a range of FCC metals with high/medium SFE to low SFE. The twinning mechanism is included in the ϕ-model to improve the shear texture predictions for low SFE metals.

In the study of BCC metal, we compare our predicted results with those predicted by the viscoplastic self-consistent (VPSC) model. We study the slip activities, texture evolutions and the evolution of yield loci. We also present a comparison with experimental textures from literatures for several BCC metals under cold rolling tests. Possible links between the parameter ϕ and the microstructure characteristics such as grain size are briefly mentioned.

The model has also been extended to HCP metals. We predict the deformation behaviors of the magnesium alloy (AZ31) for different interaction strengths. We also compare our predicted results with experimental data from literatures. Tests are carried out in plane strain compression, tensile and compression on the rolled AZ31 sheets. We show that the results predicted by the ϕ-model are in good agreement with the experimental ones.

Keywords:

Polycrystalline materials, crystal plasticity, texture evolution, visco-plasticity, intermediate model, mechanical twinning, grain interaction strength, ϕ-model.

Introduction

The polycrystalline materials consist of a large number of single crystals (called grains). Each grain shows a strong anisotropic behavior. The macroscopic mechanical behaviors of the polycrystals strongly depend on the distribution of the grain orientations and the single crystal behavior of the polycrystalline material. If the grains have a random orientation distribution, the macroscopic mechanical properties are the same in all directions and therefore the material is isotropic. In contrast, if the grains are preferably oriented in some given crystallographic directions, the material is therefore anisotropic. The distribution of crystallographic orientations of a polycrystalline sample is defined as the crystallographic texture.

For polycrystalline metals, the crystallographic texture is the main source of plastic anisotropy. It strongly influences the mechanical properties of the metals such as formability, which is important for the sheet metal forming in industrial applications. Therefore, the texture evolution should be taken into account for the modeling of anisotropy effects in forming processes.

The formulation of metallic polycrystals plasticity has been the subject of many studies and different approaches have been proposed. These homogenization techniques span from the classical bounds Taylor (i.e. Asaro and Needleman, 1985; Parks and Ahzi, 1990; Taylor, 1938) and Sachs (i.e. Ahzi et al., 2002; Leffers and Ray, 2009; Sachs, 1928) models to the more sophisticated self-consistent approaches (Abdul-Latif, 2004; Abdul-Latif and Radi, 2010; Lebensohn and Tomé, 1993; Lebensohn et al., 2007; Mercier and Molinari, 2009; Molinari et al., 1987). The main insufficiency of most existing crystal plasticity models is that they are unable to predict the results from a stiff interaction to a more compliant interaction. This insufficiency leads to a lacking ability of prediction of large scale results. For example, in rolling tests, FCC metals usually develop 2 types of texture: copper- and brass-type (Leffers and Ray, 2009). From the simulation point of view, the Sachs-type models cannot predict the copper-type texture. The Taylor-type model and the well-known visco-plastic self-consistent

(VPSC) model cannot predict the brass-type texture unless the twinning mechanism is considered (Leffers and Ray, 2009; M'Guil et al., 2009, 2011). However, certain materials with specific microstructures or under specific loading conditions can develop a brass-type texture even if no twinning has been detected (Engler, 2000; Engler et al., 1994). This lacking ability of correctly capturing texture transitions calls for new crystal plasticity models.

Ahzi and M'Guil (2008) developed a novel viscoplastic ϕ-model which includes grain interactions effects in a new and original way. The interaction law of the ϕ-model is expressed similarly to the self-consistent one but the interaction tensor is independent of the Eshelby tensor. This model is formulated by the minimization of a specific function combining the local fields' deviations (strain rate and stress) from the macroscopic ones. This function depends also on a tuning parameter, ϕ between 0 and 1 which allows the grain strength interaction to vary from a stiff interaction (small values of ϕ) to a more compliant interaction (high values of ϕ). This model provides the novelty on the formulation and shows a good performance on prediction of plastic deformation behavior and texture evolution in metals during forming processes. Although the advantage of this model is significant, it can still be modified and complemented. Therefore, the main objective of this work is to improve and extend the ϕ-model and to apply this model on the texture evolution predictions in various metals during the plastic deformation. Such a work will fulfill the need for a better understanding of plastic deformation behavior and forming of metals which allows optimizing industrial processing.

In this work, the mechanical twinning, which is one of the basic plastic deformation mechanisms in polycrystals materials, has been implemented into the ϕ-model. The coupled effect of mechanical twinning and the interaction strength (controlled by the ϕ parameter) on the texture evolution has been studied in FCC metals under different loading conditions. The possibility of the FCC rolling texture transition from copper- to brass-type textures has been discussed. The consideration of mechanical twinning also allows applying the ϕ-model

to HCP metals. In addition, the ϕ-model has been extended to BCC metals. The BCC rolling textures are predicted and compared to experimental results.

The details of each chapter are presented as follow:

Chapter I

The chapter I consists of a literature survey on the crystal plasticity modeling. We briefly present the microscopic modeling including the constitutive framework, hardening laws and twinning models. Then, the concept of texture in polycrystals and the main existing homogenization models are summarized.

Chapter II

The new visco-plastic ϕ-model is introduced in detail in this chapter. After the presentation of the ϕ-model formulation, we shortly summarize the numerical aspects of the ϕ-model in literatures (Ahzi and M'Guil, 2008; M'Guil et al., 2009, 2011). At the end of this chapter, we propose a study of the ϕ-model on the normalized stress and strain rate deviations and the evolution of the interaction tensor.

Chapter III

In the chapter III, the FCC rolling texture transition from copper- to brass-type texture has been studied using the visco-plastic ϕ-model. The prediction of the rolling texture evolution in FCC metals is controlled by interaction laws, deformation mechanisms and definition of the lattice spin. The coupled effect of these three factors on the FCC rolling texture evolution is hereby analyzed. In this work, two definitions of the lattice spin, the mathematical analysis (MA) and the plane-strain analysis (PSA), are considered in the ϕ-model. The influence of the MA and PSA definitions on the FCC rolling texture evolution is deeply analyzed in conjunction with twinning and grain interaction strength, from a stiff interaction to a more compliant interaction. A typical brass-type texture has been achieved which is usually

observed in metals with low Stacking Fault Energy (SFE).

Chapter IV

In this chapter, we show that the polycrystalline ϕ-model can be used to compute simple shear crystallographic texture transition for FCC at large strains. Predicted results are compared to experimental shear textures for high/medium SFE metals (i.e. copper) and low SFE metals (i.e. silver). We show that the ϕ-model is able to predict a clear shear texture transition characterizing a range of FCC metals having high/medium to low SFE. The twinning mechanism is included to improve the predicted shear textures for low SFE metals. The effect of twinning on the ideal shear texture components is shown and is consistent with experimental results from literature.

Chapter V

The BCC rolling textures and the corresponding yield surfaces are simulated using the ϕ-model in this chapter. We compare our results to those predicted by the visco-plastic self-consistent (VPSC) model. The results are compared in terms of predicted slip activity, texture evolution and yield loci. We also present a qualitative comparison with experimental cold rolling textures taken from the literature for several BCC metals.

Chapter VI

The ϕ-model has been extended to HCP metals. We simulated the deformation behavior of AZ31 magnesium alloy with different intergranular interaction strengths and compared the predicted results with experimental ones taken from the literatures. Tests are performed for rolling (plane strain compression) as well as for tensile and compressive tests on rolled sheets. We show that the ϕ-model predicts results in good agreement with the experimental ones.

References:

Asaro, R.J., Needleman, A., 1985. Texture development and strain hardening in rate dependent polycrystals. Acta Metall. 33, 923-953.

Parks, D.M., Ahzi, S., 1990. Polycrystalline plastic deformation and texture evolution for crystals lacking five independent slip systems. J. Mech. Phys. Solids. 38, 701-724.

Taylor, G.I., 1938. Plastic strain in metals. J. Inst. Metals. 62, 307-324.

Ahzi, S., M'Guil, S., Agah-Tehrani, A., 2002. A new formulation for the elastic-viscoplastic lower bound and intermediate modeling for polycrystalline plasticity. Mater. Sci. Forum. 408-412, 463-468.

Leffers, T., Ray, R.K., 2009. The brass-type texture and its deviation from the copper-type texture. Prog. Mater.Sci. 54, 351-396.

Sachs, G., 1928. Plasticity problems in metals. Z. Ver. Deutsch. Ing.72, 734-736.

Abdul-Latif, A., 2004. Pertinence of the grains aggregate type on the self-consistent model responses. Int. J. Sol. Struct. 41, 305-322.

Abdul-Latif, A., Radi, M., 2010. Modeling of the grain shape effect on the elastic–inelastic behavior of polycrystals with self-consistent scheme. J. Eng. Mat. Tech. 132, 011008.

Lebensohn, R.A., Tomé, C.N., 1993. A self-consistent anisotropic approach for the simulation of plastic deformation and texture development of polycrystals: application to zirconium alloys. Acta Metall. Mater. 41, 2611-2624.

Lebensohn, R.A., Tomé, C.N., Castañeda, P.P., 2007. Self-consistent modelling of the mechanical behaviour of viscoplastic polycrystals incorporating intragranular field fluctuations. Philosophical Magazine. 87, 4287-4322.

Mercier, S., Molinari, A., 2009. Homogenization of elastic-viscoplastic heterogeneous materials: Self-consistent and Mori-Tanaka schemes. Int. J. Plasticity 25, 1024-1048.

Molinari, A., Canova, G.R., Ahzi, S., 1987. A self-consistent approach of the large deformation polycrystal viscoplasticity. Acta Metall. 35, 2983-2994.

M'Guil, S., Ahzi, S., Barlat, F., Gracio, J.J., 2011. Simulation of microstructural effects and yield surface evolution in cubic metals using the viscoplastic ϕ-model. Int. J. Plasticity 27, 102-120.

M'Guil, S., Ahzi, S., Youssef, H., Baniassadi, M., Gracio, J.J., 2009. A comparison of viscoplastic intermediate approaches for deformation texture evolution in FCC polycrystals. Acta Mater. 57, 2496-2508.

Ahzi, S., M'Guil, S., 2008. A new intermediate model for polycrystalline viscoplastic deformation and texture evolution. Acta Mater. 56, 5359-5369.

Chapter I. Background: crystal plasticity modeling

I.1 Introduction of polycrystals

Metallic materials belong to the group of polycrystals, and it is one of the most common used materials in industrial application. This kind of material can usually be largely deformed during forming process due to its relative high ductility. The works of this thesis mainly focus on the micro-macro mechanic modeling of metallic materials under large plastic deformation. It is therefore important to understand the microstructure of polycrystals as well as their micro mechanisms of plastic deformation.

I.1.1 Microstructure in single crystal

The single crystal (called grain) is the basic unit in polycrystalline materials such as metals. Within each single crystal, the metal atoms are linked with metallic bonds and regularly arranged and distributed in space. The polycrystal structure and pattern of the crystal lattice space are presented in Fig. 1-1.

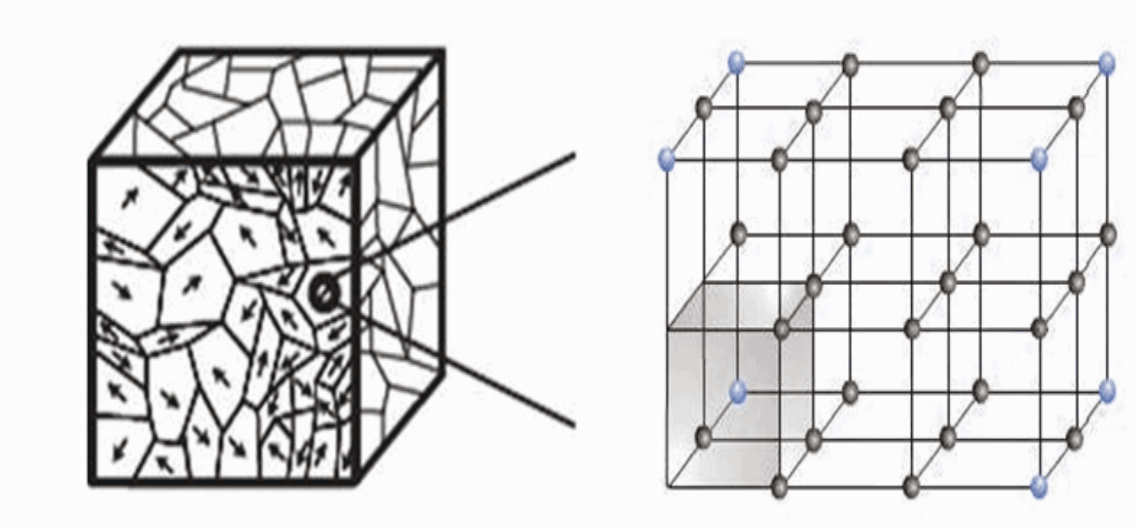

Fig. 1-1. Representation of space lattice and unit cell in grains

The atoms in single crystals may be arranged in different ways which can influence the mechanical properties of the metals. The atom arrangement can be represented by the form of the unit cell. The common crystal systems in metallic materials are: Face Centered Cubic (FCC, an extra atom on each side of the cubic unit cell), e.g. Ag, Cu, brass; Body Centered Cubic (BCC, an extra atom in the center of the cubic unit cell), e.g. Fe, Li, Mo; and Hexagonal Closed Packed (HCP), e.g. Mg, Ti.

I.1.2 Plastic deformation mechanisms in polycrystals

Usually, if an elastic deformation occurs in a material, its microstructure will not show permanent changes. The material will return to its original shape and dimension when the stress is removed. The plastic deformation usually involves the microstructure changes. In the forming process of metals, large strain is usually required. In this case, the plastic deformation is important whereas the elastic deformation can be neglected. In single crystals, the plastic deformation can be activated by several mechanisms. Two basic plastic deformation mechanisms: crystallographic slip and twinning, will be introduced in the next section.

I.1.2.1 Deformation by slip

The crystallographic slip is produced by the dislocation motion of the atoms in the single crystals. As shown in Fig. 1-2, if the shear stress suffered by a single crystal exceeds a threshold value, some parts of the crystal lattice will glide along each other. The atoms dislocate a whole space between atoms. The slip occurs only on certain planes and directions which depend on the crystal systems. Usually, the slips occur on the plans and directions in which the atoms are most closely packed due to energy reasons.

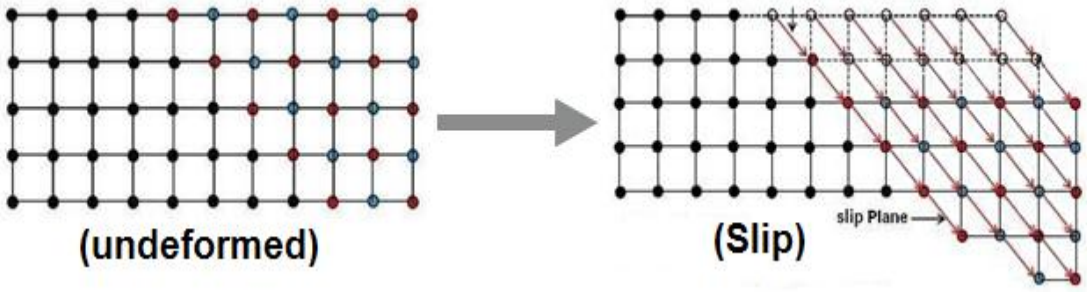

Fig. 1-2. Schematic representation of crystallographic slip.

I.1.2.2 Deformation by twinning

Mechanical twinning can be found in metals with certain properties or under certain loading conditions. The twinning mechanism is proved to be influenced by Stacking Fault Energy (SFE), temperature, strain rate etc. (Christian and Mahajan, 1995). The mechanical twinning is activated by a strong shear stress. If the twinning is activated, part of the lattice structure will be rearranged and the twinned region (child region) will become mirrored to the original region (parent region). The schematic description of twinning is presented in Fig. 1-3.

We note that the mechanical twinning can be activated only on one direction whereas the slip can be activated on both positive and negative directions. The volume fraction of the twinned region has been reported by some experimental investigations (e.g. Leffers and Ray, 2009). For example, under rolling tests, the experimental volume fraction of deformation twins is less than 25% for brass with 30% zinc content at high reduction.

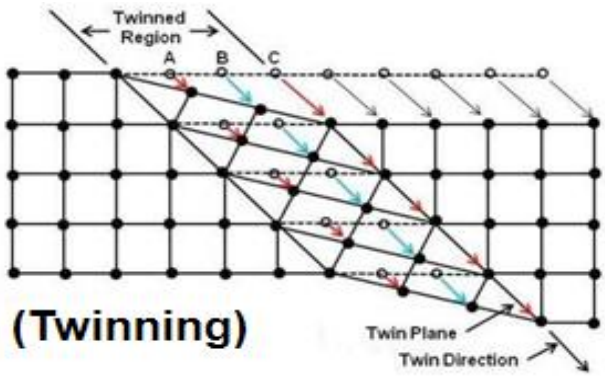

Fig. 1-3. Schematic representation of crystallographic twinning.

I.2 Description of crystallographic planes and directions

The structure of lattice and unit cell usually leads to strong anisotropic behavior because the plastic deformation mechanisms such as slip and twinning (see section I.1.2) can only occur on certain planes and directions. Therefore, in the modeling, the crystallographic planes and directions need to be specified. Three integers Miller Indices are usually used to describe the crystallographic directions and planes.

The crystallographic direction can be denoted by three normalized integer [u v w]. In cubic lattice structure, u, v, and w represent the normalized length of the projection of this vector on the three axis $O\vec{X}$, $O\vec{Y}$, $O\vec{Z}$. The Fig. 1-4a presents some crystallographic directions. We note that all the parallel directions are represented by the same indices.

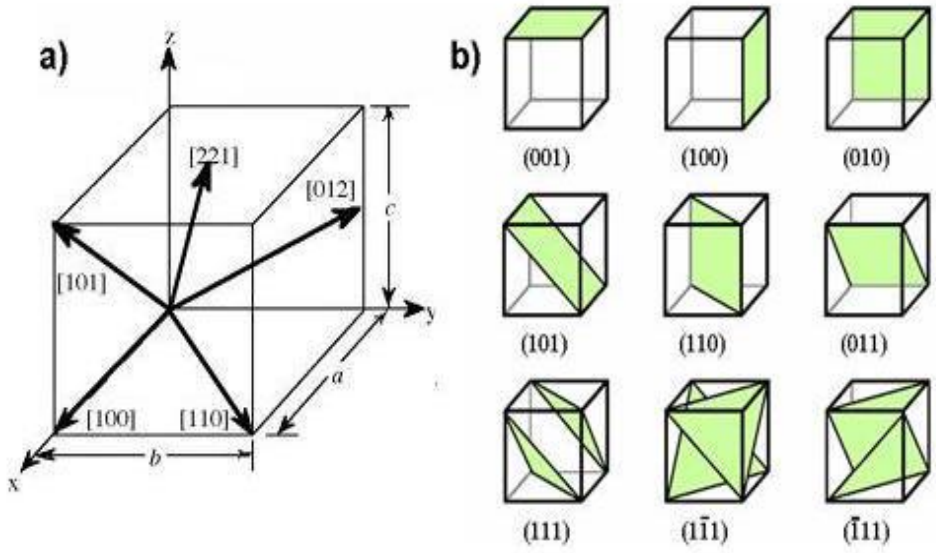

Fig. 1-4. Example of several crystallographic directions (a) and planes (b) in cubic lattice structure.

The Miller indices representing the orientation of a plane in a cubic lattice are defined as follows: We measure the intercept of the plane with the axes along the three axis. These intercepts x, y, and z are defined as fractional multiple of the length a, b and c along the three axis, respectively. The obtained integers (x y z) should be then inverted as (1/x 1/y 1/z) and reduce this set to a similar one having the smallest integers by multiplying by a common factor. This set is called Miller indices of the plane (h k l). Some crystallographic planes are shown in Fig. 1-4b as example.

In HCP lattice structure, the crystallographic directions and plans are identified using a reference frame with four coordinate axes instead of three. As shown in Fig. 1-5, $O\vec{A}_1$, $O\vec{A}_2$, $O\vec{A}_3$ and $O\vec{C}$ are the four coordinate axis. Thus, the planes and direction in HCP structures should be identified by four integers: $[u^h\ v^h\ m^h\ w^h]$ for directions and $(h^h\ k^h\ n^h\ l^h)$ for planes. Those integers can be obtained in the same way as in cubic systems.

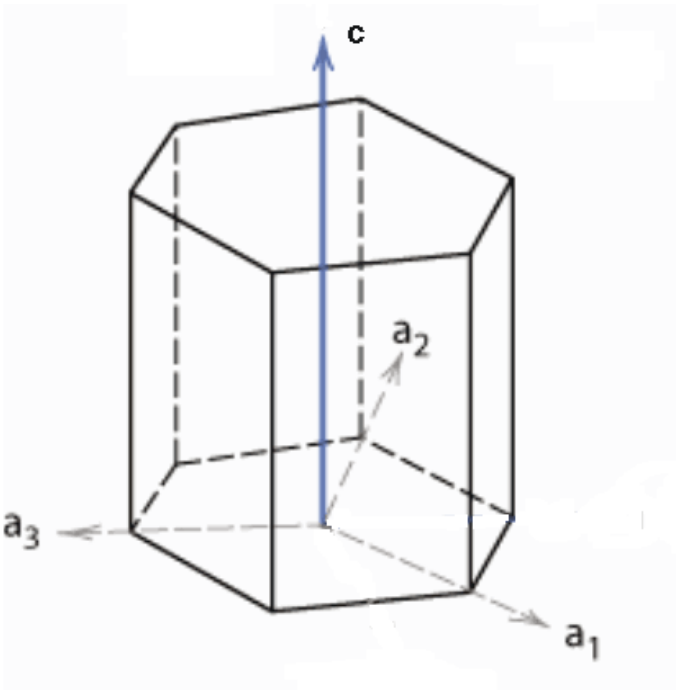

Fig. 1-5. Coordinate system to identify the crystallographic planes and directions in HCP structures.

The families of a crystallographic directions (or planes) are defined as a set of directions (or planes) which are equivalent due to symmetry operations. For example, the family of direction $\langle 110 \rangle$ includes the following directions: $[\bar{1}10]$, $[10\bar{1}]$, $[01\bar{1}]$, $[110]$, $[101]$ and $[011]$, the family of plane $\{110\}$ includes the plans: (110), (101), (011), $(\bar{1}10)$, $(\bar{1}01)$, $(0\bar{1}1)$. It is good to keep in mind that the mechanisms occurred on directions and planes from the same families are normally equivalent.

I.3 Constitutive framework for single crystal

In order to describe the deformation behavior of single crystal, both elastic and inelastic parts of deformation need to be considered. The inelastic deformation of single crystal is mainly accommodated by the plastic deformation mechanisms such as slip and twinning. The elastic part should include the elastic deformation and the lattice spin. Thus, it makes sense to make a polar decomposition of deformation

gradient, Asaro and Needleman (1985) proposes the decomposition of the deformation gradient as follows:

$$\mathbf{F} = \mathbf{F}^{*}\mathbf{F}^{\mathrm{P}} \tag{1-1}$$

Where $\mathbf{F}^{\mathrm{P}}$ is the plastic deformation gradient and $\mathbf{F}^{*}$ represents the rotation of the crystal lattice in which the elastic deformation is included, see Fig. 1-6.

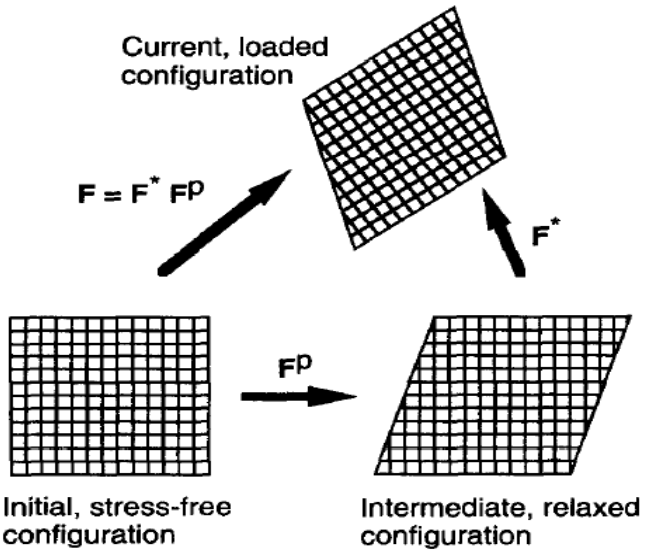

Fig. 1-6. Decomposition of deformation gradient, kinematic scheme proposed by Asaro and Needleman (1985), presented by Kalidindi (1998)

The Eq. 1-2 shows the expression of the microscopic velocity gradient $\mathbf{L}$ which can be divided into the elastic part and a plastic part:

$$\mathbf{L} = \dot{\mathbf{F}}\mathbf{F}^{-1} = \mathbf{L}^{*} + \mathbf{L}^{\mathrm{P}} \tag{1-2}$$

$\mathbf{L}^{\mathrm{P}}$ and $\mathbf{L}^{*}$ can also be divided as:

$$\mathbf{L}^{\mathrm{P}} = \dot{\mathbf{F}}^{\mathrm{P}}\mathbf{F}^{\mathrm{P}-1} = \mathbf{D}^{\mathrm{P}} + \boldsymbol{\Omega}^{\mathrm{P}} = \frac{1}{2}\left(\mathbf{L}^{\mathrm{P}} + \mathbf{L}^{\mathrm{P}\mathrm{T}}\right) + \frac{1}{2}\left(\mathbf{L}^{\mathrm{P}} - \mathbf{L}^{\mathrm{P}\mathrm{T}}\right) \tag{1-3}$$

$$\mathbf{L}^{*} = \dot{\mathbf{F}}^{\mathrm{e}}\mathbf{F}^{\mathrm{e}-1} = \mathbf{D}^{\mathrm{e}} + \boldsymbol{\Omega}^{*} \tag{1-4}$$

Here, $\mathbf{D}^{p}$ and $\mathbf{D}^{e}$ are the plastic and elastic strain rate tensors, respectively. $\mathbf{\Omega}^{p}$ is the plastic spin, and $\mathbf{\Omega}^{*}$ is the lattice spin.

We use the $\mathbf{s}^{\alpha}$ and $\mathbf{n}^{\alpha}$ vectors to represent respectively the slip direction and slip plane normal of the slip system α before deformation. These two vectors can be transformed by the rotation which is expressed as follows:

$$\mathbf{s}^{*\alpha} = \mathbf{F}^{*} \cdot \mathbf{s}^{\alpha} \tag{1-5}$$

$$\mathbf{n}^{*\alpha} = \mathbf{n}^{\alpha} \cdot \mathbf{F}^{*-1} \tag{1-6}$$

We denote that $\mathbf{s}^{\alpha}$ and $\mathbf{n}^{\alpha}$ vectors remain perpendicular after the deformation.

The Schmid tensor in slip system α is defined as:

$$\mathbf{m}^{\alpha} = \mathbf{s}^{*\alpha} \cdot \mathbf{n}^{*\alpha} \tag{1-7}$$

$\mathbf{m}^{\alpha}$ can be decomposed into the symmetric part $\mathbf{P}^{\alpha}$ and the anti-symmetric part $\mathbf{A}^{\alpha}$:

$$\mathbf{m}^{\alpha} = \mathbf{P}^{\alpha} + \mathbf{A}^{\alpha} \tag{1-8}$$

$\mathbf{P}^{\alpha}$ and $\mathbf{A}^{\alpha}$ are defined by the following relation:

$$\mathbf{P}^{\alpha} = 1/2\left(\mathbf{s}^{\alpha} \otimes \mathbf{n}^{\alpha} + \mathbf{n}^{\alpha} \otimes \mathbf{s}^{\alpha}\right) \tag{1-9}$$

$$\mathbf{A}^{\alpha} = 1/2\left(\mathbf{s}^{\alpha} \otimes \mathbf{n}^{\alpha} - \mathbf{n}^{\alpha} \otimes \mathbf{s}^{\alpha}\right) \tag{1-10}$$

Thus, the plastic velocity gradient $\mathbf{L}^{p}$ can be expressed as function of the shear rate $\dot{\gamma}^{\alpha}$:

$$\mathbf{L}^{p} = \sum_{\alpha}^{n} \dot{\gamma}^{\alpha}\left(\mathbf{P}^{\alpha} + \mathbf{A}^{\alpha}\right) = \sum_{\alpha}^{n} \dot{\gamma}^{\alpha}\left(\mathbf{s}^{\alpha} \otimes \mathbf{n}^{\alpha}\right) = \mathbf{D}^{p} + \mathbf{\Omega}^{p} \tag{1-11}$$

with

$$\mathbf{D}^{\mathrm{p}} = \sum_{\alpha}^{\mathrm{n}} \dot{\gamma}^{\alpha} \mathbf{P}^{\alpha} \quad \text{and} \quad \mathbf{\Omega}^{\mathrm{p}} = \sum_{\alpha}^{\mathrm{n}} \dot{\gamma}^{\alpha} \mathbf{A}^{\alpha} \tag{1-12}$$

The plastic deformation in single crystals is considered to be occurred by crystallographic slip and the mechanical twinning associated with slip. The slip mechanisms can be described by the visco-plastic power law which is proposed by Hutchinson (1976):

$$\dot{\gamma}^{\alpha} = \dot{\gamma}_0 \cdot \left(\frac{\tau^{\alpha}}{\mathrm{g}^{\alpha}} \right) \left| \frac{\tau^{\alpha}}{\mathrm{g}^{\alpha}} \right|^{\mathrm{n}-1} \quad \text{with} \quad \tau^{\alpha} = \mathbf{P}^{\alpha} \cdot \mathbf{S} \tag{1-13}$$

Here, $\dot{\gamma}^{\alpha}$ represents the shear rate of a given slip or twinning system α and τ^{α} is the corresponding resolved shear stress. $\dot{\gamma}_0$ is the reference shear rate. n represents the inverse rate sensitivity coefficient. **S** represents the deviatoric Cauchy stress tensor. g^{α} is the critical resolved shear stress (CRSS). The CRSS controls the activities of the slip and twinning systems and can be updated by the hardening laws during the calculation processes (see section I.5). We note that the τ^{α} value must remain positive for twinning systems as the twinning systems can be activated only on one direction. Therefore, if the calculated value of τ^{α} in a twinning system is negative, it will be set as 0.

I.4 Rigid visco-plastic formulation

A rate-sensitive constitutive law can be used to describe the rigid visco-plastic single crystal behavior by relating the plastic strain rate tensor $\mathbf{D}^{\mathrm{p}}$ (elasticity is neglected) and the deviatoric Cauchy stress tensor $\mathbf{S}$ of the single crystal:

$$\mathbf{D} = \mathbf{D}^{\mathrm{p}} = \sum_{\alpha} \left(\frac{\dot{\gamma}_0}{\mathrm{g}^{\alpha}} \right) \left(\frac{\mathbf{P}^{\alpha} \cdot \mathbf{S}}{\mathrm{g}^{\alpha}} \right)^{\mathrm{n}-1} \left(\mathbf{P}^{\alpha} \otimes \mathbf{P}^{\alpha} \right) \cdot \mathbf{S} = \mathbf{M}(\mathbf{S}) \cdot \mathbf{S} \tag{1-14}$$

Here, $\mathbf{M}$ is the microscopic fourth order visco-plastic compliance tensor.

✓ Polycrystal constitutive law

In order to numerically describe the macroscopic behavior of polycrystals, we need to firstly find the relation between the macroscopic strain and stress. This relation can be described by a macroscopic constitutive law which is proposed in a similar way of the microscopic one (Eq. 1-14):

$$\overline{\mathbf{D}} = \overline{\mathbf{M}} \cdot \overline{\mathbf{S}} \quad \text{or} \quad \overline{\mathbf{S}} = \overline{\mathbf{L}} \cdot \overline{\mathbf{D}} \tag{1-15}$$

Where $\overline{\mathbf{L}} = \overline{\mathbf{M}}^{-1}$. $\overline{\mathbf{D}}$, $\overline{\mathbf{S}}$ and $\overline{\mathbf{M}}$ represent the macroscopic plastic strain rate, the macroscopic deviatoric Cauchy stress and the macroscopic fourth order visco-plastic compliance tensor, respectively. The consistency conditions need to be fulfilled which are given by the averaging conditions:

$$\overline{\mathbf{D}} = \langle \mathbf{D} \rangle \quad \text{and} \quad \overline{\mathbf{S}} = \langle \mathbf{S} \rangle . \tag{1-16}$$

Here, $\langle \cdot \rangle$ denotes the volume average over the polycrystals.

I.5 Hardening laws

In polycrystals, hardening corresponds to the phenomena that, during the plastic deformation, the plastic mechanisms become harder to be activated due to the modification of microstructure. As results, the strength characteristics (hardness, yield strength, etc.) of materials are increased whereas the ductility is decreased.

For the modeling point of view, the hardening is usually described by the modification of the critical resolved shear stress g^{α} in the nonlinear constitutive law (Eq. 1-14). This parameter is the reference value of shear stress which describes the resistance of the activation of plastic mechanisms such as slip and twinning. The

hardening laws of Latent and Voce are commonly used to describe the microscopic strain hardening in polycrystals.

I.5.1 Latent hardening law

In the latent hardening law, the increment of CRSS in system α can be calculated as follow:

$$\dot{g}^{\alpha} = \sum_{\beta} \mathbf{H}^{\alpha\beta} \left| \dot{\gamma}^{\beta} \right| \tag{1-17}$$

Here, the $H^{\alpha\beta}$ represents the $n \times n$ hardening matrix. Kalidindi et al. (1992) proposed the expression of $H^{\alpha\beta}$ as follow:

$$\mathbf{H}^{\alpha\beta} = q^{\alpha\beta} h_0 \left[1 - \frac{g^{\alpha}}{g_{sat}} \right]^{a} \tag{1-18}$$

Here, h_0 represents the initial hardening slope. g_{sat} is the stress level for the hardening saturation. The matrix $q^{\alpha\beta}$ described the Latent hardening behavior of the single crystal (Franciosi et al., 1980; Kocks, 1970; Tomé et al., 1984). This $n \times n$ matrix (n = the total number of considered slip and twinning systems) is populated by 1 (for coplanar systems) and q (for non-coplanar systems). The q is the latent hardening ratio usually taken between 1 and 1.4 (Franciosi et al., 1980; Kocks, 1970; Tomé et al., 1984).

The Eq. 1-19 shows the form of matrix $q^{\alpha\beta}$ when the 12 FCC slip systems are considered.

$$q^{\alpha\beta} = \begin{bmatrix} \mathbf{A} & q\mathbf{A} & q\mathbf{A} & q\mathbf{A} \\ q\mathbf{A} & \mathbf{A} & q\mathbf{A} & q\mathbf{A} \\ q\mathbf{A} & q\mathbf{A} & \mathbf{A} & q\mathbf{A} \\ q\mathbf{A} & q\mathbf{A} & q\mathbf{A} & \mathbf{A} \end{bmatrix} \quad \text{with} \quad \mathbf{A} = \begin{bmatrix} 1 & 1 & 1 \\ 1 & 1 & 1 \\ 1 & 1 & 1 \end{bmatrix} \tag{1-19}$$

I.5.2 Voce hardening law

In this thesis, we use the voce hardening law (Voce, 1948) to describe the hardening effect in polycrystals. In this hardening law, the evolution of the CRSS of slip or twinning system α for a single crystal is calculated as follows:

$$\dot{g}^{\alpha}(\Gamma) = \tau_0 + (\tau_1 + \theta_1\Gamma)\left(1 - \exp\left(-\Gamma\left|\frac{\theta_0}{\tau_1}\right|\right)\right) \tag{1-20}$$

In Eq. 1-20, Γ is the shear rate accumulated in this grain. The parameters τ_0, τ_1, θ_0 and θ_1 can be determined from the experimental strain-stress curves. The parameters τ_0 and θ_0 describe the initial flow and the initial rate of hardening in the grain, respectively. The parameters θ_1 , τ_1 describe the asymptotic characteristics of strain hardening. The condition $\theta_0 \geq \theta_1$, $\tau_1 > 0$ corresponds to an increase in yield stress and a decrease in the hardening rate to a linear saturation. The linear hardening is the limiting case of this law where the four hardening parameters are set to be $\tau_0 = 1, \tau_1 \to 0$, $\theta_0 = 1$ and $\theta_1 = 1$.

A 'self' and 'latent' hardening coupling parameter $h^{\alpha\beta}$ is introduced to describe the barrier effect between the activated slip or twinning modes (Tomé et al., 1984):

$$\Delta g^{\alpha} = \frac{dg^{\alpha}}{d\Gamma}\sum_{\beta} h^{\alpha\beta}\Delta\gamma^{\beta} \tag{1-21}$$

We denote that $h^{\alpha\beta}$ is a $n \times n$ matrix where n is the total number of activated slip or twinning systems. The component of $h^{\alpha\beta}$ should be set as 1 if the α and β systems belong to the same slip or twinning mode. We denote that the voce hardening law can be used for both crystallographic slip systems and the slip systems associated with mechanical twinning.

I.6 Modeling of mechanical twinning

The mechanical twinning may affect the plastic deformation in two ways: via the orientations of twinning and via the slip associated with the formation of twinning. Several models have been proposed to describe the effect of twinning on the plastic deformation. In this section, we propose an introduction of the Van Houtte model (Van Houtte, 1978), the Anand-Kalidindi model (Kalidindi, 1998; Staroselsky and Anand, 1998) and the Predominant Twin Reorientation (PTR) scheme (Tomé et al., 1991). The PTR scheme is the one used in this thesis.

I.6.1 Van Houtte twinning model

In the model of Van Houtte, each grain is divided into several sub-grains. The sub-grains have the same orientation and are calculated independently. During the simulation, those grains are randomly picked with a fixed probability at each deformation step and the picked grains are orientated along a given twinning system. We note that the probability should be set the same as the twinning volume fraction in this step.

The Van Houtte model can successfully describe the effect of twinning in the simulations (Van Houtte, 1978). However, this model can only rotate the grains along the given twinning system which may not be the most active twinning system (Tomé et al., 1991). This disadvantage may reduce the accuracy of simulations. This model may also largely increase the required computational time because large numbers of sub-grains are needed to ensure the accuracy of the twinning volume fraction (Tomé et al., 1991).

I.6.2 Anand-Kalidindi twinning model

The Anand-Kalidindi twinning model (Kalidindi, 1998; Staroselsky and Anand, 1998) proposes another way to describe the twinning orientation. In this model, the deformation gradient is decomposed in the same way as Asaro and Needleman (1985), see section I.3. However, the deformed matrix is divided into twined region and untwined region (see Fig. 1-7). Therefore, the mechanical response needs to be expressed by the combination of those regions.

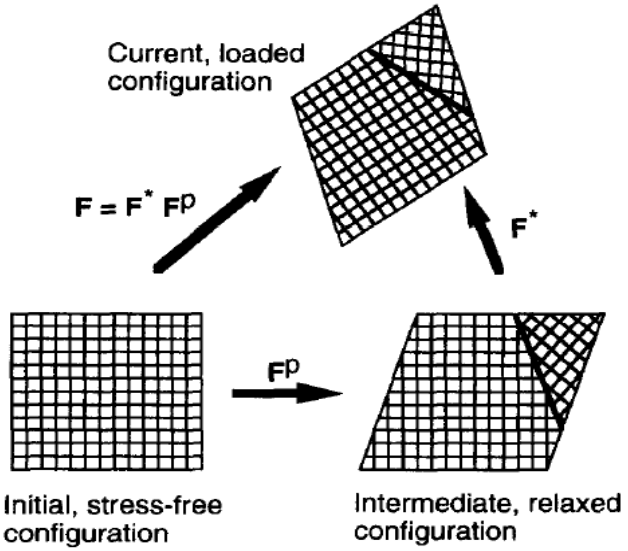

Fig. 1-7. Decomposition of deformation gradient, kinematic scheme proposed by Kalidindi (1998) and Staroselsky and Anand (1998)

Based on this idea, Kalidindi (1998) and Staroselsky and Anand (1998) split the Schmid tensor $\mathbf{m}^{\alpha}$ of the slip or twinning system $\mathbf{m}^{\alpha}$ into three parts: $\mathbf{m}^{\alpha}_{\mathbf{s\text{-}untw}}$ for the slip systems in the untwined region; $\mathbf{m}^{\alpha}_{\mathbf{tw\text{-}untw}}$ for the twinning systems in the untwined region; $\mathbf{m}^{\alpha}_{\mathbf{s\text{-}tw}}$ for the slip systems in the twined region. Thus, the plastic velocity gradient $\mathbf{L}^{P}$ in Eq. 1-11 can be extended considering the twinning volume

fraction in the matrix:

$$\mathbf{L}^{\mathrm{p}} = \mathrm{f}\sum_{\alpha}^{\mathrm{Ns-t}}\dot{\gamma}^{\alpha}\mathbf{m}_{\mathrm{s-tw}}^{\alpha} + (1-\mathrm{f})\sum_{\alpha}^{\mathrm{Ns}}\dot{\gamma}^{\alpha}\mathbf{m}_{\mathrm{s-untw}}^{\alpha} + \sum_{\alpha}^{\mathrm{Ntw}}\dot{\mathrm{f}}^{\alpha}\gamma^{\mathrm{tw}}\mathbf{m}_{\mathrm{tw-untw}}^{\alpha} \tag{1-22}$$

Here, f is the twinning volume fraction. Ns-t, Ns and Ntw represent the number of slip systems in twined region, number of slip systems in untwined region, and number of twinning systems in untwined region, respectively. f^{α} is the twinning volume fraction accumulated by twinning system α. γ^{tw} refers to the shear strain of twinning systems which is suggest to be constant (Kalidindi, 1998, 2001). In the last term, $\dot{\mathrm{f}}^{\alpha}\gamma^{\mathrm{tw}}$ represents the equivalent shear rate in twinning system α. We note that in this model, twinning is not associated with slip.

The deviatoric Cauchy stress tensor can also be divided into untwined part $\mathbf{S}^{\mathbf{untw}}$ and the twined part $\mathbf{S}^{\mathbf{tw}}$. We note that, when we calculated τ^{α} (see Eq. 1-15) for a slip (or twinning) system in twined (or untwined) region, the corresponding Cauchy stress tensor and Schmid tensor should be used. The Cauchy stress tensor in the single crystal can be calculated by a linear combination of the twined and untwined parts:

$$\mathbf{S} = (1-\mathrm{f})\cdot\mathbf{S}^{\mathbf{untw}} + \mathrm{f}\cdot\mathbf{S}^{\mathbf{tw}} \tag{1-23}$$

At each deformation step, certain amount of volume fraction may be transferred from the untwined region to the twined regions. We should notice that each twinning system may create a twined region. For a twinning system α, the transferred volume fraction can be calculated as:

$$\Delta\mathrm{f}^{\alpha} = \frac{\dot{\gamma}_0}{\gamma^{\mathrm{tw}}}\left(\frac{\tau^{\alpha}}{\mathrm{g}^{\alpha}}\right)^{\mathrm{n}}\Delta\mathrm{t} \tag{1-24}$$

We note that the $\Delta\mathrm{f}^{\alpha}$ should be set to 0 if the calculated τ^{α} is negative as the twinning can be only activated on the positive direction. The orientation of the twined

region is obtained according to the direction of corresponding twinning system.

I.6.3 The Predominant Twin Reorientation (PTR) scheme

In the single crystal plasticity framework for single crystals (see section I.3), the twinning is associated with slip and should be calculated as normal slip but only activated on the positive direction. Meanwhile, the twinning orientation (twinning volume fraction, direction of orientation, etc.) needs to be described.

In this thesis, we used the Predominant Twin Reorientation (PTR) scheme proposed by Tomé et al. (1991) which was used by several authors (Abdolvand and Daymond 2012; Beyerlein et al. 2011; Prakash et al., 2008, Schmid et al., 2007). In this model, the associated volume fraction is defined in each twinning system of one grain, as: $V^{t,g} = \gamma^{t,g} / S^t$. Here, $\gamma^{t,g}$ represents the shear strain contributed by the twin systems and S^t is the characteristic twin shear. The twinning system in this grain with the highest associated volume fraction is identified as the predominant twin system (PTS). The sum of the associated volume fraction over all twinning systems in a given twinning mode is defined as the accumulated twin fraction: $V^{acc,g} = \sum_t \gamma^{t,g} / S^t$. At each deformation incremental step, a grain is picked randomly, and the grain will be fully reoriented if the accumulated twin fraction exceeds a threshold value which is defined as:

$$V^{th} = A^{th1} + A^{th2} \frac{V^{eff}}{V^{acc}} \tag{1-25}$$

In Eq. 1-25, V^{eff}, called the effective twinned fraction, represents the volume fraction of the grains that are already reoriented, and the values of A^{th1} and A^{th2} can be determined by either single-crystal experiments or fitting to a known polycrystals response. The V^{acc} is the sum of the associated volume fraction over all

twinning systems and over all grains: $V^{acc} = \sum_{g} \sum_{t} V^{t,g}$. Once the condition is fulfilled, the grain will be completely reoriented and only the PTS is considered in the reorientation. Then, both V^{eff} and V^{acc} will be updated. This process will be repeated until either all grains are randomly picked or the V^{eff} exceeds the accumulated twin volume.

The PTR scheme can well define the direction of the twinning as only the PTS is considered in the twinning reorientation. The main disadvantage of this model is the reorientation of the entire grain. In polycrystals, only a part of the grain should be reoriented due to the twinning. Therefore, the PTR scheme could overestimate the twinning volume fraction (Beyerlein et al. 2011; Prakash et al., 2008, Schmid et al., 2007).

I.7 Crystallographic texture and its evolution

The crystallographic texture is an important source of anisotropy in polycrystals. The macroscopic mechanical behavior cannot be well predicted if the texture is not taken into account. In each single crystal, the mechanisms of the plastic deformation usually occur on certain planes and directions. Therefore, its mechanical properties are strongly influenced by the orientation of the grain and therefore anisotropic. Furthermore, the microscopic anisotropy can influence the macroscopic behavior of the polycrystals. If the grains have a random orientation distribution, the macroscopic mechanical properties are the same in all directions and therefore isotropic. In contrast, if the grains are preferably oriented in some given crystallographic directions, the material is therefore anisotropic.

The crystallographic texture is defined as the distribution of crystallographic orientations of a polycrystalline sample. The textures are considered as the main

source of the anisotropy in the polycrystals. In modeling of polycrystals, the evolution of the texture needs to be followed in the entire forming process as the grains eager to rotate to some favored orientations during the plastic deformation. These rotations depend on the mode of deformation imposed on the material and the activated mechanisms in each grain. The crystallographic texture can be predicted by the models applied on polycrystals such as Taylor-type models, Sachs-type models, self-consistent models (see section I.8).

I.7.1 Euler angles

The three Euler angles, φ_1, Φ and φ_2, are usually used to identify the grain orientations (Bunge definition). The Euler angles describe the transition from the reference frame of sample (XYZ) into the crystallographic reference frame of each individual grain (xyz) of the polycrystals. To find the orientation g, as shown in Fig. 1-8, the system xyz needs to be rotated by φ_1 about Z axis, then rotated by Φ about x axis, finally rotated by φ_2 about z axis.

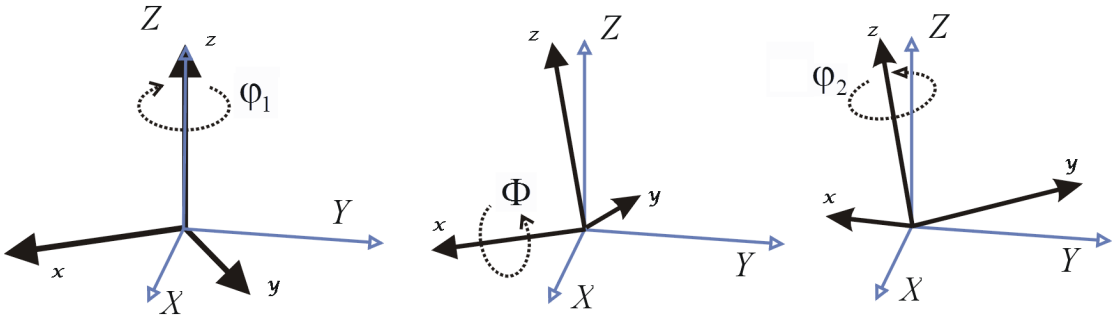

Fig. 1-8. Representation of the three Euler angles

I.7.2 Update of grain orientations

During the simulations, the 3 Euler angles representing the grain orientation are transformed into an orientation matrix **a**:

$$\mathbf{a}=\begin{bmatrix}\cos\varphi_2 & \sin\varphi_2 & 0\\ -\sin\varphi_2 & \cos\varphi_2 & 0\\ 0 & 0 & 1\end{bmatrix}\cdot\begin{bmatrix}1 & 0 & 0\\ 0 & \cos\phi & \sin\phi\\ 0 & -\sin\phi & \cos\phi\end{bmatrix}\cdot\begin{bmatrix}\cos\varphi_1 & \sin\varphi_1 & 0\\ -\sin\varphi_1 & \cos\varphi_1 & 0\\ 0 & 0 & 1\end{bmatrix} \tag{1-26}$$

$$\mathbf{a}=\begin{bmatrix}\cos\varphi_1\cos\varphi_2-\sin\varphi_1\sin\varphi_2\cos\phi & \sin\varphi_1\cos\varphi_2+\cos\varphi_1\sin\varphi_2\cos\phi & \sin\varphi_2\sin\phi\\ -\cos\varphi_1\sin\varphi_2-\sin\varphi_1\cos\varphi_2\cos\phi & -\sin\varphi_1\sin\varphi_2+\cos\varphi_1\cos\varphi_2\cos\phi & \cos\varphi_2\sin\phi\\ \sin\varphi_1\sin\phi & -\cos\varphi_1\sin\phi & \cos\phi\end{bmatrix} \tag{1-27}$$

The lattice spin $\mathbf{\Omega}^*$ is used to update the grain orientation at each calculation step. In the calculation, we should firstly obtain the rotation angle α from the $\mathbf{\Omega}^*$ (Lee et al., 2002):

$$\alpha^2=\frac{\mathrm{tr}\left(\hat{\Omega}\right)}{2}\quad\text{with}\quad\hat{\mathbf{\Omega}}=\Omega^*\Delta t \tag{1-28}$$

The incremental rotation matrix $\mathbf{A}^{\mathrm{rot}}$ is defined to calculate the update of the orientation matrix **a**. The expression of $\mathbf{A}^{\mathrm{rot}}$ is presented as follows:

$$\mathbf{A}^{\mathrm{rot}}=\mathrm{I}+\frac{\sin\alpha}{\alpha}\cdot\hat{\mathbf{\Omega}}+\frac{\left(1-\cos\alpha\right)}{\alpha^2}\cdot\hat{\mathbf{\Omega}}^2 \tag{1-29}$$

Then, the grain orientation can be updated as follows:

$$\mathbf{a}_{t+\Delta t}=\mathbf{A}^{\mathrm{rot}}\cdot\mathbf{a}_t \tag{1-30}$$

The matrix **a** of each grain should be calculated in each incremental steps. After the simulation, in order to output the final texture, the **a** matrix of each grain needs to be transformed back to the three Euler angles. To make the results more visual, the output textures are represented in three different ways: the pole figures, inverse pole figures and the orientation distribution function. The methods to translate the three Euler angles into those visual figures are introduced in the Appendix.

I.8 Main existing models for polycrystalline plasticity

I.8.1 Taylor-type model

The Taylor model (or called the upper bound approximation) is proposed in 1938 (Taylor, 1938). This model is based on the assumption of uniform strain, which means that each grain undergoes the same plastic deformation as the macroscopic. This model is usually formulated by the condition that the velocity gradient at the local level is equal to the macroscopic one:

$$\mathbf{L} = \overline{\mathbf{L}} \tag{1-31}$$

Based on the idea of Taylor (1938), several extensions have been proposed. Lin (Lin, 1957) assumes that the elasticity is isotropic and has proposed an interaction law to solve the distribution between the elastic and plastic deformation which are not imposed. Asaro and Needleman (1985) have extend the Taylor theory into elasto-viscoplastic based on the assumption of uniform deformation gradient: $\mathbf{F} = \overline{\mathbf{F}}$.

We should note that the global condition (see section I-4, Eq. 1-16) should also be fulfilled in Taylor-type model. Since the Taylor model is based on the iso-strain assumption, the average strain condition (Incompressibility condition) is automatically fulfilled. The macroscopic stress can be calculated from the average stress condition (equilibrium condition).

I.8.2 Sachs-type model

The Sachs model is proposed in 1928 (Sachs, 1928). This model is established by assuming that the stress tensor in each grain is proportional to the macroscopic one.

This assumption results in a proportional relationship between the local and global stress:

$$\boldsymbol{\sigma} = \lambda_g \overline{\boldsymbol{\sigma}} \tag{1-32}$$

In the above equation, λ_g depends on the orientation of the grain. The static model (or called lower bound approximation) is a limited case of Sachs model and is based on the assumption of the uniform stress, that is to say that the stress in each grain is equal to the macroscopic stress:

$$\boldsymbol{\sigma} = \overline{\boldsymbol{\sigma}} \tag{1-33}$$

We should keep in mind that, in the visco-plastic cases, the strain and stress are usually represented by plastic strain rate tensor $\mathbf{D}$ and deviatoric Cauchy stress tensor $\mathbf{S}$. Therefore, the Taylor model (upper bound approximation) should be expressed by the uniform plastic strain rate ($\mathbf{D} = \overline{\mathbf{D}}$), whereas the Static model (lower bound approximation) should be expressed by the uniform deviatoric Cauchy stress ($\mathbf{S} = \overline{\mathbf{S}}$).

Since the Static model is based on the iso-stress assumption, the equilibrium condition (see Eq. 1-16) will be achieved automatically. The macroscopic strain can be calculated from the Incompressibility condition.

I.8.3 Relaxed-constraints model

The classical Taylor model is too strict and shows a limit in the texture predictions especially when the grain is largely flatted. Thus, Honeff and Mecking (1981) have proposed a relaxed-constraints model. In this model, the local strain is equal to the global one as the Taylor theory and the shear deformations of relaxation are added into local strain. For the rolling cases, the relaxed-constraints models include the lath

model (with one shear deformation of relaxation along rolling direction) and the pancake model (with two shear deformations of relaxation along rolling and transverse directions). Van Houtte et al. (2005) have summarized those models by proposing a general expression of relaxation velocity gradient:

$$\mathbf{L}^{\mathbf{rlx}} = \sum_{r=1}^{R} K^{r} \dot{\gamma}_{r}^{rlx} \tag{1-34}$$

In Eq. 1-34, R is total number of relaxation modes and K^{r} denotes the velocity gradient of each mode. $\dot{\gamma}_{r}^{rlx}$ is a reference value. The $\mathbf{L}^{\mathbf{rlx}}$ is a part of the local velocity gradient, therefore, the local strain rate, which is the asymmetric part of local velocity gradient (see Eq. 1-11 and Eq. 1-12), can be expressed as:

$$\mathbf{D}^{P} = \sum_{\alpha}^{n} \dot{\gamma}^{\alpha} \mathbf{P}^{\alpha} + \sum_{r=1}^{R} B^{r} \dot{\gamma}_{r}^{rlx} \tag{1-35}$$

Here, B^{r} refers to the asymmetric part of K^{r}. The Eq. 1-35 can be used to calculate $\dot{\gamma}_{r}^{rlx}$ via a linear programming (Van Houtte, 1988; Van Houtte et al., 2005).

For each grain, the shear rates of slip systems can be determined by the minimization of the plastic work (Van Houtte et al., 2005) which is expressed as:

$$P = \sum_{\alpha} \left(g^{\alpha} \left| \dot{\gamma}^{\alpha} \right| \right) + \sum_{r} \tau_{rlx}^{r} \dot{\gamma}_{rlx}^{r} \tag{1-36}$$

In Eq. 1-36, the first term is the Taylor deformation energy (Taylor, 1938). τ_{rlx}^{r} represents the friction coefficient.

I.8.4 Multigrain model

The multigrain models refer to the models taking into account the local interaction between neighboring grains (Van Houtte, 2005). The Lamel model (Kanjarla et al.,

2010; Lee et al., 2002; Van Houtte et al., 2002, 2005, 2006) is a simplified multigrain model which is designed for the rolling tests. This model divides the material into a large amount of clusters. Each cluster contains two grains and the interface between those two grains remains parallel to the rolling plane during the deformation. The velocity gradient of each cluster is equal to the macroscopic one as the Taylor theory, whereas the relaxation shear deformation is allowed on the interface between the two grains. The relaxation, in this model, is calculated as the relaxed-constraints model (section I.8.3), but with the K^r of a grain is opposite to the one of its neighboring grain. The sum of plastic work of the two grains should be used in the minimization process to calculate the slip shear rates.

Lee et al., (2002) have proposed a generalized Lamel model which also considers two grains in each cluster. This model is formulated in a similar way than the Lamel model but the bicrystal interfaces are not necessarily parallel to certain plane during the deformation. The directions of the interfaces are taken into account in the formulation. Lee et al., (2002) used the Taylor model (the strain rate of each cluster is equal to the corresponding macroscopic ones) and Static model (the deviatoric stress of each cluster is equal to the macroscopic one) to calculate the local fields of the clusters. The strain rate, spin and the deviatoric stress of each grain can be calculated from the local fields of the clusters considering the interface continuous condition and the global equilibrium and compatibility condition (volume average of the local fields are equal to the corresponding macroscopic ones)

The grain interaction (GIA) model (Crumbach et al., 2001, 2006; Engler et al., 2005; Leffers and Ray, 2009; Van Houtte et al., 2005) is also a multigrain model but with eight grains in one cluster. The grain boundaries and the interface between the cluster and the matrix are assumed to be orthogonal arranged. The energies of dislocations on

these grain boundaries and the cluster interfaces are represented by the energies of geometrically necessary dislocations (GND) which is shown as follows:

$$P^{\theta} = \rho^{GND} \cdot \frac{G \cdot b^2}{2} \tag{1-37}$$

Here, θ is one of the GNDs. ρ^{GND} is the density of GNDs which depends on the shear strain, GND directions and the grain size. b is the Burgers vector of the GNDs. G is the shear modulus. Therefore, the total plastic work of the cluster can be presented as:

$$P^{cluster} = \sum_{nor} \sum_{\alpha} \left(g^{\alpha} \left| \dot{\gamma}^{\alpha} \right| \right) + \sum_{\theta} P^{\theta} \tag{1-38}$$

Here, nor represents all the eight grains in this cluster. Then, by the minimization of $P^{cluster}$, the relaxation deformation and the shear rate of each grain can be determined (Crumbach et al., 2006).

I.8.5 Self-consistent modeling

The self-consistent theory plays an important role in the micro-macro mechanical modeling. This type of model is widely used to predict the mechanical properties for heterogeneous materials, particularly polycrystals (e.g. Abdul-Latif, 2004; Abdul-Latif and Radi, 2010; Berveiller and Zaoui, 1979; Hill, 1965; Kröner, 1961; Mercier et al., 2005; Mercier and Molinari, 2009; Molinari et al., 1987). Unlike the classic Taylor-type and Sachs-type models, the self-consistent models can take into account the grain shape via the Eshelby theory (1957) and then describe the interaction between the grains and the polycrystals. In the self-consistent theory applied in polycrystals, each grain or grain group are treated as an inhomogeneous inclusion embedded in the "homogeneous effective medium" (HEM) which has the average properties of the aggregate. The macroscopic response of the polycrystals

results from the contribution of each grain. An interaction law should be proposed for each self-consistent model in order to solve the problem of interaction between a grain and the aggregate.

A solution of the inclusion problem is proposed by Eshelby (1957). For the case that the elasticity is isotropic and homogeneous, the relation between the total deformation $\boldsymbol{\varepsilon}^{T}$ and the plastic deformation $\boldsymbol{\varepsilon}^{p}$ of an ellipsoidal inclusion is expressed as:

$$\varepsilon_{ij}^{T} = S_{ijkl}\varepsilon_{kl}^{p} \tag{1-39}$$

Here, $\mathbf{S}$ is the Eshelby tensor which depends on the grain shape and the elastic properties of the matrix. For the spherical inclusions, the expression of the Eshelby tensor is shown as follow:

$$S_{ijkl} = \frac{5\nu - 1}{15(1-\nu)}\delta_{ij}\delta_{kl} + \frac{4-5\nu}{15(1-\nu)}\left(\delta_{ik}\delta_{kl} + \delta_{il}\delta_{jk}\right) \tag{1-40}$$

Then, for the case that $\varepsilon_{ii}^{p} = 0$, the relation in Eq. 1-40 becomes:

$$\varepsilon_{ij}^{T} = \beta\varepsilon_{ij}^{p} \quad \text{with} \quad \beta = \frac{2}{15}\frac{4-5\nu}{1-\nu} \tag{1-41}$$

In Eq. 1-41, ν denotes the Poisson ratio. The internal stress of the inclusion can be obtained as:

$$\sigma_{ij} = -2\mu\left(\varepsilon_{ij}^{e} - \left(\frac{\nu}{1-2\nu}\right)\varepsilon_{ij}^{e}\delta_{ij}\right) \tag{1-42}$$

Here, μ represents the elastic shear modulus. ε_{ij}^{e} is the elastic deformation and can be calculated as:

$$\varepsilon_{ij}^{e} = \varepsilon_{ij}^{T} - \varepsilon_{ij}^{P} = (\beta - 1)\varepsilon_{ij}^{P} \tag{1-43}$$

Therefore, we can have:

$$\sigma_{ij} = -2\mu(1-\beta)\varepsilon_{ij}^{p} \tag{1-44}$$

I.8.5.1 Kröner model

Over the past several decades, the modeling studies based on the self-consistent theory is an active field of research. Kröner (1961) proposed an elasto-plasitc self-consistent approach for the polycrystals under small deformation. The inclusions are assumed spherical. The interaction law of Kröner model is expressed as:

$$\boldsymbol{\sigma} - \overline{\boldsymbol{\sigma}} = 2\mu(1-\beta)\left(\overline{\boldsymbol{\varepsilon}}^{p} - \boldsymbol{\varepsilon}^{p}\right) \tag{1-45}$$

Here, $\beta = \frac{2}{15}\frac{4-5\nu}{1-\nu}$ as spherical inclusions are assumed to be spherical. $\boldsymbol{\varepsilon}^{p}$ and $\overline{\boldsymbol{\varepsilon}}^{p}$ are the local and global plastic deformations, respectively. $\boldsymbol{\sigma}$ and $\overline{\boldsymbol{\sigma}}$ are the local and global internal stresses. We note that the μ value is quite large and thus the plastic deformation deviation is suppressed ($\overline{\boldsymbol{\varepsilon}}^{p} - \boldsymbol{\varepsilon}^{p} \to 0$). Therefore, the predicted results of Kröner model are close to the ones of Taylor-type models (see section I.8.1).

I.8.5.2 Hill model

Hill (1965) has proposed a more complex model, which successfully take into account elasto-plastic interaction between the grains and the aggregate. The interaction law of Hill model is represented as follow:

$$\boldsymbol{\sigma} - \overline{\boldsymbol{\sigma}} = \mathbf{L}^{*} \cdot \left(\overline{\boldsymbol{\varepsilon}}^{p} - \boldsymbol{\varepsilon}^{p}\right) \tag{1-46}$$

The interaction tensor $\mathbf{L}^{*}$ is expressed as:

$$\mathbf{L}^{*} = \left\langle \mathbf{L} \cdot \left(\mathbf{L} + \overline{\mathbf{L}}\right)^{-1} \cdot \left(\mathbf{L} - \mathbf{L}^{*}\right) \right\rangle \tag{1-47}$$

Here, $\mathbf{L}$ and $\overline{\mathbf{L}}$ represent the local and global tangent modulus tensors,

respectively.

I.8.5.3 Berveiller and Zaoui model

Berveiller and Zaoui (1979) proposed a model based on the interaction law of Kröner (1961). The spherical grains are taken into consideration and the elastic propriety is assumed to be isotropic in this model. As mentioned above (see section I.8.5.1), the predicted results of Kröner model are close to the ones of Taylor-type model due to the high value of μ. In order to solve this problem, Berveiller and Zaoui (1979) added a plastic accommodation factor α into the interaction law of Kröner. When the Poisson ratio is about $1/3$ ($\beta \approx 0.5$), the interaction law of Berveiller and Zaoui (1979) can be expressed as:

$$\boldsymbol{\sigma} - \overline{\boldsymbol{\sigma}} = \alpha\mu\left(\overline{\boldsymbol{\varepsilon}}^{p} - \boldsymbol{\varepsilon}^{p}\right) \tag{1-48}$$

where:

$$\alpha = \frac{1}{1+\mu\overline{h}} \tag{1-49}$$

The parameter $\overline{h}$ depends on the state of plastification of the matrix. This parameter can be determined by strain-stress response of the tensile tests:

$$\overline{h} = \frac{2}{3}\frac{\overline{\sigma}}{\overline{\varepsilon}^{p}} \tag{1-50}$$

Therefore:

$$\alpha = \frac{1}{1+(2/3)\left(\overline{\sigma}/\overline{\varepsilon}^{p}\right)\mu} \tag{1-51}$$

I.8.5.4 Visco-plastic self-consistent model

The visco-plastic self-consistent (VPSC) model, which is formulated by Molinari et al. (1987), is a widely used model in polycrystal plasticity at large strain. The first version of the interaction law of the VPSC model is shown as follow (Molinari et al., 1987; Ahzi, 1987):

$$\mathbf{S}-\bar{\mathbf{S}}=(\mathbf{\Gamma}^{-1}+\mathbf{A}^{t})\cdot(\mathbf{D}-\bar{\mathbf{D}}) \tag{1-52}$$

Here, $\mathbf{\Gamma}$ is a fourth order interaction tensor. $\mathbf{A}^{t}$ is also a fourth order which represents tangent modulus of the polycrystals.

Molinari and Tóth (1994) and Tóth and Molinari (1994) have improved the proposed interaction law by introducing a tuning parameter α. With the consideration of the tuning parameter, the new interaction law of VPSC model is presented as:

$$\mathbf{S}-\bar{\mathbf{S}}=\alpha(\mathbf{\Gamma}^{s^{-1}}+\mathbf{A}^{s})\cdot(\mathbf{D}-\bar{\mathbf{D}}) \tag{1-53}$$

Here, $\mathbf{\Gamma}^{s}$ is a fourth order interaction tensor with $\mathbf{\Gamma}^{-1}=m\mathbf{\Gamma}^{s^{-1}}$. $\mathbf{A}^{s}$ is the fourth order tensor of secant modulus where $\mathbf{A}^{t}=m\mathbf{A}^{s}$. Here, m is the strain-rate sensitivity ($m=n^{-1}$). We can see that if the α parameter is set to be 0, the local stress will be equal to the global one. Therefore the interaction law is equivalent to the lower bound Static approximation. In the same way, the upper bound Taylor approximation can be obtained when $\alpha\to\infty$. The Secant interaction can be found when $\alpha=1$. If the α parameter is equal to m, the new interaction law (Eq. 1-53) will be the same as the first version of VPSC interaction law (Eq. 1-52). The interaction between grains and aggregate is therefore Tangent.

Lebensohn and Tomé (1993) have proposed the following interaction law which is given by:

$$\mathbf{D} - \overline{\mathbf{D}} = \mathbf{K}^{-1} \cdot \left(\mathbf{S} - \overline{\mathbf{S}}\right) \tag{1-54}$$

or

$$\mathbf{S} - \overline{\mathbf{S}} = \mathbf{K} \cdot \left(\mathbf{D} - \overline{\mathbf{D}}\right) \tag{1-55}$$

with

$$\mathbf{K} = n^{eff\,-1} \cdot \overline{\mathbf{M}}^{-1} \cdot \mathbf{E}^{-1} \cdot \left(\mathbf{I} - \mathbf{E}\right) \tag{1-56}$$

Here, $\mathbf{K}$ is the interaction tensor. $\mathbf{I}$ represents the fourth-order identity tensor. $\mathbf{E}$ is the Eshelby tensor. We denote that the interaction law in Eq. 1-55 is in the similar form of the one in Eq. 1-53. The parameter n^{eff}, as the inverse of parameter α, may be adopted to obtain different interactions: $n^{eff} = 0$ for a Taylor case, $n^{eff} \to \infty$ for a Static case, $n^{eff} = 1$ for a Secant case and $n^{eff} = n$ for a Tangent case (Lebensohn and Tomé, 1993; Lebensohn et al., 2007).

The work of this thesis mainly focuses on the visco-plastic ϕ-model (Ahzi and M'Guil, 2008) which also belongs to the group of self-consistent model. The ϕ-model will be introduced in chapter II.

References:

Abdolvand, H., Daymond, M.R., 2012. Internal strain and texture development during twinning: Comparing neutron diffraction measurements with crystal plasticity finite-element approaches. Acta Mater. 60, 2240-2248.

Abdul-Latif, A., 2004. Pertinence of the grains aggregate type on the self-consistent model responses. Int. J. Sol. Struct. 41, 305-322.

Abdul-Latif, A., Radi, M., 2010. Modeling of the grain shape effect on the elastic-inelastic behavior of polycrystals with self-consistent scheme. J. Eng. Mat. Tech. 132,

011008.

Ahzi, S., 1987. A self consistent approach to the behavior of viscoplastic polycrystals during large deformation, Ph.D. Thesis. University of Metz, France.

Ahzi, S., M'Guil, S., 2008. A new intermediate model for polycrystalline viscoplastic deformation and texture evolution. Acta Mater. 56, 5359-5369.

Asaro, R.J., Needleman, A., 1985. Texture development and strain hardening in rate dependent polycrystals. Acta Metall. 33, 923-953.

Beyerlein, I.J., Mara, N.A., Bhattacharyya, D., Alexander, D.J., Necker, C.T., 2011. Texture evolution via combined slip and deformation twinning in rolled silver-copper cast eutectic nanocomposite. Int. J. Plasticity 27, 121-146.

Chin, G.Y., Hosford, W.F., Mendorf, D.R., 1969. Accommodation of constrained deformation in f.c.c metals by slip and twinning. Proceedings of the royal society A 309, 433-456.

Christian, J.W., Mahajant, S., 1995. Deformation twinning. Prog. Mater. Sci. 39, 1-157.

Crumbach, M., Pomana, G., Wagner, P., Gottstein, G., 2001. Recrystallisation and grain growth. In: Gottstein, G., Molodov, D. (Eds.), Proceedings of the First Joint International Conference, Aachen. Springer-Verlag, pp. 1053-1060.

Crumbach, M., Goerdeler, M., Gottstein, G., 2006. Modelling of recrystallization textures in aluminium alloys: I. Model set-up and integration. Acta Mater. 54, 3275-3289.

Engler, O., Crumbach, M., Li, S., 2005. Alloy-dependent rolling texture simulation of aluminium alloys with a grain-interaction model. Acta Mater. 53, 2241-2257.

Eshelby, J.D., 1957. The determination of the elastic field of an ellipsoidal inclusion, and related problems. Proc. Roy. Soc. 241, 376-396.

Franciosi, P., Berveiller, M., Zaoui, A., 1980. Latent hardening in copper and aluminium single crystals. Acta Metall. 28, 273-283.

Hill, R., 1965. Continuum micro-mechanics of elastoplastic polycrystals. J. Mech. Phys. Solids. 13, 89-101.

Honeff, H., Mecking, H., 1981. Analysis of the deformation texture at different rolling conditions. In: Nagashima, S. (Ed.), Proceedings of ICOTOM 6, vol. 1. The Iron and Steel Institute of Japan, Tokyo, pp. 347–355.

Hutchinson, J.W., 1970. Elastic-plastic behaviour of polycrystalline metals and composites. Proc. Roy. Soc., A319, 247.

Kalidindi, S.R., 1998. Incorporation of deformation twinning in crystal plasticity

models. J. Mech. Phys. Solids. 46, 267-290.

Kalidindi, S.R., Bronkhorst, C.A., Anand, L., 1992. Crystallographic texture evolution in bulk deformation processing of FCC metals. J. Mech. Phys. Solids 40, 537-569.

Kalidindi, S.R., 2001. Modeling anisotropic strain hardening and deformation textures in low stacking fault energy fcc metals. Int. J. Plasticity 17, 837-860.

Kanjarla, A.K., Van Houtte, P., Delannay, L., 2010. Assessment of plastic heterogeneity in grain interaction models using crystal plasticity finite element method. Int. J. Plasticity 26, 1220-1233.

Kocks, U.F., 1970. The relation between polycrystalline deformation and single crystal deformation. Metall. Mater. Trans. 1, 1121-1143.

Lebensohn RA, Tomé CN. VPSC code, Version 6, Los Alamos; 2003.

Lebensohn, R.A., Tomé, C.N., 1993. A self-consistent anisotropic approach for the simulation of plastic deformation and texture development of polycrystals: application to zirconium alloys. Acta Metall. Mater. 41, 2611-2624.

Lebensohn, R.A., Tomé, C.N., Castañeda, P.P., 2007. Self-consistent modelling of the mechanical behaviour of viscoplastic polycrystals incorporating intragranular field fluctuations. Philosophical Magazine. 87, 4287-4322.

Lee, B.J., Ahzi, S., Parks, D.M., 2002. Bicrystal-based modeling of plasticity in FCC metals. J. Eng. Mater. Tech. 124, 27-40.

Leffers, T., Ray, R.K., 2009. The brass-type texture and its deviation from the copper-type texture. Prog. Mater.Sci. 54, 351-396.

Lin, T.H., 1957. Analysis of elastic and plastic strains of a face-centred cubic crystal. J.

Mech. Phys. Solids. 5, 143-149.

Mercier, S., Jacques, N., Molinari, A., 2005. Validation of an interaction law for the Eshelby inclusion problem in elasto-viscoplasticity. Int. J. Sol. Struct. 42, 1923-1941.

Mercier, S., Molinari, A., 2009. Homogenization of elastic-viscoplastic heterogeneous materials: Self-consistent and Mori-Tanaka schemes. Int. J. Plasticity 25, 1024-1048.

Molinari, A., Canova, G.R., Ahzi, S., 1987. A self-consistent approach of the large deformation polycrystal viscoplasticity. Acta Metall. 35, 2983-2994.

Molinari, A., Tóth L.S., 1994. Tuning a self consistent viscoplastic model by finite elements reultats-I. Modeling, Acta Metall. 42, 2453-2458.

Prakash, A., Hochrainer, T., Reisacher, E., Riede, H., 2008. Twinning models in self-consistent texture simulations of TWIP steels. Steel. Res. Int. 79, 645-652.

Sachs, G., 1928. Plasticity problems in metals. Z. Ver. Deutsch. Ing.72, 734-736.

Schmid, C., Kawalla, R., Walde, T., Riedel, H., Prakash, A., Poizat, C., 2007. Experimental and numerical investigation of texture development during hot rolling of magnesium alloy AZ31. Mater. Sci. Forum., 539-543, 3448-3453.

Staroselsky, A., Anand, L., 1998. Inelastic deformation of polycrystalline face centered cubic materials by slip and twinning. J. Mech. Phys. Solids. 46, 671-696.

Taylor, G.I., 1938. Plastic strain in metals. J. Inst. Metals. 62, 307-324.

Tomé, C.N., Lebensohn, R.A., Kocks, U.F., 1991. A model for texture development dominated by deformation twinning: Application to zirconium alloys. Acta Metall. Mater. 39, 2667-2680.

Tomé, C., Canova, G.R., Kocks, U.F., Christodoulou, N., Jonas, J.J., 1984. The relation between macroscopic and microscopic strain hardening in fcc polycrystals. Acta Metall. 32, 1637-1653.

Tóth, L.S., Molinari, A., 1994. Tuning a self consistent viscoplastic model by finite elements reultats-II. Application to torsion textures. Acta Metall. Mater. 42, 2459-2466.

Van Houtte, P., 1978. Simulation of the rolling and shear texture of brass by the Taylor theory adapted for mechanical twinning. Acta Metall. 26, 591-604.

Van Houtte, P., 1988. A comprehensive mathematical formulation of an extended Taylor-Bishop-Hill model featuring relaxed constraints, the Renouard-Wintenberger theory and a strain rate sensitivity model. Textures Microstruct. 8-9, 313-350.

Van Houtte, P., Delannay, L., Kalidindi, S.R., 2002. Comparison of two grain interaction models for polycrystal plasticity and deformation texture prediction. Int. J. Plasticity 18, 359-377.

Van Houtte, P., Li, S., Seefeldt, M., Delannay, L., 2005. Deformation texture prediction: from the Taylor model to the advanced Lamel model. Int. J. Plasticity 21, 589-624.

Van Houtte, P., Kanjarla, A.K., Van Bael, A., Seefeldt, M., Delannay, L., 2006. Multiscale modeling of the plastic anisotropy and deformation texture of polycrystalline materials. European Journal of Mechanics A/Solids 25, 634-648.

Voce, E., 1948. The relationship between stress and strain for homogeneous deformation. J. Inst. Metals. 74, 537-562.

Chapter II. Visco-plastic ϕ-model

II.1 Introduction

The work of this thesis mainly focus on the application, extension and evaluation of the visco-plastic ϕ-model. The ϕ-model is proposed by Ahzi and M'Guil (2008). This model is based on the micromechanical modeling of large visco-plastic deformation of polycrystalline aggregates using the physical mechanisms of the plastic deformation. The novelty and originality of this approach is the way of obtaining the interaction laws of the polycrystals. The considered polycrystalline model makes use of an interaction law which is based on a new intermediate approach that allows spanning from the upper to the lower bound models using a single interaction strength parameter ϕ. This parameter is naturally introduced in a given potential function that is minimized to obtain the interaction law (Ahzi and M'Guil, 2008). With this approach a wide range of results can be obtained by varying ϕ between 0 and 1. In addition, unlike other self-consistent approaches, this intermediate model is not based on the Eshelby-type interaction laws which are difficult to numerically implement. The simplicity of the ϕ-model against the self-consistent models is a real advantage for the numerical simulations. This new model will give a new scale to the domain of crystal plasticity mainly dominated by the self-consistent model (e.g. Molinari et al., 1987; Ahzi, 1987) and other approaches such as the upper bound (Taylor, 1938) or the lower bound (Sachs, 1928) models.

II.2 Development of the visco-plastic ϕ-model

✓ Review of the single crystal constitutive law used in the ϕ-model

As mentioned in section I.3, the visco-plastic power law is used to describe the mechanism of crystallographic slip and twinning. This law is used to express the relationship between the shear-rate, $\dot{\gamma}^{\alpha}$, of a given slip system α and the

corresponding resolved shear stress, τ^{α}. Thus, the rigid visco-plastic single crystal behavior can be described by a rate-sensitive constitutive power law relating the plastic strain rate tensor $\mathbf{D}$ (elasticity is neglected) and the deviatoric Cauchy stress tensor $\mathbf{S}$ of the single crystal (see also section I.4):

$$\mathbf{D} = \frac{\dot{\gamma}_0}{g^{\alpha}} \sum_{\alpha} \left(\frac{\mathbf{P}^{\alpha} \cdot \mathbf{S}}{g^{\alpha}} \right)^{n-1} \left(\mathbf{P}^{\alpha} \otimes \mathbf{P}^{\alpha} \right) \cdot \mathbf{S} \equiv \mathbf{M}(\mathbf{S}) \cdot \mathbf{S} \tag{2-1}$$

Here, $\dot{\gamma}_0$ is a reference shear rate, n is the inverse rate-sensitivity coefficient, $\mathbf{P}^{\alpha}$ represents the symmetric part of the Schmid tensor and g^{α} is the critical resolved shear stress (CRSS) of the slip (or twinning) system α which evolves according to the Voce hardening law (see section I.5.2) in this thesis. $\mathbf{M}$ is the macroscopic fourth order visco-plastic compliance tensor. The macroscopic behavior can be described by a similar relationship to the microscopic constitutive law (Eq. 2-1):

$$\overline{\mathbf{D}} = \overline{\mathbf{M}} \cdot \overline{\mathbf{S}} \tag{2-2}$$

Here $\overline{\mathbf{D}}$, $\overline{\mathbf{S}}$ and $\overline{\mathbf{M}}$ are the macroscopic plastic strain rate, the macroscopic deviatoric Cauchy stress and the macroscopic fourth-order visco-plastic compliance tensor, respectively.

The global conditions need to be fulfilled which is given by the averaging conditions:

$$\overline{\mathbf{D}} = \langle \mathbf{D} \rangle \quad \text{and} \quad \overline{\mathbf{S}} = \langle \mathbf{S} \rangle . \tag{2-2}$$

Here, $\langle \cdot \rangle$ denotes the volume average over the polycrystals.

✓ **Formulation of the ϕ-model**

In order to guarantee that the global conditions (Eq. 2-2) can be fulfilled, the macroscopic strain rate tensor, $\tilde{\mathbf{D}}$ and the corresponding macroscopic deviatoric

stress tensor, $\tilde{\mathbf{S}}$ have been introduced by Ahzi and M'Guil (2008). The authors assume that:

$$\tilde{\mathbf{D}} = \mathbf{K}_D \cdot \overline{\mathbf{D}} \quad \text{and} \quad \tilde{\mathbf{S}} = \mathbf{K}_S \cdot \overline{\mathbf{S}} \tag{2-3}$$

Here, $\mathbf{K}_D$ and $\mathbf{K}_S$ are fourth-order mapping tensors. The introduced macroscopic strain rate and stress are supposed to be related similarly to Eq. 2-2.

$$\tilde{\mathbf{D}} = \tilde{\mathbf{M}} \cdot \tilde{\mathbf{S}} \quad \text{or} \quad \tilde{\mathbf{S}} = \tilde{\mathbf{L}} \cdot \tilde{\mathbf{D}} \quad \text{with} \quad \tilde{\mathbf{L}} = \tilde{\mathbf{M}}^{-1} \tag{2-4}$$

Here, $\tilde{\mathbf{M}}$ is an average compliance tensor. The ϕ-model is formulated by the minimization of a specific function $\mathbf{E}$ combining the local fields' deviations (strain rate and stress) from the macroscopic ones:

$$\mathbf{E} = (1-\phi)\mathbf{E_D} + \phi \mathbf{E_S} \tag{2-5}$$

Where

$$\mathbf{E_D} = \frac{\left\| \mathbf{D} - \tilde{\mathbf{D}} \right\|^2}{\dot{\gamma}_0^2} \quad \text{and} \quad \mathbf{E_S} = \frac{\left\| \mathbf{S} - \tilde{\mathbf{S}} \right\|^2}{\tau_0^2} \tag{2-6}$$

Here, τ_0 is the initial resolved shear stress. $\dot{\gamma}_0$ represents the reference shear rate.

The function $\mathbf{E}$ in Eq. 2-5 depends on the parameter ϕ between 0 and 1 which allows spanning the entire solution domain between the upper and lower bounds. This tuning parameter ϕ allows the control of the grains interactions strength in the polycrystals. The mathematical development of the ϕ-model can be found in the work of Ahzi and M'Guil (2008). By minimization of the function $\mathbf{E}$ ($\partial \mathbf{E} / \partial \mathbf{D} = 0$), the dual interaction laws are derived as:

$$\mathbf{D} = \mathbf{A} \cdot < \mathbf{A} >^{-1} \cdot \overline{\mathbf{D}} \quad \text{and} \quad \mathbf{S} = \mathbf{B} \cdot < \mathbf{B} >^{-1} \cdot \overline{\mathbf{S}} \tag{2-7}$$

with

$$\mathbf{A}=\left[\mathbf{M}^{-1}-\beta n\left(\frac{\phi-1}{\phi}\right)\mathbf{M}\right]^{-1}\left[\tilde{\mathbf{M}}^{-1}-\beta n\left(\frac{\phi-1}{\phi}\right)\mathbf{M}\right] \tag{2-8}$$

$$\mathbf{B}=\left[\mathbf{I}-\beta n\left(\frac{\phi-1}{\phi}\right)\mathbf{M}\cdot\mathbf{M}\right]^{-1}\left[\mathbf{I}-\beta n\left(\frac{\phi-1}{\phi}\right)\mathbf{M}\cdot\tilde{\mathbf{M}}\right] \tag{2-9}$$

In Eq. 2-8 and Eq. 2-9, $0<\phi<1$, $\beta=\left(\tau_0/\dot{\gamma}_0\right)^2$ is a normalizing coefficient, n is the inverse strain rate coefficient, $\mathbf{A}$ and $\mathbf{B}$ are fourth-order strain-rate and stress interaction tensors, respectively. The inverse of the ensemble average compliance tensor $\tilde{\mathbf{M}}$ is given by:

$$\tilde{\mathbf{M}}^{-1}=<\mathbf{B}>^{-1}\cdot<\mathbf{M}^{-1}\cdot\mathbf{A}> \tag{2-10}$$

The interaction tensors $\mathbf{A}$ and $\mathbf{B}$ depend on the local and global compliance tensors, on the inverse rate sensitivity coefficient n and on the parameter ϕ. The computation of these interaction tensors is much easier to handle than those involved in a self-consistent scheme. We note that in our interaction law, the Taylor and the static models results can be retrieved by setting $\phi\to 0$ or $\phi\to 1$, respectively.

We notice that original stress and deformation tensors (e.g. strain rate tensor **D** and stress tensor **S**) are 3x3 matrixes. However, in the numeric calculations of ϕ-model, these tensors are vectorized into 5x1 matrixes which can be expressed as (Ahzi, 1987):

$$\mathbf{D}=\left(D_1,D_2,D_3,D_4,D_5\right)=\left\{\frac{D_{22}-D_{11}}{\sqrt{2}},\sqrt{\frac{3}{2}}D_{33},\sqrt{2}D_{23},\sqrt{2}D_{13},\sqrt{2}D_{12}\right\}^{T} \tag{2-11}$$

And

$$\mathbf{S} = (S_1, S_2, S_3, S_4, S_5) = \left\{ \frac{S_{22} - S_{11}}{\sqrt{2}}, \sqrt{\frac{3}{2}} S_{33}, \sqrt{2} S_{23}, \sqrt{2} S_{13}, \sqrt{2} S_{12} \right\}^T \quad (2\text{-}12)$$

Other tensors should be vectorized in the same way.

The general algorithm of the ϕ-model is presented in Fig. 2-1. After the calculation of local strain rate $\mathbf{D}$, the Newton-Raphson method is used to solve the non-linear constitutive law and calculate the local stress tensor $\mathbf{S}$. We note that the first guess of $\mathbf{S}$ is made based on the Static model in which the local stress is assumed to be equal to the macroscopic one.

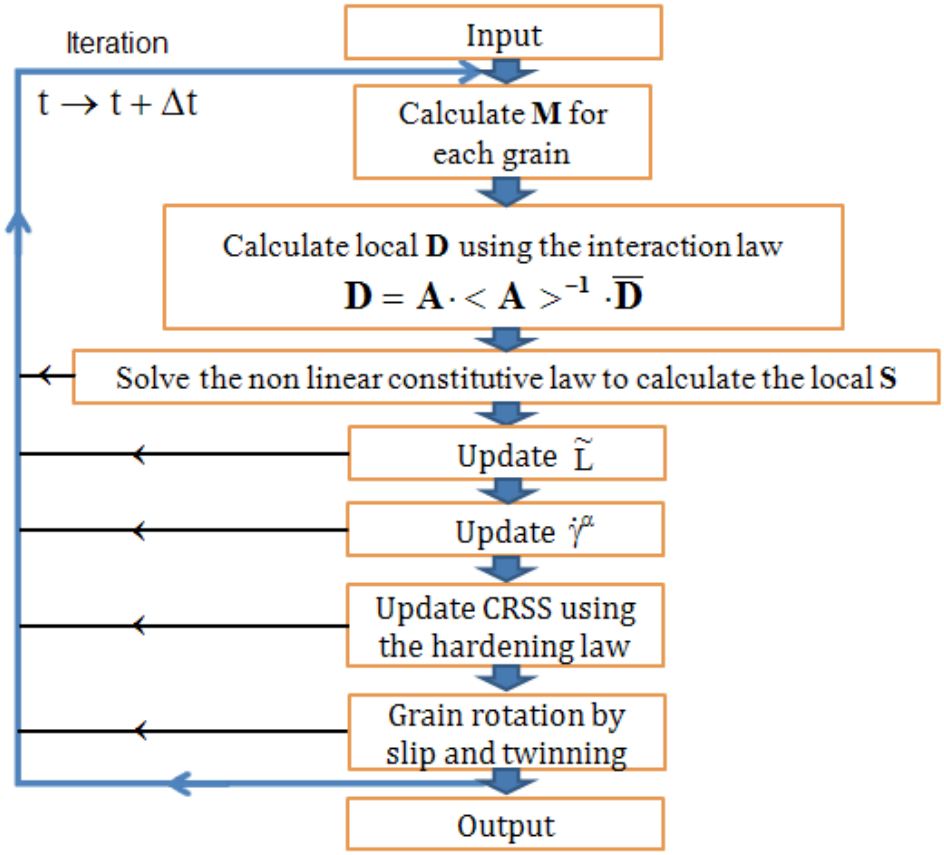

Fig. 2-1. General calculation algorithm of the ϕ-model.

II.3 General numerical aspects

In previous works (Ahzi and M'Guil, 2008; M'Guil et al., 2009, 2011), this model has

been applied to FCC metals under tensile, compression and rolling tests. By varying the ϕ value from 0 to 1, the ϕ-model is able to predict large scale results from a stiff interaction (small values of ϕ) to a more compliant interaction (high values of ϕ). Fig. 2-2 shows the strain-stress curves of FCC tensile tests predicted by Ahzi and M'Guil (2008) using the ϕ-model. The curve on the top is predicted by Taylor model (upper bound approxiamation) whereas the one on the bottom is predicted by Static model (low bound approxiamation). The curves predicted by various ϕ values show a transition between the upper and lower bound approaches.

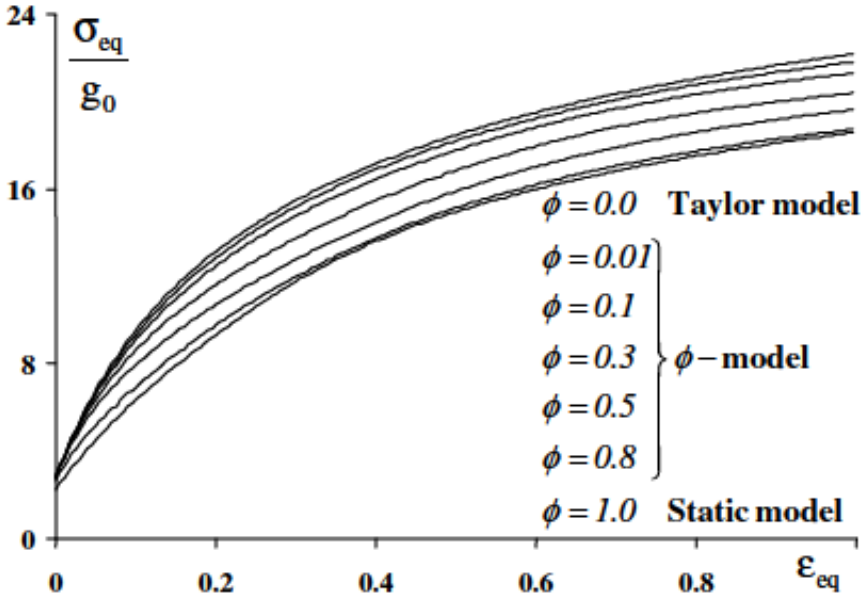

Fig. 2-2. Predicted strain-stress curves for different ϕ values under tensile test in FCC metals (Ahzi and M'Guil, 2008). The curves from higher to lower correspond to ϕ values from 0 to 1.

The result transitions of the ϕ-model can also be found in the predicted textures. We present the textures of FCC metals under rolling and tensile tests in Fig. 2-3 and Fig. 2-4 as examples. Compared with the VPSC model, the ϕ-model shows a better performance in the texture transition (M'Guil et al., 2009).

Finally, we underline that the computational time required for the ϕ-model simulations is of the same order as that for the classical Taylor model. This low computing time makes the ϕ-model suitable for large scale computations and simulations of metal forming processes (M'Guil et al., 2011).

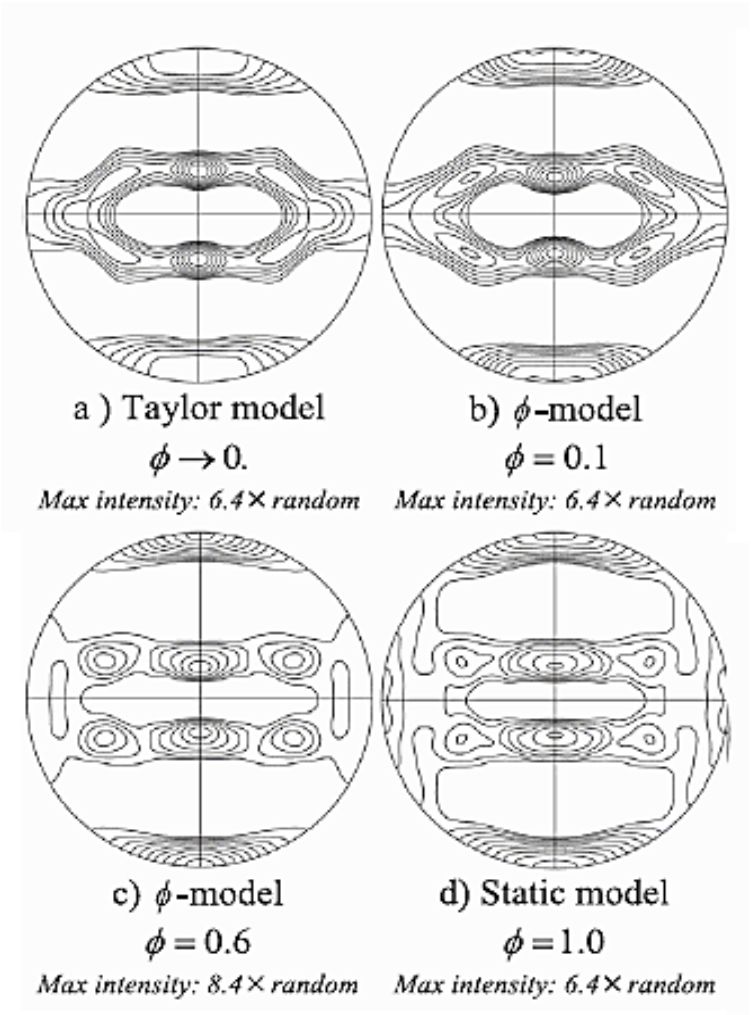

Fig. 2-3. FCC rolling texture transition predicted by ϕ-model representing in terms of (111) pole figure (M'Guil et al., 2011).

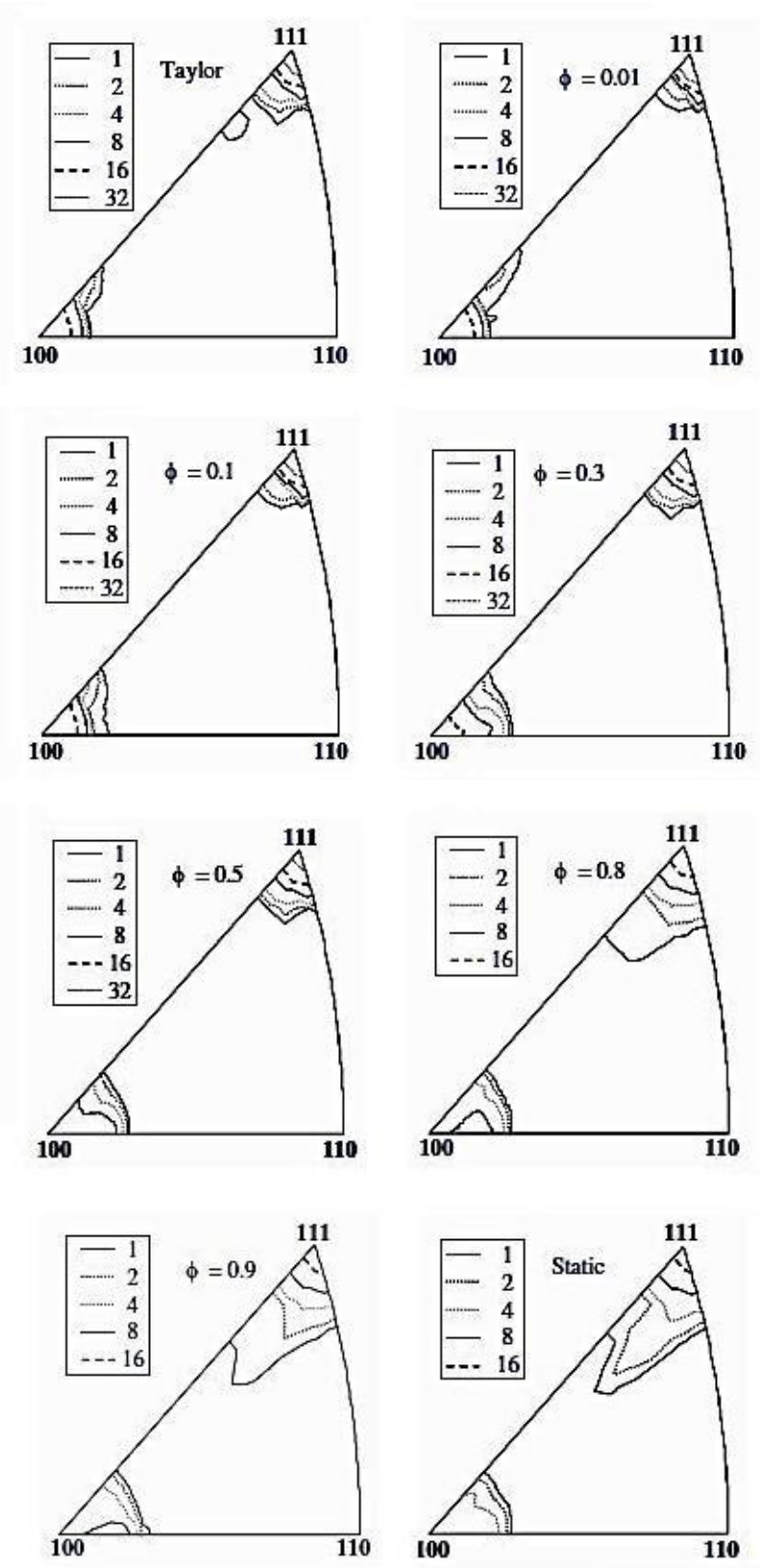

Fig. 2-4. FCC tensile texture transition predicted by ϕ-model representing in terms of inverse pole figure (Ahzi and M'Guil, 2008)

II.4 Stress and strain rate deviations

In this section, we analyzed the statistical deviations of the local stresses and strain rates from their corresponding macroscopic ones. The normalized local strain rate deviation, D_d and normalized local stress deviation, S_d are defined as:

$$D_d = \frac{\|D\| - \|\overline{D}\|}{\|\overline{D}\|} \quad \text{and} \quad S_d = \frac{\|S\| - \|\overline{S}\|}{\|\overline{S}\|} \tag{2-13}$$

We plot on Fig. 2-5 and Fig. 2-6 the normalized local strain rate deviation and local stress deviation from their average quantities in the case of plane strain compression test at $\varepsilon_{eq} = 60\%$ for FCC metals (only {111}<110> slip is considered). The Fig. 2-5 shows that the normalized local strain-rate deviation, D_d, increases as the parameter ϕ increases towards the static model. This Fig. 2-5 also shows that the normalized local strain-rate deviation, D_d, is quite different for various "small" ϕ values : $\phi = 0.0001$ (Fig. 2-5a; $\phi = 0.005$ (Fig. 2-5b) and $\phi = 0.1$ (Fig. 2-5c). This means that the ϕ-model, even for small ϕ values, deviates from the Taylor upper bound model. On the other hand, The Fig. 2-6 shows that the normalized local stress deviations, S_d, decreases as the parameter ϕ increases towards the static model. Here again, we can say that the ϕ-model for high ϕ values deviates from the Static lower bound model.

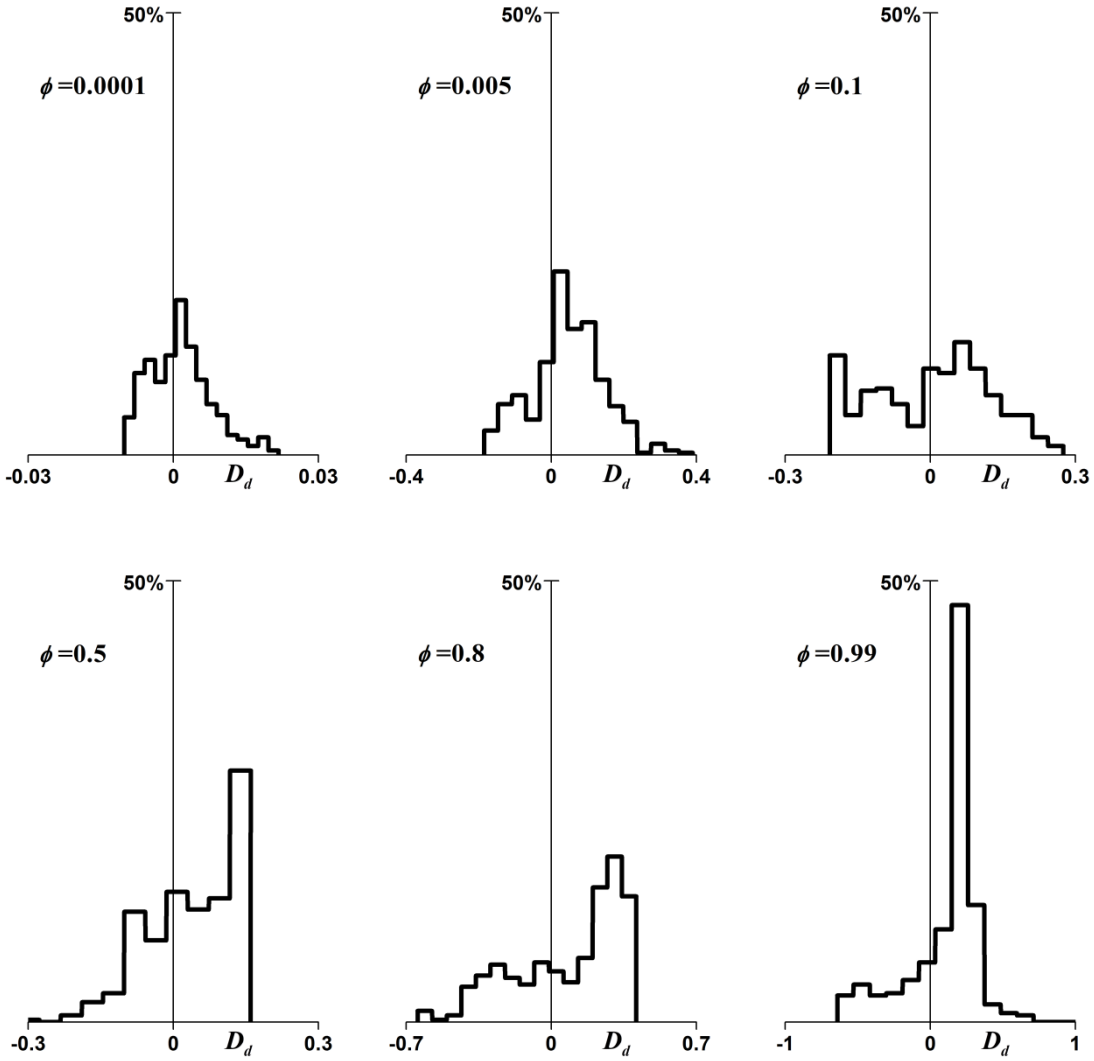

Fig. 2-5. Deviation of the norm of the local strain-rate under plane strain compression test (% of grain vs. $D_d = \frac{\|D\| - \|\overline{D}\|}{\|\overline{D}\|}$) at $\varepsilon_{eq} = 60\%$ for ϕ-model.

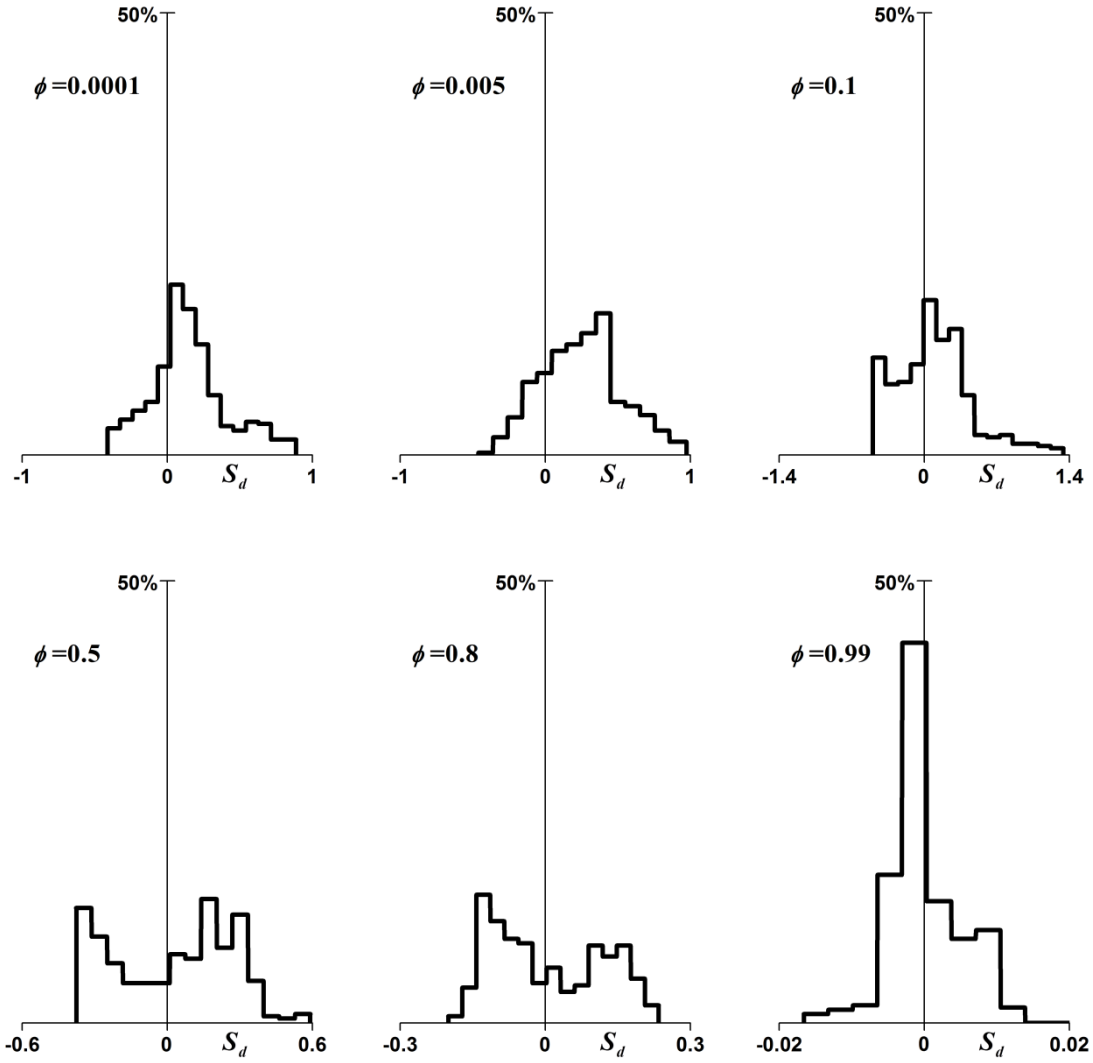

Fig. 2-6. Deviation of the norm of the local stress under plane strain compression test (% of grain vs. $S_d = \frac{\|S\| - \|\bar{S}\|}{\|\bar{S}\|}$) at $\varepsilon_{eq} = 60\%$ for ϕ-model.

According to these results, we can conclude that the ϕ-model with small ϕ values (< 0.1) predicts standard deviations (and thus results) that are far from the ones predicted by the Taylor upper bound model. The ϕ-model, with small ϕ (<0.1) values, should not be considered as an almost iso-strain approach. In the same way, the ϕ-model predictions with high ϕ values (> 0.8) predicts standard deviations (and thus results) that are quite different from those predicted with the lower Static bound model. The ϕ-model, with large ϕ (>0.8) values, should not be seen as an almost iso-stress model.

II.5 Evolution of the interaction tensor

The interaction tensor is one of the indicators of the interaction behavior in self-consistent models. The evolution of the interaction tensor in self-consistent models has been studied by several works (e.g. Ahzi, 1987). To define the interaction tensor, we need to express the interaction law in the following form:

$$\mathbf{S} - \overline{\mathbf{S}} = \mathbf{K} \cdot \left(\mathbf{D} - \overline{\mathbf{D}} \right) \tag{2-14}$$

or

$$\mathbf{D} - \overline{\mathbf{D}} = \mathbf{K}^{-1} \cdot \left(\mathbf{S} - \overline{\mathbf{S}} \right) \tag{2-15}$$

Here, **K** is the interaction tensor.

We notice that, for the ϕ-model and the VPSC model, the strain rate tensor and the stress tensor are vectorized in the calculation (see Eq. 2-11 and Eq. 2-12). Therefore, the tensor **K** is a 5x5 matrix.

✓ Interaction tensor of the ϕ-model

For the visco-plastic ϕ-model, the interaction law is presented in Eqs. 2-7 to 2-9. In order to calculate the interaction tensor **K**, we need to combine the Eq. 2-14 with the interaction law of ϕ-model (Eq. 2-7). Thus, we can obtain:

$$\mathbf{S} - \langle \mathbf{B} \rangle \cdot \mathbf{B}^{-1} \cdot \mathbf{S} = \mathbf{K}^{\phi} \cdot \left(\mathbf{D} - \langle \mathbf{A} \rangle \cdot \mathbf{A}^{-1} \cdot \mathbf{D} \right) \tag{2-16}$$

And then:

$$\left(\mathbf{I} - \langle \mathbf{B} \rangle \cdot \mathbf{B}^{-1} \right) \cdot \mathbf{S} = \mathbf{K}^{\phi} \cdot \left(\mathbf{I} - \langle \mathbf{A} \rangle \cdot \mathbf{A}^{-1} \right) \cdot \mathbf{D} \tag{2-17}$$

The relation between **D** and **S** is described in Eq. 2-1. So we can get:

$$\left(\mathbf{I} - \langle \mathbf{B} \rangle \cdot \mathbf{B}^{-1} \right) = \mathbf{K}^{\phi} \cdot \left(\mathbf{I} - \langle \mathbf{A} \rangle \cdot \mathbf{A}^{-1} \right) \cdot \mathbf{M} \tag{2-18}$$

Finally, the interaction tensor **K** can be expressed as:

$$\mathbf{K}^{\phi} = \left(\mathbf{I} - \langle \mathbf{B} \rangle \cdot \mathbf{B}^{-1} \right) \cdot \mathbf{M}^{-1} \cdot \left(\mathbf{I} - \langle \mathbf{A} \rangle \cdot \mathbf{A}^{-1} \right)^{-1} \tag{2-19}$$

$$\mathbf{K}^{\phi^{-1}} = \left(\mathbf{I} - \langle \mathbf{A} \rangle \cdot \mathbf{A}^{-1} \right) \cdot \mathbf{M} \cdot \left(\mathbf{I} - \langle \mathbf{B} \rangle \cdot \mathbf{B}^{-1} \right)^{-1} \tag{2-20}$$

To study the evolution of the interaction tensor, we perform simulations of tensile tests in FCC metals with only the {111}<110> slip considered. The simulations start with a random texture and the linear hardening is used. The boundary condition (macroscopic velocity gradient) is set to be:

$$\bar{\mathbf{L}} = \dot{\varepsilon}_0 \begin{bmatrix} -0.5 & 0 & 0 \\ 0 & -0.5 & 0 \\ 0 & 0 & 1 \end{bmatrix} \tag{2-21}$$

We should note that the interaction tensor is different for each grain. We randomly pick one grain and its interaction tensor evolutions are calculated. We choose the ϕ value of 0.01, 0.1, 0.7 and 0.99. The evolutions of the five components on the trace of

the 5x5 matrixes are presented in Fig. 2-7 to Fig. 2-9 for the n value of 3, 5 and 9. For the results of n=9, we present the inverse of **K** tensor for $\phi = 0.01$ and $\phi = 0.1$ in order to avoid the numerical errors.

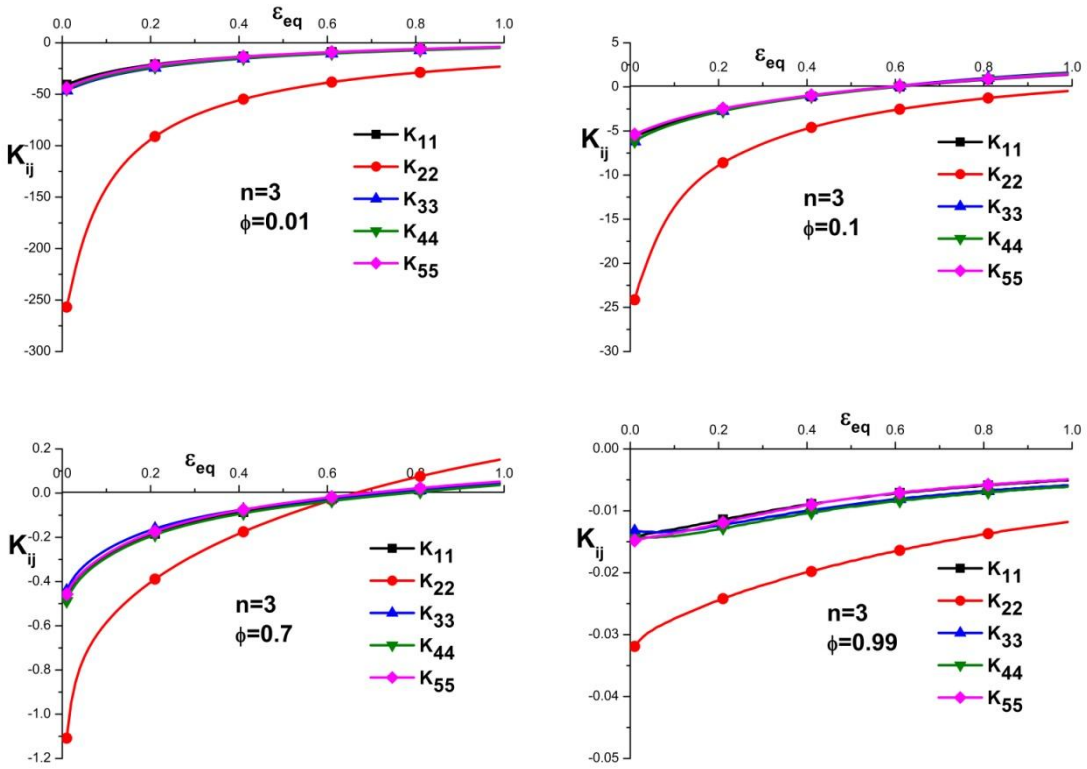

Fig. 2-7. Evolution of the interaction tensor of ϕ-model for n=3.

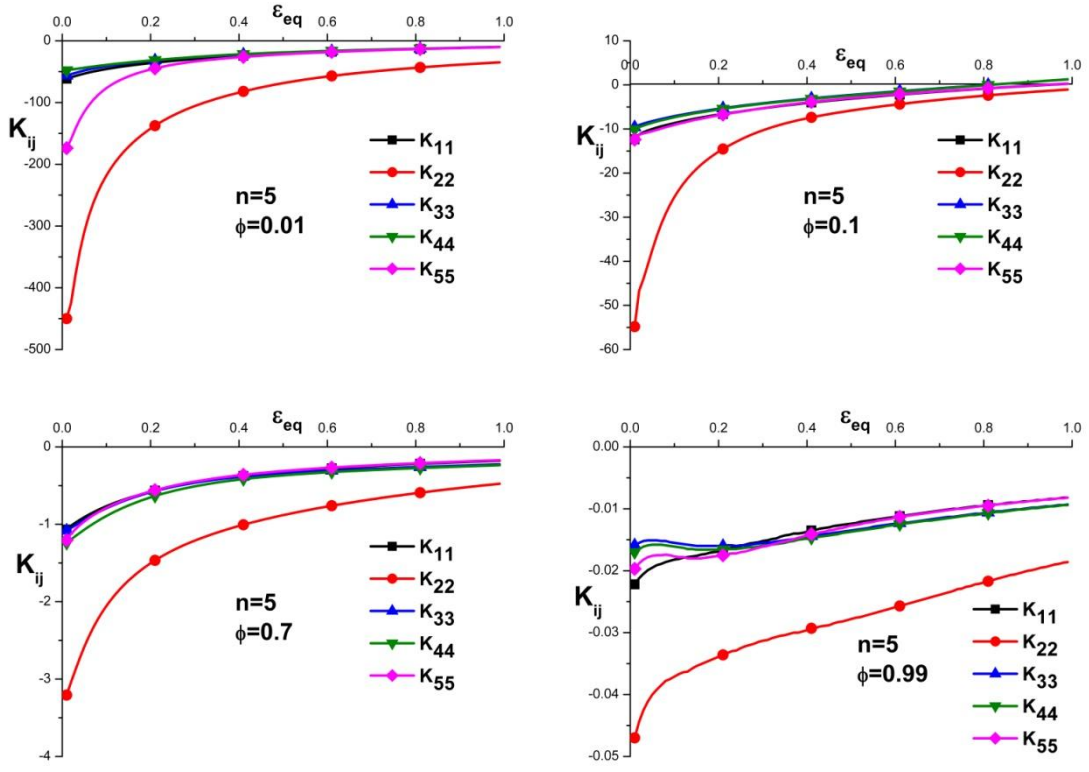

Fig. 2-8. Evolution of the interaction tensor of ϕ-model for n=5.

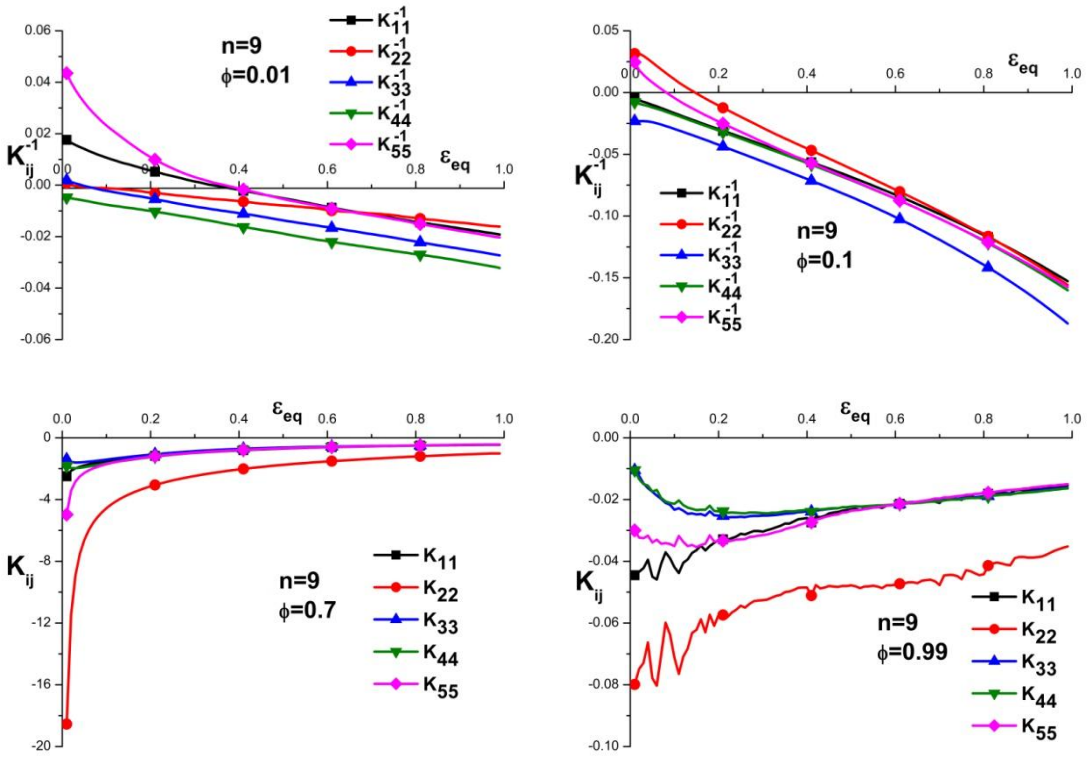

Fig. 2-9. Evolution of the interaction tensor of ϕ-model for n=9.

From those results, we can see that, for all n values, a lower ϕ value will lead to a stronger interaction tensor **K** (larger absolute value of K_{ij}). It is reasonable because for a stiff interaction (low ϕ values), the difference between $\mathbf{D}$ and $\overline{\mathbf{D}}$ will be limited whereas the difference between $\mathbf{S}$ and $\overline{\mathbf{S}}$ will be enlarged. When ϕ is close to 1, the values of K_{ij} are very close to 0.

We note that the values of K_{ij} evolve with the strain increase. This phenomenon can be explained by the texture evolution. The results for n=9 show the waviness at $\phi = 0.99$. This may be explained by the fast transition of the grain orientation. That is to say, when a compliant interaction (high ϕ values) is used, some grains may rotate very fast due to the kinematic freedom.

✓ **Interaction tensor of the VPSC model**

As shown in section I.8.5.4, the interaction tensor of the VPSC model, which is obtained directly from its interaction law, can be expressed as:

$$\mathbf{K}^{\mathbf{VPSC}} = \mathrm{n}^{\mathrm{eff}-1} \cdot \overline{\mathbf{M}}^{-1} \cdot \mathbf{E}^{-1} \cdot (\mathbf{I} - \mathbf{E}) \qquad (2\text{-}22)$$

Then, we carried out a similar simulation with the same input parameters than the one using the ϕ-model. The grain shape is calculated individually in each grain. The simulation is performed using the Tangent and Secant interactions and we present the evolution of the interaction tensors on the same grain as the previous simulation using the ϕ-model (Fig. 2-10 to Fig. 2-12).

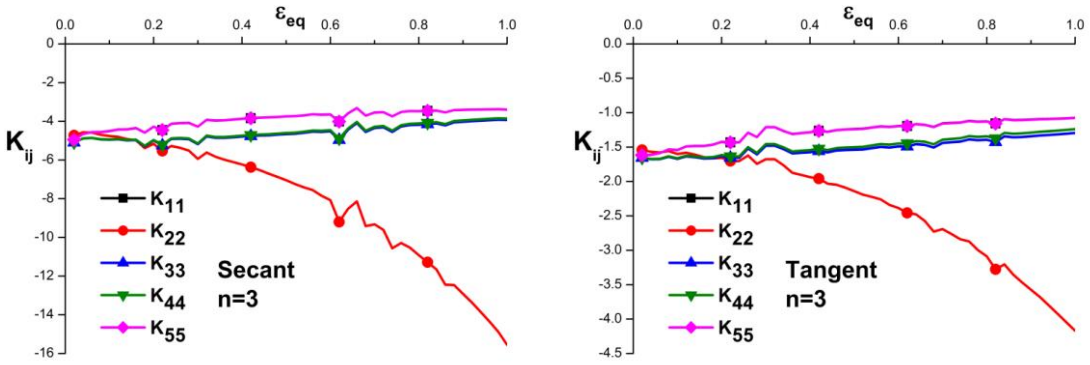

Fig. 2-10. Evolution of the interaction tensor of the VPSC model for n=3.

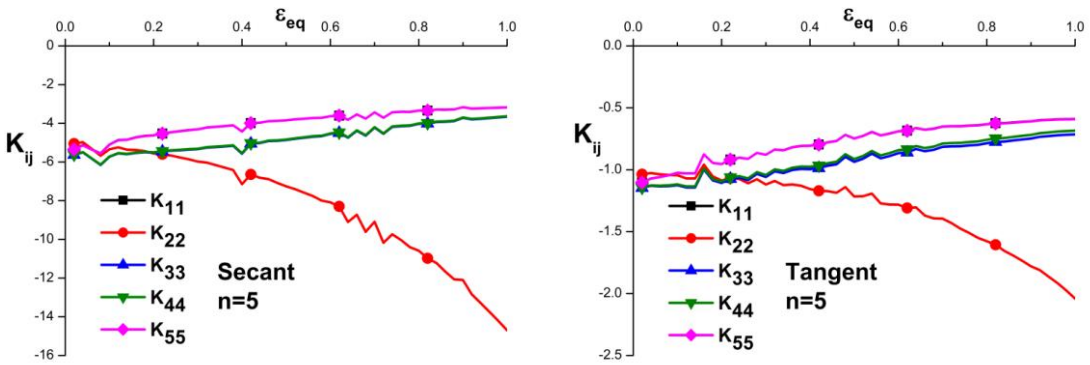

Fig. 2-11. Evolution of the interaction tensor of the VPSC model for n=5.

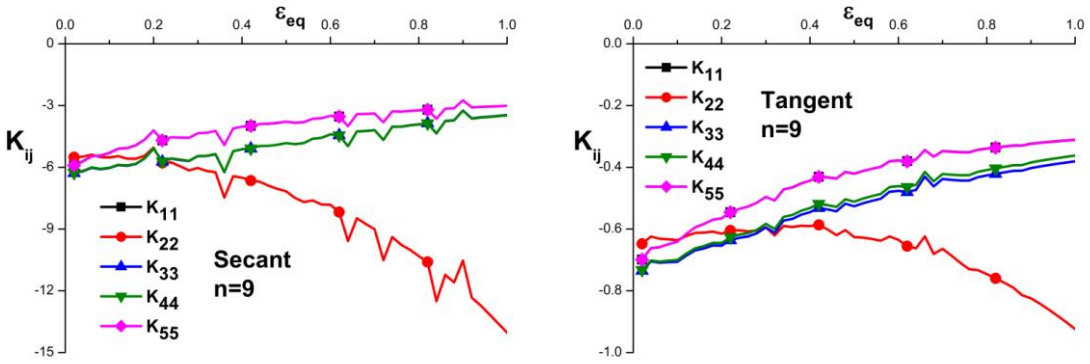

Fig. 2-12. Evolution of the interaction tensor of the VPSC model for n=9.

From these results (Fig. 2-10 to Fig. 2-12), we can see that the n value can slightly increase the absolute values of the **K** components. Moreover, the absolute values of the **K** components for the Secant case are about n times stronger than the ones for the Tangent case. This is a reasonable result due to the definition of these two interactions (see section I.8.5.4).

We should notice that the evolution of the $\mathbf{K}_{22}$ component of the VPSC model shows a different evolution tendency than the ϕ-model (Fig. 2-7 to Fig. 2-9). Here, we cannot judge the predicted results of K evolution since such results in experiments cannot be achieved so far. However, we can perform a study of the information contained in $\mathbf{K}^{\phi}$ and $\mathbf{K}^{VPSC}$. According the expressions of $\mathbf{K}^{\phi}$ (Eq. 2-19) and $\mathbf{K}^{VPSC}$ (Eq. 2-22), they both contain the n and $\overline{M}$. The $\mathbf{K}^{VPSC}$ can take into account the grain shape effect via the Eshelby tensor which cannot be found in $\mathbf{K}^{\phi}$. However, we believe that the grain shape effect may also be considered in $\mathbf{K}^{\phi}$ via the ϕ value. That is to say, the evolution of the grain shape may correspond to the evolution of the ϕ value. The work on this point will be carried out in future. Furthermore, we should also notice that the forth order compliance tensor $\mathbf{M}$ can be found in the expression of $\mathbf{K}^{\phi}$ (Eq. 2-19), which contains the information of the crystallographic orientation of the grains. Such information is absent from the interaction tensor of the VPSC model.

References:

Ahzi, S., 1987. A self consistent approach to the behavior of viscoplastic polycrystals during large deformation, Ph.D. Thesis. University of Metz, France.

Ahzi, S., M'Guil, S., 2008. A new intermediate model for polycrystalline viscoplastic deformation and texture evolution. Acta Mater. 56, 5359-5369.

Asaro, R.J., Needleman, A., 1985. Texture development and strain hardening in rate dependent polycrystals. Acta Metall. 33, 923-953.

M'Guil, S., Ahzi, S., Barlat, F., Gracio, J.J., 2011. Simulation of microstructural effects and yield surface evolution in cubic metals using the viscoplastic ϕ-model. Int. J. Plasticity 27, 102-120.

M'Guil, S., Ahzi, S., Youssef, H., Baniassadi, M., Gracio, J.J., 2009. A comparison of viscoplastic intermediate approaches for deformation texture evolution in FCC polycrystals. Acta Mater. 57, 2496-2508.

Molinari, A., Canova, G.R., Ahzi, S., 1987. A self-consistent approach of the large deformation polycrystal viscoplasticity. Acta Metall. 35, 2983-2994.

Sachs, G., 1928. Plasticity problems in metals. Z. Ver. Deutsch. Ing.72, 734-736.

Taylor, G.I., 1938. Plastic strain in metals. J. Inst. Metals. 62, 307-324.

Chapter III. Application of ϕ-model in FCC rolling tests: coupled effects of the lattice rotation definition, twinning and interaction strength

III.1 Introduction

The development of texture during rolling is one of the most important factors that influence the properties of the rolled sheets and their behavior in subsequent forming processes. The FCC rolling textures have been analyzed in many works (e.g. Carstensen et al., 2002; El-Danaf et al., 2011; Leffers, 1993, 1996, 2001a,b, 2012; Leffers and Bilde-Sørensen, 1990; Leffers and Pedersen, 2002; Leffers and Juul Jensen, 1988; Leffers and Ray, 2009; Leffers and Van Houtte, 1989; Staroselsky and Anand, 1998; Van Houtte, 1978; Wen et al., 2012a). Two different types of FCC rolling texture, the copper-type and brass-type textures, can be observed in FCC metals with different properties and loading conditions (Leffers and Ray, 2009). Usually, the copper-type textures were observed in FCC metals with high stacking fault energy (SFE) whereas the brass-type texture can be obtained for low SFE. Sources influencing the development of copper- or brass-type texture are : stacking fault energy (SFE), twinning, micro-shear banding, twin barrier effect, hardening etc. (Beyerlein et al., 2011; El-Danaf et al., 2000, 2001, 2011; Lebensohn et al., 2007; Leffers and Ray, 2009; Miraglia et al., 2007, Paul et al., 2007, 2009).

From a simulation point of view, the prediction of FCC rolling texture transition can be controlled by the interaction law (Leffers and Ray, 2009; Leffers, 2012) and the consideration of {111}<112> mechanical twinning (Leffers and Ray, 2009, Van Houtte, 1978). Another factor that influences the predicted rolling texture is the definition of the lattice spin (Hosford, 1977; Lebensohn and Leffers, 1999; Wierzbanowski et al., 2011).

The mathematical analysis (MA) and the plane-strain analysis (PSA) are usually used to calculate the lattice spin in solid mechanics (Hosford, 1977; Lebensohn and Leffers, 1999; Wierzbanowski et al., 2011). The MA derives naturally from kinematic analysis

in continuum mechanics whereas the PSA is derived from geometrical condition under rolling. The PSA calculation is suitable to simulate rolling process at large strain when the grains are elongated and flattened (Hosford, 1977; Lebensohn and Leffers, 1999; Wierzbanowski et al., 2011).

The effects of each of these three factors (interaction laws, consideration of twinning and definition of lattice spin) on FCC rolling texture transition, from copper- to brass-type, have been addressed by many authors (Beyerlein et al., 2011; Lebensohn and Leffers, 1999; Leffers, 1968, 1993, 1996, 2012; Leffers and Ray, 2009; Leffers and Van Houtte, 1989; Van Houtte, 1978; Wierzbanowski et al., 2011). The plastic deformations in FCC metals are mainly accumulated by the activation of {111}<110> slip and {111}<112> mechanical twinning. The copper-type texture is usually achieved when only {111}<110> slip mode is considered using Taylor model, the upper bound approximation (e.g. Taylor, 1938, Van Houtte, 2005). In this case, the effect of the lattice spin definition can be neglected as the MA and PSA calculations are theoretically equal when the Taylor model is used. Leffers (1996) have obtained a brass-type texture using PSA and a modified Sachs approach (e.g. Ahzi et al., 1993, 2002, Sachs, 1928) where only {111}<110> slip mode is considered. However, the {111}<112> mechanical twinning was suggested to be the explanation of the formation of the brass-type texture (Leffers and Ray, 2009). Van Houtte (1978) obtained a typical brass-type texture by using a Taylor model with the consideration of twinning.

In this work, both MA and PSA definitions have been considered into the visco-plastic ϕ-model. The textures calculated by the PSA definition are compared with the ones of MA under plane strain compression tests (approximation of the rolling). The results are presented in terms of pole figures, Orientation Distribution Function (ODF)

sections. The ideal rolling texture components (cube (C), brass (B), goss (G), copper (Cu) and S components) are analyzed as function of increasing strain. The coupled effect of the plastic deformation mechanisms (with or without twinning), the grain strength interaction (parameter ϕ from 0 to 1) and the lattice spin definition (MA or PSA) on the FCC rolling texture transition is deeply studied. We note that in this work, no attempt to link the parameter ϕ to microstructural features of the material is proposed. This parameter is merely used as a measure of interaction strength (from stiff to more compliant interaction). The results presented in this chapter can be found in the work of Wen et al. (2012b).

III.2 Calculation of the lattice spin: MA and PSA definitions

The lattice spin $\mathbf{\Omega}^*$ was defined in two ways, $\mathbf{\Omega}^{*(MA)}$ in MA and $\mathbf{\Omega}^{*(PSA)}$ in PSA. The single crystal velocity gradient $\mathbf{L}$ can be decomposed into the strain rate $\mathbf{D}$ and the spin $\mathbf{\Omega}$ as follows:

$$\mathbf{L} = \mathbf{D} + \mathbf{\Omega} \tag{3-1}$$

where $\mathbf{D} = 1/2\left(\mathbf{L} + \mathbf{L}^{\mathbf{T}}\right)$ and $\mathbf{\Omega} = 1/2\left(\mathbf{L} - \mathbf{L}^{\mathbf{T}}\right)$. In the MA definition, $\mathbf{\Omega}$ is described as the sum of the plastic spin $\mathbf{\Omega}^{\mathbf{P}}$ and MA lattice spin $\mathbf{\Omega}^{*(MA)}$ of a grain:

$$\mathbf{\Omega} = \mathbf{\Omega}^{*(MA)} + \mathbf{\Omega}^{\mathbf{p}} \tag{3-2}$$

Here, the grain shape is assumed to be spherical. Therefore, the local spin $\mathbf{\Omega}$ is equal to the macroscopic one: $\mathbf{\Omega} = \overline{\mathbf{\Omega}}$.

We note that the macroscopic spin is null for the case of rolling. Hence, the MA definition for rolling can be expressed as:

$$\mathbf{\Omega}^{*(MA)} = -\mathbf{\Omega}^{p} = -1/2\left(\mathbf{L}^{p} - \left(\mathbf{L}^{p}\right)^{T}\right) \tag{3-3}$$

The PSA definition is based on the assumption that the shape of each grain should follow that of the sample (Hosford, 1977; Lebensohn and Leffers, 1999; Wierzbanowski et al., 2011). Therefore, one can impose the following constraint: the shear components of local and global velocity gradient should remain the same: $L_{ij}=\overline{L}_{ij}$ $(i \neq j)$. In the rolling case, we have $\overline{L}_{ij}=0$ for $i \neq j$, hence: $L_{ij}=\overline{L}_{ij}=0$ for $i \neq j$. Moreover, $L_{ij}=L_{ij}^{p}+\Omega_{ij}^{*}$. Therefore, the definition of PSA can be expressed as:

$$\Omega_{ij}^{*(PSA)} = -L_{ij}^{p} \tag{3-4}$$

It can be seen that the difference in the shear components between the MA and PSA rotation defined by Eqs. 3-3 and 3-4 can be present as (Wierzbanowski et al., 2011):

$$\Omega_{ij}^{*(MA)} - \Omega_{ij}^{*(PSA)} = -1/2\left(L_{ij}^{p} - \left(L_{ij}^{p}\right)^{T}\right) + L_{ij}^{p} = 1/2\left(L_{ij}^{p} + \left(L_{ij}^{p}\right)^{T}\right) = D_{ij}^{p} \approx D_{ij} \tag{3-5}$$

In the upper-bound approximation, the local strain is assumed to be equal to the macroscopic one: $\mathbf{D}=\overline{\mathbf{D}}$. Meanwhile, the shear components of $\overline{\mathbf{D}}$ are equal to 0 for the rolling process, so: $D_{ij}=\overline{D}_{ij}$ $(i \neq j)$. Thus, for rolling, the MA and PSA definition are theoretically equal when the Taylor model is used (Wierzbanowski et al., 2011).

III.3 Simulations under plane strain compression test

III.3.1 Ideal FCC rolling component

The {001}<100> cube (C), {110}<112> brass (B), {110}<001> goss (G), {112}<111> copper (Cu) and the {123}<634> S components are the main orientations for FCC metals. The location of these texture components in the Euler space can be represented by the following Euler angles : (φ_1, Φ, φ_2): $(90^{o}, 35^{o}, 45^{o})$ for Cu component; $(55°, 90°, 45°)$ for B component; $(90°, 90°, 45°)$ for G component; $(59°,$

$37°, 63°$) for S component; and ($45°, 0°, 45°$) for C component. The positions of these orientations in the ODF section at $\varphi_2 = 45°$ and in (111) pole figure are represented in Fig. 3-1. The copper-type texture can be described as the superposition of Cu, S and B components. The brass-type texture can be described by the superposition of the B and G components (M'Guil et al., 2010, 2011).

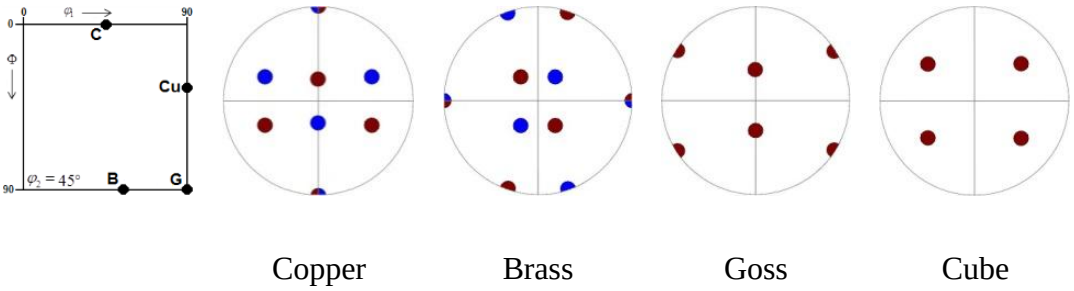

Fig. 3-1. Schematic representation of the main orientations in FCC materials, ODF sections at $\varphi_2 = 45°$ and (111) pole figures.

The evolution of these FCC rolling components can affect the metal properties during the forming applications. For instance, the material formability decreases with the rise of the G component whereas stronger C, B and S components lead to higher formability (M'Guil et al., 2010, 2011). For the two types of FCC rolling texture (copper- and brass-type), their specific components evolution have been described in many works (e.g. Carstensen et al., 2002; Leffers and Juul Jensen, 1988; Leffers and Ray, 2009). These works usually focus on the evolution of the Cu and the B components. Leffers and Juul Jensen (1988) have studied the rolling texture for copper and brass. Their results showed that the brass-type texture has a lower intensity of the Cu component and a higher intensity of the B component. As the Ni-Co alloys can give a texture transition from the copper- to brass-type texture by increasing the content of cobalt, Carstensen et al. (2002) have compared the evolution of textures measured from rolled Ni-30%Co (high SFE) to Ni-60%Co (low SFE). In the Ni-30%Co which develops a texture close to copper-type, the intensity of the Cu

component increases gradually whereas the intensity of the B component does not show a significant change with increasing strain. Moreover, in the Ni-60%Co, the intensity of the Cu component remains at a constant level and the intensity of the B component increases linearly with increasing strain.

III.3.2 Input parameters

The simulation of FCC rolling texture was approximated by the plane strain compression test which neglects the effect of shear involved in the rolling process. The initial texture is represented by 500 random orientations (grains). The simulations are conducted with a linear strain hardening using Voce law. The inverse strain rate sensitivity coefficient is chosen as $n=11$. In order to explain the crystallographic reorientation by twinning, we used the PTR scheme of Tomé et al. (1991). When twinning is considered, the parameters of the PTR scheme are set to be the same as the ones used in the work of Beyerlein et al. (2011): $A^{th1}=0.25$, $A^{th2}=0.1$ and $S^{t}=0.707$. The ratio between the critical resolved shear stress (CRSS) in twinning and in slip (called α value by Van Houtte (1978)) is chosen to be 0.8 as in the work of Van Houtte (1978). In order to study the effect of the interaction strength, we choose several values of ϕ: 0.1, 0.3, 0.5, 0.7, as well as extreme values of ϕ to be close to Taylor case with $\phi \to 0$ ($\phi = 10^{-6}$) and close to the lower bound (static model) with $\phi \to 1$ ($\phi = 0.999$). We note that the low values of ϕ, such as 0.1, allow for an important deviation from the upper bound Taylor model. Similarly, high ϕ values, such as 0.9, also allow for an important deviation from the static model (M'Guil et al., 2009).

The plane strain compression test is a crude approximation of a symmetric rolling process. In fact, we neglect the effect of shear involved in the rolling process. Thus, we describe only the neutral (central) zone of the rolled sheet where shear effects

vanish. This simplification allows for the use of homogeneous boundary conditions. In the following, deformation is simulated imposing successive deformation increments. At each deformation step, the boundary conditions are imposed in terms of the overall velocity gradient, $\overline{\mathbf{L}}$, corresponding to a constant strain rate $(\dot{\varepsilon}_0)$. In this study, the macroscopic velocity gradient is assumed constant and fully prescribed. Here, $\vec{x}$ represents the flow direction and $\vec{z}$ the normal direction:

$$\overline{\mathbf{L}} = \dot{\varepsilon}_0 \begin{bmatrix} 1 & 0 & 0 \\ 0 & 0 & 0 \\ 0 & 0 & -1 \end{bmatrix} \tag{3-5}$$

III.3.3 Texture evolution in terms of ODF sections and pole figures

In this section, the textures calculated by the MA and the PSA definitions are compared. The results are presented in terms of pole figures and ODF section at $\varphi_2 = 45°$ as function of interaction strength (ϕ) and twinning. We choose the equivalent strain $\varepsilon = 140\%$ ($\approx 75\%$ rolling reduction) which is a relatively high strain.

✓ **MA definition**

The textures calculated by MA definition are shown in Figs. 3-2 to 3-5. In this case, when twinning is not considered, the calculated pole figures with low ϕ values (Fig. 3-2, $\phi \to 0$ and $\phi = 0.1$) show a typical copper-type texture. With all values of ϕ and twinning, the predicted pole figures (Fig. 3-3) present a trend to the brass-type texture. For $\phi > 0.3$ and without twinning (Fig.3-2), we predict a texture with a relatively strong Cu component. In the corresponding ODF sections, for the case without twinning (Fig. 3-4), the Cu and B components do not show an evident

intensity difference for different ϕ values. However, the B component presents an evident shift towards lower φ_1 values. Meanwhile, the effect of twinning on the intensity of these two components is much stronger than the effect of the interaction strength. With twinning (Fig. 3-5), the intensity of the Cu component is strongly decreased and the B component is strongly increased. The reduction of Cu component is known to be caused by twinning and responds to the formation of brass-type texture (Vercammen et al., 2004).

✓ **PSA definition**

The predicted textures with the PSA definition are presented in Figs. 3-6 to 3-9. Since the MA and PSA definitions are theoretically equal when Taylor model is used (see section III.2), the pole figures predicted by these two definitions are similar when $\phi \to 0$. For the case without twinning, the predicted pole figures (Fig. 3-6) show a complete texture transition from copper- to brass-type with the decreasing of the interaction strength (increasing of ϕ). When twinning is considered, the predicted pole figures (Fig. 3-7) tend to yield a texture close to brass-type texture for all ϕ values. In their corresponding ODF sections, for the case without twinning (Fig. 3-8), the intensity of the B component increases while the intensity of the Cu component decreases gradually as the ϕ value increases. The shift phenomenon of component B that was reported in the MA case (Fig. 3-4) with high ϕ values is not found with the PSA case. When twinning is considered (Fig. 3-9), the effect of the parameter ϕ on the component B is not significant. The Cu component shifts from its ideal position from $\phi = 0.3$. At $\phi = 0.7$ and $\phi \to 1$, a strong component appears near the location of $\Phi = 90^o$ and $\varphi_1 = 0^o$.

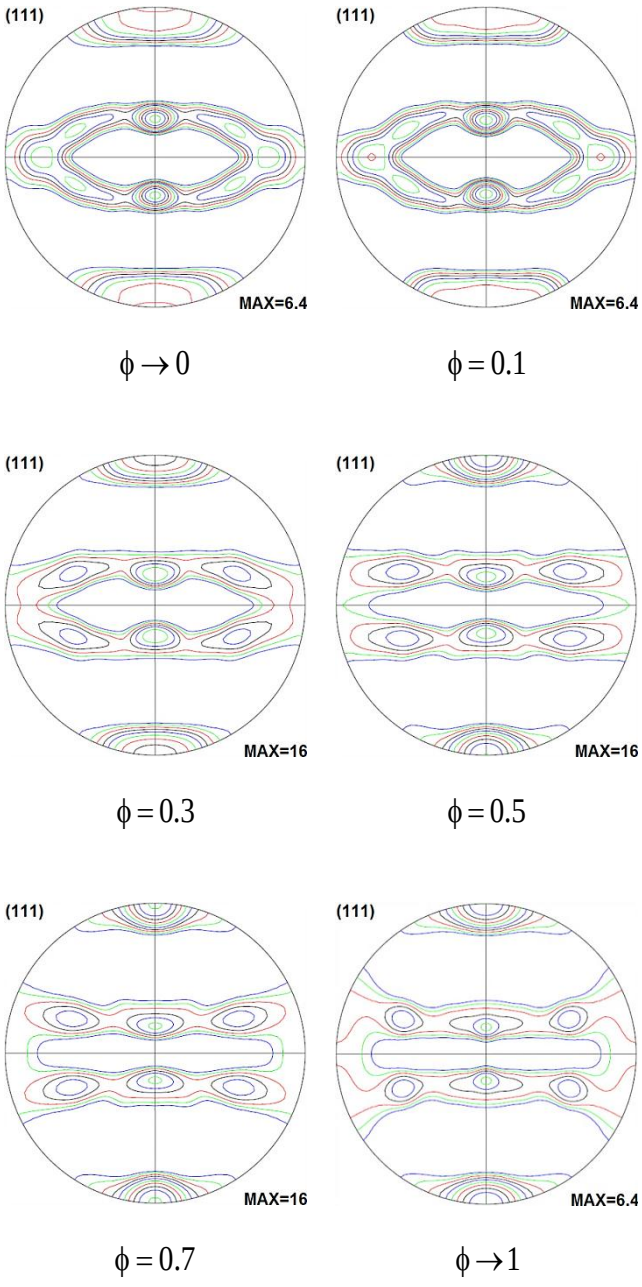

Fig. 3-2. Effect of ϕ on predicted textures in terms of (111) pole figures at $\varepsilon_{eq} = 140\%$ for MA definition, without twinning

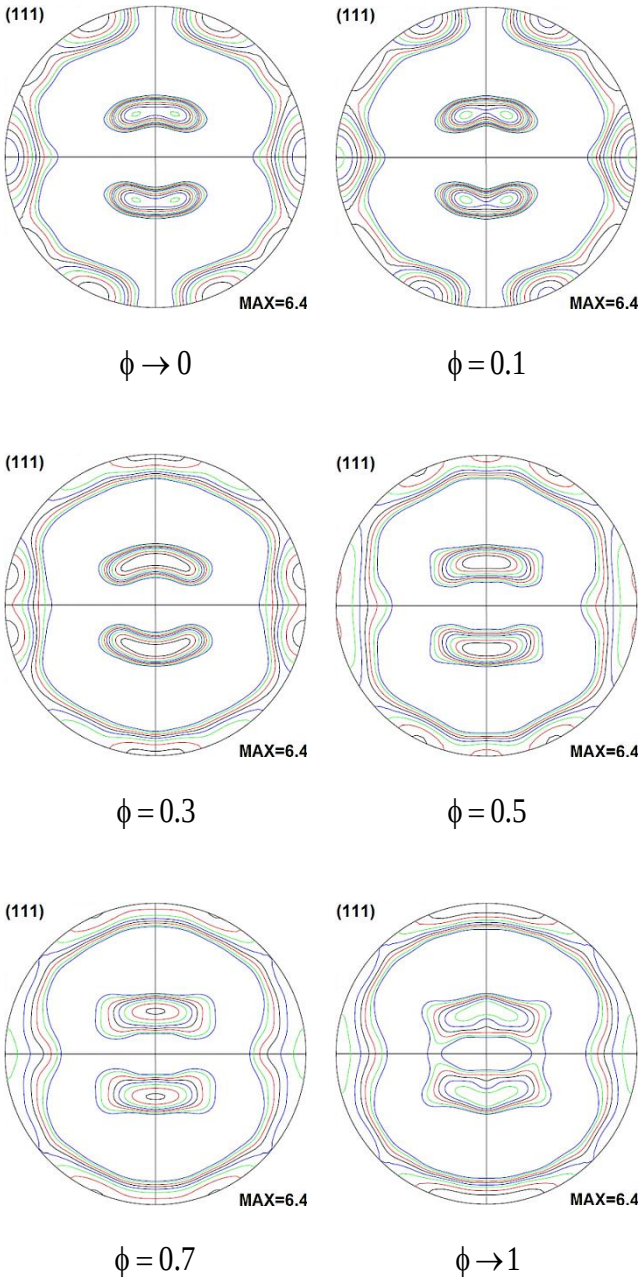

Fig. 3-3. Effect of ϕ on predicted textures in terms of (111) pole figures at $\varepsilon_{eq} = 140\%$ for MA definition, with twinning

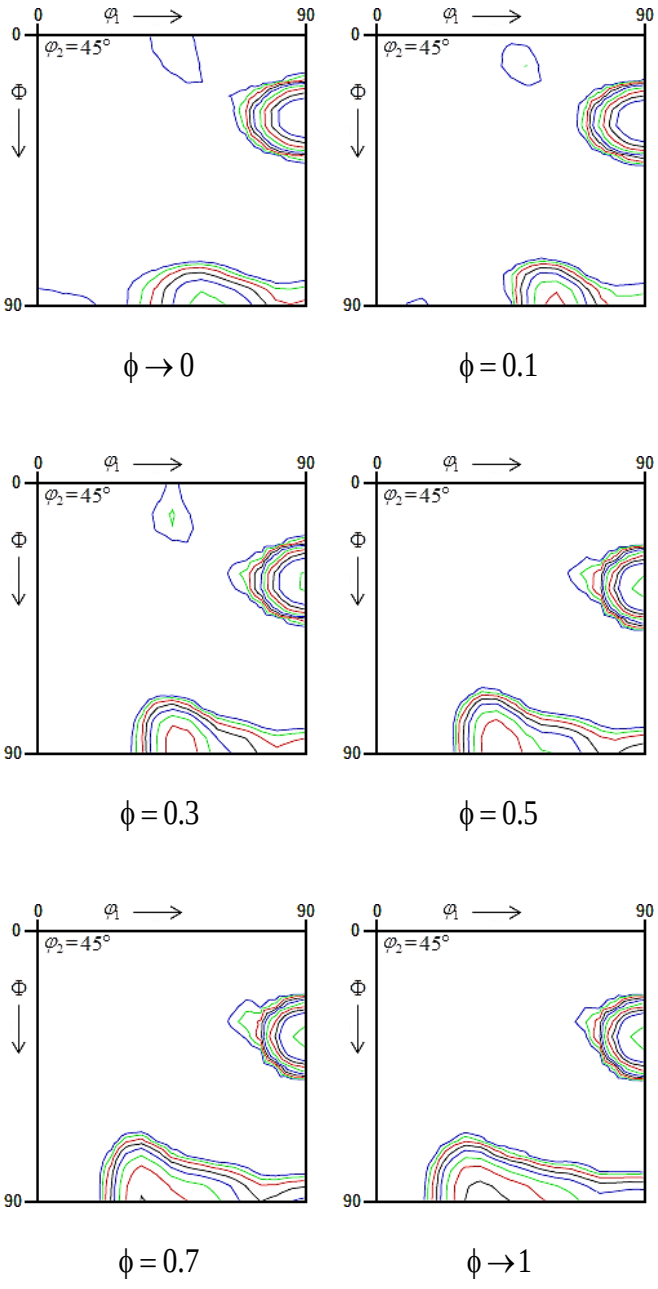

Fig. 3-4. Effect of ϕ on predicted textures in terms of ODF sections ($\varphi_2 = 45^\circ$) at $\varepsilon_{eq} = 140\%$ for MA definition, without twinning

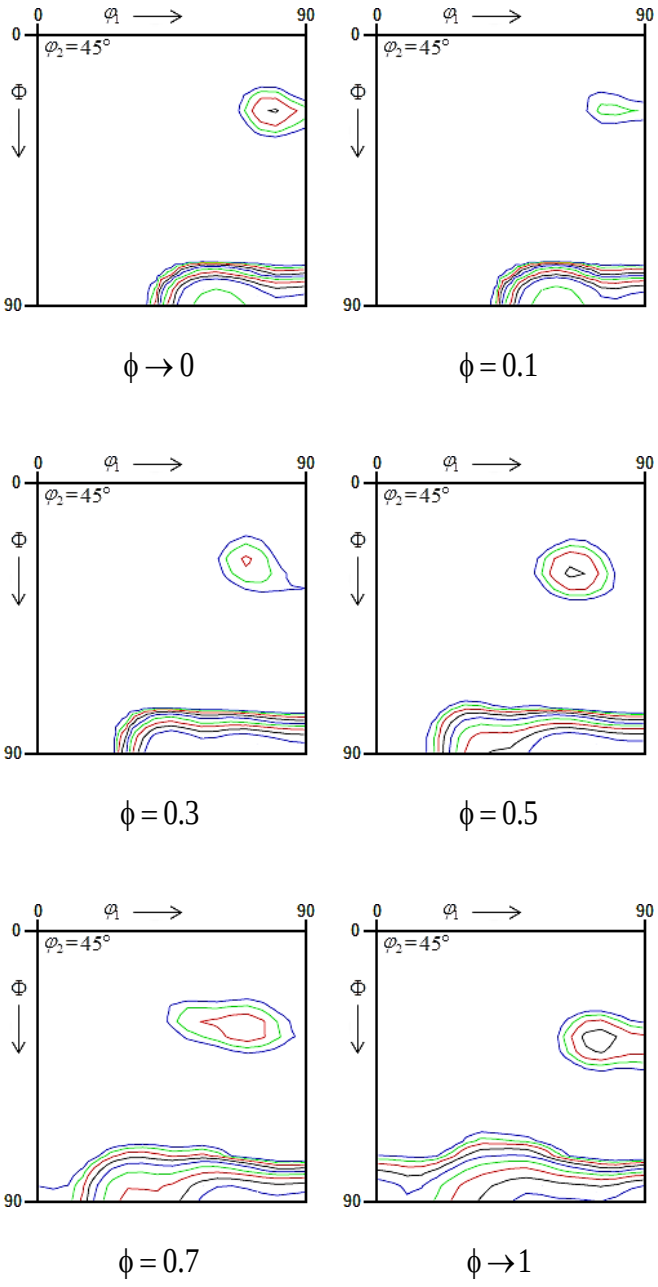

Fig. 3-5. Effect of ϕ on predicted textures in terms of ODF sections ($\varphi_2 = 45^\circ$) at $\varepsilon_{eq} = 140\%$ for MA definition, with twinning

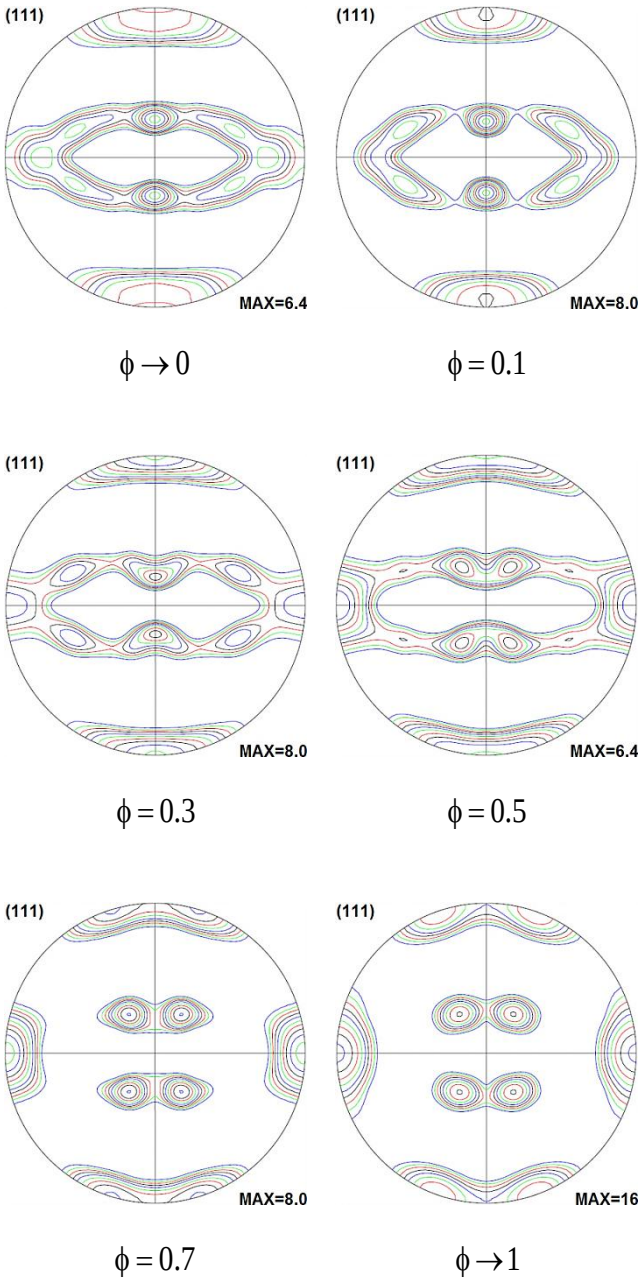

Fig. 3-6. Effect of ϕ on predicted textures in terms of (111) pole figures at $\varepsilon_{eq} = 140\%$ for PSA definition, without twinning

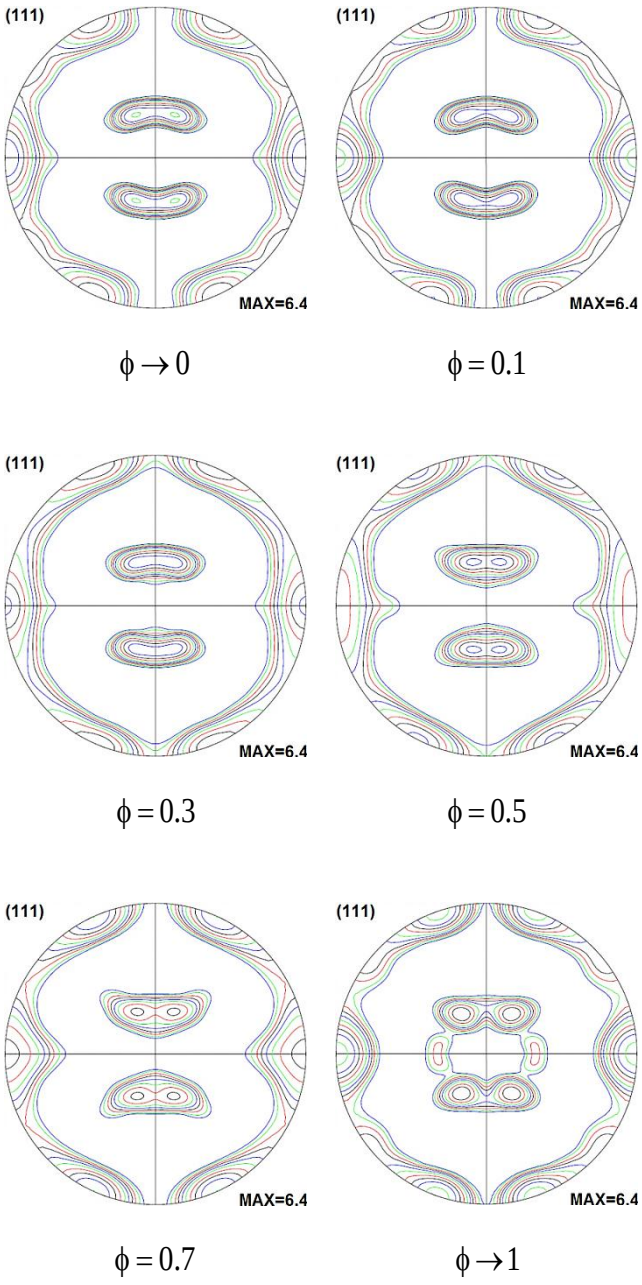

Fig. 3-7. Effect of ϕ on predicted textures in terms of (111) pole figures at $\varepsilon_{eq} = 140\%$ for PSA definition, with twinning

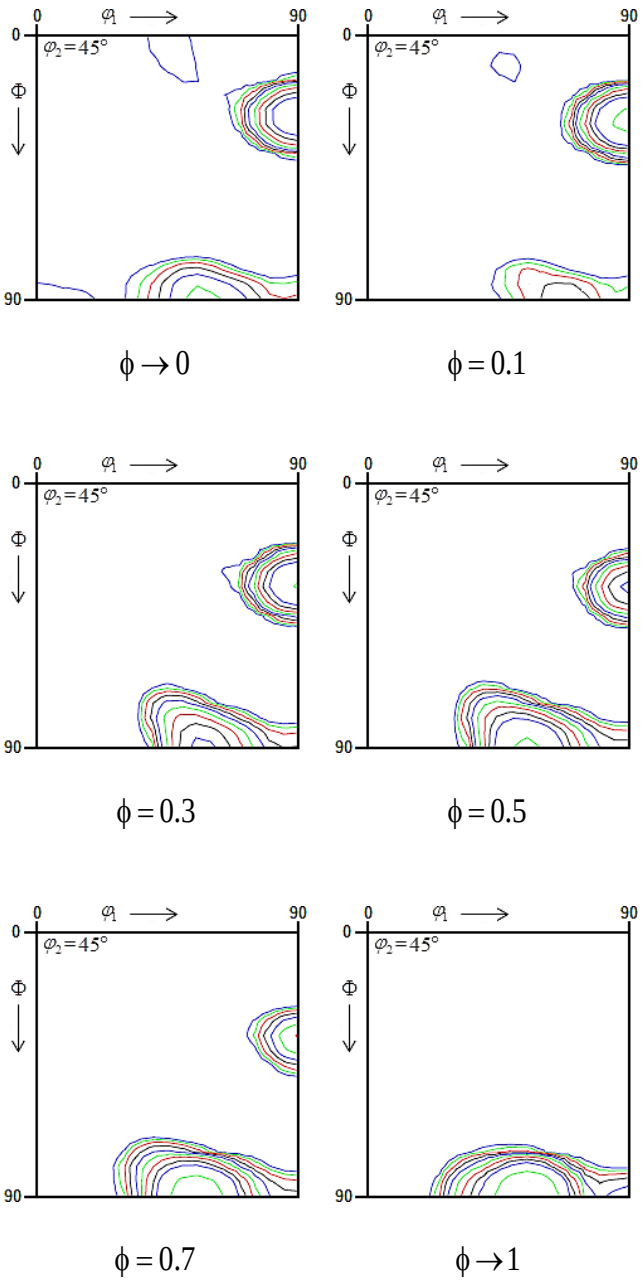

Fig. 3-8. Effect of ϕ on predicted textures in terms of ODF sections ($\varphi_2 = 45^\circ$) at $\varepsilon_{eq} = 140\%$ for PSA definition, without twinning

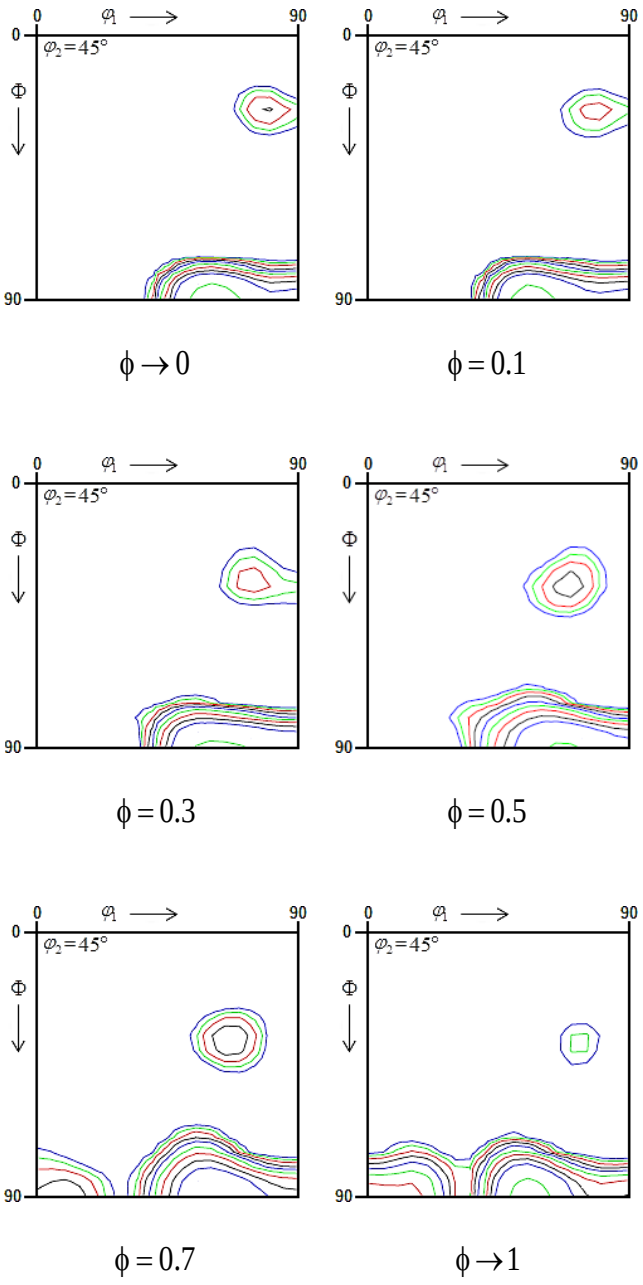

Fig. 3-9. Effect of ϕ on predicted textures in terms of ODF sections ($\varphi_2 = 45^\circ$) at $\varepsilon_{eq} = 140\%$ for PSA definition, with twinning

III.3.4 Texture evolution in terms of texture components

In this section, the evolution of the important FCC rolling components with increasing strain is analyzed. The volume fractions of the components, using a spread of 15^o around the exact position, obtained from each simulation are compared. The effect of ϕ value and twinning are also studied. The results in terms of volume fraction evolution (not the intensity) are presented from Fig. 3-10 to Fig. 3-13.

III.3.4.1 Results without twinning

✓ **MA definition**

The results for MA definition without twinning are shown in Fig. 3-10. At low ϕ values ($\phi \to 0$ and $\phi = 0.1$), the texture are dominated by S and Cu components, and then by the B component. The superposition of these three components leads to the formation of a copper-type texture (M'Guil et al., 2010, 2011). The B component does not show an important change as the ϕ value increases. For the Cu component, its volume fraction is gradually increased with the increasing strain and weakly increased with the increasing ϕ value. The S component is gradually increased with strain at low ϕ values. However, from $\phi = 0.3$, its volume fraction increases at lower strain but strongly decreases at higher strain. Hence, at high ϕ values, the textures become dominated only by the Cu component at larger strain. This explains the strong Cu component in the (111) pole figure simulated by MA without twinning at high ϕ value (Fig. 3-2). The G component increases slightly as ϕ increases but is almost insensitive to the strain level.

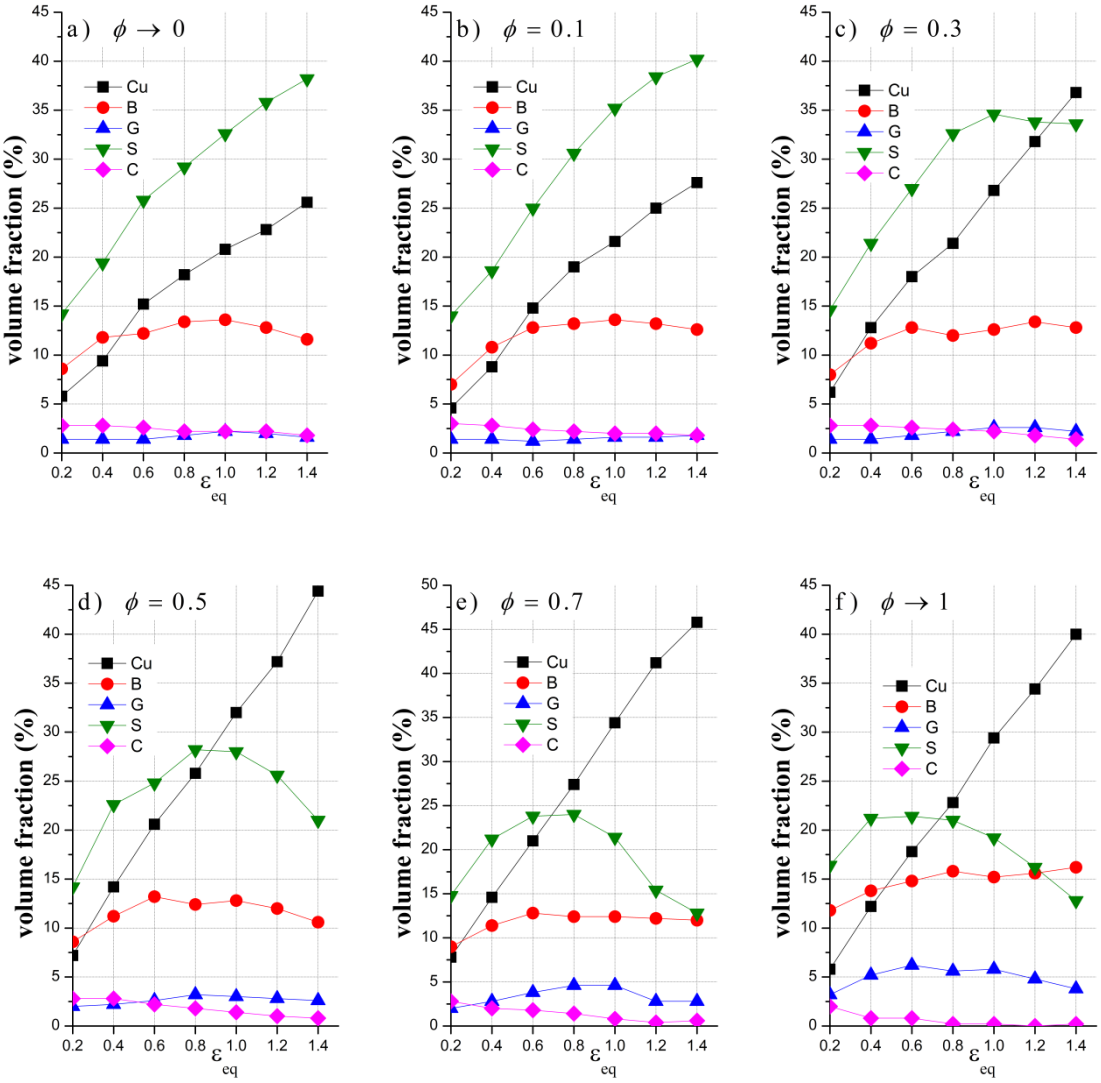

Fig. 3-10. Effect of ϕ on the evolution of rolling components for MA definition without twinning.

✓ **PSA definition**

The results for PSA without twinning are shown in Fig. 3-11. At low ϕ values, the volume fractions of the components are similar to the case MA without twinning. The volume fractions of Cu and S components increase gradually with increasing strain while B component generally remains at constant level. When the ϕ value increases, the volume fraction of the B component is strongly increased. For the high values of ϕ ($\phi \geq 0.5$), the volume fractions of Cu and S components first increase and then

decrease during the rolling process. Hence, the textures are dominated by the B component for higher strain. Moreover, the G component seems to be independent of ϕ value and does not show a significant change with increasing strain.

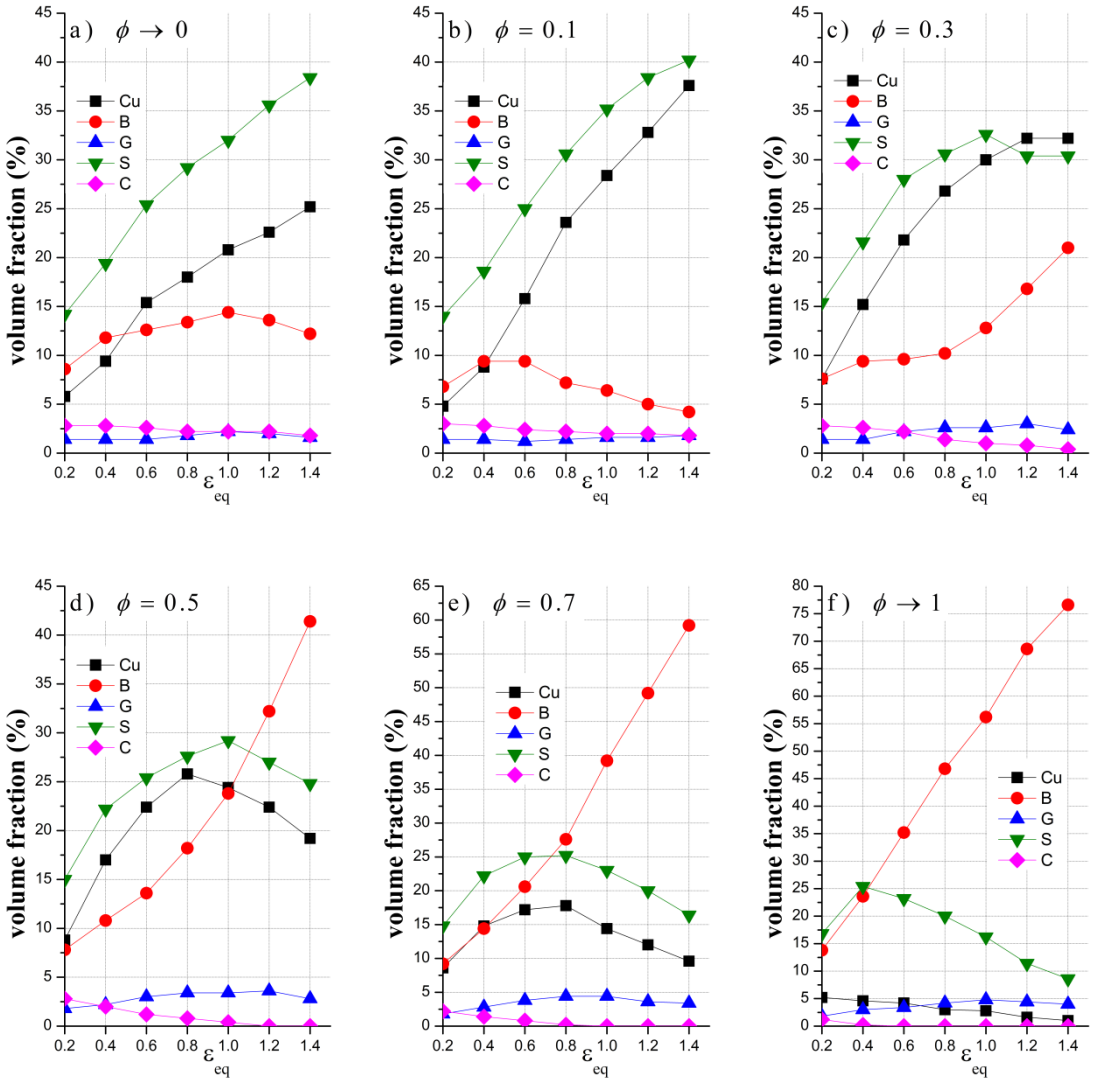

Fig. 3-11. Effect of ϕ on the evolution of rolling components for PSA definition without twinning.

III.3.4.2 Results with twinning

✓ **MA definition**

When twinning is considered, with the MA definition (Fig. 3-12), the results for low

ϕ values show a strong B component followed by G and S components. The superposition of B and G components leads to a brass-type texture (M'Guil et al., 2010, 2011). We note that the strongest B component can be found at $\phi = 0.1$. From $\phi = 0.3$, the volume fraction of the B component begins to decrease with increasing ϕ. Compared to the case of MA without twinning (Fig. 3-10), the volume fraction of the Cu component is strongly decreased whereas the one of B component and G component are strongly increased when twinning is accounted for. This is in agreement with the literature such as Vercammen et al. (2004) who suggested that the change in Cu and G components is due to the mechanical twinning by which the Cu component is transformed to a position close to the G component.

PSA definition

The results for PSA with twinning are shown in Fig. 3-13. The evolutions of the components are similar to the case of MA with twinning at low ϕ values. The B and G components are relatively strong which leads to a brass-type texture for $\phi < 0.5$. For high values of ϕ, the volume fraction of B component is no longer monotone increasing with strain. The predicted wavy evolution of the component B for $\phi \geq 0.5$ is in agreement with the experimental results of El-Danaf et al. (2000) (see Fig. 3-33). We note that this waviness of the evolution of the component B as function of strain is also obtained in the case of MA with twinning and for $\phi \geq 0.5$.

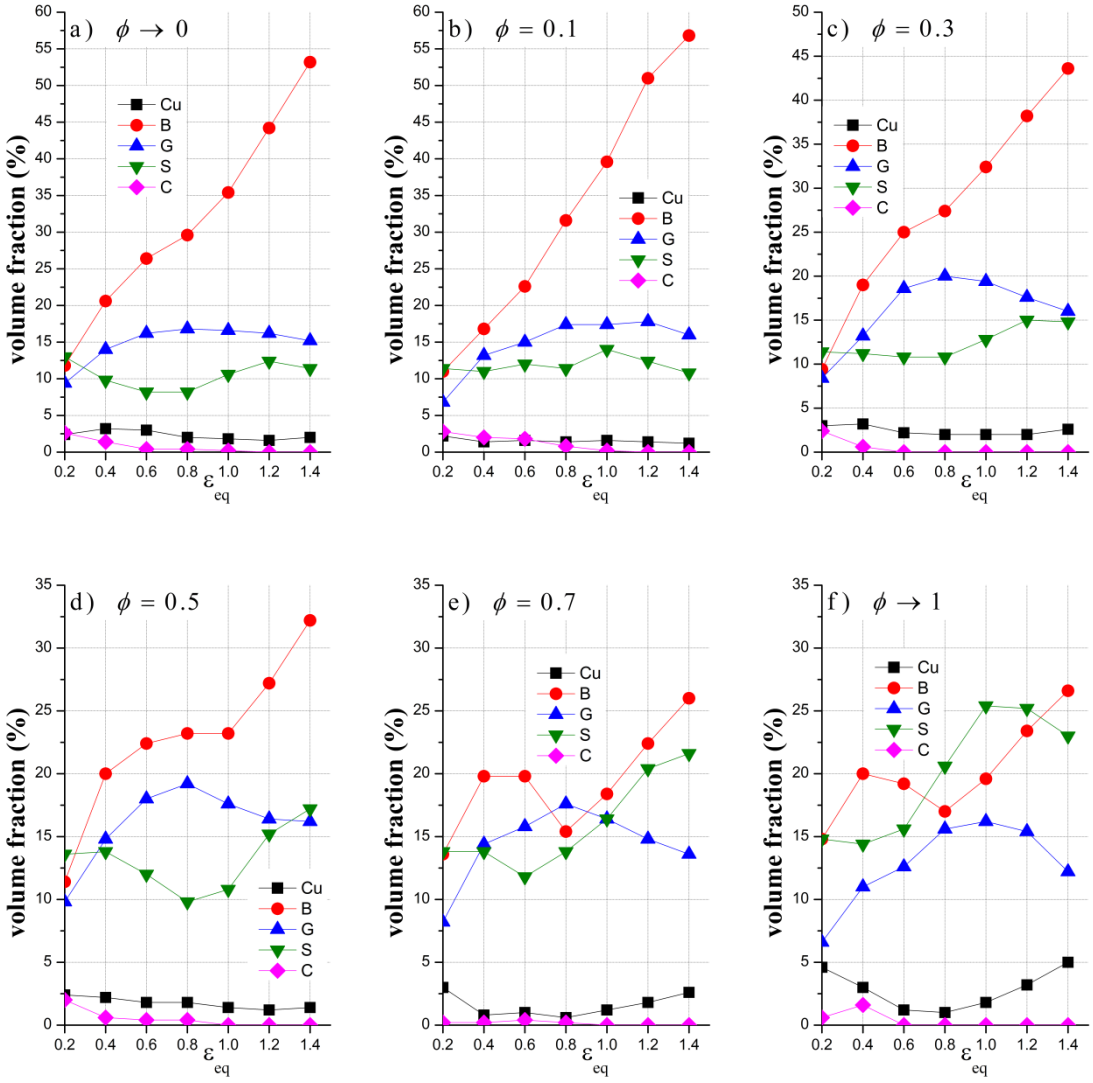

Fig. 3-12. Effect of ϕ on the evolution of rolling components for MA definition with twinning.

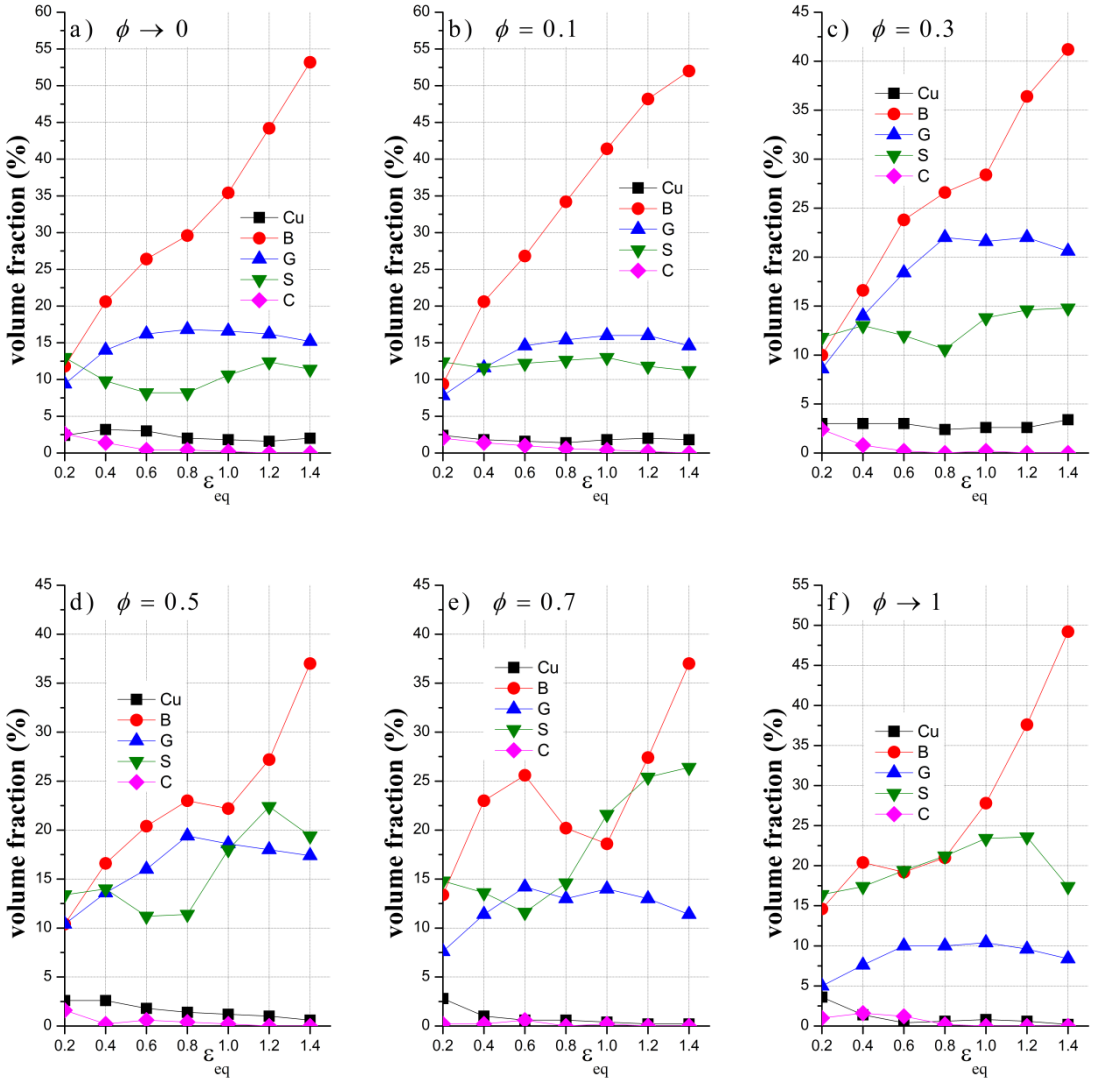

Fig. 3-13. Effect of ϕ on the evolution of rolling components for PSA definition with twinning.

III.4 Effect of relative slip/twinning activities on texture evolutions

The activation of deformation twinning can affect the texture evolution. This influence can be more evident if the relative activity of twinning to slip is stronger. The relative activities of crystallographic slip and twinning can be controlled by the α value ($\alpha = \tau_0^{tw} / \tau_0^{slip}$) defined by Van Houtte (1978). Previously, we choose $\alpha = 0.8$

as in the work of Van Houtte (1978). In this section, we will compare the slip/twinning activities and predicted textures for α values of 0.8, 1.0 and 1.2. The relative slip/twinning activities are presented for MA (Fig 3-14) and PSA (Fig 3-15) definitions and for various ϕ values. It can be seen that a higher α value leads to a lower activity of twinning. The activities of twinning are extremely weak for $\alpha = 1.2$.

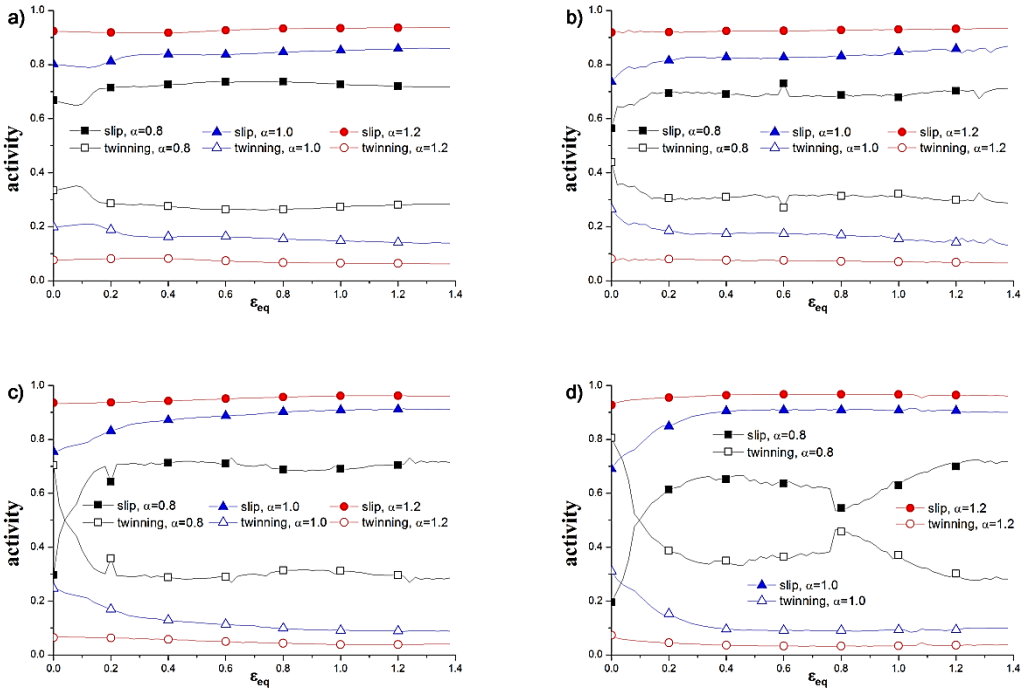

Fig. 3-14. Effect of α value on slip/twinning activities for $\phi \to 0$ (a), $\phi = 0.1$ (b), $\phi = 0.7$ (c) and $\phi \to 1$ (d), MA definition.

The texture evolutions are shown in terms of FCC rolling texture components in Figs 3-16 to 3-23. The results without twinning are also presented which can be considered as the limited case of $\alpha \to \infty$. In these results, we can see that the effect of α value is explicit in some cases. For example, a higher α value leads to a stronger Cu component for both MA and PSA definitions (Figs 3-17 and 3-21); B and S components are reduced with the increase of α when ϕ value is low. For other

cases, the α value does not have a monotone effect on the texture components. This may be explained by the multiple effects of deformation twinning. When deformation twinning is activated, it would affect the deformation texture in two ways (in both modeling and in experiment): (1) via the orientations of twinning (or called volume effects of twinning) and (2) via the {111}<211> slip associated with the formation of twinning. If the effects of α value on the texture components via those two ways are different, the tendencies of results may be difficult to describe.

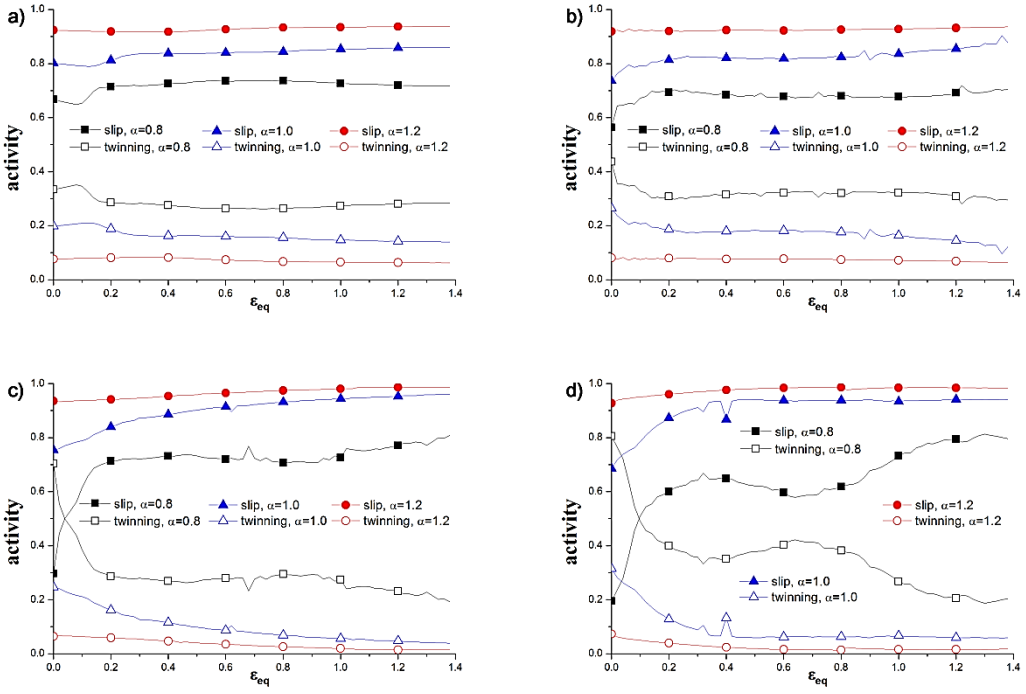

Fig. 3-15. Effect of α value on slip/twinning activities for $\phi \to 0$ (a), $\phi = 0.1$ (b), $\phi = 0.7$ (c) and $\phi \to 1$ (d), PSA definition.

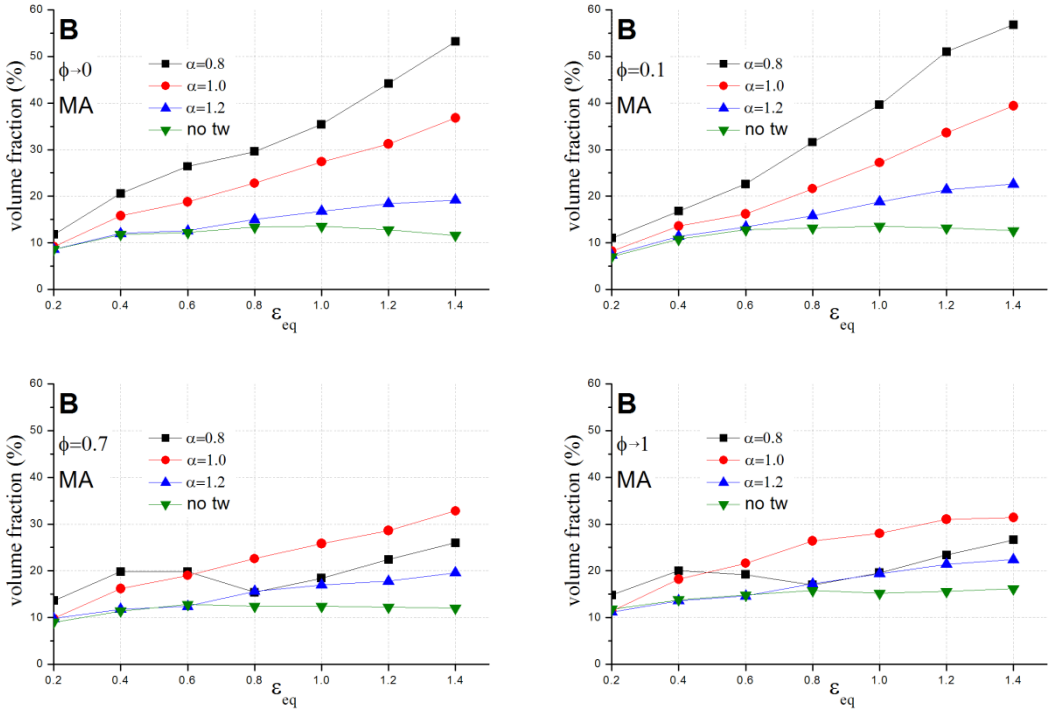

Fig. 3-16. Effect of α value on B component evolution for various ϕ values, MA definition.

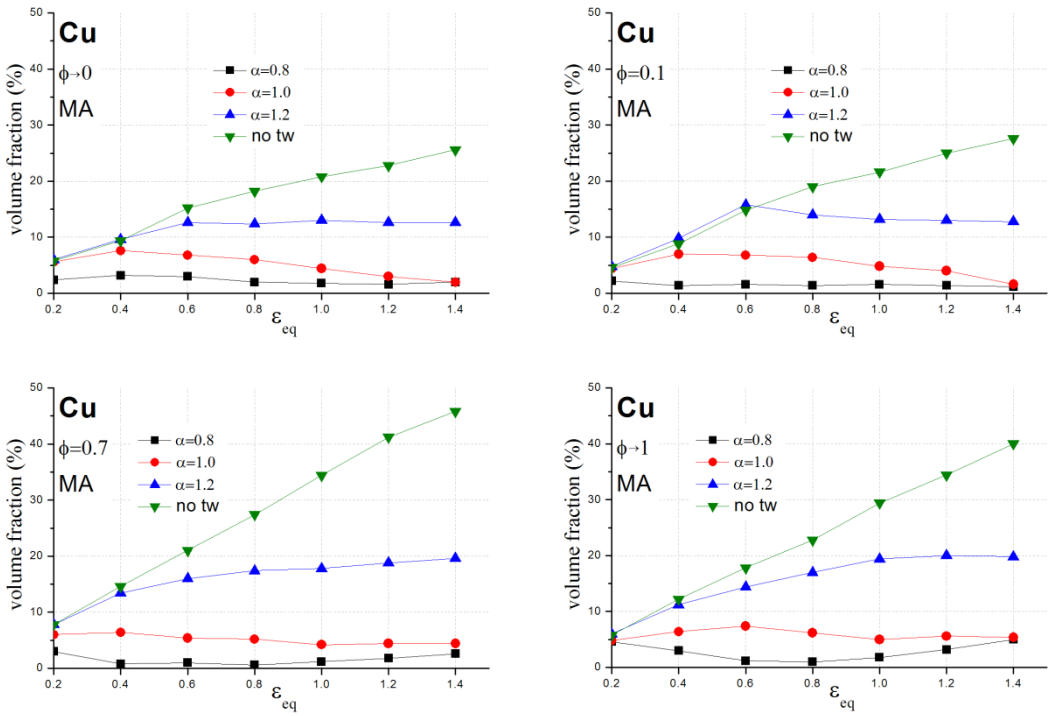

Fig. 3-17. Effect of α value on Cu component evolution for various ϕ values, MA definition.

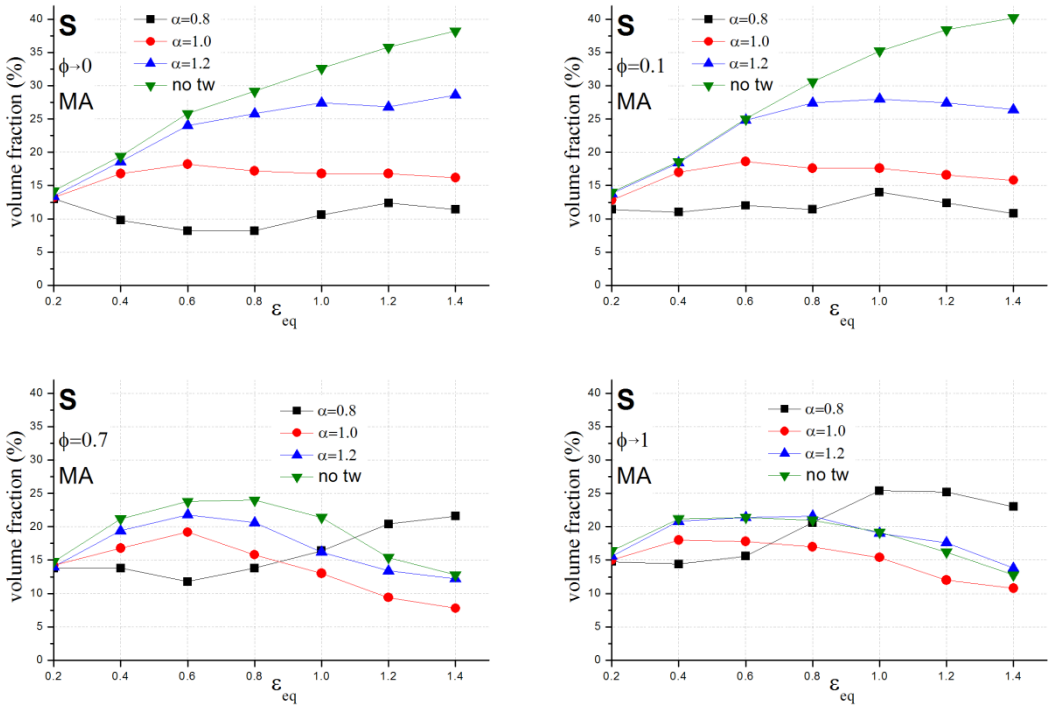

Fig. 3-18. Effect of α value on S component evolution for various ϕ values, MA definition.

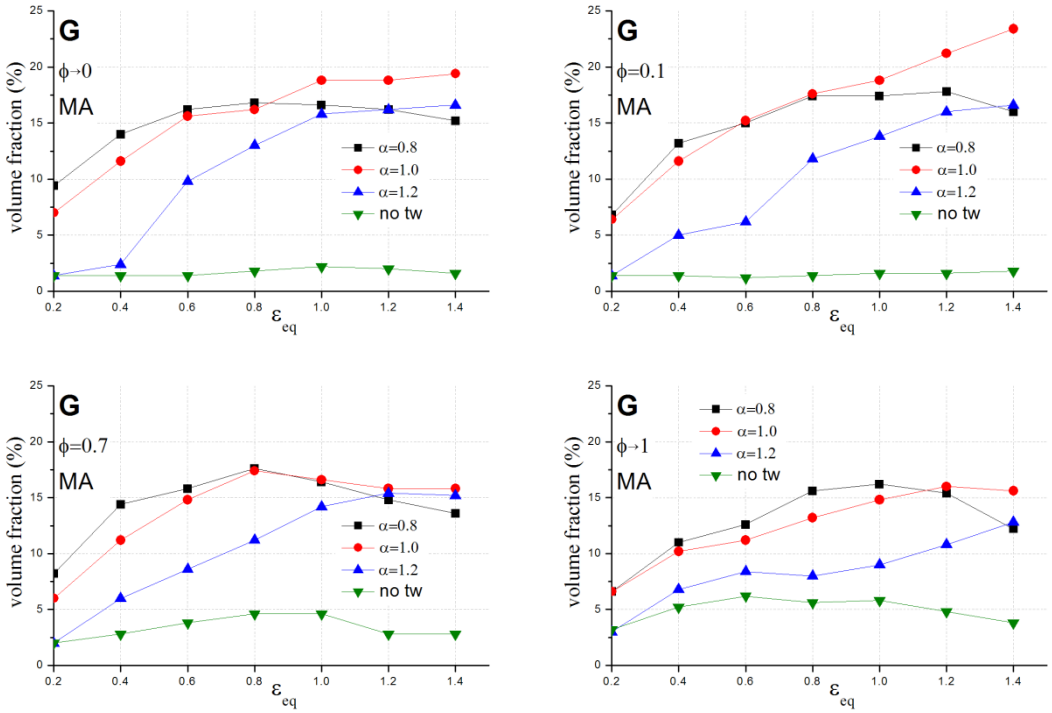

Fig. 3-19. Effect of α value on G component evolution for various ϕ values, MA definition.

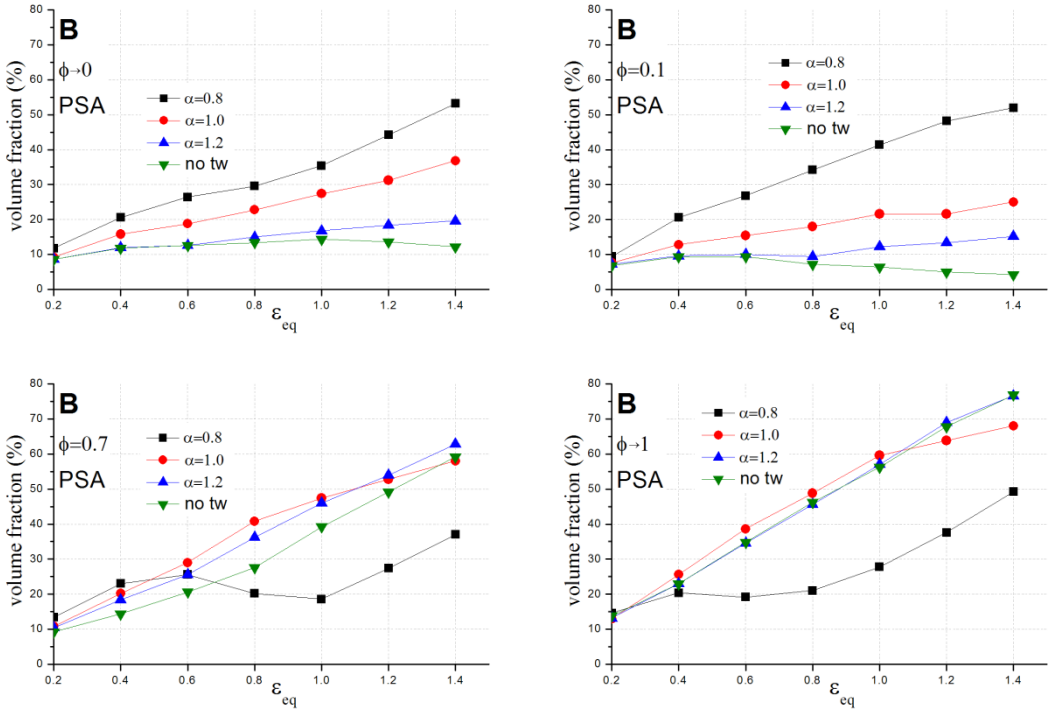

Fig. 3-20. Effect of α value on B component evolution for various ϕ values, PSA definition.

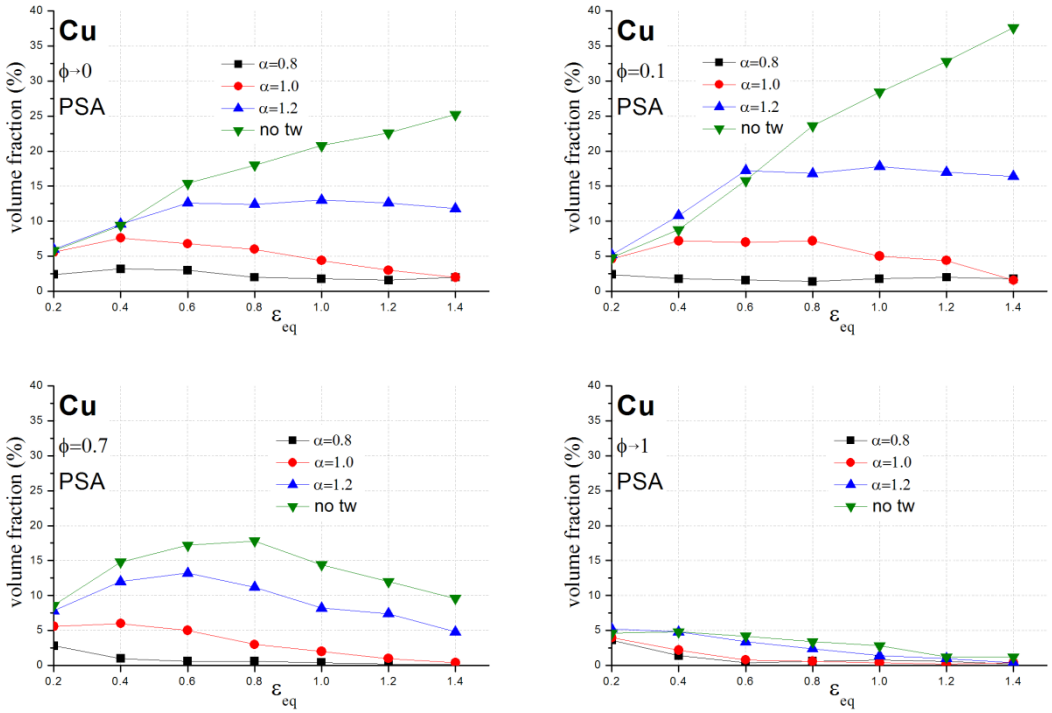

Fig. 3-21. Effect of α value on Cu component evolution for various ϕ values, PSA definition.

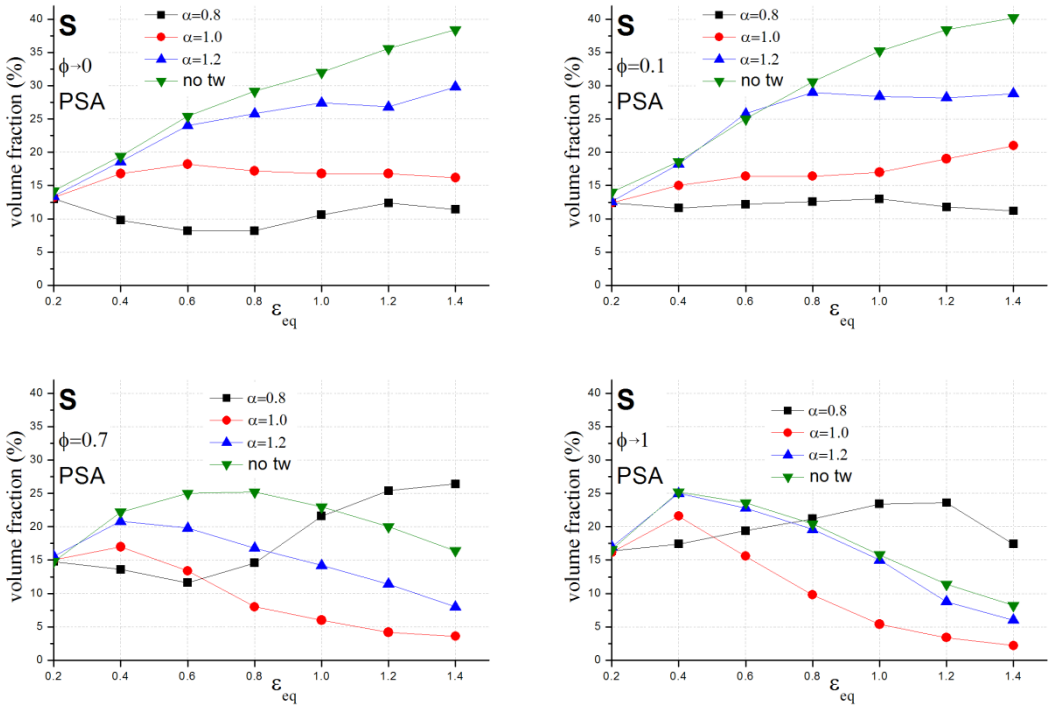

Fig. 3-22. Effect of α value on S component evolution for various ϕ values, PSA definition.

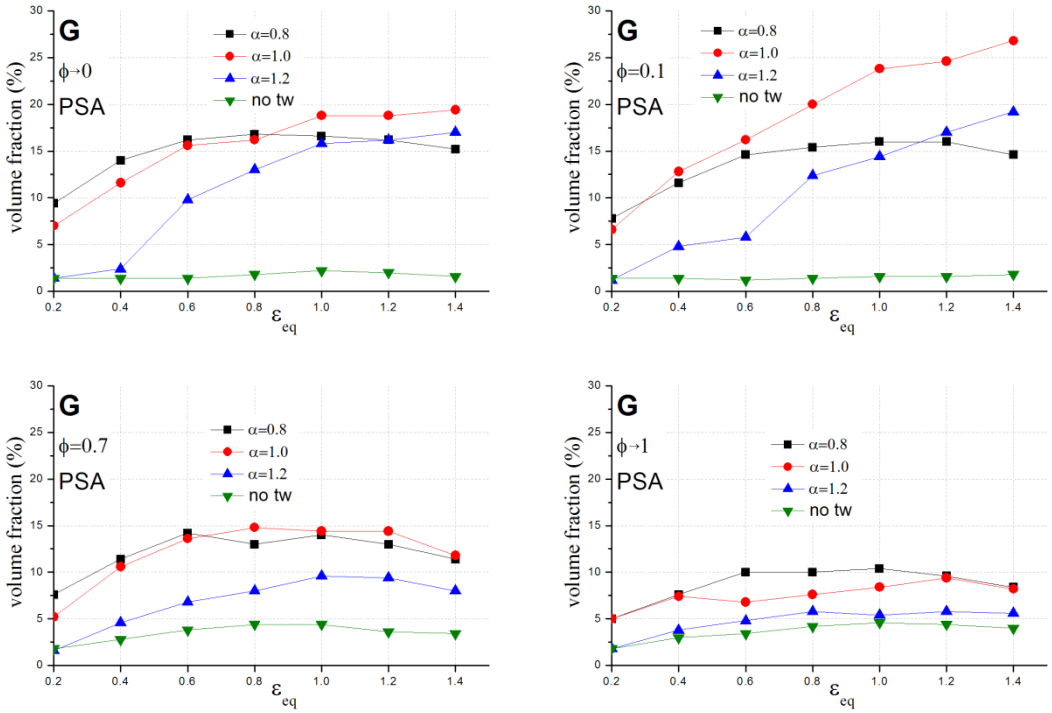

Fig. 3-23. Effect of α value on G component evolution for various ϕ values, PSA definition.

III.5 Volume effects of deformation twinning

The volume effect of twinning is one of the ways that the twinning affects the texture evolution. The twinning volume fraction represents the volume fraction of the twinned region in grains during the deformation. Several experimental works have been carried out to determine the twin volume fraction in FCC metals with low SFE (e.g. Leffers and Ray, 2009; Leffers and Kayworthl, 1973; Hutchinson et al. 1979). According to these works, the twinning volume fraction is less than 25% for about 75% rolling reduction ($\varepsilon_{eq} \approx 140\%$) and can be neglected under about 40% rolling reduction ($\varepsilon_{eq} \approx 51\%$).

In order to correctly predict the texture evolutions, the predicted twin volume fraction should meet an agreement with the experimental ones. However, in the works above, the predicted volume fraction cannot be related to the experiments as it is strongly overestimated with the PTR scheme (Beyerlein et al. 2011; Prakash et al., 2008, Schmid et al., 2007).

In this section, we carried out a simulation study of the volume effect of twinning. In order to relate our results with experiments, we used the voce hardening parameters of silver that are presented in the work of Beyerlein et al. (2011), see Tab. 3-1. In the PTR scheme, the characteristic twin shear parameter S^t can be linked with the twin volume fraction. It is suggested to be 0.707 for cubic material (e.g. Beyerlein et al., 2011; Prakash et al., 2008). However, this value will lead to an overestimation of the twin volume fraction.

Here, we tried to control the twin volume fraction by increasing the value of S^t. In Fig. 3-24, the twin volume fractions for $S^t = 0.707$ are around 20% at 50% equivalent strain (40% rolling reduction) and are around 40% to 80% for larger strain

up to 140% equivalent strain (75% rolling reduction). The volume fractions are therefore overestimated by this value of S^t. By increasing S^t up to 2.5, the twin volume fraction can be reduced to a reasonable range for both MA and PSA lattice spin definitions. We therefore analyzed texture evolution for three values of S^t: 0.707, 1.5 and 2.5.

	τ_0 (MPa)	τ_1 (MPa)	θ_0 (MPa)	θ_1 (MPa)
Slip	33.0	466.8	65.0	2.0
Twinning	45.0	4317.5	50.0	1.25

Tab. 3-1. Voce hardening parameters used to evolve the critical resolved shear stresses of the slip and twinning systems for sliver (Beyerlein et al., 2011)

The effect of S^t on FCC rolling components for different ϕ are presented in Fig. 3-25 to Fig. 3-32. Generally, lower twin volume fraction (higher S^t value) leads to stronger Cu and S components and weaker B and G components for all ϕ values and for both MA and PSA definitions. The tendencies of texture components evolution are in agreement with Vercammen et al. (2004) who quoted that the twinning eagers to rotate the grains around Cu component to a position near the G component. For MA definition, the brass-type texture (B component stronger than Cu component) can be only obtained for high twin volume fraction. On the other hand, the brass-type texture can be obtained with PSA for high ϕ values when twin volume fraction is low.

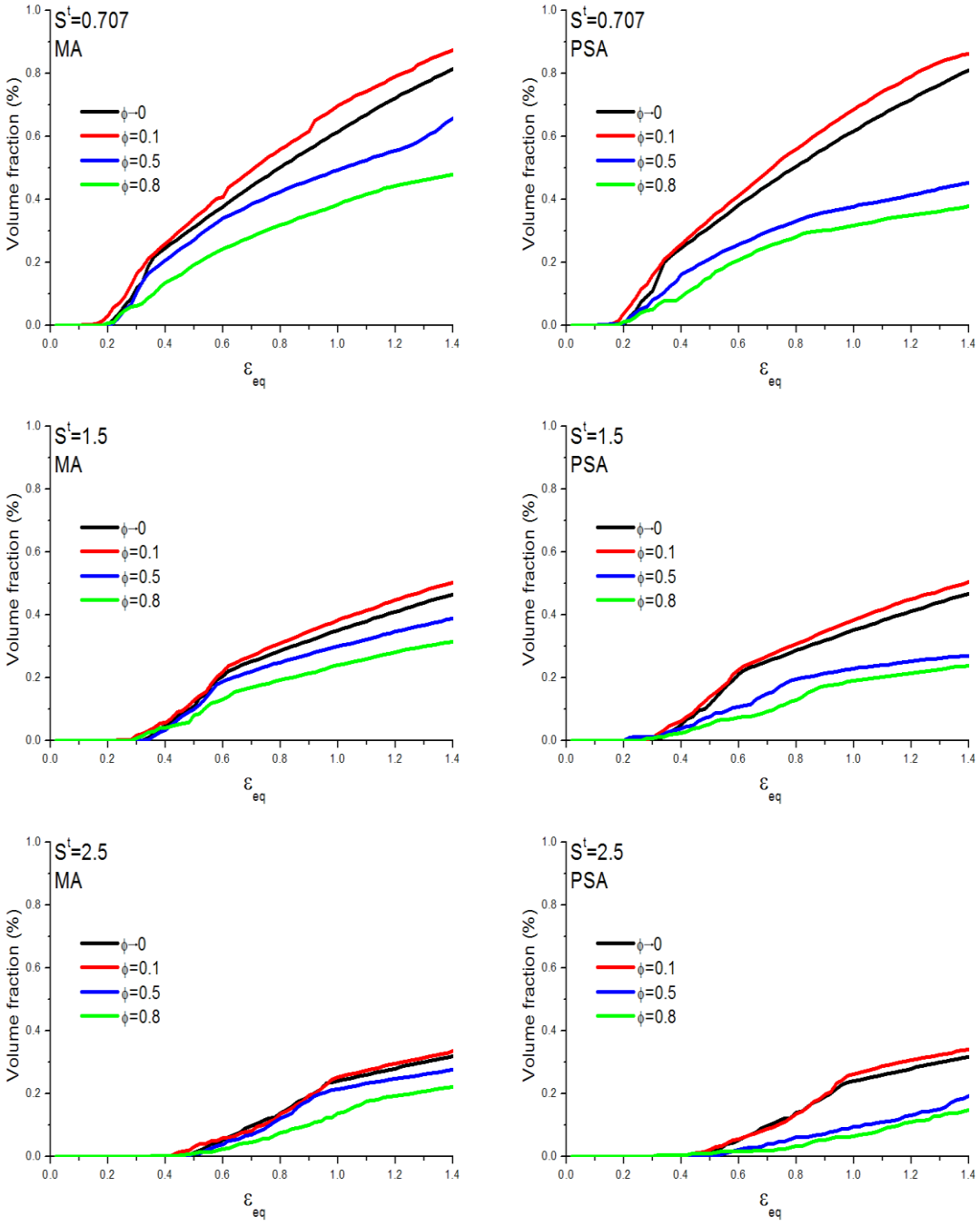

Fig. 3-24. Effect of S^t on the twinning volume fraction for different ϕ values and different lattice spin definitions (MA and PSA).

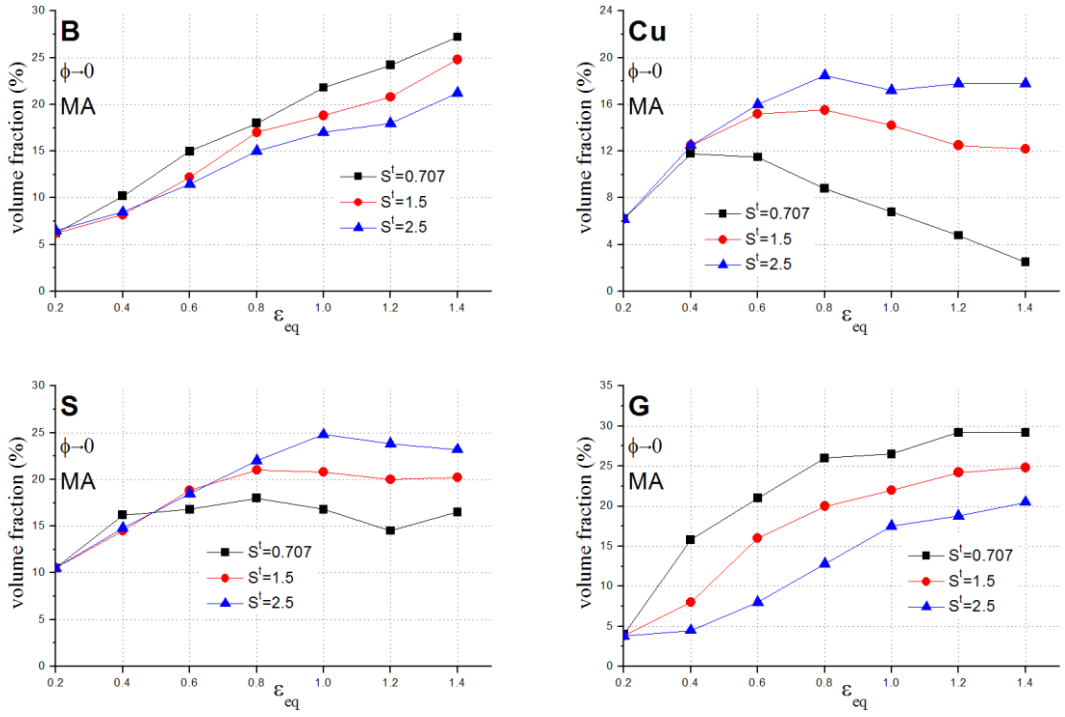

Fig. 3-25. Effect of S^t on the FCC rolling components (B, Cu, S and G) for $\phi \to 0$, MA definition.

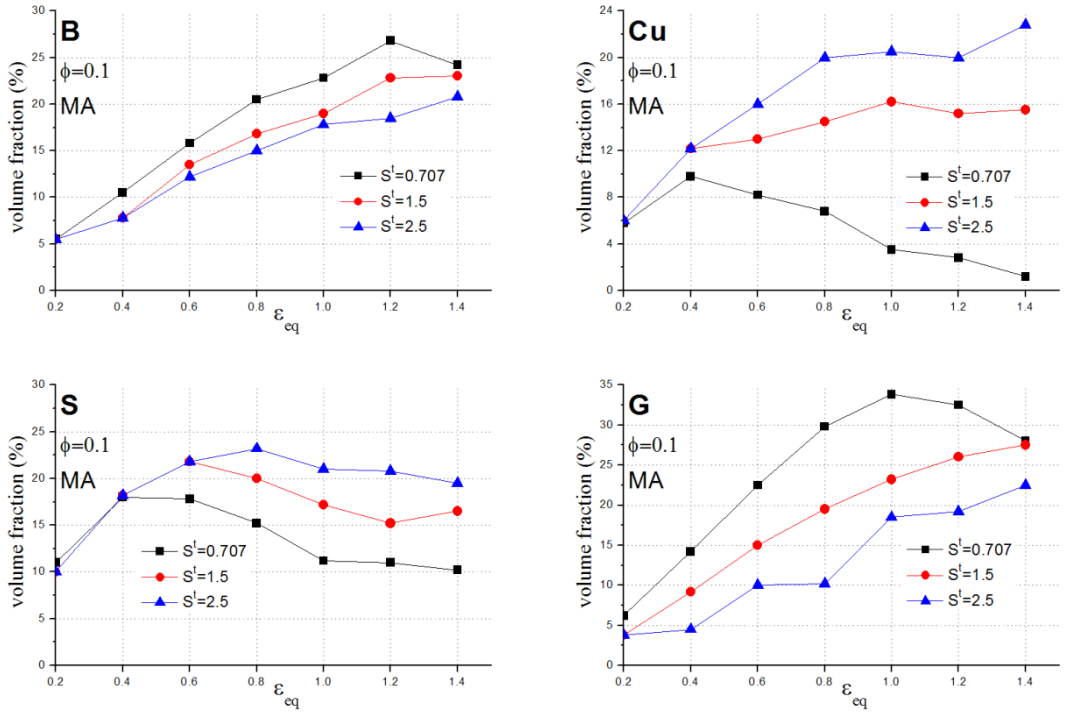

Fig. 3-26. Effect of S^t on the FCC rolling components (B, Cu, S and G) for $\phi = 0.1$, MA definition.

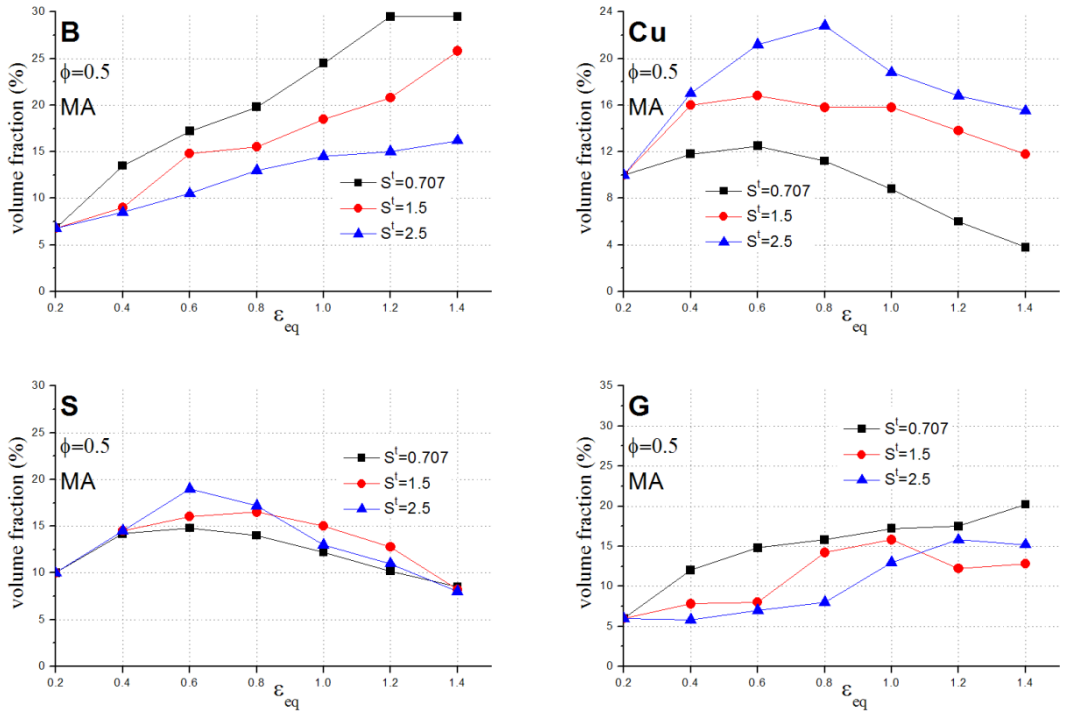

Fig. 3-27. Effect of S^t on the FCC rolling components (B, Cu, S and G) for $\phi = 0.5$, MA definition.

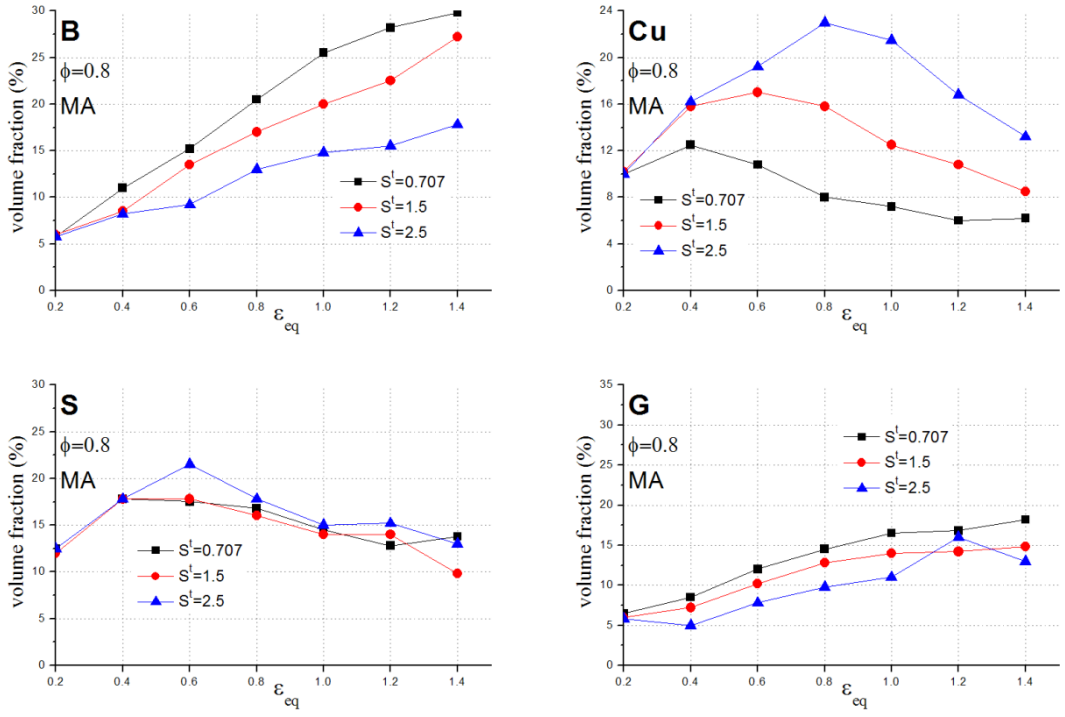

Fig. 3-28. Effect of S^t on the FCC rolling components (B, Cu, S and G) for $\phi = 0.8$, MA definition.

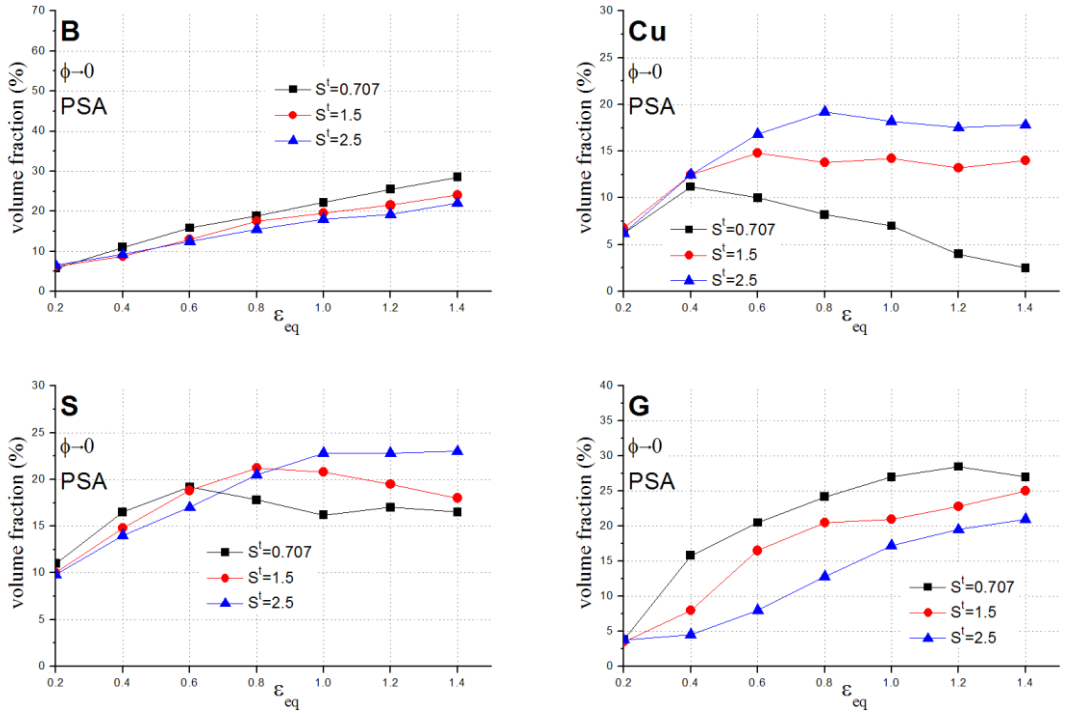

Fig. 3-29. Effect of S^t on the FCC rolling components (B, Cu, S and G) for $\phi \to 0$, PSA definition.

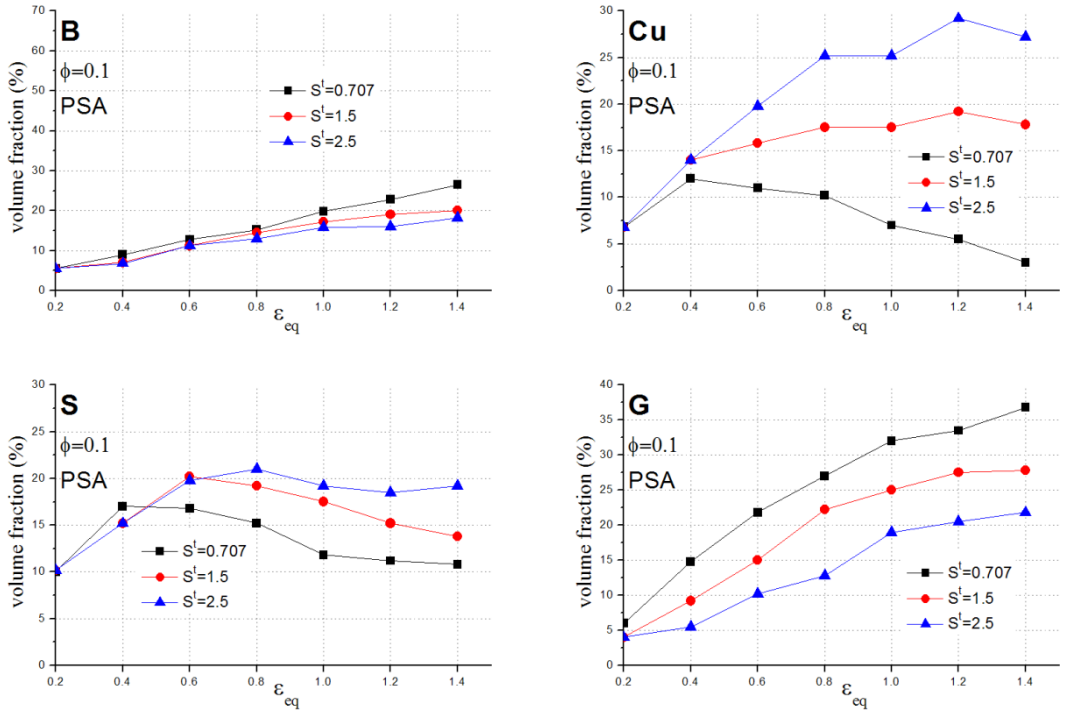

Fig. 3-30. Effect of S^t on the FCC rolling components (B, Cu, S and G) for $\phi = 0.1$, PSA definition.

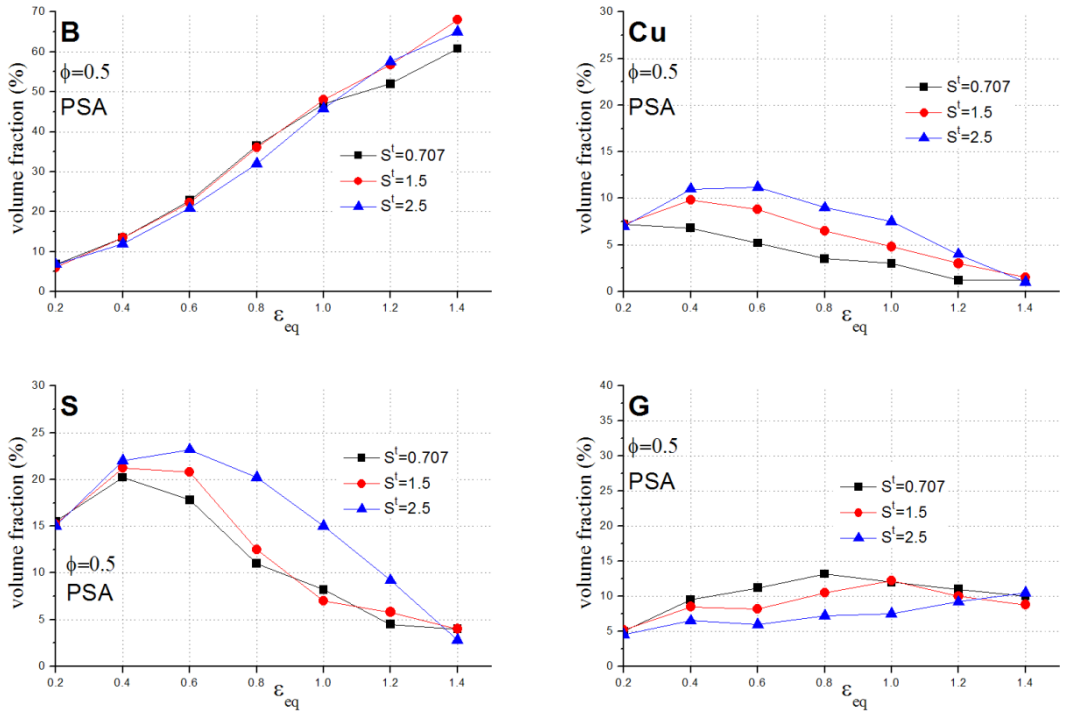

Fig. 3-31. Effect of S^t on the FCC rolling components (B, Cu, S and G) for $\phi = 0.5$, PSA definition.

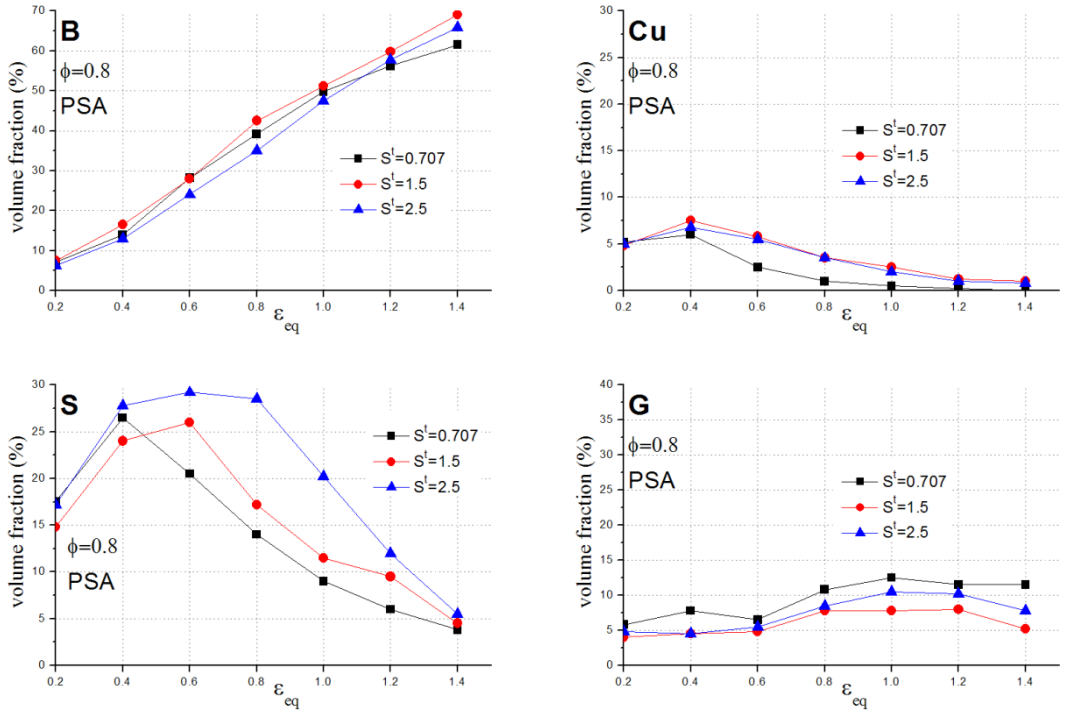

Fig. 3-32. Effect of S^t on the FCC rolling components (B, Cu, S and G) for $\phi = 0.8$, PSA definition.

III.6 Conclusion

In this work, two definitions for the calculation of the lattice rotation, MA and PSA, have been compared under plane strain compression by using the visco-plastic ϕ -model. Firstly, the coupled effect of twinning, interaction strength (inversely proportional to ϕ) and the used definition for the lattice spin on the texture evolution has been deeply analyzed. In the second part, we perform parametric studies by varying the parameters controlling the slip/twinning activities and the twin volume fractions. The effects of these parameters on the texture evolutions are studied.

In the first part, we showed that the MA and PSA definitions are equal when the Taylor model (limiting case of $\phi = 0$) is used. Therefore, the results at very low ϕ values ($\phi \to 0$) do not show a significant difference between the MA and PSA definitions. The deviation between the predict texture by MA and PSA definition increases with increasing ϕ values. At high interaction strength (low ϕ values, $\phi \to 0$ and $\phi = 0.1$), both definitions can be used to predict a copper-type texture if only the {111}<110> slip is considered. The brass-type texture can be obtained by either using PSA definition without twinning at low interaction strength (high ϕ values, from $\phi = 0.7$) or using both MA or PSA definitions with twinning. However, these two methods of the brass-type texture prediction show an evident difference in the G component. The latter method presents a stronger G component which is suggested to be caused by mechanical twinning (Vercammen et al., 2004).

The predict results, in terms of pole figures and ODF sections, show a tendency towards brass-type texture when ϕ is small with twinning and when ϕ is high with twinning. However, when we analyze texture components, in a more detailed way, the brass-type texture is well predicted only by high ϕ value with twinning (around $\phi = 0.7$). This is proven by the comparison of our results with the experimental results

of 70/30 brass (El-Danaf et al., 2000) reported in Fig. 3-33 which shows the waviness in the evolution of B component and the B and S component are nearly equal strong (see Fig. 3-33).

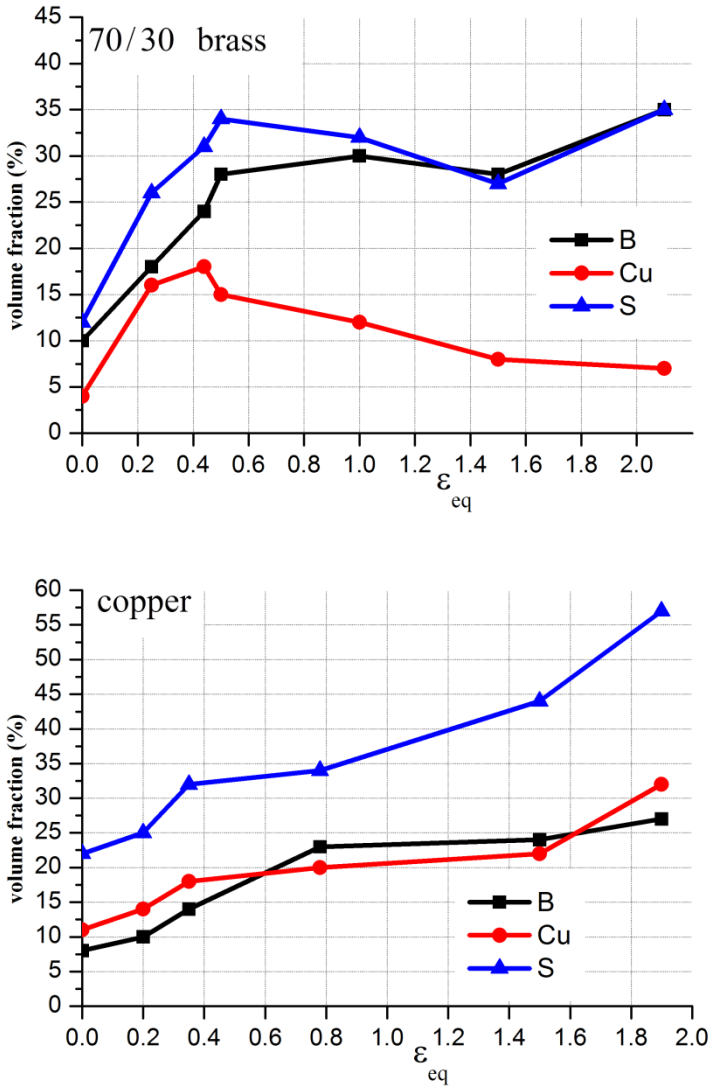

Fig. 3-33. Evolution of rolling components B, Cu and S for 70/30 brass and copper after El-Danaf et al. (2000).

The Cu components are relatively weak when twinning is considered. We believe that this can be explained by the strong activation of the twinning systems and the overestimation of twinning volume fraction by the PTR scheme. This point is

supported by the following parameter studies in which we showed that the Cu component can be elevated by high activities of twinning and high twin volume fraction.

The mechanical twinning can be detected in most rolled materials developing brass-type texture such as brass and silver (El-Danaf, 2000; Leffers and Juul Jensen, 1988; Leffers and Ray, 2009; Sekine and Wang, 1999). Hence, the consideration of twinning for simulating texture evolution in these materials is logical. However, certain materials with specific microstructures or under specific loading conditions can develop a rolling texture that deviates from copper-type such as Cu-Mn alloy (Engler, 2000; Engler et al., 1994). This alloy develops a brass-type texture even if no twinning has been detected in this metal (Engler, 2000; Engler et al., 1994). In this case, the rolling texture evolution of the Cu-Mn alloy may be predicted by the ϕ-model with high ϕ values without twinning and using the PSA definition.

To precisely predict the rolling texture transition, other mechanisms such as shear banding and twin barrier effect were suggested. However, the modeling studies of these mechanisms are still in progress. The shear banding is suggested to be responsible for the formation of the brass-type texture and have been studied in many works (e.g. Duggan et al., 1978; El-Danaf et al., 2000, 2011; Gil Sevillano et al., 1977; Kalidindi, 2001; Leffers and Ray, 2009; Paul et al., 2007; 2009). However, shear banding is an extremely complex process and therefore the modeling work of this mechanism is complicated. Quantitative modeling of shear banding effects on texture has not been reported except several highly simplified models (Gil Sevillano et al., 1977; Kalidindi, 2001). The twin barrier effect occurs due to the boundaries of the fine twins. When the twinning region appears in a grain, non-coplanar slip with the twinning plane becomes harder to be activated. Lebensohn et al. (2007) and Beyerlein

et al. (2011) have taken into account this effect via the latent hardening. However, the simulated textures show some deviations from the typical brass-type texture.

References:

Ahzi, S., Asaro, R.J., Parks, D.M., 1993. Application of crystal plasticity theory for mechanically processed BSCCO superconductors. Mech. Mater. 15, 201-222.

Ahzi, S., M'Guil, S., 2008. A new intermediate model for polycrystalline viscoplastic deformation and texture evolution. Acta Mater. 56, 5359-5369.

Ahzi, S., M'Guil, S., Agah-Tehrani, A., 2002. A new formulation for the elastic-viscoplastic lower bound and intermediate modeling for polycrystalline plasticity. Mater. Sci. Forum. 408-412, 463-468.

Beyerlein, I.J., Mara, N.A., Bhattacharyya, D., Alexander, D.J., Necker, C.T., 2011. Texture evolution via combined slip and deformation twinning in rolled silver-copper cast eutectic nanocomposite. Int. J. Plasticity 27, 121-146.

Carstensen, J.V., Ray, R.K., Leffers, T., 2002. Texture development in Ni-Co alloys rolled to moderate reductions. Mater. Sci. Forum. 408-412, 607-612.

Duggan, B.J., Hutchinson, W.B., Hatherly, M., 1978. Recrystallization studies in 70:30 brass using a high voltage electron microscope. Scr. Metall. 12, 293-295

El-Danaf, E., Kalidindi, S.R., Doherty, R.D., Necker, C., 2000. Deformation texture transition in brass: critical role of micro-scale shear bands. Acta Mater. 48, 2665-2673.

El-Danaf, E., Al-Mutlaq, A., Soliman, M.S., 2011. Role of stacking fault energy on the deformation characteristics of copper alloys processed by plane strain compression. Mater. Sci. Eng. A 528, 7579-7588.

El-Danaf, E., Kalidindi, S.R., Doherty, R.D., 2001. Influence of deformation path on the strain hardening behavior and microstructure evolution in low SFE FCC metals. Int. J. Plasticity 17, 1245-1265.

Engler, O., 2000. Deformation and texture of copper-manganese alloys. Acta Mater. 48, 4827-4840.

Engler, O., Pithan, C., Lücke, K., 1994. Rolling texture development in Cu-Mn alloys, Mater. Sci. Forum. 157-162, 679-683.

Gil Sevillano, J., Van Houtte, P., Aernoudt, E., 1977. The contribution of macroscopic shear bands to the rolling texture of FCC metals. Scripta Metall. 11, 581-585.

Hosford, W.F., 1977. On orientation changes accompanying slip and twinning. Text. Cryst. Solids. 2, 175-182.

Kalidindi, S.R., 2001. Modeling anisotropic strain hardening and deformation textures in low stacking fault energy fcc metals. Int. J. Plasticity 17, 837-860.

Kalidindi, S.R., Bronkhorst, C.A., Anand, L., 1992. Crystallographic texture evolution in bulk deformation processing of FCC metals. J. Mech. Phys. Solids 40, 537–569.

Lebensohn, R.A., Leffers, T., 1999. The rules for the lattice rotation accompanying slip as derived from a self-consistent model. Textures Microstruct. 31, 217-230.

Lebensohn, R.A., Tomé, C.N., 1993. A self-consistent anisotropic approach for the simulation of plastic deformation and texture development of polycrystals: application to zirconium alloys. Acta Metall. Mater. 41, 2611-2624.

Lebensohn, R.A., Tomé, C.N., Castañeda, P.P., 2007. Self-consistent modelling of the mechanical behaviour of viscoplastic polycrystals incorporating intragranular field fluctuations. Philosophical Magazine. 87, 4287-4322.

Leffers, T., 1968. Deformation rate dependence of rolling texture in brass containing 5% zinc. Scripta Metall. 2, 447-452.

Leffers, T., 1993. On the development of the brass-type texture. Textures Microstruct. 22, 53-58.

Leffers, T., 1996. The brass-type texture once again, in: Z. Liang et al. (Eds.), Proceedings ICOTOM 11, International Academic Publishers, Beijing, pp. 299-306.

Leffers, T., 2012. The brass-type texture-How close are we to understand it? Mater. Sci. Forum. 702-703, 216-223.

Leffers, T., Bilde-Sørensen, J.B., 1990. Intra- and intergranular heterogeneities in the plastic deformation of brass during rolling. Acta Metall. Mater. 38, 1917-1926.

Leffers, T., Juul Jensen, D., 1988. The early stages of the development of rolling texture in copper and brass. Textures Microstruct. 8-9, 467-480.

Leffers, T., Pedersen, O.B., 2002. The activation energy for the fcc rolling-texture transition as related to the activation energy for cross slip. Scripta Mater. 46, 741-746.

Leffers, T., Ray, R.K., 2009. The brass-type texture and its deviation from the copper-type texture. Prog. Mater.Sci. 54, 351-396.

Leffers, T., Van Houtte, P., 1989. Calculated and experimental orientation distributions of twin lamellae in rolled brass. Acta Metal. 37, 1191-1198.

M'Guil, S., Ahzi, S., Barlat, F., Gracio, J.J., 2011. Simulation of microstructural effects and yield surface evolution in cubic metals using the viscoplastic ϕ-model. Int. J. Plasticity 27, 102-120.

M'Guil, S., Ahzi, S., Youssef, H., Baniassadi, M., Gracio, J.J., 2009. A comparison of viscoplastic intermediate approaches for deformation texture evolution in FCC polycrystals. Acta Mater. 57, 2496-2508.

M'Guil, S., Wen, W., Ahzi, S., 2010. Numerical study of deformation textures, yield locus, rolling components and Lankford coefficients for FCC polycrystals using the new polycrystalline ϕ-model. Int. J. Mech. Sci. 52, 1313-1318.

Miraglia, M., Dawson, P., Leffers, T., 2007. On the influence of mechanical environment on the emergence of brass textures in FCC metals. Acta Mater. 55, 799-812.

Paul, H., Driver, J.H., Maurice, C., Piątkowski, A., 2007. The role of shear banding on deformation texture in low stacking fault energy metals as characterized on model Ag crystals. Acta Mater. 55, 575-588.

Prakash, A., Hochrainer, T., Reisacher, E., Riede, H., 2008. Twinning models in self-consistent texture simulations of TWIP steels. Steel. Res. Int. 79, 645-652.

Paul, H., Morawiec, A., Driver, J.H., Bouzy, E., 2009. On twinning and shear banding in a Cu–8 at.% Al alloy plane strain compressed at 77 K. Int. J. Plasticity 25, 1588-1608.

Sachs, G., 1928. Plasticity problems in metals. Z. Ver. Deutsch. Ing.72, 734-736.

Schmid, C., Kawalla, R., Walde, T., Riedel, H., Prakash, A., Poizat, C., 2007. Experimental and numerical investigation of texture development during hot rolling of magnesium alloy AZ31. Mater. Sci. Forum., 539-543, 3448-3453.

Sekine, K., Wang, J., 1999. Characteristic features of rolling texture development in FCC alloys having very low stacking fault energies. Mater. Trans. 1, 1-6.

Staroselsky, A., Anand, L., 1998. Inelastic deformation of polycrystalline face centered cubic materials by slip and twinning. J. Mech. Phys. Solids. 46, 671-696.

Taylor, G.I., 1938. Plastic strain in metals. J. Inst. Metals. 62, 307-324.

Tomé, C.N., Lebensohn, R.A., Kocks, U.F., 1991. A model for texture development dominated by deformation twinning: Application to zirconium alloys. Acta Metal. Mater. 39, 2667-2680.

Van Houtte, P., 1978. Simulation of the rolling and shear texture of brass by the Taylor theory adapted for mechanical twinning. Acta Metal. 26, 591-604.

Van Houtte, P., Li, S., Seefeldt, M., Delannay, L., 2005. Deformation texture prediction: from the Taylor model to the advanced Lamel model. Int. J. Plasticity 21, 589-624.

Vercammen, S., Blanpain, B., De Cooman, B.C., Wollants, P., 2004. Cold rolling behavior of an austenitic Fe-30Mn-3Al-3Si TWIP-steel: the importance of deformation twinning. Acta Mater. 52, 2005-2012.

Wierzbanowski, K., Wronski, M., Baczmanski, A., Bacroix, B., Lipinski, P., Lodini, A., 2011. Problem of lattice rotation due to plastic deformation. example of rolling of f.c.c materials. Arch. Metall. Mater. 56, 575-584.

Wen, W., M'Guil, S., Ahzi., 2012a. Rolling texture transition in FCC metals using the viscoplastic ϕ-model and considering mechanical twinning. Mater. Sci. Forum. 702-703, 241-244

Wen, W., M'Guil, S., Ahzi, Gracio, J.J., 2012b. Coupled effects of the lattice rotation definition, twinning and interaction strength on the FCC rolling texture evolution using the viscoplastic ϕ-model. Int. J. Plasticity.
http://dx.doi.org/10.1016/j.ijplas.2012.09.009

Chapter IV. Application to FCC metals: analysis of shear deformation by slip and twinning in low and high stacking fault energy metals

IV.1 Introduction

In order to validate new plasticity modeling theories, simulations until very large plastic deformation must be performed. In such a way, severe plastic deformation methods such as torsion test (Canova et al., 1984; Lin and Havner, 1996; Tóth et al., 1992) or Equal Channel Angular Extrusion (ECAE) method (Beyerlein et al., 2007, 2009; Gazder et al., 2006; Li, 2008; Li et al., 2005a,b, 2006a,b; Segal, 1995; Suwas et al., 2003, 2009; Tóth, 2003) can be used. These tests involving shear stresses allow material to be deformed to very high plastic strain that cannot be obtained with more conventional processes, such as rolling. These tests usually lead to a very fine microstructure with extraordinary mechanical properties, such as simultaneous ultrahigh strength and high ductility. An extended review on texture evolution during ECAE can be found in the work of Beyerlein and Tóth (2009). Except subtle differences in terms of location of the respective components (see Fig. 4-1), the textures that develop during ECAE are similar to those seen in torsion, in which deformation occurs by simple shear (Beyerlein et al., 2007; Gazder et al., 2006; Li, 2008; Li et al., 2005a,b, 2006a; Suwas et al., 2003; Tóth, 2003; Tóth and Molinari, 1994). Thus, it is commonly accepted that the deformation process during ECAE can be well approximated by simple shear (Segal, 1995).

From the modeling point of view, many of crystal plasticity models have been applied to the study of shear texture development in polycrystalline metals (Beyerlein et al., 2007; Li and Havner, 1996; Li et al., 2005a,b, 2006a,b, 2008; Suwas et al., 2009; Tóth and Molinari, 1994). In this chapter, we focus on the simulation of large plastic deformation and texture evolution under simple shear by using the ϕ-model. Our results show that the visco-plastic ϕ-model can be used to correctly predict shear texture evolution in FCC metals and to predict texture transition that other models

such as the VPSC cannot predict. Although some similarities in the shear texture components are obtained, a wide range of shear texture predictions in both low stacking fault energy (SFE) metals (i.e. silver) and medium SFE metals (i.e. copper) is only obtained with the ϕ-model. We note that in this chapter, we do not consider dynamic recrystallization, we do not take into account the Swift effect (Tóth et al., 1992; Swift, 1947) and we neglect the effect of substructure evolution (Beyerlein et al., 2009). The results presented in this chapter can be found in the work of M'Guil et al. (2012).

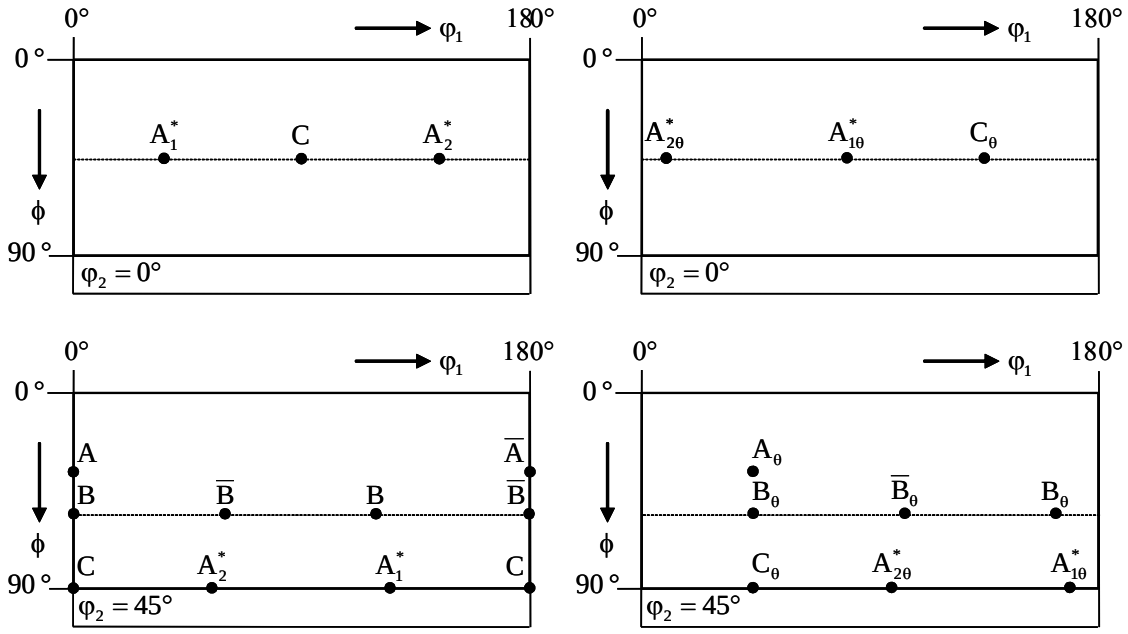

a) Simple shear b) ECAE process (with angle = 90°)

Fig. 4-1. Ideal orientations for simple shear (a) and ECAE (b) texture components observed in the $\varphi_2 = 0°$ and $\varphi_2 = 45°$ sections of ODF for FCC metals (Li et al., 2005b)

IV.2 Experimental shear textures for FCC metals

IV.2.1 Preferred orientations for simple shear textures

The main ideal simple shear texture components of FCC metals are usually presented as a key figure in the $\varphi_2 = 0°$ and $\varphi_2 = 45°$ sections of the Orientation Distribution Function (ODF), see Fig. 4-1a (Li et al., 2005b). This ODF representation allows for showing each ideal shear components separately. The corresponding Euler angles (φ_1, Φ, φ_2) and Miller indices of these components are listed in Tab. 4-1 (Li et al., 2005b). Simple shear textures are characterized by two partial fibres: the 'A' partial fiber indexed as {111}<uvw> and the 'B' partial fiber indexed as {hkl}<110>. There exist also the 'C' ideal orientation indexed as {001}<110>. However, the C position is just a special position on the B fiber (Canova et al., 1984). As shown in Fig. 4-1a and in Tab. 4-1, the partial 'A' fiber contains the $A/\overline{A}$, A_1^* and A_2^* ideal components, and the partial 'B' fiber is composed of $A/\overline{A}$, $B/\overline{B}$ and C ideal components.

Components	Miller indices	Euler angles (°)		
		φ_1	Φ	φ_2
A	$(11\bar{1})[1\bar{1}0]$	0	35.26	45
$\overline{A}$	$(\bar{1}\bar{1}1)[\bar{1}10]$	180	35.26	45
A_1^*	$(11\bar{1})[2\bar{1}1]$	35.26/215.26 125.26	45 90	0/90 45
A_2^*	$(1\bar{1}1)[\bar{2}\bar{1}1]$	144.74 54.74/234.74	45 90	0/90 45
B	$(11\bar{2})[1\bar{1}0]$	0/120/240	54.74	45
$\overline{B}$	$(\bar{1}\bar{1}2)[\bar{1}10]$	60/180	54.74	45
C	$(100)[0\bar{1}1]$	90/270 0/180	45 90	0/90 45

Tab. 4-1. Location of the ideal orientations of shear textures in Euler space for FCC metals (Li et al., 2005b)

In order to clarify the analysis of shear texture development under an ECAE process, we also plot the main ideal ECAE components in the $\varphi_2 = 0°$ and $\varphi_2 = 45°$ sections of ODF, see Fig. 4-1b. We can observe that the ideal ECAE components are close to those of ideal shear components. The main ideal orientations in ECAE with an die angle of 90 °are : $A^*_{1\theta}$, $A^*_{2\theta}$, $A_\theta / \overline{A}_\theta$, $B_\theta / \overline{B}_\theta$ and C_θ (see Fig. 4-1b).

IV.2.2 Description of experimental shear texture for a medium SFE metal

In this section, we describe the shear texture for a medium SFE metals such as copper. This description is based on the work of Tóth and Molinari (1994) for an OFHC copper bars subjected to large strain free end torsion. The tests were performed at room temperature to avoid dynamic recrystallization. Experimental shear textures were measured at shear strains of $\gamma = 2$ and $\gamma = 5.5$. The initial experimental texture is plotted in Fig. 4-2 for $\varphi_2 = 0°$ and $\varphi_2 = 45°$ sections of the ODF. This initial texture will be used as input for the simulations. This initial texture shows that the sharpest orientations are the A^*_1, A^*_2 and the $A/\overline{A}$ components, which are part of the <111> tensile fiber produced when the copper bars were drawn.

Fig. 4-3 represents the measured textures at shear strains of $\gamma = 2$ and $\gamma = 5.5$ in which the positions of ideal orientations are marked in $\varphi_2 = 0°$ and $\varphi_2 = 45°$ sections of the ODF. We observe on these figures that all ideal components are well developed at $\gamma = 2$, see Fig. 4-3a. At larger strain ($\gamma = 5.5$), see Fig. 4-3b, the important difference with the smaller strain ($\gamma = 2$) is that the A^*_1 and A^*_2 components decrease and the C orientation becomes the most important component. Thus, deformation under torsion leads to the intensification of the C component as well as the appearance of the $B/\overline{B}$ component. As the strain is increased from 2 to 5.5, the principal change noted is the gradual weakening of the A^*_1 and of the A^*_2

components.

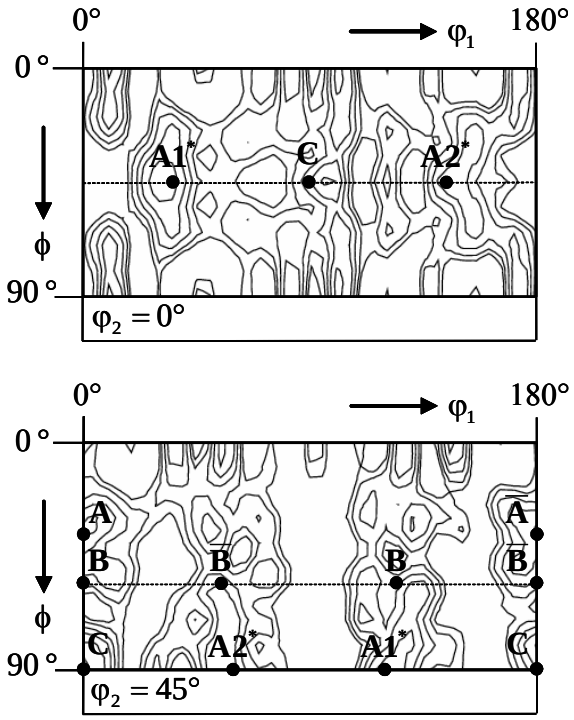

Fig. 4-2. ODF's sections of the initial texture

Isovalues : 0.8, 1.0, 1.3, 1.6, 2.0, 2.5, 3.2, 4.0, 5.0, 6.4 (Tóth and Molinari, 1994)

IV.2.3 Description of experimental shear texture for a low SFE metals

During ECAE deformation, Suwas et al. (2003) and Beyerlein et al. (2007) have studied the development of shear texture for pure polycrystalline silver, a low SFE metal. In this chapter, we will compare our predicted shear textures of silver to those of Suwas et al. (2003) which where obtained for an ECAE test. However, we note again that the texture development during ECAE is close to that obtained under a simple shear test (Beyerlein et al., 2007; Gazder et al., 2006; Li, 2008; Li et al., 2005 a,b, 2006a; Suwas et al., 2003; Tóth, 2003; Tóth and Molinari, 1994).

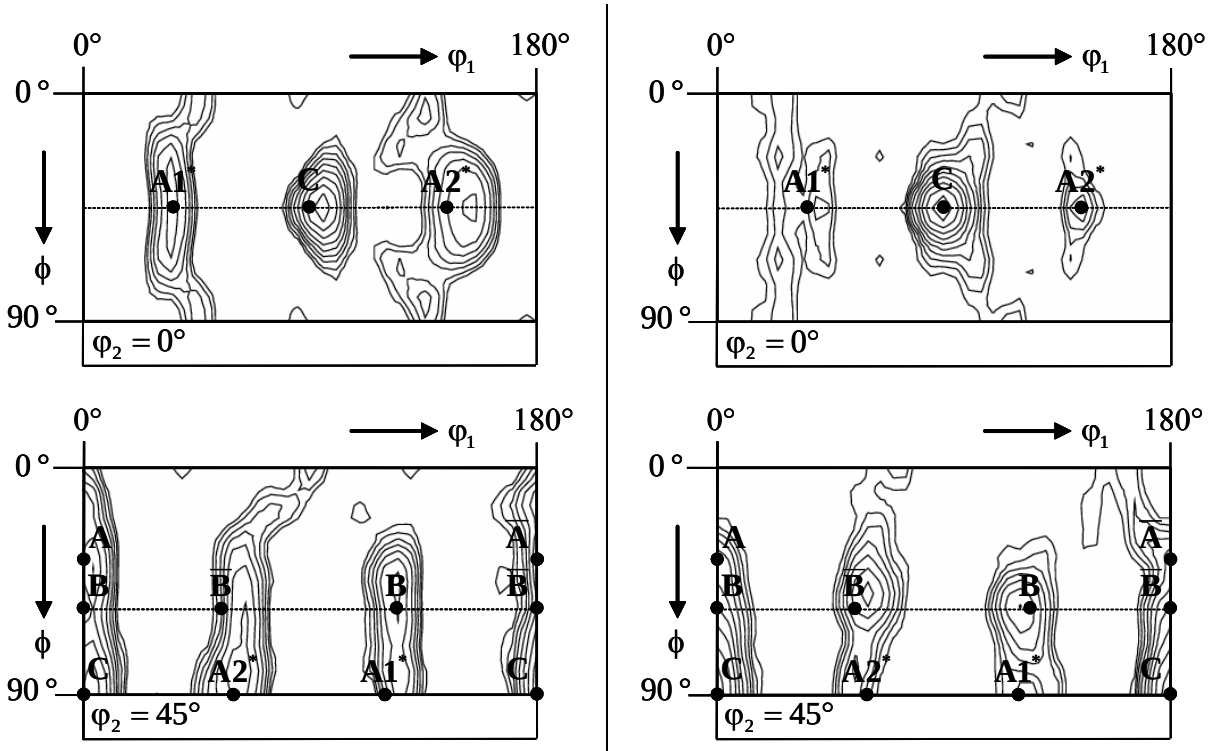

Isovalues: 0.8, 1.0, 1.3, 1.6, 2.0, 3.2, 4.0, 5.0, 6.0

a) $\gamma = 2$

Isovalues: 1.0, 1.3, 1.6, 2.0, 3.2, 4.0, 5.0, 6.0, 8.0

b) $\gamma = 5.5$

Fig. 4-3. Experimental shear textures of OFHC copper at shear deformations of $\gamma = 2$ (a) and $\gamma = 5.5$ (b) (Tóth and Molinari, 1994)

In this section, we present the main concluding remarks reported by Suwas et al. (2003) relative to the description of shear texture evolution. During ECAE of silver, strong texture develops and it continues to strengthen with the number of passes. These authors observed, that for the first pass, the main ideal components are: a strong component near to the ideal B and $\overline{B}$, a relatively strong component A_1^*, a weak A_2^* and a very weak C components. These components, however, are significantly rotated from their respective ideal positions : $20°$ for the A_1^*, $16°$ for C and $9°$ for the A_2^* components. All these rotations are in the decreasing φ_1 direction (Suwas et al., 2003).

These tendencies for silver are different from those of high/medium SFE FCC metals like aluminium, copper and nickel. For high/medium SFE metals, the C, A_1^* and $B/\overline{B}$ components are the strongest whereas the A_2^* component is the weakest. In fact, for high SFE FCC metals, simple shear textures are typically found to consist of a partial <110> fibre and a less strong partial {111} fibre. On the other hand, the simple shear texture of silver has been reported to be {112}<$1\bar{1}0$>, which are the $B/\overline{B}$ components (Suwas et al., 2003).

In the extended work of Beyerlein and Tóth (2009), the authors enumerate the reasons in texture differences between copper and silver: differences in SFE, initial texture effects (initially silver had a random texture and copper had a strong initial fiber texture) and deformation twinning. Beyerlein et al. (2007), using experimental observations and simulation tool, have attributed these significant differences in the texture evolution between silver and copper to deformation twinning in silver (Beyerlein et al. 2007). For instance, experimental microscopy investigations confirmed the presence of twins in each pass of ECAE as well as significant grain refinement for silver (Beyerlein et al., 2007; Suwas et al., 2003). Beyerlein et al. (2007) performed polycrystalline simulations of the ECAE process with the PTR scheme for twinning (Lebensohn et al., 1991) which confirmed that twinning caused the texture differences between a low and medium/high SFE. Beyerlein and Tóth (2009) also note that the strain path changes in ECAE process is important and may influence the twinning in each pass. However, in our study, we do not perform ECAE test but simple shear test and thus, we totally neglect the effect of strain path. To conclude this paragraph, under the same processing conditions, the shear textures for silver (a low SFE) are clearly distinct from those of copper (a medium SFE) (Beyerlein et al., 2007).

IV.3 Shear texture transition as function of SFE

IV.3.1 SFE effect on plastic deformation mechanisms

The SFE is a microstructural material parameter which varies in pure metals and can be lowered by alloying. Examples of high to medium SFE FCC materials are aluminum (167.5 mJ/m^2), nickel (128 mJ/m^2) and copper (78 mJ/m^2). Low SFE FCC materials include gold (45 mJ/m^2) and silver (19-22 mJ/m^2) (Beyerlein and Tóth, 2009). The SFE has a strong impact on the plastic deformation mechanisms and on the dislocations movements. The mechanisms of deformation in FCC metals are strongly influenced by the SFE which controls the crystallographic slip planarity and the dislocations motion. Materials with high SFE permit dislocations to cross slip easily around obstacles. In materials with low SFE, cross slip is difficult and dislocations are constrained to move in a more planar fashion and the dislocation mobility decreases (Beyerlein et al., 2007). Low SFE metals may present mechanical twinning in addition to the crystallographic slip during plastic deformation (Beyerlein et al., 2007). Thus, metals with medium to high SFE values deform by slip only, while those with low SFE values deform by both slip and twinning. When the SFE of metals is lowered, the twinning mechanism is increased and some noticeable texture transitions take place (Beyerlein and Tóth, 2009; Suwas et al., 2003). Hu et al. (1961) have studied the texture transition in High-Purity silver and correlated this transition with the SFE. Leffers (1968) suggested that the Taylor upper bound assumption is too strict and is only applicable to FCC metals having high SFE where extensive cross-slip lead to a reasonably homogeneous deformation. We note that Van Houtte (1978) have used the Taylor upper bound model in order to simulate and interpret the rolling and torsion textures in FCC metals with a wide variety of SFE .

IV.3.2 Torsion texture development as function of SFE

Stout et al. (1998) and Hughes and Wenk (1988) studied the variation in torsion texture development after relatively large deformation with the variation of the SFE. Below, we summarize some of their observations during torsion tests for low and high SFE metals. These authors noted that for shear texture the $B/\overline{B}$ fiber is present to various degrees in all materials. Futhermore, Hughes et al. (2000) found that the $B/\overline{B}$ component was strong after large strains for a wide range of SFE. Hughes et al. (2000) also found that the C component strengthens for the medium to high SFE metals while it weakens in a low SFE metals.

For low SFE metals, Hughes and Wenk (1988) showed that the C component is weaker in silver than in aluminum and copper (results reported in Beyerlein et al, 2007). The C component weakens with increasing amount of shear and vanishes after a very large shear strain ($\gamma = 5.8$). These authors have identified the major components for low SFE metals as A, $B/\overline{B}$ and A_1^*.

During the first pass of ECAE deformation of silver, the $B_\theta/\overline{B}_\theta$ components were found to be the strongest followed by the $A_{2\theta}^*$ and C_θ, and then the weakest $A_{1\theta}^*$ component (Beyerlein et al, 2007). In the subsequent passes, the $B_\theta/\overline{B}_\theta$ component strengthens even further and the $A_{2\theta}^*$ component maintains approximately the same strength, whereas the $A_{1\theta}^*$ and C_θ components weaken (Beyerlein et al, 2007). Beyerlein et al. (2007) showed experimentally that in silver, the $A_{2\theta}^*$ and the $B_\theta/\overline{B}_\theta$ components are the least likely to twin, and thus are the relatively more stable components and consequently remain the strongest components during shear deformation. On the other hand, Beyerlein et al. (2007) showed that the C_θ and $A_{1\theta}^*$ components are induced primarily by slip and weaken due to twinning activation. In contrast, in copper under ECAE deformation, the C_θ, $A_{1\theta}^*$, and $B_\theta/\overline{B}_\theta$

components are the strongest after the first pass, whereas the $A_{2\theta}^{*}$ component is the weakest. In the subsequent passes, the C_{θ}, $A_{2\theta}^{*}$, and $B_{\theta}/\overline{B}_{\theta}$ components weaken in copper (Beyerlein et al, 2007).

As a consequence, the distinctive features of texture in silver (from those of copper) are the weak $A_{1\theta}^{*}$ component and the strong $A_{2\theta}^{*}$ and $B_{\theta}/\overline{B}_{\theta}$ components. The changes during ECAE deformation are a gradual weakening of the $A_{1\theta}^{*}$ and C_{θ} components with increasing pass number (Beyerlein et al, 2007).

IV.4 Shear texture predictions without twinning mechanism

IV.4.1 Input parameters

In this section, we performed various simulations in order to power the ϕ-model against experimental and predicted (using other widely used models) shear textures for FCC polycrystals. In this way, for the visco-plastic ϕ-model, we choose several values for the parameter, ϕ, between 0 and 1. This parameter is microstructure and strain path dependent (M'Guil et al., 2009, 2010, 2011a,b), but, in this chapter, no specific way exists for deriving this parameter and thus, it can simply be regarded as a tuning parameter. In the case of simple shear tests of FCC metals, we selected $\phi = 0.005$ and $\phi = 0.1$. The first value of 0.005 yields results that significantly deviate from the Taylor upper bound results even though one may think the opposite. For the second value of 0.1, the results deviate drastically from those of the Taylor model and are surprisingly close to those obtained by the static lower bound predictions.

In addition to the comparison of the ϕ-model and upper and lower bounds, we also

compared these results to those obtained using the VPSC model. For this, we select two values of the tuning parameter n^{eff} corresponding to different formulations of the macroscopic moduli: the secant formulation ($n^{eff} = 1$) and the tangent formulation ($n^{eff} = n$).

These simulations were conducted with strain hardening according to the Voce law. The Voce hardening parameters are obtained by fitting the results of the upper bound Taylor model to experimental shear stress/shear strain curves given in the work of Tóth and Molinari (1994) for OFHC copper. The best fitting is obtained for: $\tau_0 = 16$ MPa, $\tau_1 = 120$ MPa, $\theta_0 = 190$ MPa and $\theta_1 = 7$ MPa. These parameters are kept the same for all simulations with different models. Small modifications of the hardening coefficients will lead to a better agreement between the measured and the predicted stress-strain curves but not in a significant change in the texture development. Tóth and Molinari (1994) have pointed out that important differences in the texture can only be seen when the model assumptions are changed, i.e. when the Taylor assumption, self-consistent approach, shape effects, or changes in the value of the strain rate sensitivity were considered. However, in this work, the hardening effect will be analyzed, through a comparison between predicted results with non-linear hardening, with a linear hardening and also without hardening. These simulations showed that the ϕ-model and the lower bound approach are sensitive to hardening parameters. As in the work Tóth and Molinari (1994), the strain rate sensitivity parameter for the crystallographic slip is chosen to be $n = 7$.

In order to compare our predictions to the results of Tóth and Molinari (1994), we used their initial texture, for OFHC copper, represented by 400 orientations and shown in Fig. 4-2. For silver, since we do not have an experimental starting texture, we used the same initial texture as the one shown in Fig. 4-2. Based on the results for

these two FCC materials, we attempt to qualitatively correlate the experimental shear textures and SFE of FCC metals based on the ϕ-model predictions.

In the simulations, deformation is simulated imposing successive deformation increments using the 12 {111}<110> FCC slip systems. At each deformation step, the boundary conditions corresponding to a constant equivalent strain rate, $\dot{\varepsilon}_0$, are imposed. In other words, we assume homogeneous boundary conditions where the imposed macroscopic velocity gradient $\overline{\mathbf{L}}$ is constant. The prescribed velocity gradient $\overline{\mathbf{L}}$ of simple shear is thus taken as:

$$\overline{\mathbf{L}} = \dot{\varepsilon}_0 \begin{bmatrix} 0 & 1 & 0 \\ 0 & 0 & 0 \\ 0 & 0 & 0 \end{bmatrix} \tag{4-1}$$

IV.4.2 Results for shear texture evolutions

In order to compare our predictions to the experimental shear textures of Tóth and Molinari (1994), we simulated simple shear tests up to a total shear strain of $\gamma = 2$ and $\gamma = 5.5$. For $\gamma = 2$, the predicted texture results by the ϕ-model are shown by the ODF sections for $\phi = 0.005$ and $\phi = 0.1$ in Fig. 4-4. The ODF figures of the crystallographic texture have been obtained with the MTM-FHM software developed by Van Houtte (1995). For comparison of these results with those predicted by the widely used models, we show the results of the VPSC in Fig. 4-5 and those predicted by the upper-bound Taylor and lower-bound static models in Fig. 4-6. Theses predicted shear textures had to be compared to the experimental ones for copper, a medium SFE (plotted in Fig. 4-3) and to the experimental ones for silver, a typical low SFE.

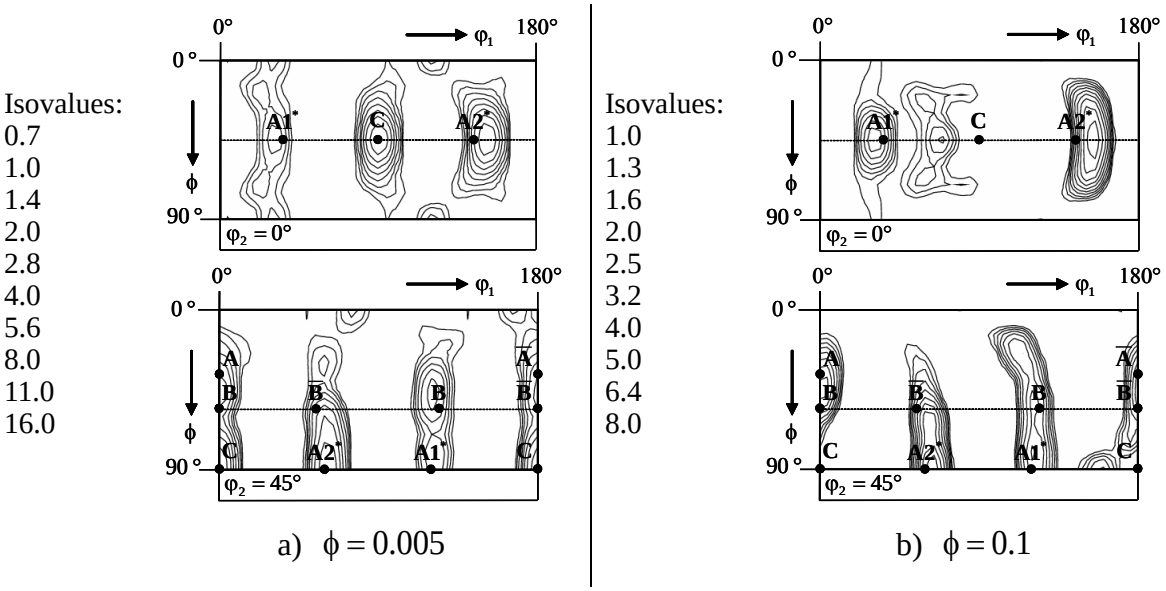

a) $\phi = 0.005$ b) $\phi = 0.1$

Fig. 4-4. Simulated shear textures obtained by the ϕ-model: $\phi = 0.005$ (a) and $\phi = 0.1$ (b)

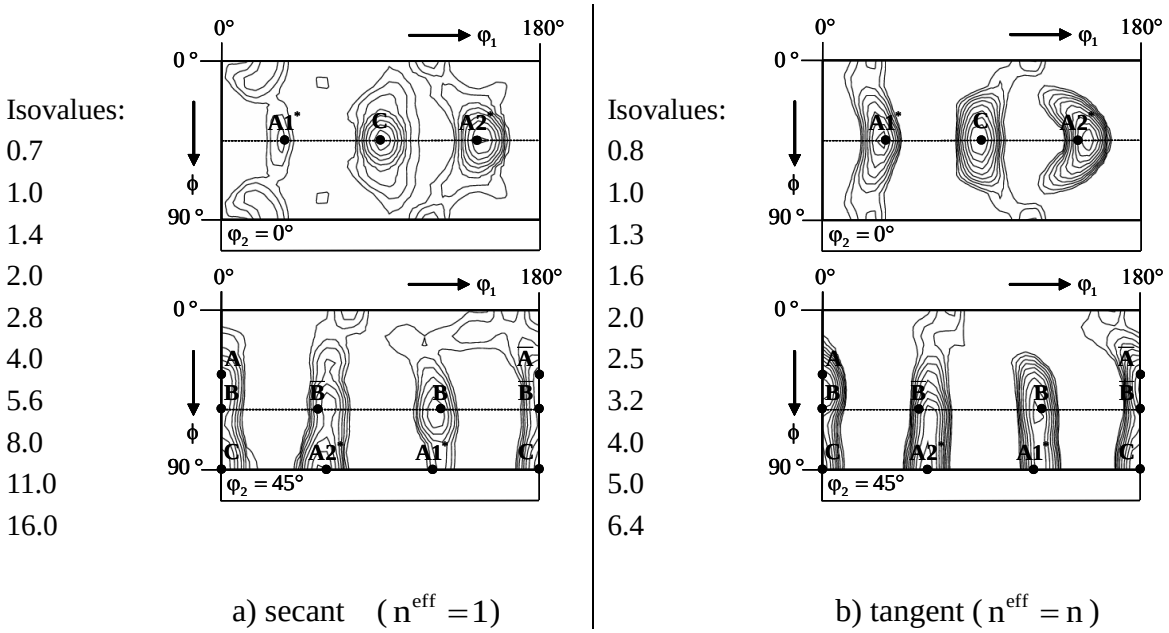

a) secant ($n^{eff} = 1$) b) tangent ($n^{eff} = n$)

Fig. 4-5. Simulated shear textures obtained by the secant (a) and tangent (b) VPSC models

For the ϕ-model, the predicted shear textures differs considerably with the values of the parameter ϕ, see Fig. 4-4. For $\phi = 0.005$, we mainly recovered the VPSC predictions (see Fig. 4-5) which are close to the copper experimental ones. The ϕ-model for small values of ϕ reproduces the positions of the main shear texture

components for copper, a high SFE material. For a higher value, $\phi = 0.1$, the shear predictions are very different from the lower values of ϕ. For example, the C component is progressively shifted from ideal orientations along the φ_1 axis in a decreasing sense as the parameter ϕ increases. The C component also progressively weakens as the parameter ϕ increases and totally vanishes for ϕ close to 1. These texture predictions are mainly close to the experimental values for silver, a low SFE metal, as described in the previous section. For the VPSC model, Fig. 4-5 shows that all the predicted shear textures for different formulations (tangent and secant) are close to each other. The main differences between them are only the intensity of the predicted texture components. Thus, by varying the value of the parameter n^{eff} in the VPSC, a very weak texture transition is obtained with this model. By comparison to experimental results reported in Fig. 4-3 for copper, we see that all the VPSC predictions are close to the ideal components for copper. These results show that the VPSC model does not predict the shear texture components that are generally observed for low SFE metals (i.e. silver). We also note that the Taylor predictions (see Fig. 4-6a) are close to the secant VPSC model (see Fig. 4-5a) as well as ϕ-model predictions for $\phi = 0.005$ (see Fig. 4-4a). The Taylor shear textures predictions are close to the copper type. On the other hand, the static predictions (see Fig. 4-6b) are close to the ϕ-model predictions for large values of ϕ (see Fig. 4-4b) and are close to a silver type texture. Thus, for a shear strain of $\gamma = 2$, only the ϕ-model is able to reproduce (at least qualitatively) a shear texture transition for high-to-low SFE by varying ϕ between 0 to 1. This shows that this parameter allows for the prediction of the texture transition and therefore it can be linked to the microstructural features controlling this transition in FCC metals (M'Guil et al., 2009, 2010,2011a).

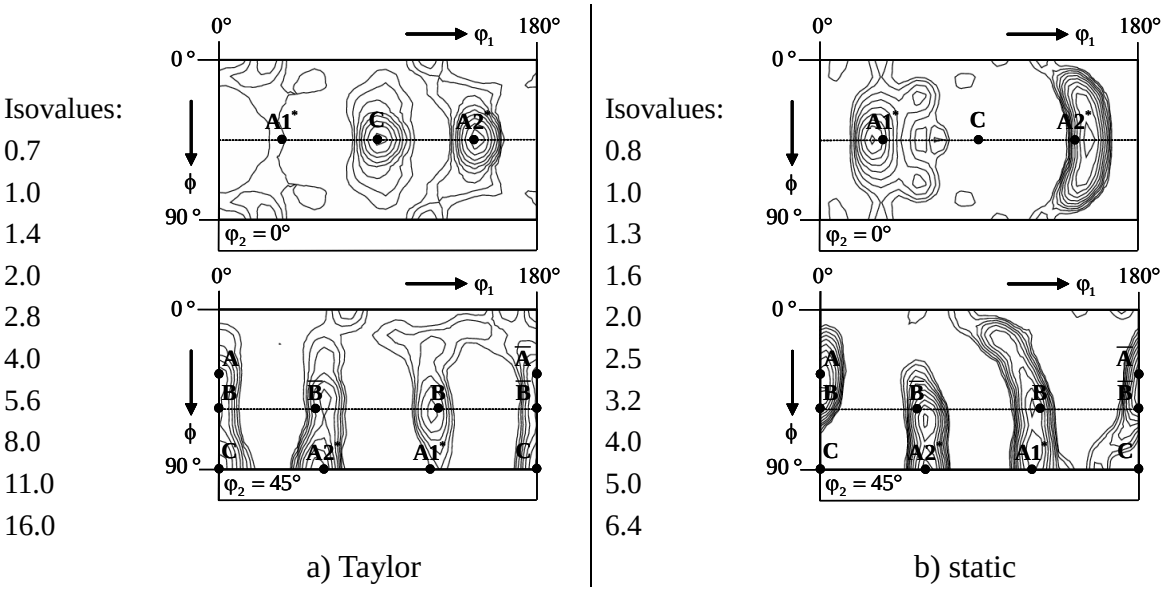

Fig. 4-6. Simulated shear textures obtained by the Taylor (a) and static (b) models

We should note that the grain shape is not updated in the VPSC calculations and this effect is not included in the ϕ-model. Since, we do not take into account the effect of substructure evolution which is due to the severe plastic deformation (Beyerlein and Tóth, 2009), we limit our analysis to a shear strain of $\gamma = 2$. Under larger strains and strain path changes, Beyerlein and Tóth (2009) have pointed out that some deficiencies in models (Taylor and VPSC) can affect texture predictions.

IV.4.3 Effect of microscopic hardening on predicted shear texture

In this section, the hardening effect is analyzed through a comparison between predicted shear textures with non-linear hardening ($\tau_0 = 16$ MPa, $\tau_1 = 120$ MPa, $\theta_0 = 190$ MPa; $\theta_1 = 7$ MPa), with a linear hardening ($\tau_0 = 1$ MPa, $\tau_1 = 0$ MPa, $\theta_0 = 1$ MPa; $\theta_1 = 1$ MPa) and without hardening ($\tau_0 = 1$ MPa, $\tau_1 = 0$ MPa, $\theta_0 = 0$ MPa and $\theta_1 = 0$ MPa).

The predictions show that the ϕ-model is quite sensitive to variations of hardening

parameters. A difference in texture predictions (intensities and position of ideal shear components) is observed with different hardening assumptions; see Fig. 4-4 (with hardening) and Fig. 4-7a (without hardening) and Fig. 4-7b (with a linear hardening). However, we should note that the A, B, and C textures components appear in all of the hardening assumptions but with different intensities as was already reported by others (Li and Havner, 1996). On the other hand, for the VPSC model, the effect of hardening is negligible and the predicted texture without hardening is almost indistinguishable from that with hardening. We have not reported these results in this work since these observations for the VPSC model are in accord with other results in literature such as those of Li et al. (2006). Similar conclusion is applied to the Taylor model. Thus, the VPSC model and the Taylor model are negligibly sensitive to variations in hardening parameters. On the other hand, the high sensitivity of the ϕ-model to hardening parameters makes it the most capable model to reproduce a large number of experimental observations by correctly adjusting the value of hardening parameter versus the value of ϕ. We note that the static model (results not reported) is also found to be sensitive to variations in hardening parameters.

IV.5 Shear texture predictions with twinning mechanism

In this section, we take into account the twinning mechanism to improve predicted shear texture for silver which is an FCC metal that can twin during plastic deformation (Beyerlein et al., 2007). In fact, silver is a low SFE metal and thus presents twinning deformation mode in addition to crystallographic slip during plastic deformation. On the other hand, a high/medium SFE metal, such as copper, deforms mainly by crystallographic slip.

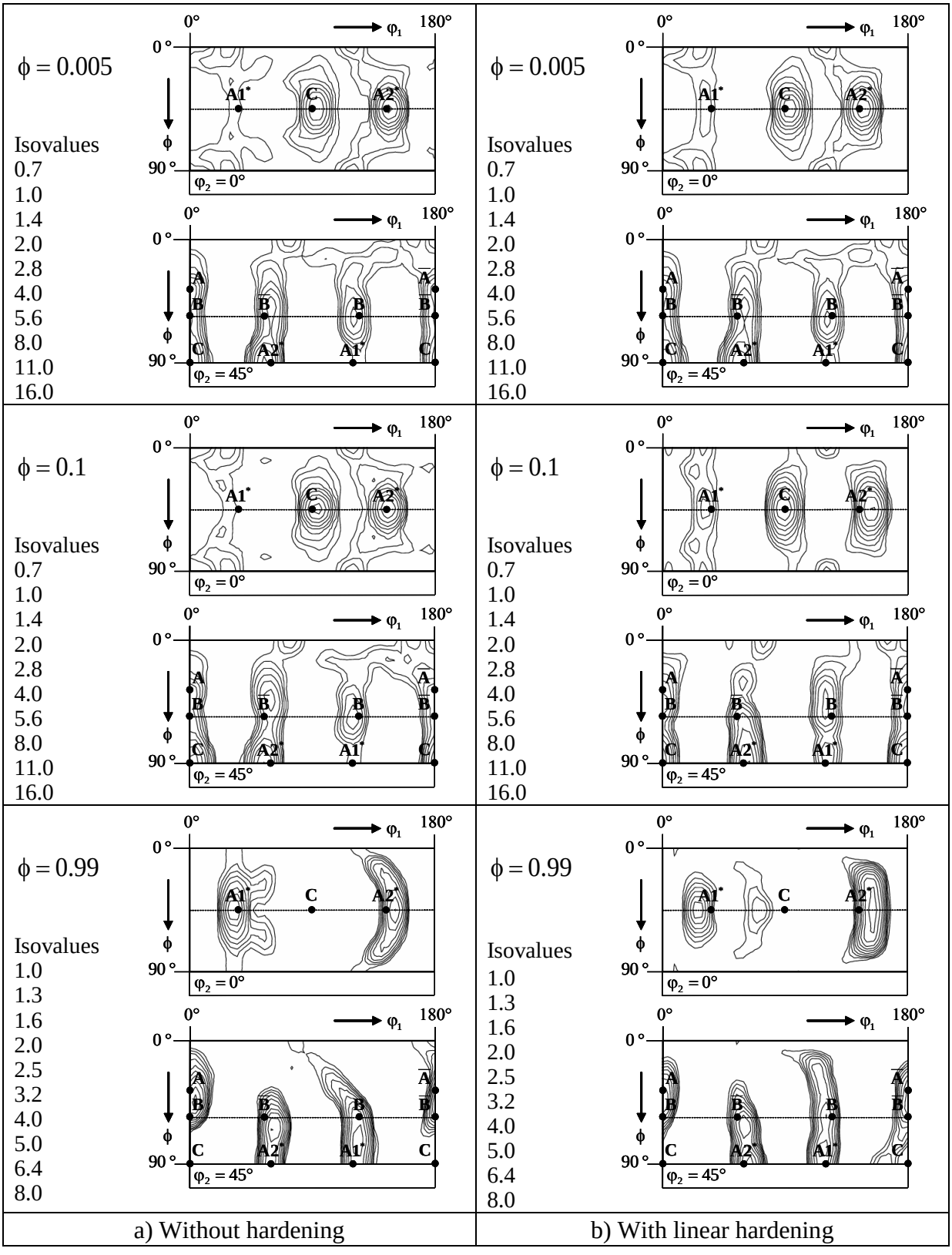

a) Without hardening | b) With linear hardening

Fig. 4-7. Simulated shear textures obtained by the ϕ-model without hardening (a) and with linear hardening (b)

In order to check the influence of twinning, we conducted simulations adding 12 twinning systems {111}<112> to the 12 slip systems {111}<110>. We consider that the critical resolved shear stress of slip and twinning are equal ($\tau_{0(slip)} = \tau_{0(twin)}$). The PTR scheme (Tomé et al., 1991) is used here to describe the twinning orientations. For the parameters relative to twinning, we used the same values as Beyerlein et al. (2007): $A^{th1} = 0.25$, $A^{th2} = 0.1$ and $S^t = 0.707$. For cubic FCC metals, the parameter S^t is usually equated equal to 0.707 (Beyerlein et al., 2011). In these simulations, we consider a linear hardening for both twinning and slip modes.

In this section, we choose $\phi = 0.2$ and $\phi = 0.8$ for the simulations. We selected these values for ϕ because they lead to the most noticeable differences between the shear textures predicted with and without twinning mechanism. Figs. 4-8, 4-9 show the predicted shear textures, at $\gamma = 2$, without and with twinning for $\phi = 0.2$ and $\phi = 0.8$.

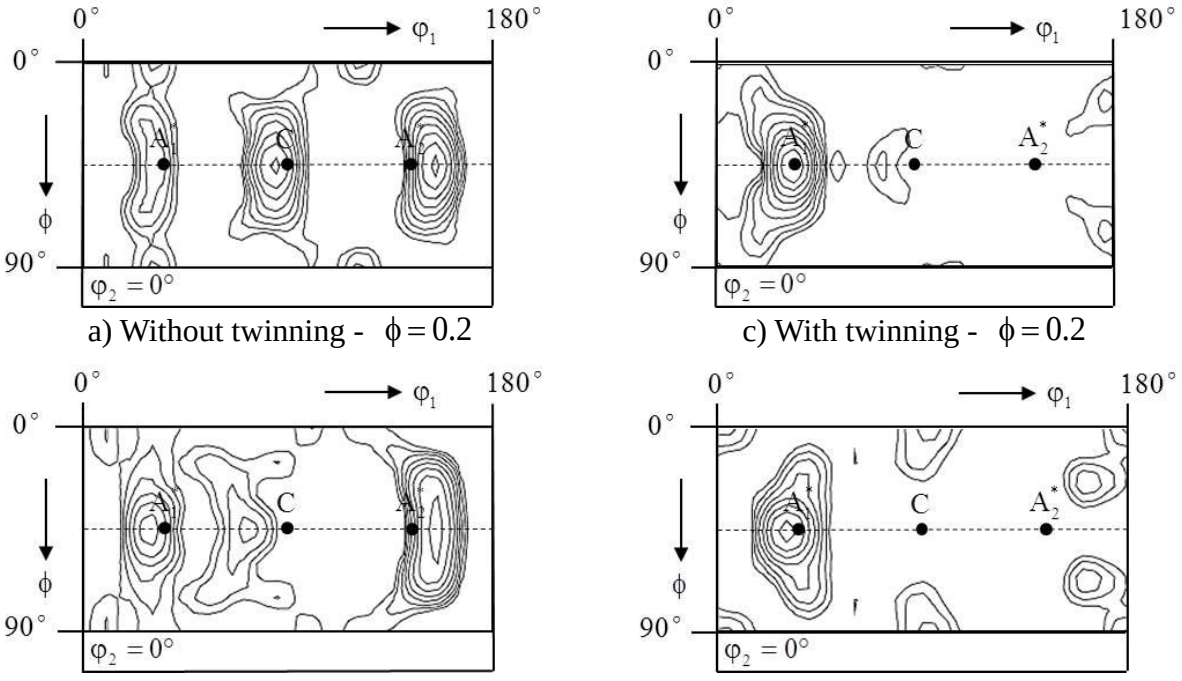

a) Without twinning - $\phi = 0.2$

c) With twinning - $\phi = 0.2$

b) Without twinning - $\phi = 0.8$

d) With twinning - $\phi = 0.8$

Fig. 4-8. Simulated shear textures without (a-b) and with (b-d) twinning for $\phi = 0.2$ and $\phi = 0.8$ (in the $\varphi_2 = 0°$ section of the ODF)

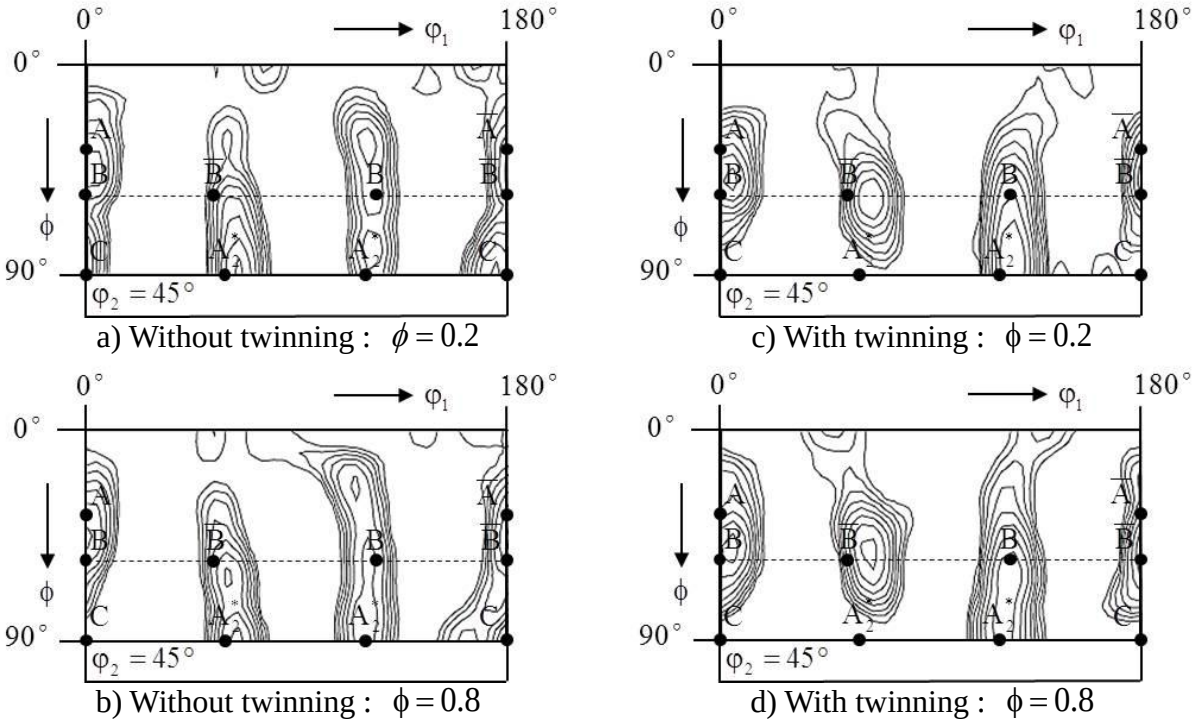

Fig. 4-9. Simulated shear textures without (a-b) and with (c-d) twinning for $\phi = 0.2$ and $\phi = 0.8$ (in the $\varphi_2 = 45°$ section of the ODF)

To be more accurate, we also display, along the φ_1 axis, the evolution of the ideal shear texture A_1^*, C and A_2^* components (see Fig. 4-10). The evolution, along the φ_1 axis, of the ideal shear texture $B/\overline{B}$ component is plotted in Fig. 4-11. This representation allows quantifying the effect of twinning on shear texture components. In Fig. 4-10, we observe that with twinning, both A_2^* and C components strongly decrease and the A_1^* component clearly increases. Obviously, these modifications in intensity as function of twinning depend on ϕ.

Our simulations are in accord with the experimental results in the literature. In fact, Beyerlein et al. (2007) have shown that grains near the $A_{1\theta}^*$ (corresponding to C component under shear test) orientation twin readily under simple shear which explains why this component is consistently weak in silver. Using the VPSC/PTR scheme and microscopy, Beyerlein et al. (2007) showed that the primary consequence of twinning, under ECAE deformation is the reorientation of the $A_{1\theta}^*$ ideal

orientations into the $A_{2\theta}^{*}$ orientation which results in a weak $A_{1\theta}^{*}$ and a strong $A_{2\theta}^{*}$ component. Note that these components for ECAE, $A_{1\theta}^{*}$, $A_{2\theta}^{*}$, correspond to C and A_{1}^{*}, respectively, for simple shear test (see Fig. 4-1). In fact, the $A_{2\theta}^{*}$ component is the least likely to twin, which explains why this component is the strongest (Beyerlein et al., 2007). These results are consistent with our simulations which show a decrease of the component C (see Fig. 4-10) and an increase of the component A_{1}^{*} when twinning mechanism is accounted for (see Fig. 4-10). On this Fig. 4-10, the shift of the components A_{1}^{*}, C and A_{2}^{*} from the ideal position is clearly visible. In Fig. 4-11, we analyze the effect of twinning on the $B/\overline{B}$ components. We can observed that these shear components are strongly increased by twinning.

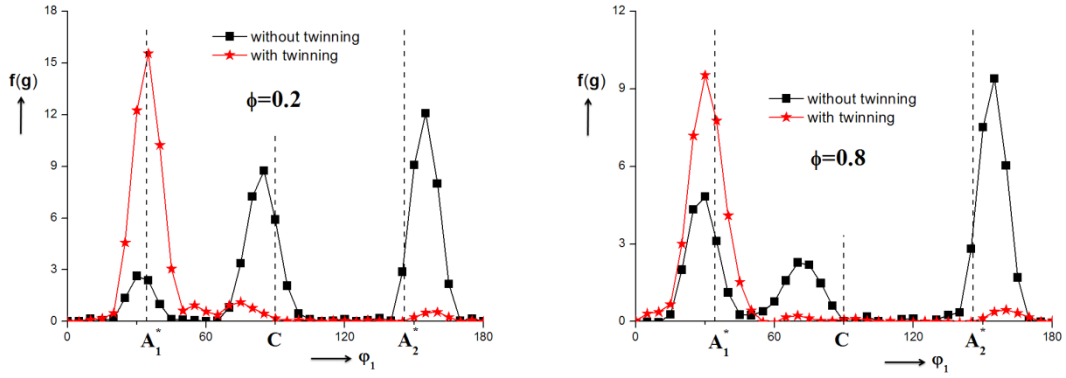

a) $\phi = 0.2$ b) $\phi = 0.8$

Fig. 4-10. Evolution of the shear texture components: A_{1}^{*}, C and A_{2}^{*}, with and without twinning for $\phi = 0.2$ (a) and $\phi = 0.8$ (b)

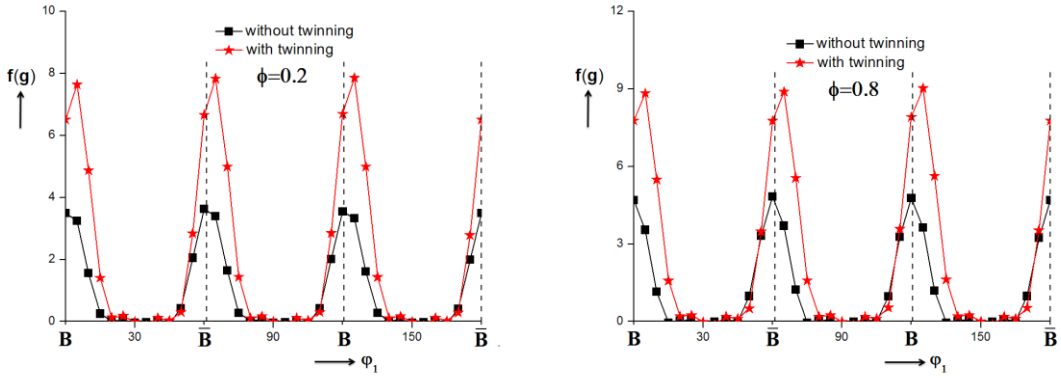

a) $\phi = 0.2$ b) $\phi = 0.8$

Fig. 4-11 Evolution of shear texture components : $B / \overline{B}$, with and without twinning for $\phi = 0.2$ (a) and $\phi = 0.8$ (b)

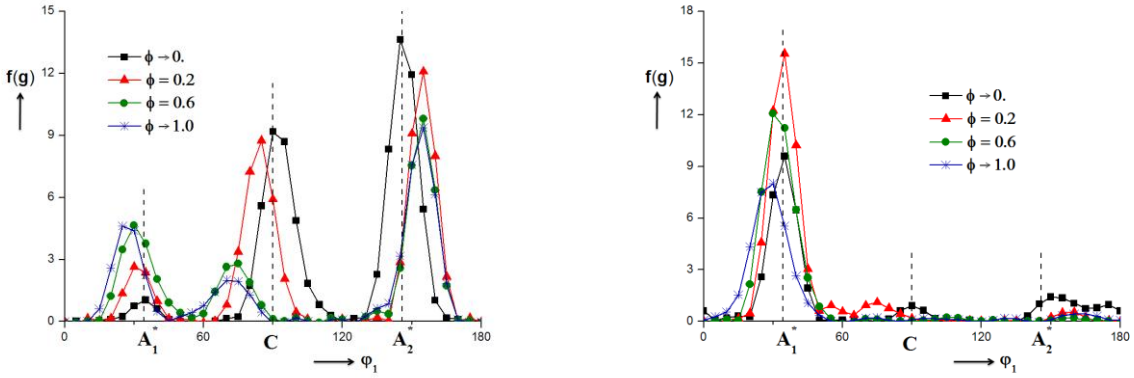

a) Without twinning b) With twinning

Fig. 4-12. Evolution of the shear texture components: A_1^*, C and A_2^*, in function of the parameter ϕ, without (a) and with twinning (b)

Finally, we plot the evolution of the ideal shear texture components A_1^*, C and A_2^* in function of ϕ (see Fig. 4-12) without and with twinning. In Fig. 4-12a (without twinning) and Fig. 4-12b (with twinning), we can see that by increasing the value of ϕ (between 0 and 1), the components A_1^*, C and A_2^* are shifted from their ideal orientation. For the components A_1^*, C, the shift is observed in a decreasing φ_1 direction while the A_2^* shifts in the increasing φ_1 direction. We

note that a shift, for silver, was already reported by Suwas et al. (2003). These authors have obtained the smallest shift for this component A_2^* (9°) by comparison to the components A_1^* (20°) and C (16°). Thus our predictions are consistent with their results except for the A_2^* component. However, we have noticed a decrease of this component A_2^* when twinning is included which is in an accord with the experiments of Suwas et al. (2003). We should underline that the imposed boundary conditions in our simulations (simple shear) are not fully adequate for ECAE test and this may explain the obtained deviation for the component A_2^*.

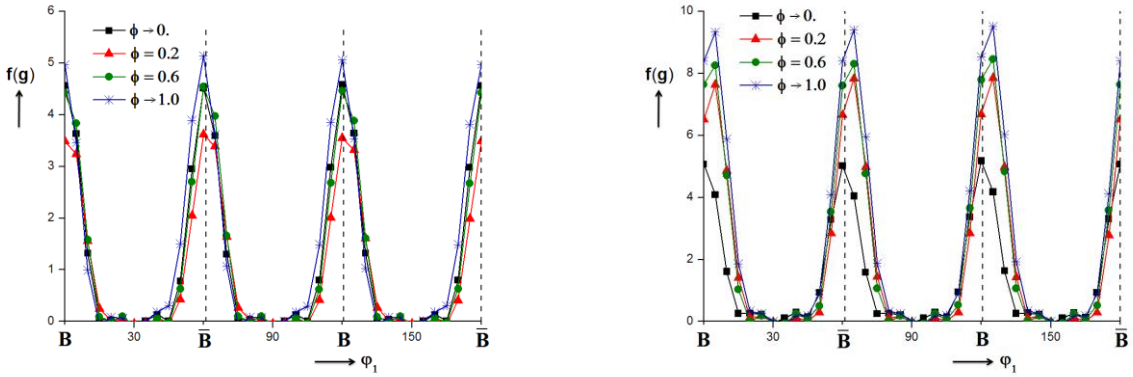

a) Without twinning b) With twinning

Fig. 4-13. Evolution of the shear texture components: $B/\overline{B}$, in function of the parameter ϕ, without (a) and with twinning (b)

We also note, that the evolution, as function of ϕ, of the $B/\overline{B}$ components, see Fig. 4-13, is quite stable which is in accord with literature (Suwas et al., 2003). In fact, without (Fig. 4-13a) and with twinning (Fig. 4-13b), we do not obtain any shift from ideal orientations for these $B/\overline{B}$ components. For the tangent VPSC model, the simulations, without hardening, show that both the components C and A_2^* totally vanish at $\gamma = 2$ if twinning is taken into account, see Fig. 4-14. To close this section, we conclude that in order to accurately predict the shear texture evolution in silver, twinning mechanism must be taken into account. This is in accord with the results

from literature such as those of Beyerlein et al. (2007).

IV.6 Parametric studies

IV.6.1 Effect of relative slip/twinning activities

In this section, we study the influence of slip/twinning activities on the FCC shear textures. The relative slip/twinning activities are controlled by the α value ($\alpha = \tau_0^{tw} / \tau_0^{slip}$) as in chapter II. We note that, in the previous sections of this chapter, the CRSS of slip and twinning are set to be equal ($\alpha = 1$).

Here we carry out simulations with a linear hardening and the α values are chosen to be 0.8, 1.0 and 1.2. All other parameters, including the twinning parameters, are set to be the same than the previous simulations of this chapter. In Fig. 4-14 and Fig. 4-15, the relative activities of slip and twinning as function of α value are presented for $\phi = 0.2$ and $\phi = 0.8$. It can be seen that, for both ϕ values, a higher α value will lead to a lower relative activity of twinning. For $\alpha = 1.2$, only 10% of plastic deformation is accumulated by twinning.

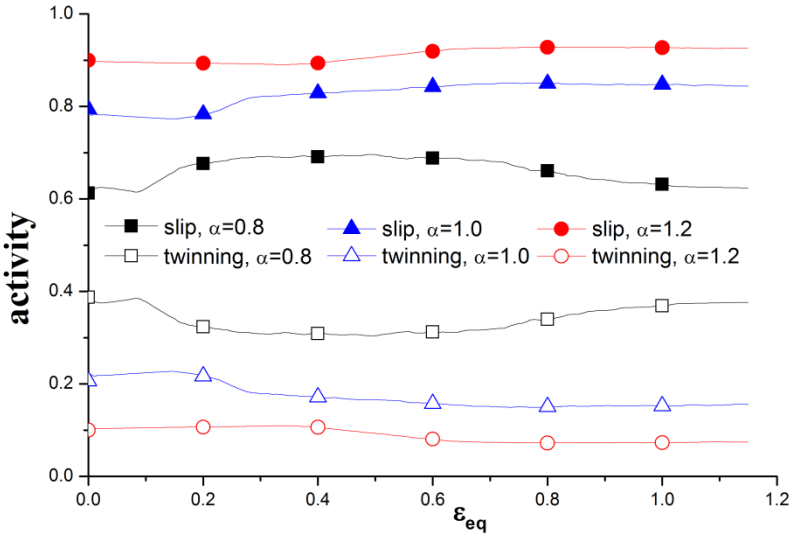

Fig. 4-14. Effect of α value on slip/twinning activities for $\phi = 0.2$.

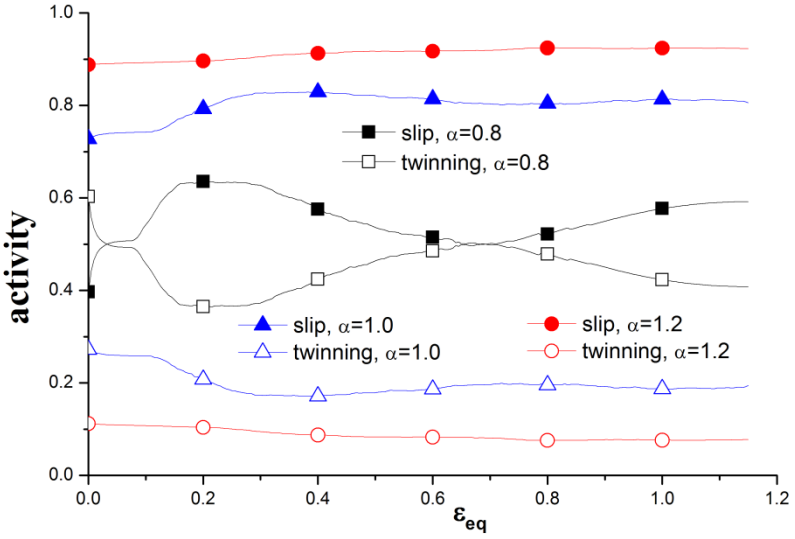

Fig. 4-15. Effect of α value on slip/twinning activities for $\phi = 0.8$.

The effects of the α value on the ideal shear texture A_1^*, C and A_2^* components are presented in Fig 4-16. For $\phi = 0.8$, we can see that the A_1^* component is increased and the C and A_2^* components are decreased with the increase of α value (inversely proportional to the relative activity of twinning). However, for

$\phi = 0.2$, the evolution tendencies of these components with α values are not clear. The strongest A_1^* component and the weakest C and A_2^* components can be obtained for $\alpha = 1.0$. On the other hand, as shown in Fig 4-17, the $B/\overline{B}$ components are weakly reduced for higher α values.

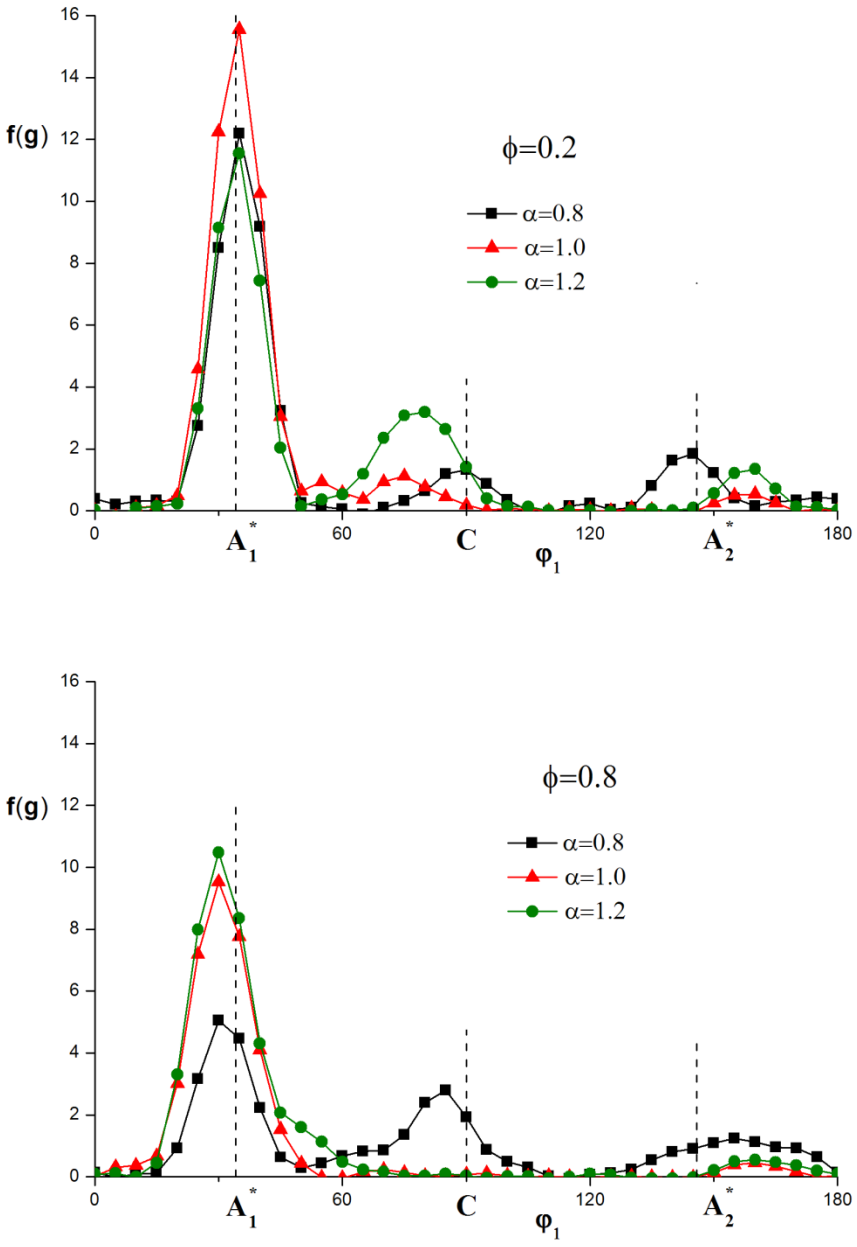

Fig. 4-16. Effect of α value on the shear texture components: A_1^*, C and A_2^* for $\phi = 0.2$ and $\phi = 0.8$.

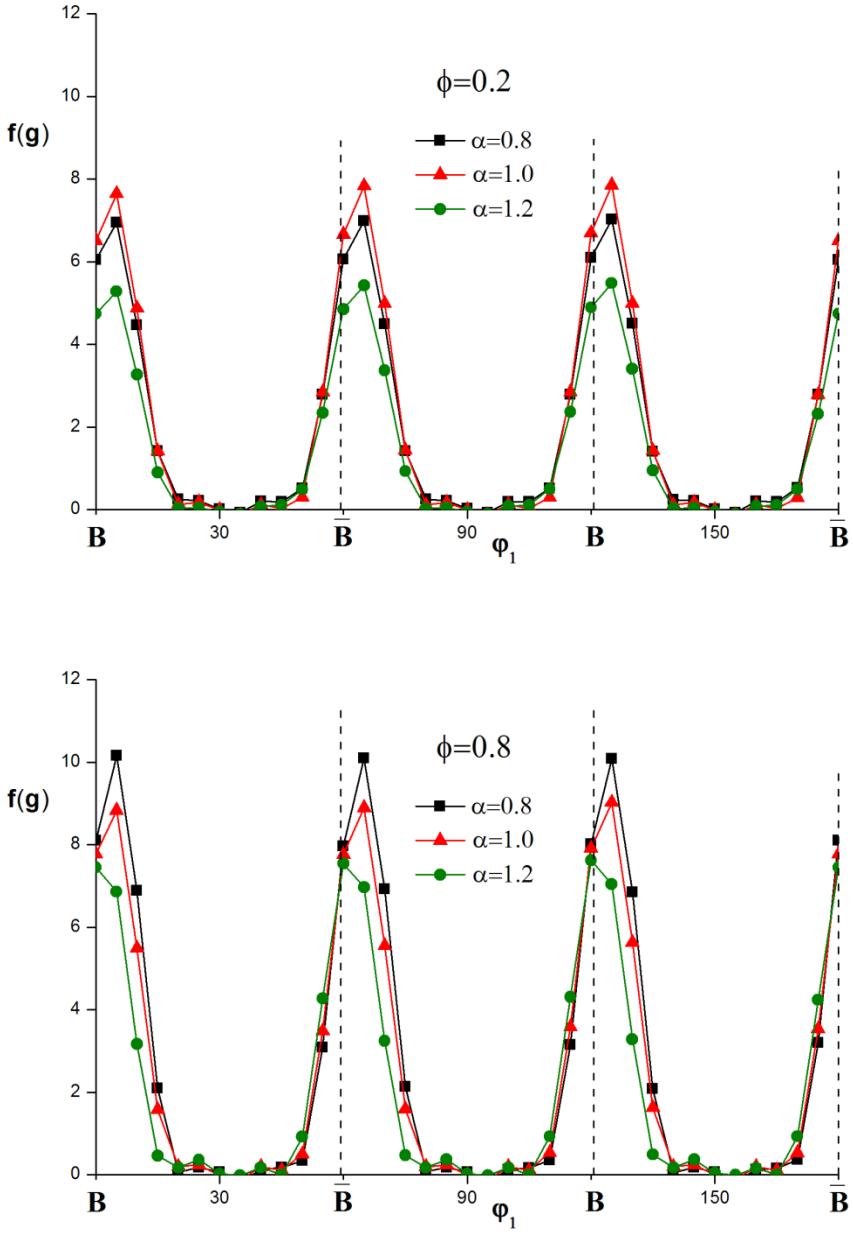

Fig. 4-17. Effect of α value on the shear texture $B/\overline{B}$ components for $\phi = 0.2$ and $\phi = 0.8$.

IV.6.2 Volume effects of deformation twinning

The volume effects of twinning on the FCC shear will be investigated in this section. The voce hardening parameters of silver (see Tab. 2-1 in chapter II) are used here to relate the predicted results with experiment. The twin volume fraction will be

controlled by the characteristic twin shear parameter S^t of the PTR scheme (Tomé et al., 1991). As shown in chapter II, the twin volume fraction can be suppressed by increasing this parameter. The predicted twin volume fraction are presented in Fig 4-18 for $\phi = 0.2$ and $\phi = 0.8$. By increasing the S^t value from 0.707 (suggested value for cubic materials, e.g. Beyerlein et al., 2011; Prakash et al., 2008) to 2.5, the predicted twin volume fraction is reduced from over 35% to around 15%. Higher ϕ value will leads to lower twin volume fraction.

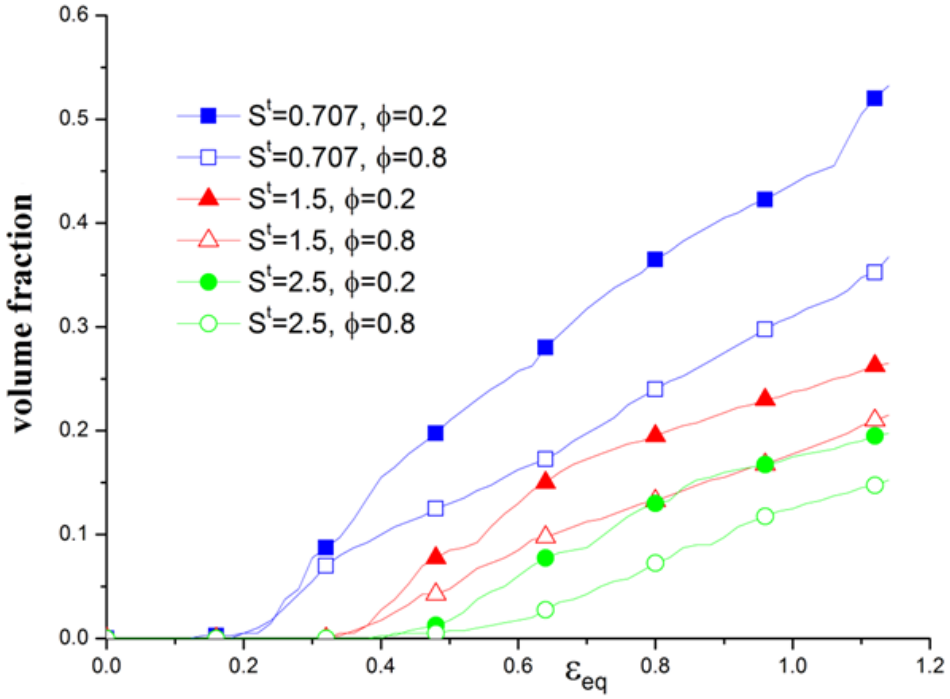

Fig. 4-18. Effect of S^t on the volume fraction for $\phi = 0.2$ and $\phi = 0.8$

The evolutions of ideal shear texture A_1^*, C and A_2^* components as function of S^t are shown in Fig. 4-19. For $\phi = 0.2$, the effects of S^t on the components C and A_2^* are clear where the C and A_2^* components are inversely proportional to S^t. The evolution of A_1^* component with S^t is not monotone. The strongest A_1^* component is obtained at $S^t = 1.5$. For $\phi = 0.8$, the effect of S^t are not clear. However, the strongest A_1^* component and the weakest C and A_2^* components are always

obtained for $S^t = 0.707$. We notice that, for both ϕ values, the results for $S^t = 2.5$ (lowest twin volume fraction) fit the best with the experimental results of silver (Beyerlein et al., 2007) where the A_1^* component is about 2~3 times stronger than C and A_2^* components.

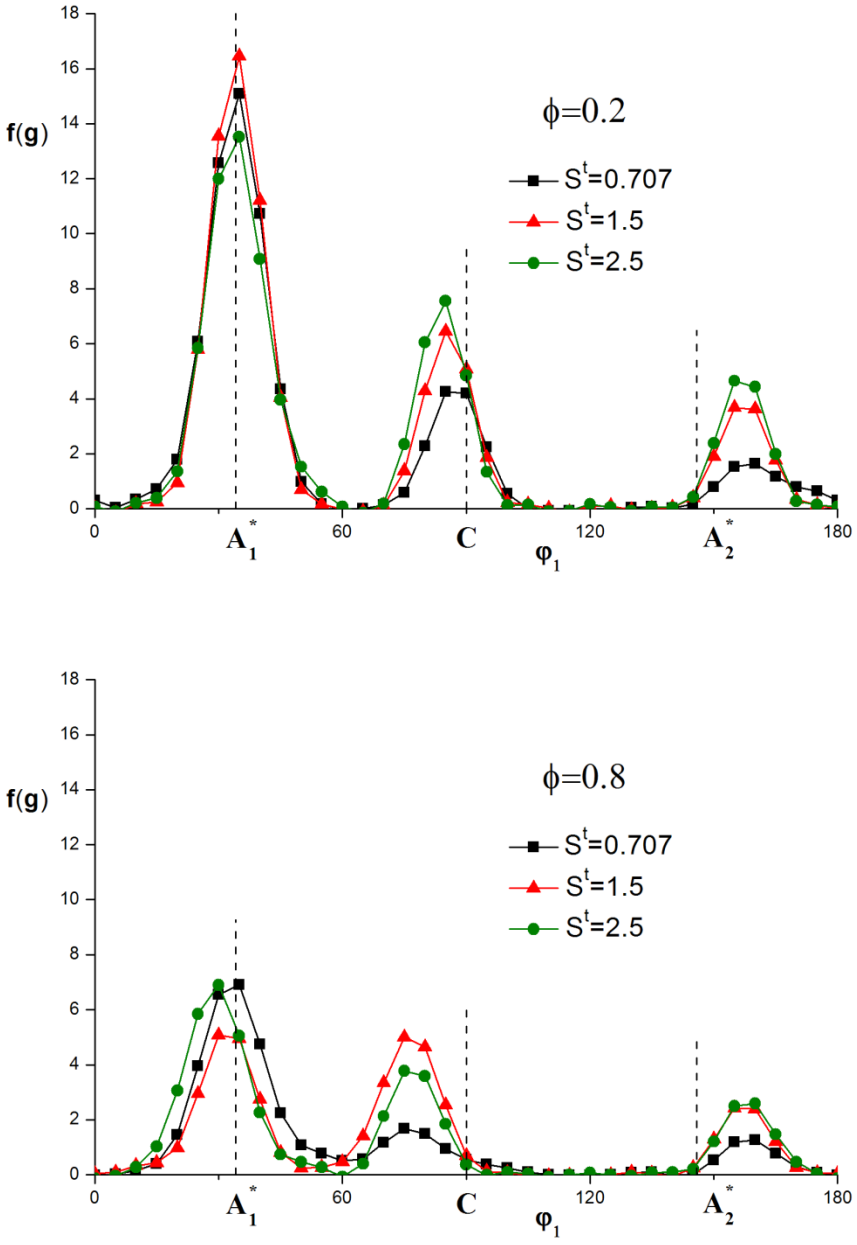

Fig. 4-19. Effect of S^t value on the shear texture A_1^*, C and A_2^* components for $\phi = 0.2$ and $\phi = 0.8$.

The corresponding results of $B/\overline{B}$ components are presented in Fig. 4-20. It can be seen that the $B/\overline{B}$ components can be decreased with the increasing S^t value. When we take into account all those FCC shear texture components (Fig. 4-19 and Fig 4-20), it could be noticed that the high ϕ value ($\phi = 0.8$) leads to a better agreement with experimental results of Beyerlein et al. (2007) where the $B/\overline{B}$ components is a little stronger than A_1^* component.

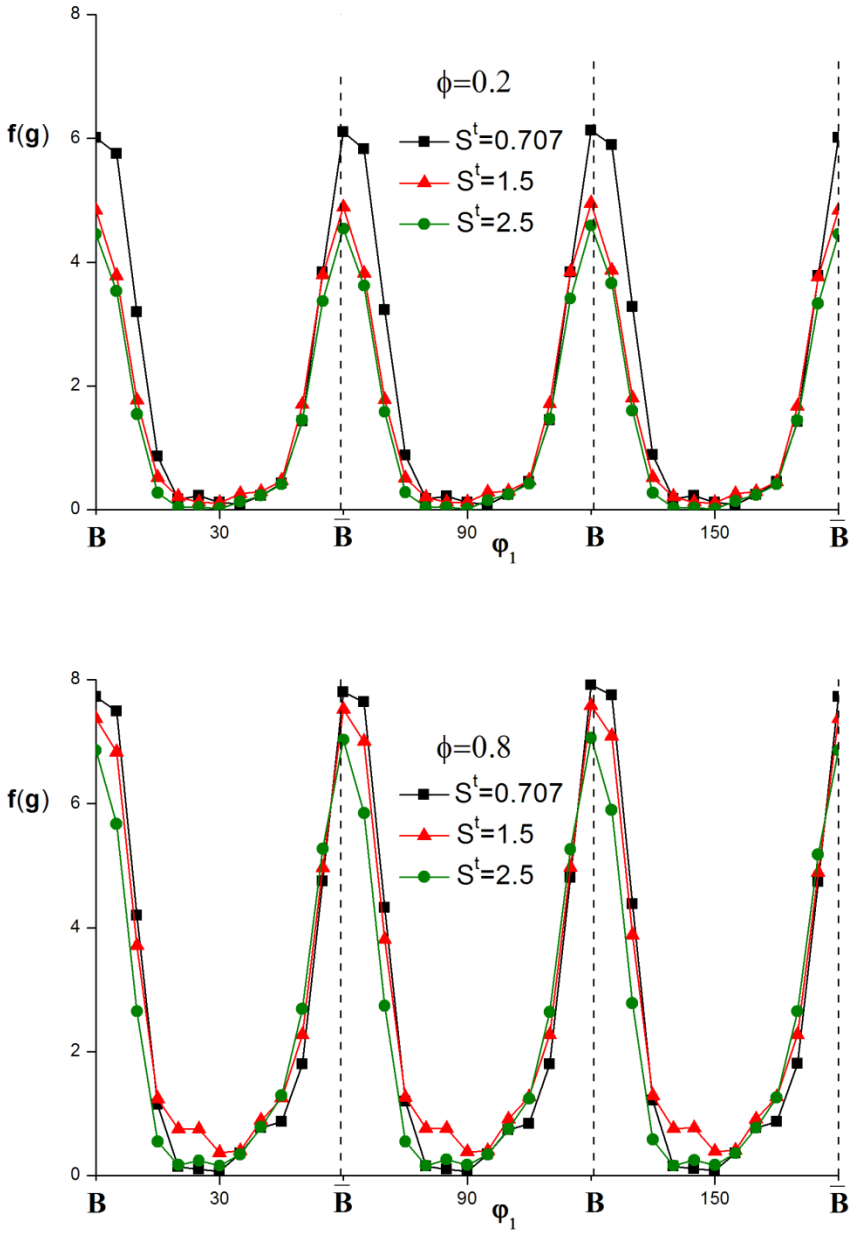

Fig. 4-20. Effect of S^t value on the $B/\overline{B}$ components for $\phi = 0.2$ and $\phi = 0.8$.

IV.7 Conclusion

In this chapter, we have extended the validation of the visco-plastic ϕ-model under shear test up to large strains by comparing predicted results for texture evolution to the experimental ones from the literature.

In the first part of the chapter, by considering only crystallographic slip and by varying ϕ, we showed that the ϕ-model predictions are consistent with experimental shear textures of high/medium to low SFE FCC metals. As in the case of plane strain compression (or rolling) test where a texture transition is obtained from the copper-type to the brass-type, a shear texture transition is also predicted by varying ϕ between the values 0 and 1.

In the second part of the chapter, in order to improve the predicted results for low SFE metals, we added the twinning mechanism to the crystallographic slip. We also observed a shear texture transition by varying ϕ and show that our predicted results (with twinning) are consistent with related results from literature and particularly for low SFE metals such as silver. The effect of twinning on the ideal shear texture components is clearly shown for silver. The tendencies of the evolution of the ideal shear texture component (A_1^*, A_2^*, C, $B/\overline{B}$) with or without twinning, are in accord with experimental results in the literature.

In this work, we showed that in order to predict the shear texture evolution of low SFE metals such as silver, twinning was needed to accommodate plastic deformation.

By comparison of our results, as function of the parameter ϕ, to the experimental shear textures of both medium and low SFE FCC metals, the predicted texture-transitions suggest that the parameter ϕ should be correlated to the SFE of the polycrystalline material. Here again, we can roughly assume that a high value of

ϕ is adequate to low SFE and that a low value for ϕ is adequate for to high/medium SFE.

We also proposed the parametric studies by varying the slip/twinning activities (controlled by α value) and twin volume fraction (controlled by S^t value). The effects of those parameters on the shear texture evolution are analyzed. We have shown that when the real hardening parameters of low SFE metal are used, the best fitted results with experiment could be found when the high ϕ value is used and the twin volume fraction is reduced to reasonable values.

References:

Canova, G.R., Kocks, U.F., Jonas, J.J., 1984. Theory of torsion texture development. Acta Metall. 32, 211-226.

Beyerlein, I.J., Tóth, L.S., 2009. Texture evolution in equal-channel angular extrusion. Prog. Mater. Sci. 54, 427-510.

Beyerlein, I.J., Tóth, L.S., Tomé, C.N., Suwas, S., 2007. Role of twinning on texture evolution of silver during equal channel angular extrusion. Philos. Mag. 87, 885-906.

Beyerlein, I.J., Mara, N.A., Bhattacharyya, D., Alexander, D.J., Necker, C.T., 2011. Texture evolution via combined slip and deformation twinning in rolled silver-copper cast eutectic nanocomposite. Int. J. Plasticity 27, 121-146.

Hu, H., Cline, R.S., Goodman, S.R., 1961. Texture transition in high-purity silver and its correlation with stacking fault. J Appl Phys 32, 1392-1399.

Hughes, D.A., Lebensohn, R.A., Wenk, H.R., Kumar, A., 2000. Stacking fault energy and microstructure effects on torsion texture evolution. Proc. R. Soc. London, Ser. A, 456, 921-953.

Hughes, D.A., Wenk, H.R., Kalland, S., Gottstein, G., (Eds.). 1988. 8th Int. Conf. on Textures of Materials, the Metallurgical Society, Warrendale, PA, P.455.

Gazder, A.A., Dalla Torre, F., Gu, C.F., Davies, C.H.J., Pereloma, E.V., 2006. Microstructure and texture evolution of bcc and fcc metals subjected to equal channel angular extrusion. Mater. Sci. Eng. A 415, 126-139.

Leffers, T., 1968. Deformation rate dependence of rolling texture in brass containing 5% zinc. Scripta Metall. 2, 447-452.

Li, S., 2008. Orientation stability in equal channel angular extrusion. Part I: Face-centered cubic and body-centered cubic materials. Acta Mater. 56, 1018-1030.

Li, S., Beyerlein, I.J., Alexander, D.J., 2006a. Characterization of deformation textures in pure copper processed by equal channel angular extrusion via route A. Mater. Sci. Eng. A 431, 339-345.

Li, S., Beyerlein, I.J., Alexander, D.J., Vogel, S.C., 2005a. Texture evolution during multi-pass equal channel angular extrusion of copper: Neutron diffraction characterization and polycrystal modeling. Acta Mater. 53, 2111-2125.

Li, S., Beyerlein, I.J., Bourke, M.A.M., 2005b. Texture formation during equal channel angular extrusion of fcc and bcc materials: comparison with simple shear Mater. Sci. Eng. A 394, 66-77.

Li, S., Beyerlein, I.J., Necker, C.T., 2006b. On the development of microstructure and texture heterogeneity in ECAE via route C. Acta Mater. 54, 1397-1408.

Li, S., Donohue, B.R., Kalidindi, S.R., 2008. A crystal plasticity finite element analysis of cross-grain deformation heterogeneity in equal channel angular extrusion and its implications for texture evolution. Mater. Sci. Eng. A 480, 17-23.

Lin, G., Havner, K.S., 1996. A comparative study of hardening theories in torsion using the Taylor polycrystal model. Int. J. Plast. 12, 695-781.

M'Guil, S., Ahzi, S., Barlat, F., Gracio, J.J., 2011a. Simulation of microstructural effects and yield surface evolution in cubic metals using the viscoplastic ϕ-model. Int. J. Plasticity 27, 102-120.

M'Guil, S., Ahzi, S., Youssef, H., Baniassadi, M., Gracio, J.J., 2009. A comparison of viscoplastic intermediate approaches for deformation texture evolution in FCC

polycrystals. Acta Mater. 57, 2496-2508.

M'Guil, S., Wen, W., Ahzi, S., 2010. Numerical study of deformation textures, yield locus, rolling components and Lankford coefficients for FCC polycrystals using the new polycrystalline ϕ-model. I. J. Mech. Sci. 52, 1313-1318.

M'Guil, S., Wen, W., Ahzi, S., Gracio, J.J., 2011b. Modeling of large plastic deformation behavior and anisotropy evolution in cold rolled BCC steels using the viscoplastic ϕ-model-based grain-interaction. Mater. Sci. Eng. A 528, 5840-5853.

M'Guil, S., Wen, W., Ahzi, S., Gracio, J.J., 2013. Analysis of shear deformation by slip and twinning in low and high stacking fault energy FCC metals using the ϕ-model. Submitted to Mater. Sci. Eng. A.

Segal, V.M., 1995. Materials processing by simple shear. Mater. Sci. Eng. A 197, 157-164.

Stout, M.G., Kallend, J.S., Kocks, U.F., Przystupa, M.A., Rollet, A.D., 1998. In: Kallend JS, Gottstein G. editors. Proceedings of the ICOTOM 8, 8th Int. Conf. on Textures of Materials, Santa Fe, P. 479.

Suwas. S, Arruffat Massion, R., Tóth, L.S., Fundenberger, J.J., Beausir, B., 2009. Evolution of texture during equal channel angular extrusion of commercially pure aluminum: Experiments and simulations. Mater. Sci. Eng. A 520, 134-146.

Suwas, S., Tóth, L.S., Fundenberger, J.J., Eberhardt, A., Skrotzki, W., 2003. Evolution of crystallographic texture during equal channel angular extrusion of silver. Scripta Mater. 49, 1203-1208.

Swift HW, Engineering 1947;163:253.

Tomé, C.N., Lebensohn, R.A., Kocks, U.F., 1991. A model for texture development dominated by deformation twinning: Application to zirconium alloys. Acta Metal. Mater. 39, 2667-2680.

Tóth, L.S., 2003. Texture evolution in severe plastic deformation by equal channel angular extrusion. Adv. Eng. Mater. 5, 308-316.

Tóth, L.S., Jonas, J.J., Daniel, D., Bailey, J.A., 1992. Texture development and length changes in copper bars subjected to free end torsion. Text. Microstruct. 19, 245-262.

Tóth, L.S., Molinari, A., 1994. Tuning a self consistent viscoplastic model by finite element results-II. Application to torsion textures. Acta Metall. Mater. 42, 2459-2466.

Van Houtte P. User Manual MTM-FHM software version 2 MTM-KU Leuven (1995).

Van Houtte, P., 1978. Simulation of the rolling and shear texture of brass by the Taylor theory adapted for mechanical twinning. Acta Metal. 26, 591-604.

Chapter V. Application to BCC metals: large plastic deformation behavior and anisotropy evolution in cold rolled steels

V.1 Introduction

The simulation of large plastic deformation behavior of BCC metals have been studied using different approaches. The Taylor type models (including full constraint and "Relaxed constrained" models) have been mostly used for the simulation of the behavior of BCC metals such as low carbon steels (Hölsher et al., 1991; Liao et al., 1998; Raabe, 1995a,b; Raabe and Lücke, 1992; Raphanel and Van Houtte, 1985), ferritic stainless steels (Bate and Quinta da Fonseca, 2004; Hölsher et al., 1991, 1994; Raabe and Lücke, 1993), Interstitial-Free (IF) steel (Bate and Quinta da Fonseca, 2004), iron aluminides (Raabe, 1996) and tantalum (Lee et al., 1997). In other few existing works, the Sachs type models have also been applied to BCC metals such as martensite (Raabe, 1997). Raabe (1995c) explained the appropriate choice of the Sachs model for the martensite because of the low stacking fault energy of this phase. The self-consistent approaches have been also applied to BCC metals such as low carbon steels (Paquin et al., 2001), duplex stainless steel (Jia et al., 2008) and IF-steel (Delannay et al., 2009). To account for non-homogeneous boundary conditions, the Crystal Plasticity Finite Element Methods (CPFEM) have also been applied to BCC metals such as low carbon steels (Raabe et al., 2005a,b), ferritic steel (Tikhovskiy et al., 2006, 2008) and IF-steel (Bate and Quinta da Fonseca, 2004; Delannay et al., 2009). An extended review on CPFEM models is given by Roters et al. (Roters et al., 2010).

In this chapter, we consider either the restricted glide ({110}<111>) or the pencil glide ({110}<111>+{112}<111>+{123}<111>) as the slip modes (Becker, 1995; Liao et al., 1998; Raabe, 2005a,b; Raabe and Lücke, 1993). We also show that the bi-plane slip mode ({110}<111>+{112}<111>) yields results similar to the pencil glide case. In this chapter, as in the work of Raabe (1995a), we do not consider the twinning

mechanism. We should note that the assumption used here for pencil glide is more restrictive than the real {hkl}<111> pencil glide.

The evolution of texture in BCC metals under cold rolling boundary conditions is simulated using the VPSC model (Molinari et al., 1987) and the intermediate ϕ-model (Ahzi and M'Guil, 2008). We also present the results of the predicted yield loci of rolled BCC metals. The visco-plastic Taylor model and the visco-plastic Static model are also used to define the upper and lower bound estimates of the results. The results of the VPSC model are also presented for comparison with those obtained with the intermediate ϕ-model. The results are compared and discussed in terms of predicted textures, slip activity and yield loci.

Moreover, we present a comparison of our predicted texture results with various experimental BCC cold rolling textures, taken from the literature, for the electrical steels FeCr/FeSi (e.g. Fe3%Si) (Hölscher et al., 1991), ferritic steels (e.g. Fe16%Cr and Fe11%Cr) (Raabe and Lücke, 1993), IF-steels (Bate and Quinta da Fonseca, 2004; Nicaise et al., 2011; Wang et al., 2006) and low carbon steel (Raabe, 2005b). The comparison study shows that the ϕ-model predictions are in accord with the experimental results for BCC metals. In particular, the evolution of the α-fiber is predicted during the cold rolling process as function of the parameter ϕ, which also means for different interaction strengths (from a stiff to a more compliant interaction). We also analyzed the evolution of the α-fiber as function of the rolling reduction ratio and number of available slip systems (restricted slip systems versus pencil glide). We show that the ϕ-model could predict a very large and sensitive range of cold rolling texture transitions as well as the corresponding yield loci. Lastly, we show that the pencil glide assumption yields predicted results that are in a better agreement with experimental results in the literature for low carbon and IF steels. On the other hand,

the restricted slip assumption is well suited for ferritic and electrical steels. The results shown in this chapter can be found in the work of M'Guil et al. (2011b).

V.2 Application and results for plane strain compression (cold rolling)

V.2.1 Slip systems for BCC metals

For the BCC crystallographic structure, the slip mainly occurs on the <111> direction. In this work, we considered the restricted {110}<111>, the bi-plane {110}<111>+{112}<111>, or the pencil glide {110}<111>+{112}<111>+{123}<111> slip modes (Liao et al., 1998; Raabe, 1995a,b; Tikhovskiy et al., 2008). Since using two ({110}<111>+{112}<111>) or three slip modes (pencil glide) give very similar results, we do not present results obtained with two slip modes. Consequently, we only present results for the restricted slip and pencil glide. As in the work of other authors (Bate and Quinta da Fonseca, 2004; Raabe, 2005a), we assumed the same initial critical resolved shear stress for all of these slip families.

V.2.2 Ideal cold rolling texture for BCC metals

The cold rolling texture of BCC metals could be described in terms of fibers. Some important fibers and ideal rolling texture components for BCC metals are presented in Tab. 5-1. In general, for BCC metals under cold rolling, the typical crystallographic texture components include the fibers α and γ. Fig. 5-1 and Tab. 5-2 show the corresponding location of these two fibers and other ideal components in the Euler space. In this study, we particularly focused on the α-fiber (crystallographic fiber axis <110> parallel to the rolling direction including the major components: {001}<110>, {112}<110> and {111}<110>) and the γ-fiber (crystallographic fiber

axis <111> parallel to the normal direction including the major components {111}<110> and {111}<112>).

Fiber name	Fiber axis	Important texture components
α-fiber	<110> parallel to RD	{001}<110>, {112}<110>, {111}<110>
γ-fiber	<111> parallel to ND	{111}<110>, {111}<112>
η-fiber	<001> parallel to RD	{001}<100>, {011}<100>
ζ-fiber	<011> parallel to ND	{011}<100>, {011}<211> {011}<111>, {011}<011>
ε-fiber	<011> parallel to TD	{001}<110>, {112}<111>, {4411}<11118>, {111}<112>, {11118}<4411>, {011}<100>
θ-fiber	<001> parallel to ND	{001}<100>, {001}<110>
β-skeleton line	≈<111> close to ND	{111}<110>, {557}<583>, {111}<112>

Tab. 5-1. Some important fibers and texture components for crystallographic textures of BCC alloys (RD : rolling direction, ND : normal direction and TD : transverse direction) (Engler et al., 2000)

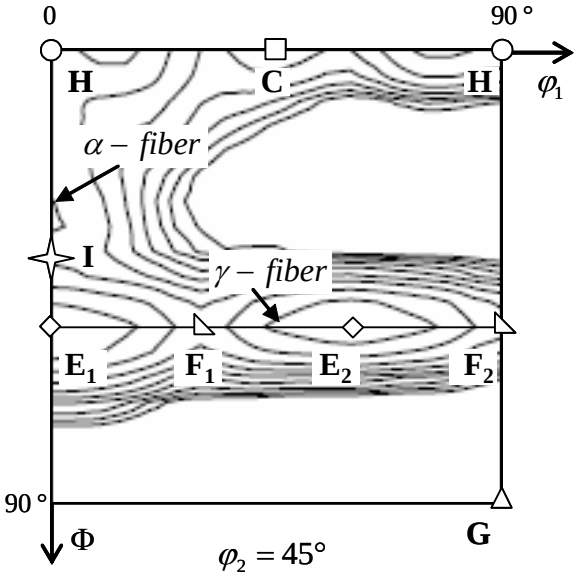

Fig. 5-1. Description of α-fiber and γ-fiber (Engler et al., 2000)

Components	{hkl}<uvw>	φ_1	Φ	φ_2
C	{001}<100>	45 °	0 °	45 °
H	{001}<110>	0 °	0 °	45 °
E_1	{111}<110>	0 °	55 °	45 °
E_2	{111}<110>	60 °	55 °	45 °
F_1	$\{111\}<11\bar{2}>$	30 °	55 °	45 °
F_2	$\{111\}<11\bar{2}>$	90 °	55 °	45 °
I	$\{112\}<\bar{1}10>$	0 °	35 °	45 °
G	{110}<001>	90 °	90 °	45 °

Tab. 5-2. Ideal rolling component for BCC metals

V.2.3 Parameters of the simulations

We consider an initial random texture represented by 500 orientations. We simulated plane strain compression test up to a total plastic strain $\varepsilon = 100\%$ corresponding to 63% cold rolling reduction. These simulations were conducted without strain hardening. However, the global conclusions do not change when strain hardening is used since the results follow a similar trend with or without hardening. The inverse strain rate sensitivity coefficient for the crystallographic slip is taken as $n = 11$. For the visco-plastic ϕ-model, we choose several values for ϕ : $\phi = 0.01$ (close to Taylor), $\phi = 0.1$, $\phi = 0.2$, $\phi = 0.5$, $\phi = 0.7$ and $\phi = 0.99$ (close to Static). For the VPSC code, we selected two values for n^{eff} : $n^{eff} = 1$ (secant formulation) and $n^{eff} = n$ (tangent formulation). The results obtained by the Taylor and Static models are also shown for comparison.

V.2.4 Results

V.2.4.1 Predicted cold rolling textures

For the restricted slip and pencil glide, Figs. 5-2 to 5-4 show the predicted rolling textures by the (100), (110) and (111) pole figures at $\varepsilon = 100\%$ for the tangent VPSC model (Fig. 5-2) and the ϕ-model ($\phi = 0.1$ in Fig. 5-3 and $\phi = 0.7$ in Fig. 5-4). In these figures, one may note significant differences between the restricted slip results and pencil glide results for all models. In addition, one may also observe the development of the two fibers α and γ with some differences between the models.

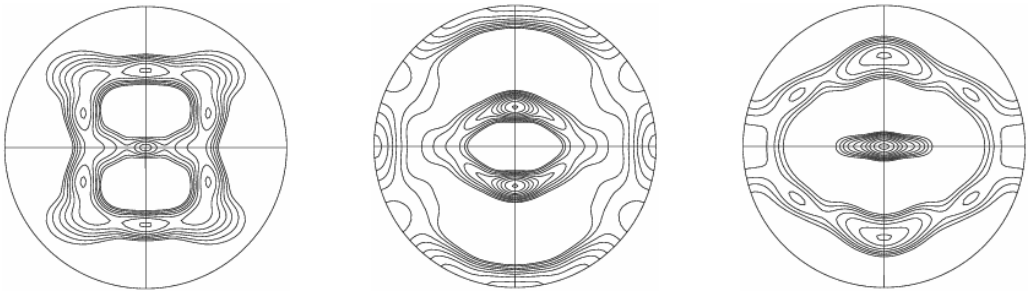

(100) (110) (111)

Max intensity: 6.4 Max intensity: 6.4 Max intensity: 8.0

a) tangent VPSC model using restricted slip

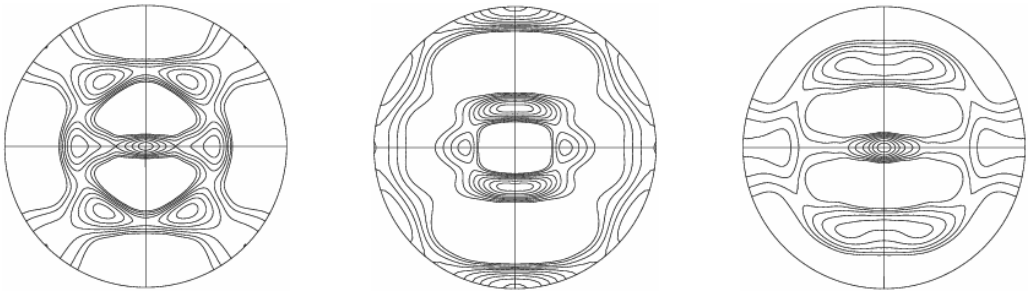

(100) (110) (111)

Max intensity: 6.4 Max intensity: 6.4 Max intensity: 16.

b) tangent VPSC model using pencil glide

Fig. 5-2. Predicted texture for the tangent VPSC model at $\varepsilon = 100\%$ for restricted slip (a) and pencil glide (b)

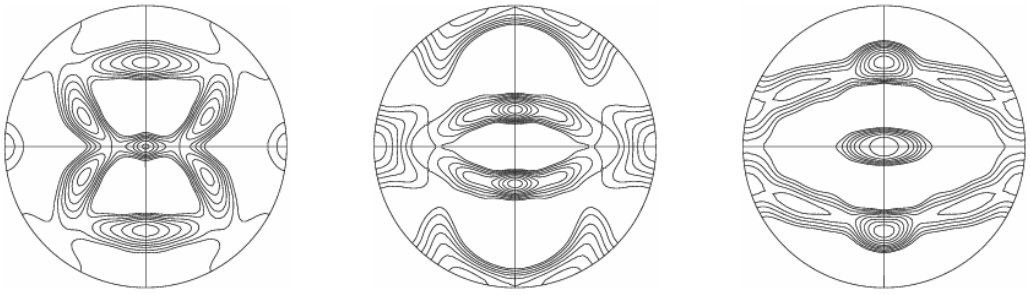

(100) (110) (111)

Max intensity: 6.4 Max intensity: 6.4 Max intensity: 6.4

a) $\phi = 0.1$ using restricted slip

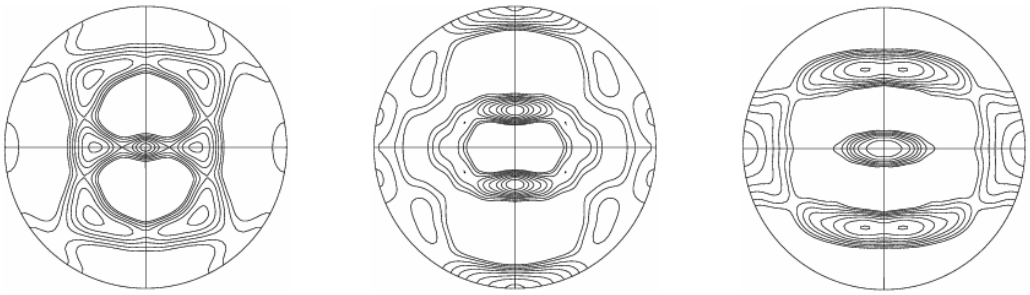

(100) (110) (111)

Max intensity: 6.4 Max intensity: 6.4 Max intensity: 6.4

b) $\phi = 0.1$ using pencil glide

Fig. 5-3. Predicted texture for $\phi = 0.1$ (ϕ-model) at $\varepsilon = 100\%$ for restricted slip (a) and pencil glide (b)

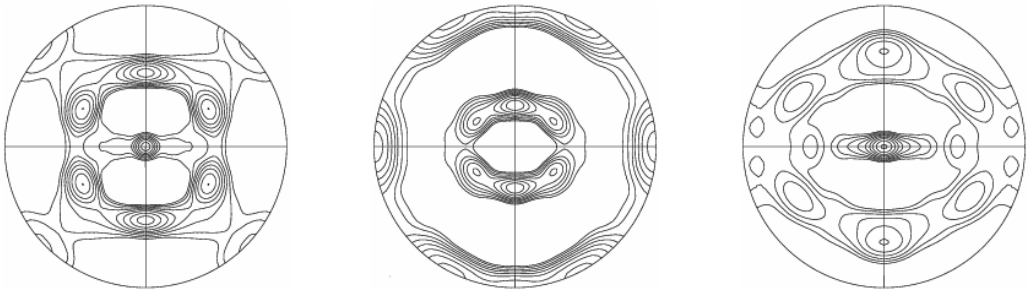

(100) (110) (111)

Max intensity: 6.4 Max intensity: 6.4 Max intensity: 16.

a) $\phi = 0.7$ using restricted slip

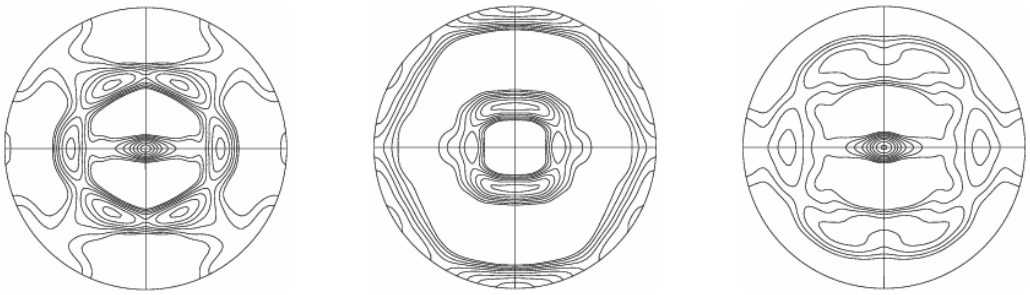

(100) (110) (111)

Max intensity: 6.4 Max intensity: 6.4 Max intensity: 16.4

b) $\phi = 0.7$ using pencil glide

Fig. 5-4. Predicted texture for $\phi = 0.7$ (ϕ-model) at $\varepsilon = 100\%$ for restricted slip (a) and pencil glide (b)

To quantitatively address the differences in predicted textures from these models, we plot the texture results in terms of orientation distribution function (ODF) sections (see Fig. 5-5).

For both restricted and pencil glide, Fig. 5-5 shows the ODF sections for $\varphi_2 = 45^\circ$ as predicted by the tangent VPSC model and by the visco-plastic intermediate ϕ-model ($\phi = 0.1$ and $\phi = 0.7$). On these figures, one can observe the development of the two fibers α and γ which correspond, more or less, to the ideal case. One may also note that the number of available slip systems (restricted or pencil) influences the evolution of these fibers. We can also see that the VPSC results are rather close to those predicted by the ϕ-model with $\phi = 0.7$.

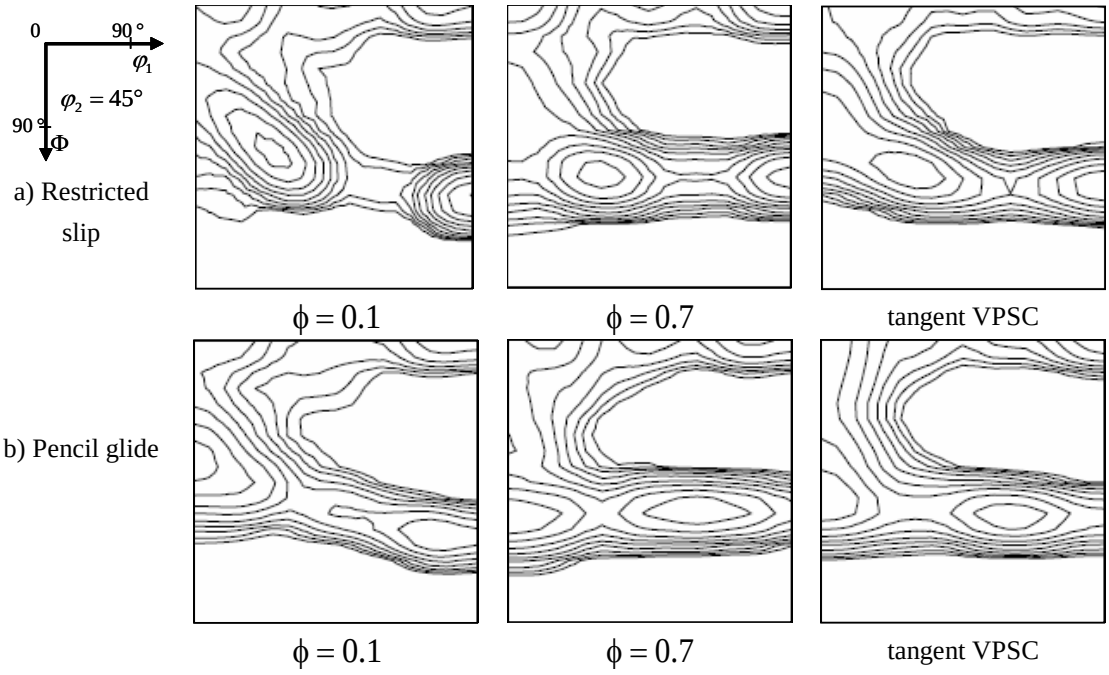

Fig. 5-5. ODF's sections for $\varphi_2 = 45°$ for the ϕ-model and tangent VPSC model for restricted slip (a) and pencil glide (b) at $\varepsilon = 100\%$ (Max intensity: 16.0)

To be more accurate in our comparison, for all models we plot the evolution of the intensity of the α-fiber (see Figs. 5-6a, 5-7a, 5-8 for restricted slip and Figs. 5-6b, 5-7b, 5-9 for pencil glide). We thus performed an analysis of the evolution of the α-fiber as function of the rolling reduction ratio for $\phi = 0.1$ (Figs. 5-8a and 5-9a), $\phi = 0.2$ (Figs. 5-8b and 5-9b), $\phi = 0.5$ (Figs .5-8c and 5-9c) and $\phi = 0.7$ (Figs. 5-8d and 5-9d). The predictions from the upper and lower bound models are also presented in Fig. 5-6 as well as those from the tangent VPSC model (Fig. 5-7).

For all models, the results show that the α-fiber increases continuously with strain. This result is in accord with the results of Raabe (1995b). These figures also show differences in the predictions of the evolution of the α-fiber as function of the considered slip systems (restricted versus pencil) for all models. However, these differences are more pronounced for the ϕ-model and the bounds. These differences are expressed in terms of intensity, number of "peeks" and location (i.e. shift along the Φ axis) of the α-fiber. We note that the particular orientation {001}<110> (H component) increases drastically under restricted slip for all models except the tangent VPSC. The relative insensitivity of the tangent VPSC model to the number of available slip systems is in accord with previous studies such as those of Raabe (1995b). Thus, as for FCC metals (Ahzi and M'Guil, 2008; M'Guil et al., 2009, 2011a), the ϕ-model is very sensitive and may be more appropriate to predict texture transition in BCC metals.

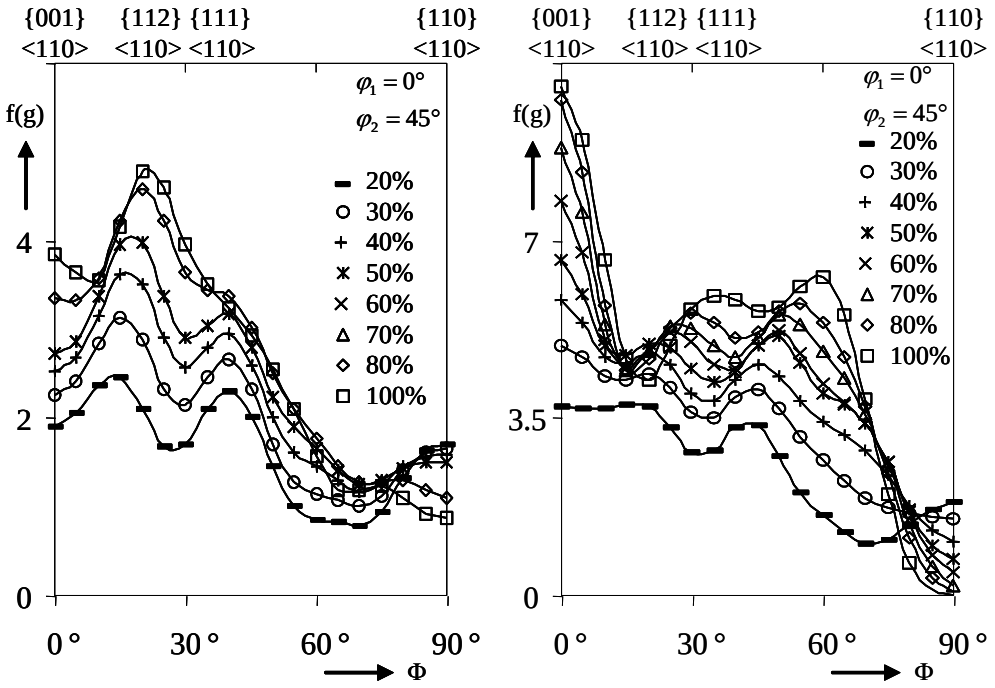

a_1) Taylor model a_2) Static model

a) Restricted slip

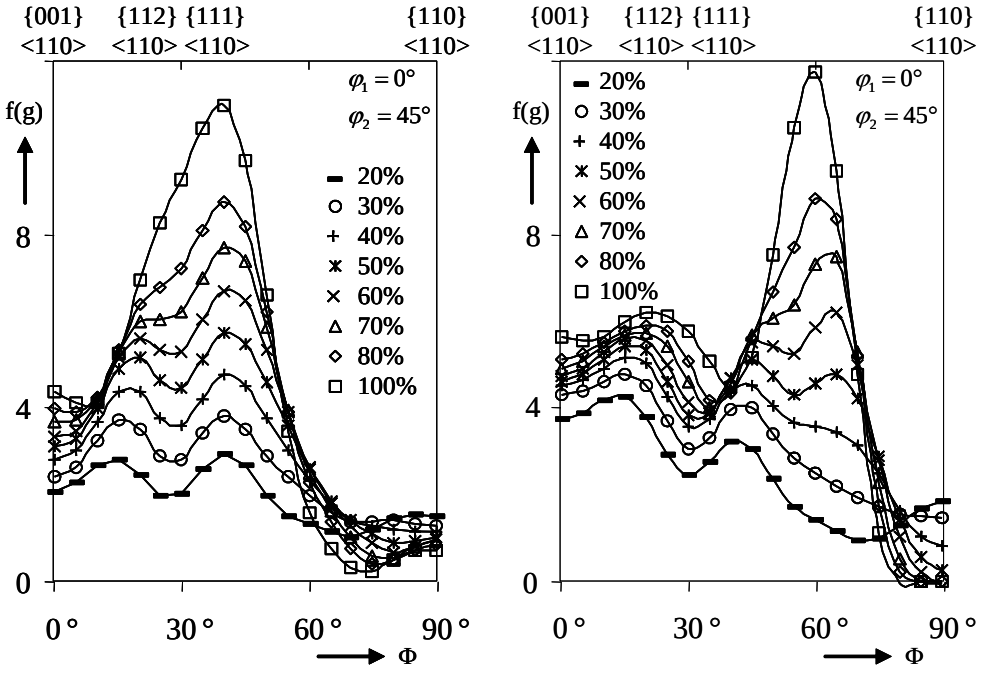

b_1) Taylor model b_2) Static model

b) Pencil glide

Fig. 5-6. Simulated evolution of BCC cold rolling texture (α-fiber) using restricted slip (a) and pencil glide (b) for Taylor and Static models

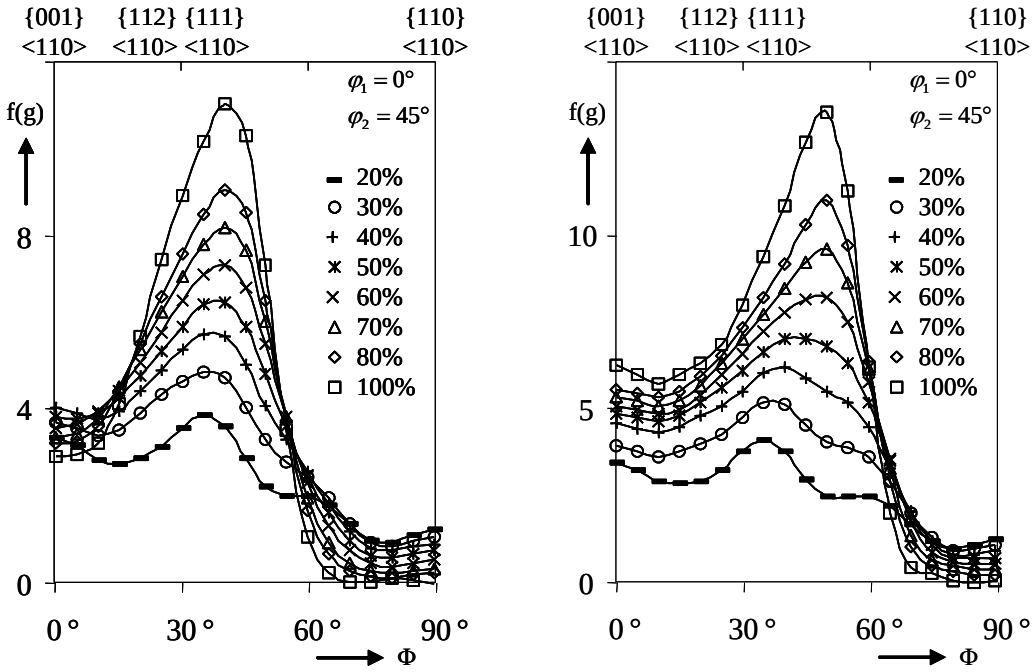

a) Restricted slip b) Pencil glide

Fig. 5-7. Simulated evolution of BCC cold rolling texture (α-fiber) using restricted slip (a) and pencil glide (b) for tangent VPSC model

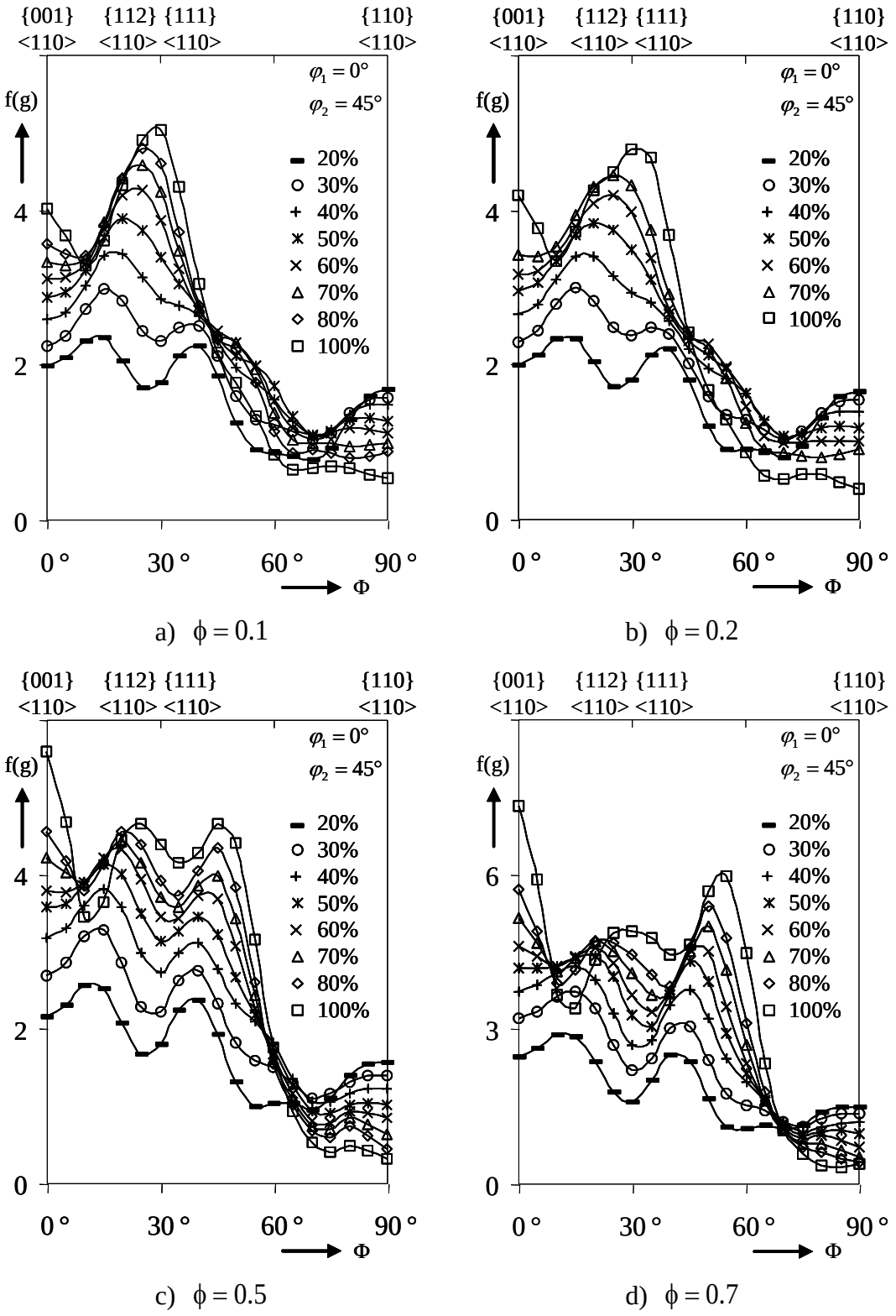

Fig. 5-8. Simulated evolution of BCC cold rolling texture (α-fiber) using restricted slip for ϕ-model: $\phi = 0.1$ (a), $\phi = 0.2$ (b), $\phi = 0.5$ (c) and $\phi = 0.7$ (d)

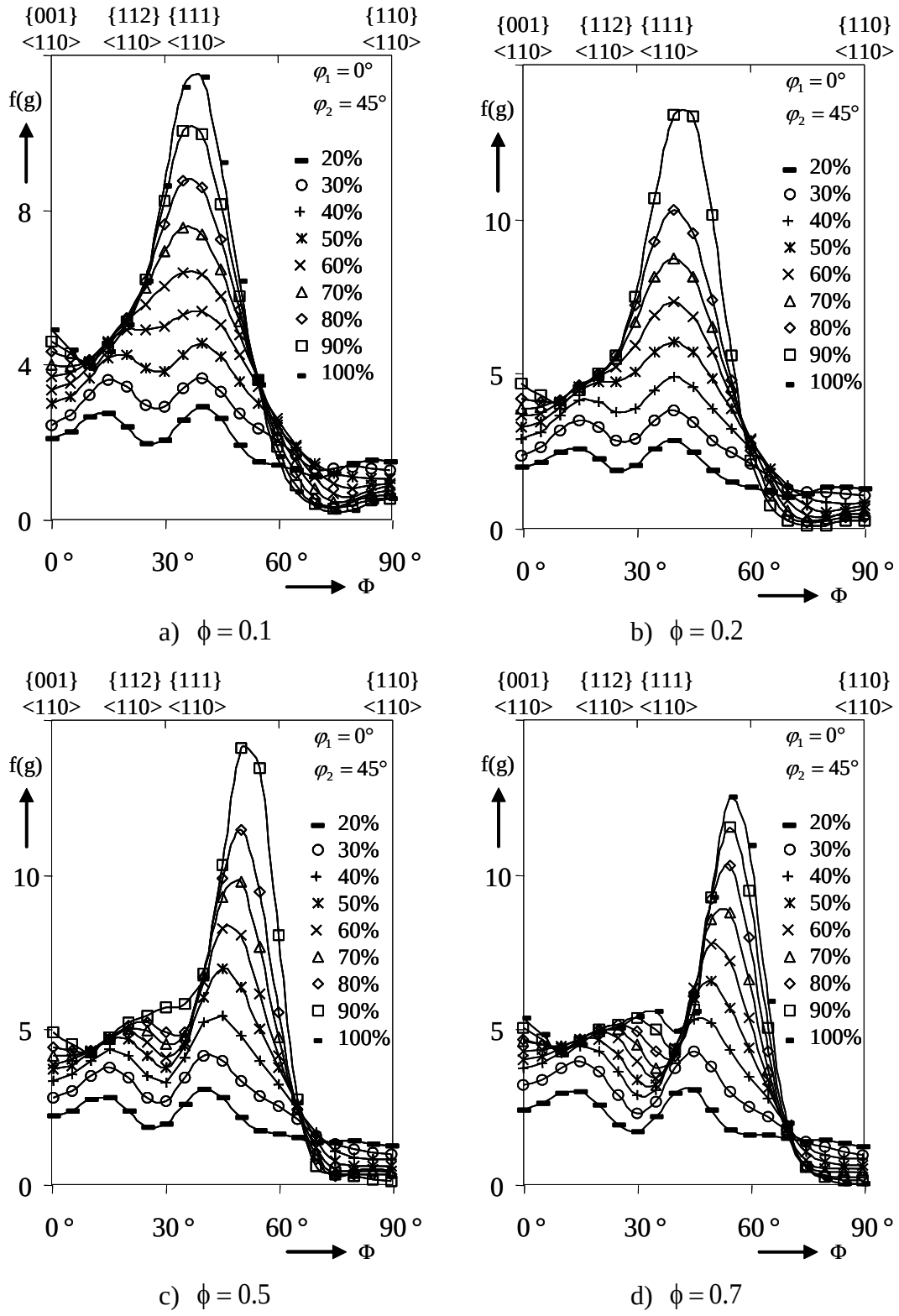

Fig. 5-9. Simulated evolution of BCC cold rolling texture (α-fiber) using pencil glide for ϕ-model: $\phi = 0.1$ (a), $\phi = 0.2$ (b), $\phi = 0.5$ (c) and $\phi = 0.7$ (d)

For all models, the case of pencil glide increases the intensity of the α-fiber. For example, the intensity increases from about 5.3 (for restricted glide) to about 11.36 (for pencil glide) for $\phi = 0.1$ (see Figs. 5-8a and 5-9a) and from about 5.94 to about 12.51 for $\phi = 0.7$ (see Figs. 5-8d and 5-9d). As expected, the intensity of the α-fiber, obtained with the tangent VPSC model, is less sensitive to the number of available slip systems: from about 10.91 to about 13.42 in intensity (see Fig. 5-7).

Fig. 5-10 shows the α-fiber and γ-fiber at $\varepsilon = 100\%$ for the Taylor, Static, ϕ-model ($\phi = 0.1$ and $\phi = 0.7$) and the tangent VPSC model. In the case of restricted slip, one can observe that the tangent VPSC model (Fig. 5-10a) predicts the highest intensity for the α-fiber. However, in the case of pencil glide, the prediction of the tangent VPSC model is rather close to that of the ϕ-model with $\phi = 0.7$ (see Fig. 5-10b).

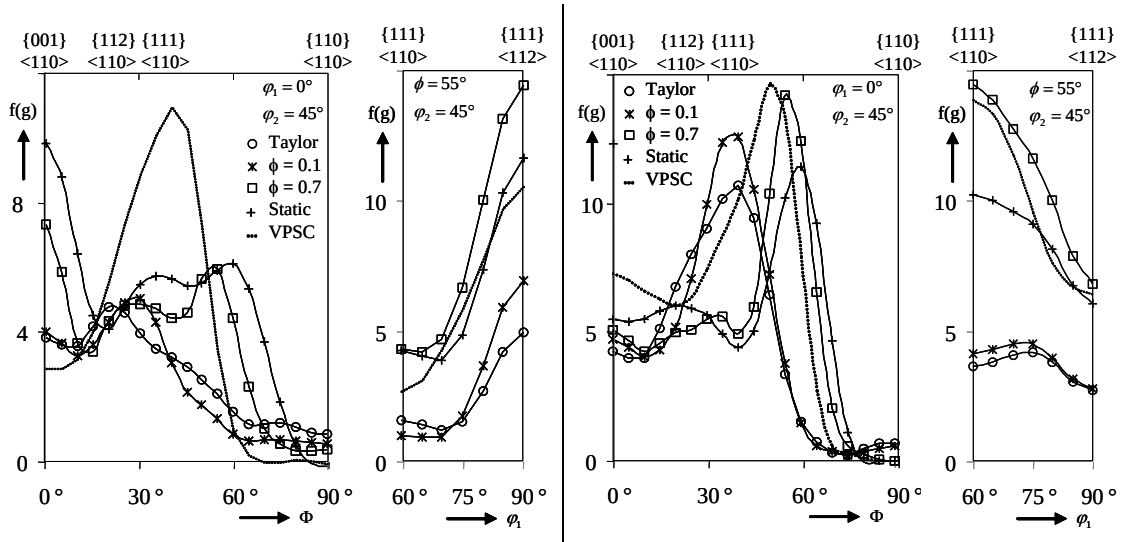

Fig. 5-10. Simulated evolution of BCC cold rolling texture (α-fiber and γ-fiber) for ϕ-model ($\phi = 0.1$, $\phi = 0.7$) and tangent VPSC model using restricted slip (a) and pencil glide (b)

To understand the contribution of each of the slip systems in the pencil glide to texturing, we plot the texture evolution (α-fiber) by considering each slip family (<112}<111> or {123}<111> or {110}<111>) separately. Theses textures are shown in Fig. 5-11 for 100% strain. With these results, and for the three considered intermediate models ($\phi = 0.1$, $\phi = 0.7$ and VPSC), one may rank the three slip families in the following decreasing contribution to texture development (in terms of intensity): {112}<111>, {123}<111> then {110}<111>.

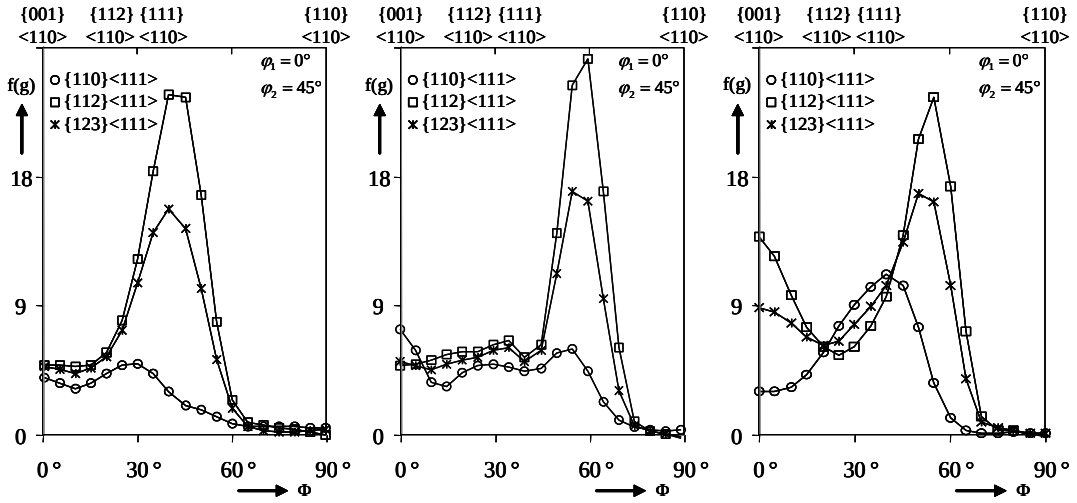

a) $\phi = 0.1$ b) $\phi = 0.7$ c) VPSC

Fig. 5-11. Contribution to texture development of slip systems for $\phi = 0.1$ (a), $\phi = 0.7$ (b) and tangent VPSC (c)

V.2.4.2 Computation of yield loci

Yield surfaces are commonly used to characterize the macroscopic yield behavior of polycrystalline metals. However, the yield loci cannot be well determined without considering the evolution of the microstructure such as the crystallographic texture. The detail of the computation of the yield loci with the ϕ-model is given in the work of M'Guil et al. (2011a) and briefly explained in the following. With the visco-plastic ϕ-model, the predicted polycrystal yield surfaces are generated by stopping the

simulations after 100% equivalent strain, under plane strain compression, and probing the polycrystalline aggregate by different loading directions, accounting for the actual texture at such deformation. In the case of restricted slip, Fig. 5-12 shows the corresponding predicted yield loci for the visco-plastic ϕ-model (Fig. 5-12a) and the VPSC model (Fig. 5-12b). In these figures, we can see that only the ϕ-model could predict a large range in size and shape of the yield loci for BCC metals as function of ϕ. This can be explained by the fact that the ϕ-model predicts a wide range of textures as function of ϕ.

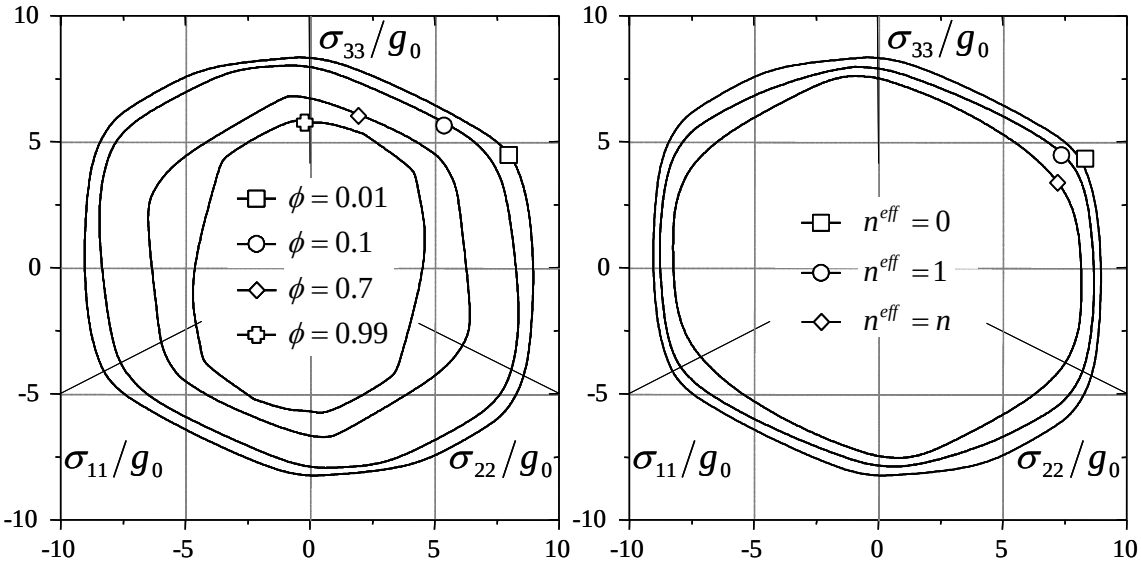

a) ϕ-model b) VPSC model

Fig. 5-12**.** Yield loci for restricted slip at $\varepsilon = 100\%$ for ϕ-model (a) and VPSC model (b)

For the visco-plastic ϕ-model, we have reported the effect of the pencil glide on the yield loci in Fig. 5-13. This figure shows the results obtained for $\phi = 0.1$ (Fig. 5-13a) and $\phi = 0.7$ (Fig. 5-13b). In these figures, the anisotropy decreases in the case of pencil glide. This is in agreement with other results in the literature (Liao and al., 1998). Liao and al. (1998) used the Taylor model and obtained results for the yield

surfaces, based on the <111> pencil glide, that present a smoother contour than those based on restricted slip.

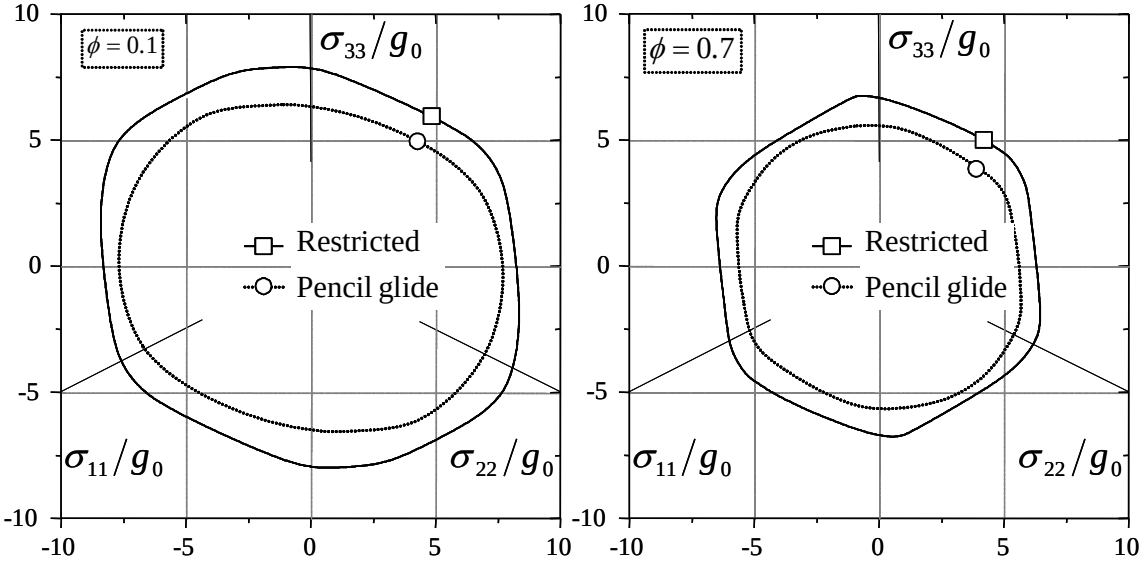

a) $\phi = 0.1$ b) $\phi = 0.7$

Fig. 5-13. Yield loci for the ϕ-model at $\varepsilon = 100\%$, $\phi = 0.1$ (a) and $\phi = 0.7$ (b)

V.2.4.3 Slip activity

In order to compare the slip activity, we have represented the variation of the number of active slip systems (based on a threshold shear rate) as a function of the equivalent plastic strain for both restricted slip and pencil glide (see Fig. 5-14). Similar slip activities are reported on these figures for ϕ-model (Fig. 5-14a) and the VPSC (Fig. 5-14b). The slip activity predicted by the VPSC approach shows a decrease of the number of slip systems as n^{eff} increases. For the ϕ-model, the slip activity decreases as we span from small to large values of ϕ. This leads to higher anisotropy (due to lower slip activity) which is observed on the corresponding yield loci as well (see Figs. 5-13).

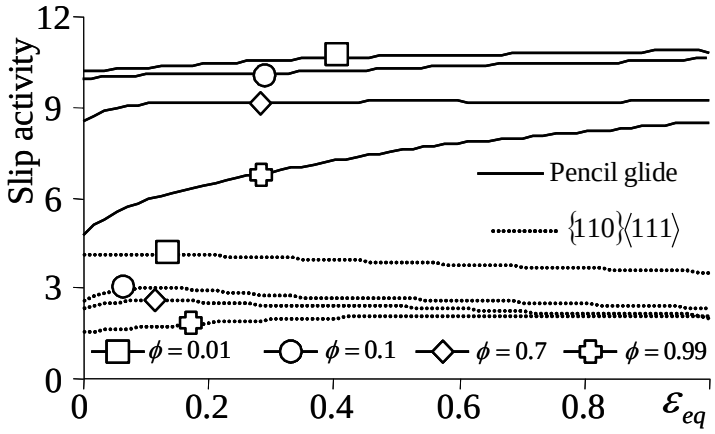

a) ϕ-model

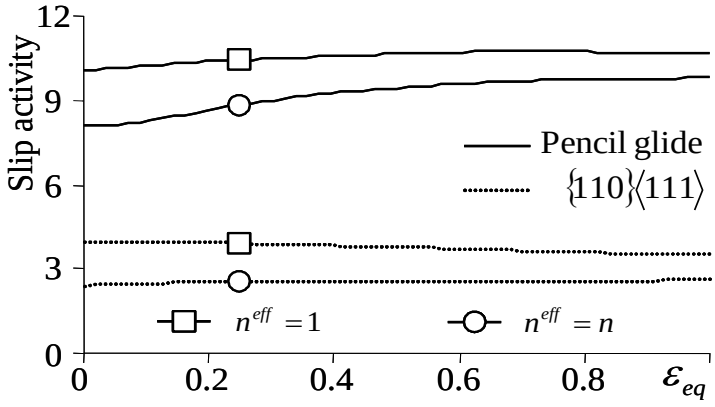

b) VPSC model

Fig. 5-14. Slip activity for the ϕ-model (a) and the VPSC model (b)

Fig. 5-15 represents the relative contribution, to deformation, of each of the three slip systems in the pencil glide for the ϕ-model ($\phi = 0.1$). The contribution of the {123}<111> is quite important compared to those of the {110}<111> and {112}<111> slip modes. When the three slip modes are simultaneously used, slip activity is dominated by the {123}<111> slip, since it has 24 systems, as opposed to 12 for each of the other two slip modes. The pencil glide offers an increase in kinematic freedom as was already reported by other authors (Liao et al., 1998). These previous studies showed that the <111> pencil glide increases the slip activity and thus reduces the anisotropy which can be seen on the yield loci shape and size evolution (see Fig. 5-13).

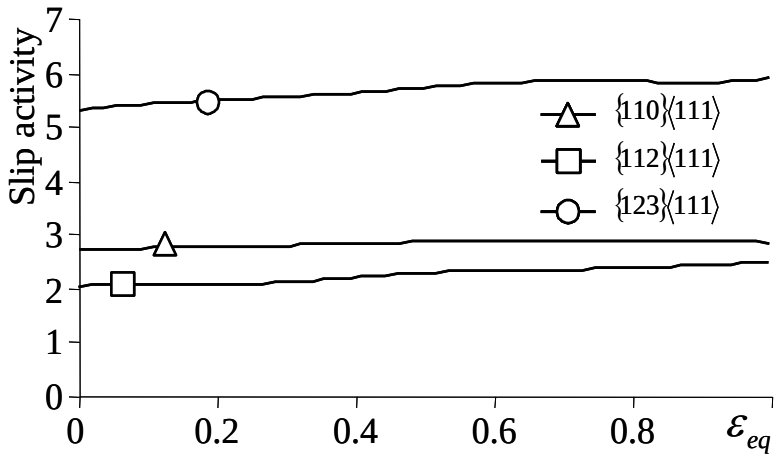

Fig. 5-15. Slip activity for the ϕ-model ($\phi = 0.1$)

V.3 Comparison to experimental results under cold rolling of BCC metals

In this section, we present a comparative study with experimental cold rolling textures (α-fiber) taken from the literature for a few BCC metals: electrical steels FeCr/FeSi (e.g. Fe3%Si) (Hölscher et al., 1991), ferritic steels: Fe16%Cr and Fe11%Cr (Raabe and Lücke, 1992), IF-steels (Bate and Quinta da Fonseca, 2004; Nicaise et al., 2011; Wang et al., 2006) and low carbon steel (Raabe, 2005b). This literature study of the experimental cold rolling textures of BCC metals allowed us to divide the comparison with our predicted results into two parts. The first part presents results where a good correlation with the ϕ-model predictions are obtained under restricted slip assumption. The second part presents results where a good correlation with the experimental results is obtained under pencil glide assumption. Since we do not have the exact input parameters such as the initial texture, test temperature, exact hardening law, our analysis may be regarded as a qualitative comparison. Moreover, we only analyze the cold rolling texture in the center of the sheets and neglect the through-thickness texture gradient of the rolled BCC steels. In this section, we focus on the analysis of the α-fiber at $\varepsilon = 90\%$ under plane strain compression. To

simplify our comparative analysis of texture development, we normalized the intensity of the α-fiber relative to the corresponding maximum intensity. The parameters of the simulations are the same as those described in the previous section.

V.3.1 Comparison under restricted slip assumption

In this section, we have digitalized the experimental α-fibers, taken from the literature, for ferritic steels (Fe16%Cr, Fe11%Cr) (Raabe and Lücke, 1992) and electrical steel FeCr/FeSi (e.g. Fe3%Si) (Hölscher et al., 1991). Fig. 5-16 presents the experimental and predicted α-fibers by the upper bound Taylor model and the ϕ-model ($\phi = 0.2$) for the electrical steel (Fig. 5-16a), the first ferritic steel Fe16%Cr (Fig. 5-16b), and the second ferritic steel Fe11%Cr (Fig. 5-16c). On these figures, we can observe that the ϕ-model predictions, under restricted slip assumption, are in a relative good agreement with the experimental α-fiber texture for these BCC metals. In particular, the ϕ-model predicts well the position of the maximal intensity of the α-fiber corresponding to the strongest texture component (i.e. {111}<110> orientation) in all of the three considered materials. We can also point out that the Taylor model is not able to correctly predict the exact position (on the Φ-axis) of this texture component of the α-fiber for these considered BCC metals (see Fig. 5-16).

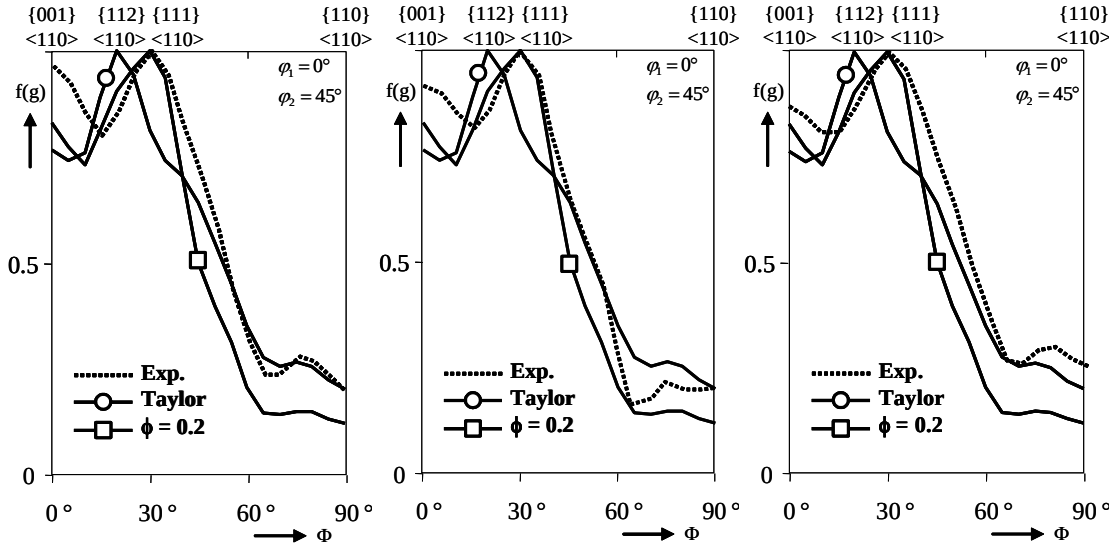

a) FeCr/FeSi b) Fe-16%Cr c) Fe-11%Cr

Fig. 5-16. Comparison to experimental α-fiber for FeCr/FeSi (Hölscher et al., 1991) (a), Fe16%Cr (Raabe and Lücke 1993) (b) and Fe11%Cr (Raabe and Lücke 1993) (c) (under restricted slip assumption)

We can conclude that for ferritic and electrical steels, the best correlation with experimental results for texture development is obtained under restricted slip assumption and for relatively small value of the parameter ϕ (around 0.2). However, we should note that the effects of microstructure (grain size, stacking fault energy, hardening…) may require some adjustment of the value of ϕ. For example, Raabe and Lücke (1993) have observe that increasing the Cr content in ferritic stainless steel causes a shift of the {112}<110> orientation to higher Φ angles on the α-fiber. The difference between the ferritic stainless steels is the content of Cr which also means different stacking fault energies.

V.3.2 Comparison under pencil glide assumption

In this part, we present results where the pencil glide assumption gives the best correlation with the experimental α-fiber. This is the case for IF-steels (IF-steel-1

(Hölscher et al., 1991), IF-steel-2 (Nicaise et al., 2011), IF-steel-3 (Wang et al., 2006)) and low carbon steels (Raabe, 1995b). This part is divided in two subsections: a first one where small values of ϕ yield a good correlation with experimental results and a second one where higher values of ϕ give a relatively good trend in comparison to experimental results.

V.3.2.1 Pencil glide assumption and small values of ϕ

The experimental α-fibers have been taken from the literature and digitalized for IF-steel-1 at $\varepsilon = 0.75$ (Hölscher et al., 1991) and low carbon steel (Raabe, 1995b) at $\varepsilon = 0.9$. Fig. 5-17 presents the comparison with the ϕ-model and the Taylor model for IF-steel-1 (Fig. 5-17a) and low carbon steel (Fig. 5-17b). For these BCC steels, the best correlation between experimental results and ϕ-model predictions is obtained for small values of ϕ ($\phi = 0.1$) under pencil glide assumption. In this figure, we can see that the ϕ-model predictions are very close to the experimental results for IF-steel-1 (see Fig. 5-17a) along the entire Φ-axis of the α-fiber. Moreover, the peak of the maximal intensity is better reproduced with the ϕ-model than with the Taylor model. A small shift towards higher Φ-axis is obtained with the Taylor model. For low carbon steel (Fig. 5-17b), a fair agreement with the experimental results is obtained along the Φ-axis for $\Phi > 30°$ by both Taylor and ϕ-model with $\phi = 0.1$. We see that in this case, the ϕ-model ($\phi = 0.1$) and the Taylor model predictions are very close. Nevertheless, for low carbon steel (see Fig. 5-17b), we note that the strong {001}<110> component is experimentally observed at large strain but is not correctly predicted by any model. Raabe (1995a) have already obtained this similar result for low carbon steel with a Taylor type modeling.

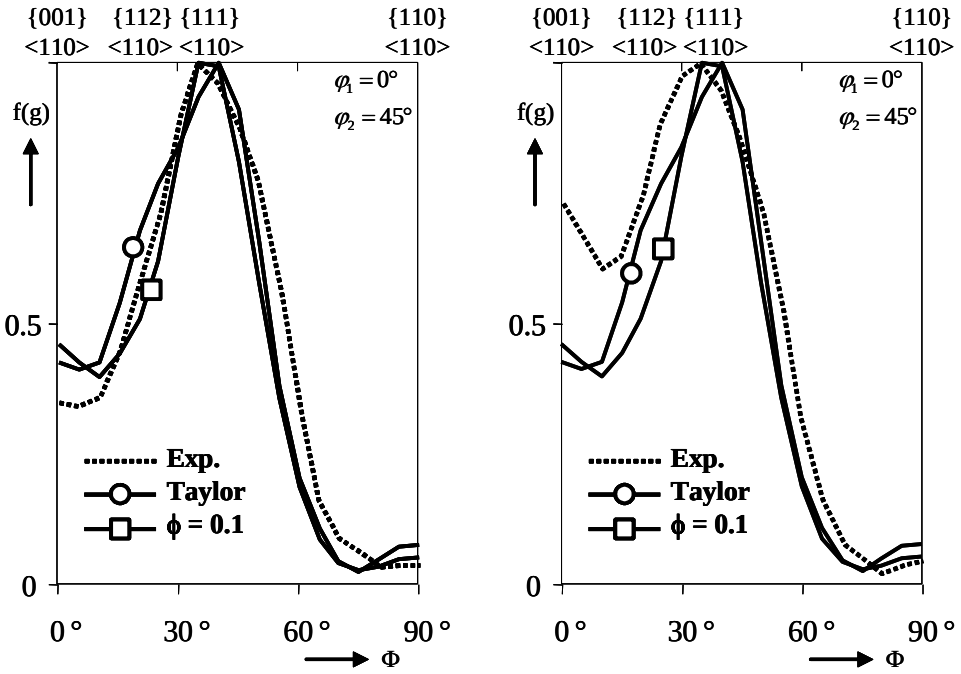

a) IF-steel-1 b) low carbon

Fig. 5-17. Comparison to experimental α-fiber for IF-steel-1 (Bate and Quinta da Fonseca, 2004) (a) and low carbon steel (Raabe, 1995b) (b) (under pencil glide assumption)

This qualitative comparison to the experimental results, for low carbon steel and IF-steel, shows that the pencil glide case gives the best rolling texture predictions than the restricted slip mode. This is in accord with previous studies which concluded that the pencil glide-based results can fit the experimental low carbon steel rolling texture better than the restricted slip-based predictions (Raabe. 1995a,b; Tikhovskiy et al., 2008). The herein considered low carbon steel has small globular grains of about $12\,\mu m$ size (Raabe, 1995b). M'Guil et al. (2009) have hypothesized that small values of ϕ may correspond to metals which have small grain size. The results from our current simulations, for low carbon steel, are thus in accord with this hypothesis.

To conclude, contrary to ferritic and electrical steels, the texture development in IF-steel-1 and low carbon steel is better predicted by the ϕ-model under pencil glide

assumption. In this subsection, the best correlation is obtained with small value of ϕ which is not the case of the next subsection.

V.3.2.2 Pencil glide assumption and large value of ϕ

From the literature, we have found a few experimental cases for which the ϕ-model predictions are in good accord with experimental α-fiber for higher values of ϕ and under pencil glide assumption. Among these materials are an IF-steel-2 and IF-steel-3. Fig. 5-18 shows the comparison of our simulations to these experimental ones. We can see that the best correlation with the experimental results is obtained for higher values of ϕ (between 0.5 and 0.7). The maximal intensity, around $\Phi = 50°$, is fairly predicted with the ϕ-model for $0.5 < \phi < 0.7$ as well as with the static model. However, we note that the ϕ-model predicts better the position of the peak on the Φ-axis (see Fig. 5-18a). The ϕ-model, with $\phi = 0.5$ and $\phi = 0.7$, predicts bounds for the peak along the Φ-axis.

The main difference between these experimental results (Fig. 5-18 for IF-steel 2 and 3) and the previous one (Fig. 5-17a for IF-steel 1) is the microstructure and the chemical composition of theses IF-steels (alloying element and percentage), as shown in Table 5-3. The IF-steel-2 and 3 seem to be more alloyed than the IF-steel-1. This difference in alloying may cause difference in the stacking fault energies which, in turn, leads to different texture developments.

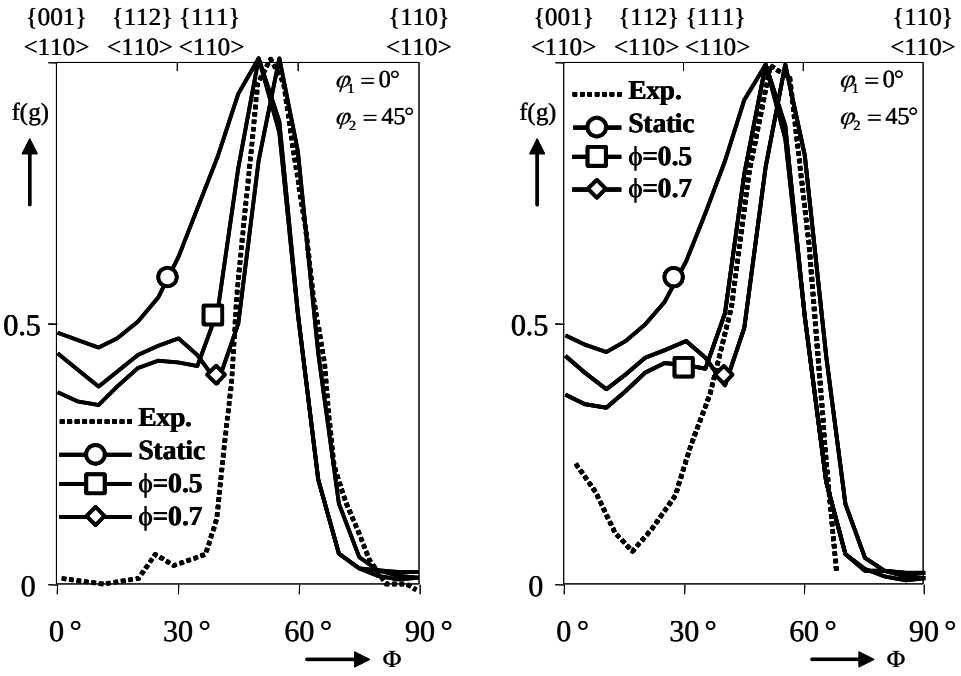

a) IF-steel-2 b) IF-steel-3

Fig. 5-18. Comparison to experimental α-fiber for IF-steel-2 (Nicaise et al., 2011) (a) and IF-steel-3 (Wang et al., 2006) (b) (under pencil glide assumption)

	C	N	Mn	Ti	Al	P	S	Si	Cu	Ni	Cr	Nb
IF-steel 1	0.003	0.003	0.15	0.08	0.05							
IF-steel 2	0.0016	0.0023	0.113	0.089	0.037	0.074	0.006	0.008	0.006	0.016	0.021	
IF-steel 3	0.004	0.0028	0.12	0.068	0.034	0.007	0.007	0.015				<0.005

Tab. 5-3. Chemical composition in weight percent of IF-steel-1 (Bate and Quinta da Fonseca, 2004), IF-steel-2 (Nicaise et al., 2011) and IF-steel-3 (Wang et al., 2006)

Ahzi and M'Guil (2008) and M'Guil et al. (2009) have hypothesized that higher values of ϕ may corresponds to metals which have lower stacking fault energy. On the other hand, small values of ϕ may correspond to polycrystals with high stacking fault energy. The results from our current simulations for If-steels seem to be in

accord with this hypothesis. However, we must note that the differences between the IF-steels' texture may be also explained by the differences in the mechanical processing and recrystallization, especially for IF-steel-3 (Wang et al., 2006) versus IF-steel-1 (Hölscher et al., 1991). In addition, grain size effects may also contribute to these texture differences as pointed out in the work of Nicaise et al. (2011). To conclude this part, we can note that the ϕ-model predictions under pencil glide assumption, for different values of ϕ, is well suited for low carbon steel and IF-steels.

V.4 Conclusion

With the visco-plastic ϕ-model, a large and sensitive range in the predictions of cold rolling textures of BCC metals can be obtained by simply varying the value of the parameter ϕ. Independently of the number of the available slip systems, one can note important differences in the predictions of the α-fiber as function of the value of ϕ. These differences are shown in terms of the intensity of the α-fiber, number of peeks and their positions along the Φ-axis of this fiber.

For BCC metals, taking into account the pencil glide, one may obtain predicted results closer to the experimental ones as already reported in the literature, especially for low carbon steels and IF-steels. However, for ferritic and electrical steels, the restricted slip assumption is well suited and gives predicted results closer to the experimental textures. The ϕ-model is thus able to predict texture transition in BCC metals as already shown for FCC metals by simply varying the value of the parameter ϕ. Our predicted yield surfaces reflect the effect of these texture transitions in BCC metals. Thus, the parameter ϕ controls the shape and size of these yield loci. In fact, the parameter ϕ scales the strength of the grain/aggregate interaction from a stiff (small values of ϕ) to a more compliant interaction (high values of ϕ).

In a future work, it is necessary to attempt to link the parameter ϕ to the microstructure of the considered metal's microstructure such as grain size and stacking fault energy. For instance in the particular case of BCC metals, one can try to directly link the shift of the α-fiber along the Φ-axis to the stacking fault energy. One may also analyze the evolution of the intensity of various preferential orientation as function of different microstructural features (grain size, stacking fault energy, …) for several BCC metals. This may help in developing a way for adjusting the parameter ϕ as function of these microstructural parameters.

References:

Ahzi, S., M'Guil, S., 2008. A new intermediate model for polycrystalline viscoplastic deformation and texture evolution. Acta Mater. 56, 5359-5369.

Bate, P.S., Quinta da Fonseca, J., 2004. Texture development in the cold rolling of IF steel. Mater. Sci. Eng. A 380, 365-377.

Becker, R., 1995. Pencil glide formulation for polycrystal modeling. Scripta Metall. Mater. 32, 2051-2054.

Delannay, L., Melchior, M.A., Signorelli, J.W., Remacle, J.-F., Kuwabara, T., 2009. Influence of grain shape on the planar anisotropy of rolled steel sheets - evaluation of three models. Comp. Mater. Sci. 45, 739-743.

Engler, O., Tomé, C.N., Huh, M.-Y., 2000. A study of through-thickness texture gradients in rolled sheets Metall. Mater. Trans. A 31, 2299-2315.

Hölscher, M., Raabe, D., Lücke, K., 1991. Rolling and recrystallization textures of bcc steels. Steel Research 62. 12, 567-575.

Hölscher, M., Raabe, D., Lücke, K., 1994. Relationship between rolling textures and shear textures in f.c.c. and b.c.c. metals. Acta Metall. Mater. 42, 879-886.

Jia, N., Peng, R.L., Wang, Y.D., Johansson, S., Liaw, P.K., 2008. Micromechanical behavior and texture evolution of duplex stainless steel studied by neutron diffraction and self-consistent modeling. Acta Mater. 56, 782-793.

Lee, B.J., Vecchio, K.S., Ahzi, S., Schoenfeld, S., 1997. Modeling the mechanical behavior of tantalum. Metall. Mater. Trans. 28, 113-122.

Liao, K.C., Friedman, P.A., Pan, J., Tang, S.C., 1998. Texture development and plastic anisotropy of B.C.C. strain hardening sheet metals. Int. J. Sol. Struct. 36, 5205-5236.

M'Guil, S., Ahzi, S., Youssef, H., Baniassadi, M., Gracio, J.J., 2009. A comparison of viscoplastic intermediate approaches for deformation texture evolution in FCC polycrystals. Acta Mater. 57, 2496-2508.

M'Guil, S., Ahzi, S., Barlat, F., Gracio, J.J., 2011a. Simulation of microstructural effects and yield surface evolution in cubic metals using the viscoplastic ϕ-model. Int. J. Plasticity 27, 102-120.

M'Guil, S., Wen, W., Ahzi, S., Gracio, J.J., 2011b. Modeling of large plastic deformation behavior and anisotropy evolution in cold rolled bcc steels using the viscoplastic ϕ-model-based grain-interaction. Mater. Sci. Eng. A 528, 5840-5853.

Nicaise, N., Berbenni, S., Wagner, F., Berveiller, M., Lemoine, X., 2011. Coupled effects of grain size distributions and crystallographic textures on the plastic behaviour of IF steels. Int. J. Plasticity 27, 232-249.

Paquin, A., Berbenni, S., Favier, V., Lemoine, X., Berveiller, M., 2001. Micromechanical modeling of the elastic-viscoplastic behavior of polycrystalline steels having different microstructures. Int. J. Plast. 17, 1267-1302.

Raabe, D., 1995a. Simulation of rolling textures of b.c.c metals considering grain interactions and crystallographic slip on {110} {112} and {123} planes. Mater. Sci. Eng. A 197, 31-37.

Raabe, D., 1995b. Investigation of contribution of {123} slip planes to development of rolling textures in bcc metals by use of Taylor models. Mater. Sci. Tech. 11, 455-460.

Raabe, D., 1995c. Textures of strip cast and hot rolled ferritic and austenitic stainless steel. Mater. Sci. Tech. 11, 461-468.

Raabe, D., 1996. Taylor simulation and experimental investigation of rolling textures of polycrystalline iron aluminides with special regard to slip on {112} planes. Acta Mater. 44, 937-951.

Raabe, D., 1997. Texture and microstructure evolution during cold rolling of a strip cast and of a hot rolled austenitic stainless steel. Acta Mater. 45, 1137-1151.

Raabe, D., Lücke, K., 1992. Texture and microstructure of hot rolled steel. Scr. Metall. Mater. 26, 1221-1226.

Raabe, D., Lücke, K., 1993. Textures of ferritic stainless steels, Mater. Sci. Techn. 9, 302-312.

Raabe, D., Roters, F., Y. Wang, 2005a. Simulation of earing during deep drawing of bcc steel by use of a texture component crystal plasticity finite element method. Mater. Sci. Forum. 495-497, 1529-1534.

Raabe, D., Wang, Y., Roters, F., 2005b. Crystal plasticity simulation study on the influence of texture on earing in steel. Comp. Mater. Sci. 34, 221-234.

Raphanel, J.L., Van Houtte, P., 1985. Simulation of the rolling textures of b.c.c. metals by means of the relaxed taylor theory. Acta Metall. 33, 1481-1488.

Roters, F., Eisenlohr, P., Hantcherli, L., Tjahjanto, D.D., Bieler, T.R., Raabe, D., Overview of constitutive laws, kinematics, homogenization and multiscale methods in crystal plasticity finite-element modeling: Theory, experiments, applications. Acta Mater. 58 (2010) 1152-1211.

Tikhovskiy, I., Raabe, D., Roters, F., 2006. Simulation of the deformation texture of a 17%Cr ferritic stainless steel using the texture component crystal plasticity finite element method considering texture gradients. Scripta Mater. 54, 1537-1542.

Tikhovskiy, I., Raabe, D., Roters, F., 2008. Simulation of earing of a 17% Cr stainless steel considering texture gradients. Mater. Sci. Eng. A 488, 482-490.

Wang, Z.D., Guo, Y.H., Sun, D.Q., Liu, X.H., Wang, G.D., 2006. Texture comparison of an ordinary IF steel and a high-strength IF steel under ferritic rolling and high-temperature coiling. Mater. Chara. 57, 402-407.

Chapter VI. Application to HCP metals: deformation behavior and texture evolution in magnesium alloy

VI.1 Introduction

As light weight structural materials, several hexagonal metals have been used in industries mainly for a significant reduction of weight. For example, magnesium and its alloys, with a low density, have been used as structural components in automotive, computer, communication and consumer electronic appliances (Wang and Huang, 2003). Another example is titanium and its alloys, applied in high performance engineering industries such as aerospace industry. Zirconium alloys, also hexagonal materials, are used as cladding materials in nuclear reactor fuels.

The main challenges of hexagonal metals as structural materials are the limited ductility and the poor room temperature formability, which are primarily due to the restricted number of slip systems (Agnew and Duygulu, 2005; Parks and Ahzi, 1990; Scheonfeld et al., 1995). At room temperature, hexagonal materials possess fewer easy glide systems than cubic metals, resulting in greater crystal anisotropy. However, at high temperatures and moderate strain rates, hexagonal metals can be ductile and readily formable due to lower flow resistance and the activation of addition slip systmes.

The main crystallographic slip families in hexagonal close-packed (HCP) structures are the basal $\langle a \rangle$, prismatic $\langle a \rangle$ and pyramidal $\langle a \rangle$ slip systems. The first- and the second-order pyramidal $\langle c+a \rangle$ slip systems occur mainly at high temperature and were held responsible for the good elevated temperature ductility of HCP metals such as magnesium alloys. The $\langle a \rangle$ slip comprises only four independent slip systems and, thus, cannot accommodate plastic deformation in the crystallographic c direction of the single crystal. The basal $\langle a \rangle$ and the prismatic $\langle a \rangle$ planes are mutually orthogonal. However, because the $\langle 11\bar{2}0 \rangle$ (or $\langle a \rangle$) slip directions are perpendicular to the c-axis and confined to the basal plane, there are only two independent slip

systems of each type. Thus, basal $\langle a \rangle$ and prismatic $\langle a \rangle$ slips together possess only four independent slip systems. Therefore, HCP metals are often nearly inextensible along their c-axis. Pyramidal $\langle c+a \rangle$ systems, if activated, will provide the additional fifth independent slip system, necessary for the accommodation of an arbitrary plastic deformation. However, the slip resistance of pyramidal $\langle c+a \rangle$ slip systems are usually much higher than those of basal and prismatic systems. Even when five independent slip systems are available, the difference of the critical resolved shear stresses between different deformation mechanisms (basal, prismatic and $\langle c+a \rangle$ pyramidal) can be large enough to introduce an important plastic anisotropy at the single crystal level. Therefore, the mechanical behavior of HCP metals is controlled by the relative strengths and substantially different hardening responses of the various slip modes (Francillette et al., 1998; Fundenberger et al., 1997). The schematic diagram of these slip and twinning systems are presented in Fig. 6-1.

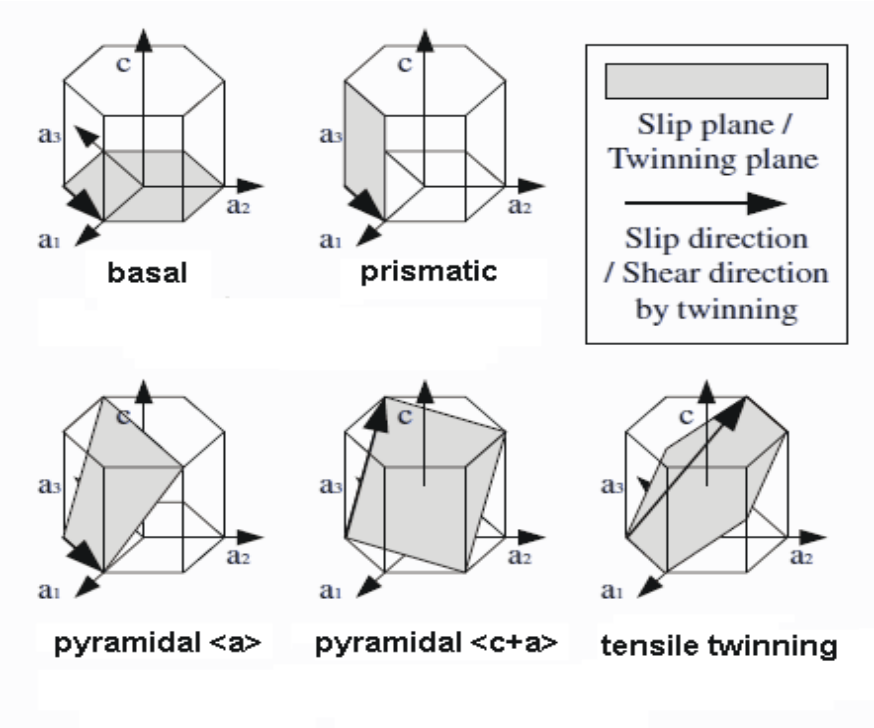

Fig. 6-1. Schematic diagram of slip and twinning systems in HCP metals (Mayama et al., 2009).

For many HCP crystals, the resistance to plastic shearing can vary by an order of magnitude (or even higher) from one mechanism to another (Francillette et al., 1998; Fundenberger et al., 1997). A random aggregate of such crystals will deform only by their soft modes (e.g. $\langle a \rangle$ slip). As the deformation proceeds, the aggregate becomes highly textured (elastically stiff) and the activation of the hard modes is possible only after a high degree of alignment that leads to materials' locking, resulting into microcraking and materials failure.

It is well known that in addition to crystallographic slip from dislocation movement, HCP materials exhibit a greater tendency to mechanically twin than cubic materials. In the absence of pyramidal $\langle c+a \rangle$ slip, twinning may supplement the $\langle a \rangle$ slip for full kinematic freedom. Twinning provides additional deformation which relaxes the requirements for five independents slip modes and may help a material to satisfy the Taylor criterion (Agnew et al., 2001; Brown et al., 2005; Kocks and Westlake, 1967). However, as a polar mechanism (Agnew and Duygulu, 2005), twinning depends strongly on temperature, alloying content, stacking fault energy and crystal lattice structure. It makes the modeling of the interaction between slip and twinning complicated (Prantil et al., 1995). At low temperature, twinning will compete with slip to accommodate the crystal motion. In warmer processing regimes, however, twinning may become less favorable deformation mechanism than slip.

Polycrystals plasticity and texture evolution of hexagonal materials are characterized by the diversity of possible deformation mechanisms such as basal slip, prismatic slip, pyramidal slip and several twinning modes. The low symmetry nature of these polycrystals may presents high anisotropy, kinematic deficiencies, and associated locking nature at high strains. The difficulty of modeling of the plastic behavior of HCP metals is mainly due to the fact that less than five independent soft modes are

available owing to the hexagonal symmetry of the lattice cell. In other words, hard glide systems should be activated to accommodate any arbitrary deformation (Kocks, 1970).

Several crystal plasticity models have recently been used to simulate the mechanical deformation behavior and texture evolution of HCP metals such as the Taylor type model (e.g. Inal and Mishra, 2012), fast Fourier transforms model (e.g. Lebensohn et al., 2012) and self-consistent type model (e.g. Brown et al., 2012; Oppedal et al., 2012; Wang et al., 2012). We note that self-consistent approaches, such as the VPSC approach (Molinari et al., 1987, Tomé et al. 1987), are well-suited to HCP crystals since the hard systems may not be activated as long as the polycrystal is not highly textured. This model has been applied by several authors to a wide variety of hexagonal metals and alloys, such as zirconium (Lebensohn and Tomé, 1993; Plunkett et al., 2006), titanium (Lebensohn and Canova, 1997; Suwas et al. 2011), and magnesium (Yi et al. 2006). In the work of M'Guil et al. (2006), the Sachs, the self-consistent and the Constrained-Hybrid models were utilized to predict texture evolution in a class of low symmetry crystals comprising less than five independent slip systems. In the previous work, the ϕ-model and the VPSC model have been used to simulate the deformation behavior of HCP metals deforming by both soft and hard slip modes (M'Guil et al., 2009). The ϕ-model is able to reproduce similar results as the VPSC model, particularly the plastic locking of HCP metals at high strains (see Fig. 6-2).

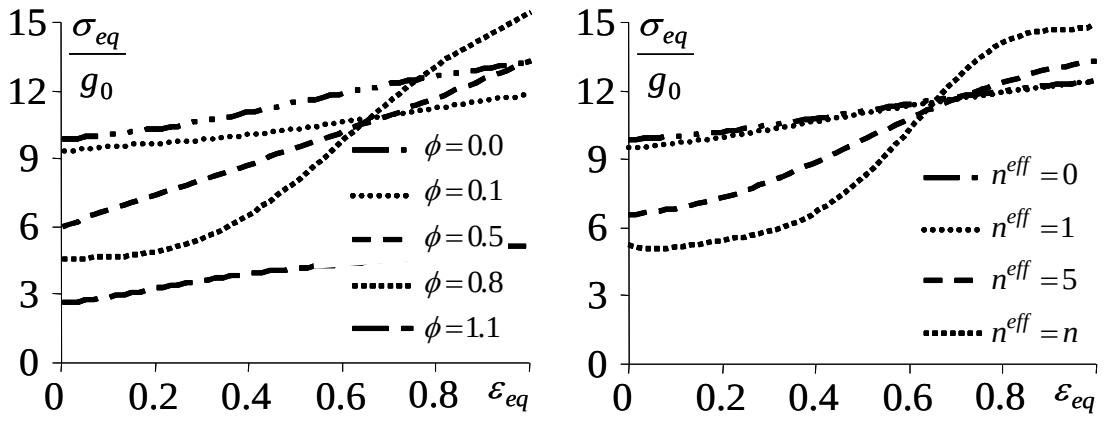

Fig. 6-2. Stress-Strain curves for (a) visco-plastic ϕ-model and (b) VPSC model (M'Guil et al., 2009)

In the first part of this chapter, the visco-plastic ϕ-model is used to predict the texture evolution of rolled Mg alloy sheet. Agnew et al. (2001) have proposed a simulation of rolled Mg alloy sheet using VPSC model with different relative activities of $\langle c+a \rangle$ pyramidal slip. We carry out similar simulation and compare our results with the ones of Agnew et al. (2011). In the second part, the ϕ-model is used for the analysis of texture evolution in HCP polycrystals with specific application to AZ31 magnesium alloy. In this alloy, the $\langle a \rangle$ slip (basal and prismatic) as well as the $\langle c+a \rangle$ pyramidal slip and tensile twinning are considered as the mechanisms of plastic deformation (Jain and Agnew, 2007; Proust et al., 2009; Styczynski et al., 2004; Wang et al., 2010). We have applied the ϕ-model to simulate rolling texture development using an initially isotropic polycrystal. Tensile and compressive deformation behaviors of a rolled sample are also simulated. Comparing with experimental results in the literature (Jain and Agnew, 2007; Styczynski et al., 2004; Ulacia et al., 2010a, b; Wang et al., 2010), simulation results using the ϕ-model are discussed in terms of the effect of interaction strength, via the ϕ parameter, on texture evolution and activation of different deformation mechanisms.

VI.2 Simulations

VI.2.1 Simulations of texture evolution of rolled Mg alloy: effect of relative activity of <c+a> pyramidal slip

VI.2.1.1 Simulations without prismatic slip

Agnew et al. (2001) have proposed an experiment study on rolled Mg alloys containing lithium (Li) or yttrium (Y). As shown in Fig. 6-2, a typical (0002) basal texture can be obtained from the rolled pure Mg. However, for the textures of Mg-1Y (1 wt% Y) and Mg-3Li (3 wt% Li), the basal poles have been spread and rotated towards the RD.

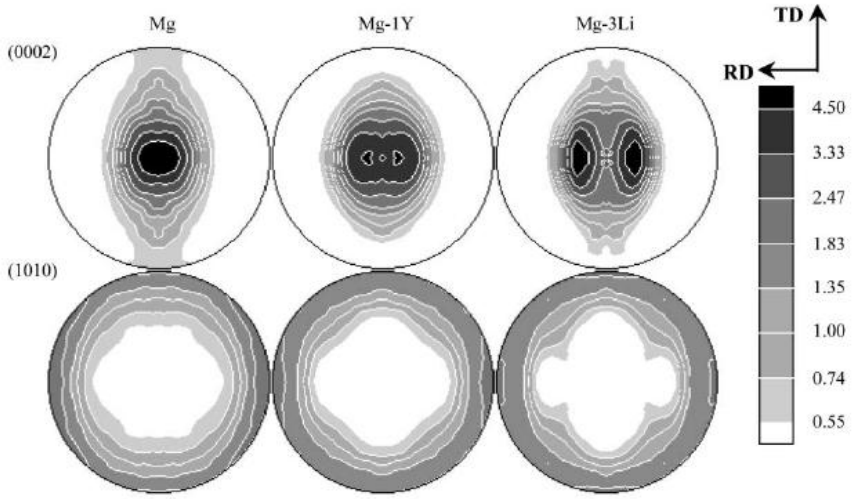

Fig. 6-2. Experimental (0002) and $(10\bar{1}0)$ textures for pure Mg, Mg-1Y and Mg-3Li under plane strain compression test at $\varepsilon_{true} = 30\%$ (Agnew et al., 2001).

Agnew et al. (2001) suggested that this texture transition can be predicted by varying the relative activity of pyramidal $\langle c+a \rangle$ slip.

✓ **Simulations with the VPSC model**

Agnew et al. (2001) carried out a simulation with the VPSC model. They considered the basal slip, pyramidal $\langle c+a \rangle$ slip and tensile twinning. In the simulation, the relative CRSS of these systems are set to be $\tau_{basal} : \tau_{<c+a>} : \tau_{tw} = 1 : X : 2$. The relative activity of pyramidal $\langle c+a \rangle$ slip is therefore controlled by the X value. In the work of Agnew et al. (2001), the X values of 12, 6 and 3 were chosen and the interaction parameter of the VPSC model was set to be 10 (see section I.3.5.3). The predicted results are shown in Fig. 6-3.

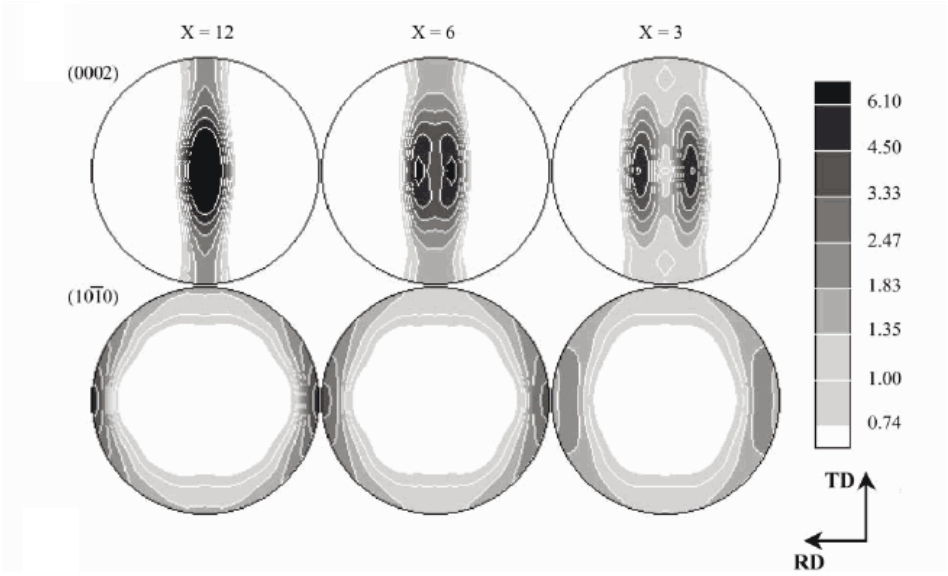

Fig. 6-3. Predicted rolling texture by Agnew et al. (2001). (0002) and $(10\bar{1}0)$ pole figures for X=12, 6 and 3 ($\tau_{basal} : \tau_{<c+a>} : \tau_{tw} = 1 : X : 2$), $\varepsilon_{eq} = 34\%$.

✓ **Simulations with the ϕ-model**

We carry out a similar simulation using the ϕ-model. The n value is set to be 11. The predicted results for various ϕ values are presented in Figs. 6-4 to 6-6. We can see that lower ϕ value leads to a stronger spread of basal poles towards RD in the (0001) pole figures. The spread of basal poles can be reduced by increasing the X value. The results for high ϕ values are close to the one predicted by Agnew et al. (2001).

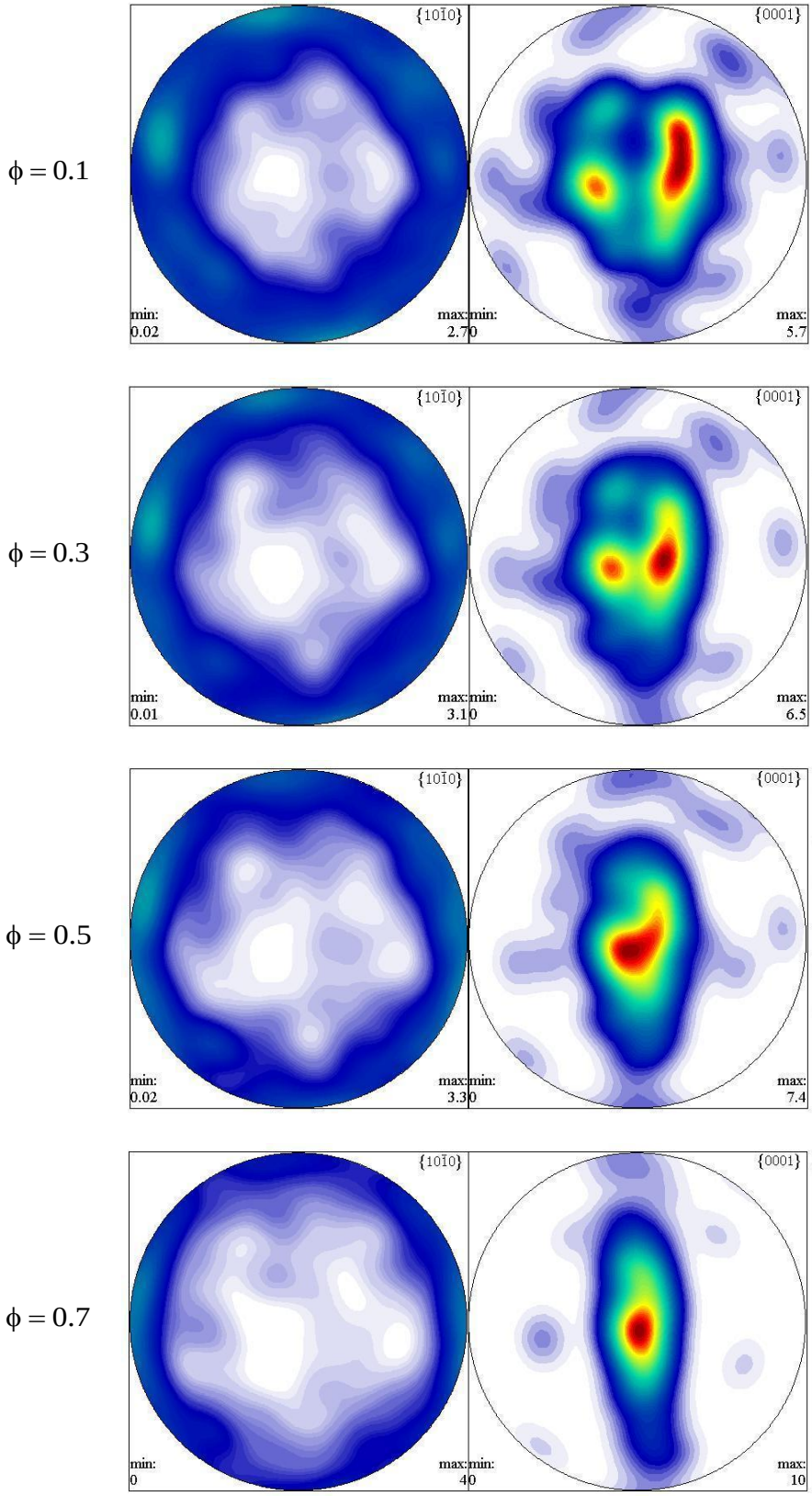

Fig. 6-4. Predicted rolling texture for X=12 ($\tau_{basal} : \tau_{<c+a>} : \tau_{tw} = 1 : X : 2$). (0002) and $(10\bar{1}0)$ pole figures using the ϕ-model, $\varepsilon_{eq} = 34\%$.

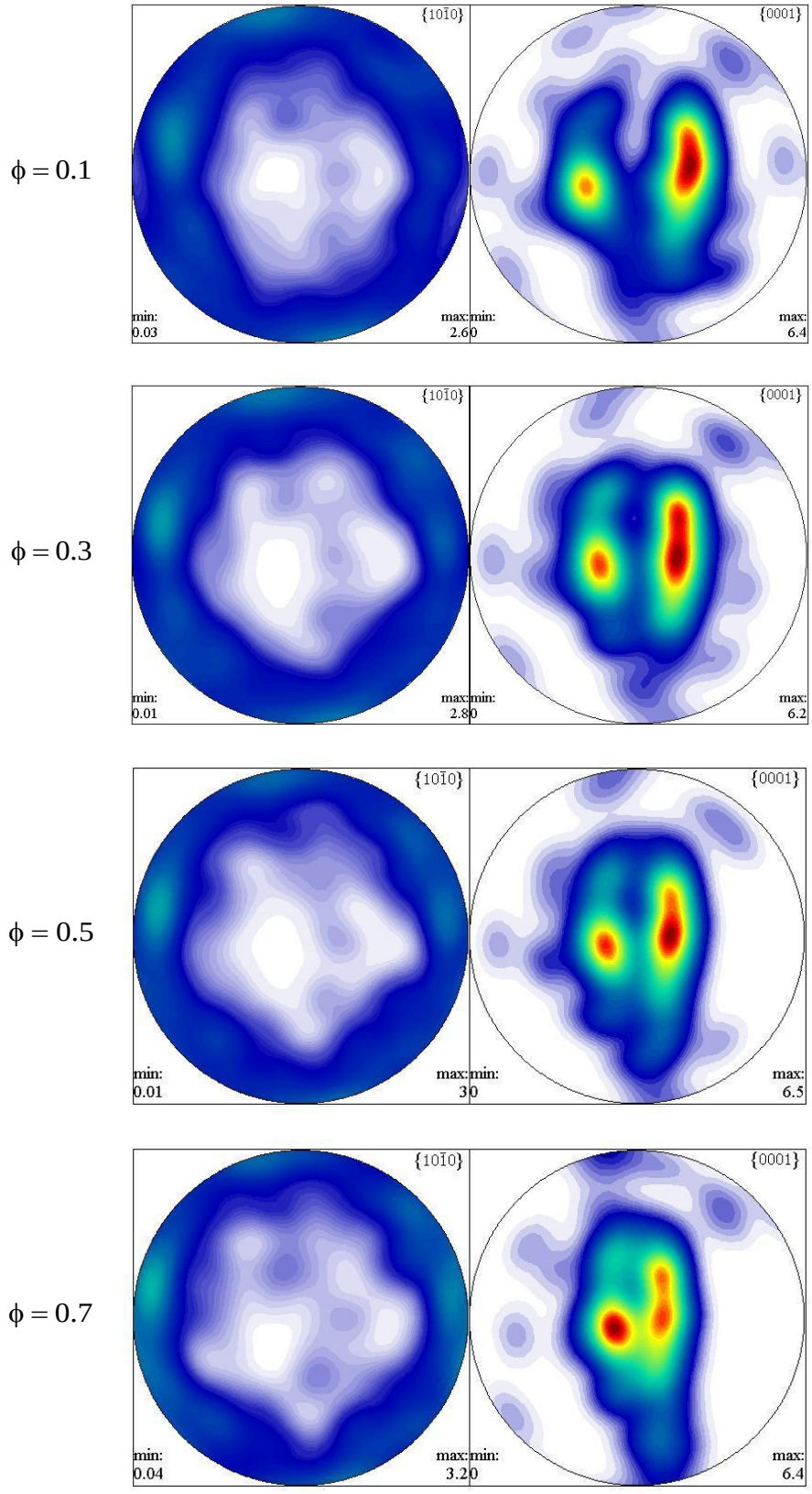

Fig. 6-5. Predicted rolling texture for X=6 ($\tau_{basal} : \tau_{<c+a>} : \tau_{tw} = 1 : X : 2$). (0002) and $(10\bar{1}0)$ pole figures using the ϕ-model, $\varepsilon_{eq} = 34\%$.

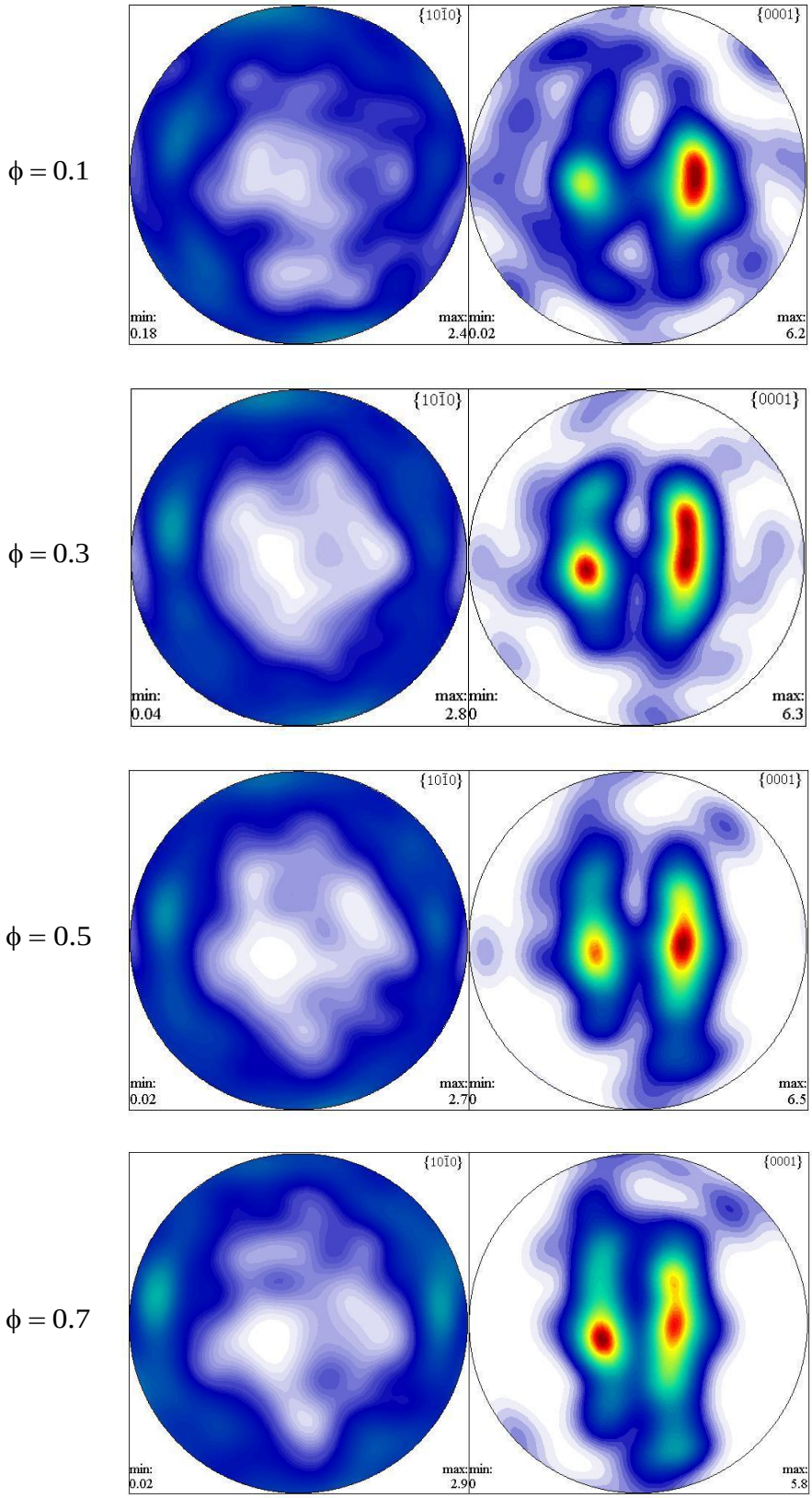

Fig. 6-6. Predicted rolling texture for X=3 ($\tau_{basal} : \tau_{<c+a>} : \tau_{tw} = 1 : X : 2$). (0002) and $(10\bar{1}0)$ pole figures using the ϕ-model, $\varepsilon_{eq} = 34\%$.

The corresponding relative activities of slip and twinning systems are shown in Fig. 6-7 to Fig. 6-9. As expected, the lower X value increase the relative activities of pyramidal $\langle c+a \rangle$ slip, and therefore decrease the ones of basal slip. A higher ϕ value will also leads to a stronger basal slip. The activities of twinning are relative weak and decreased with the increasing strain. If we link the slip and twinning activities to the predicted texture (Fig. 6-4 to Fig. 6-6), we can see that the strong basal slip can reduce the spread of basal poles and respond to the formation of typical basal textures.

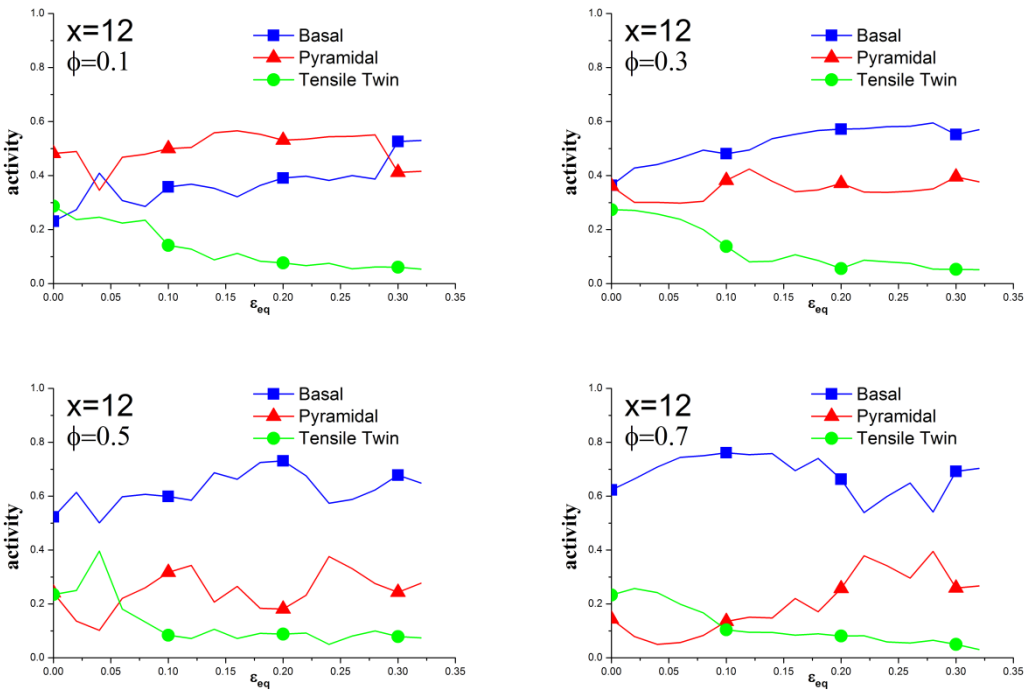

Fig. 6-7. Effect of ϕ value on the slip and twinning activities for X=12 ($\tau_{basal} : \tau_{<c+a>} : \tau_{tw} = 1 : X : 2$).

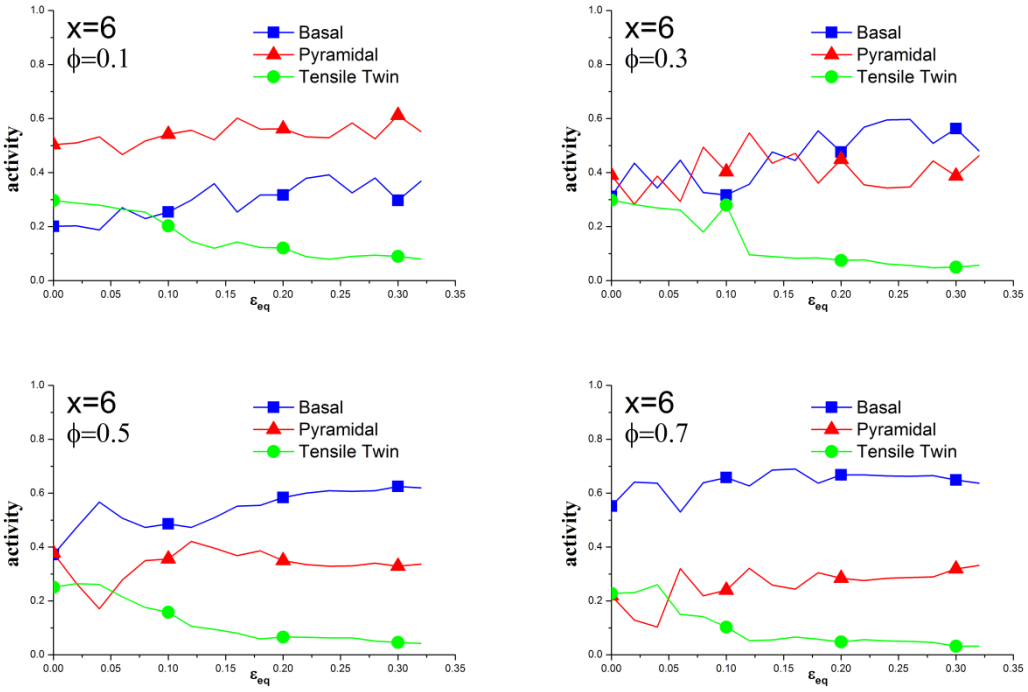

Fig. 6-8. Effect of ϕ value on the slip and twinning activities for X=6 ($\tau_{basal} : \tau_{<c+a>} : \tau_{tw} = 1 : X : 2$).

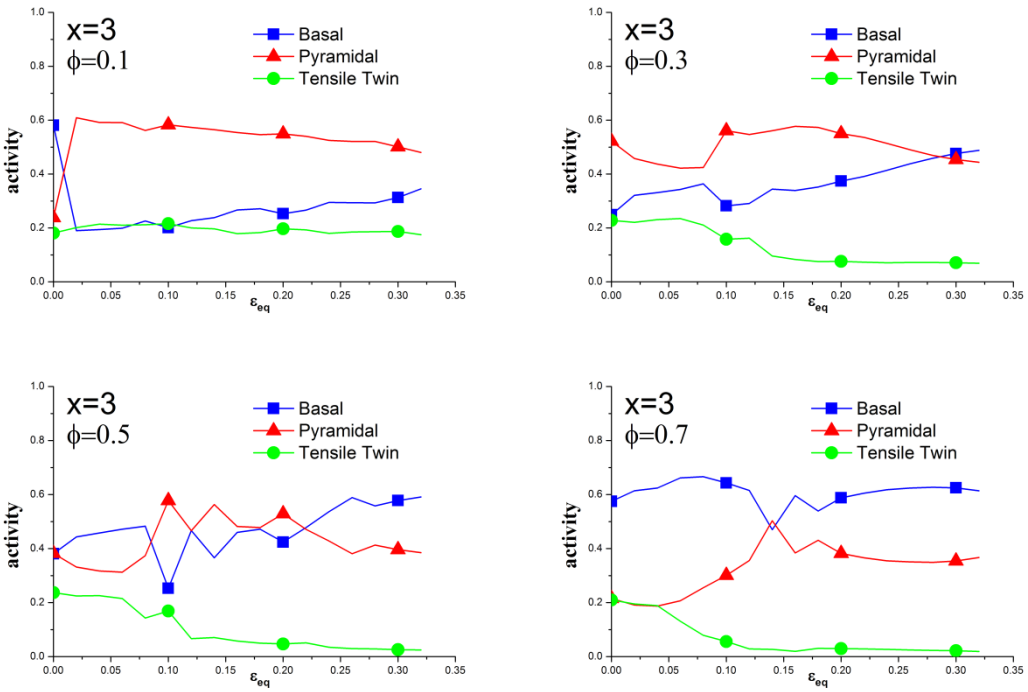

Fig. 6-9. Effect of ϕ value on the slip and twinning activities for X=3 ($\tau_{basal} : \tau_{<c+a>} : \tau_{tw} = 1 : X : 2$).

VI.2.1.2 Simulations with prismatic slip

✓ **Simulations with the VPSC model**

Agnew et al. (2001) have also proposed a similar simulation but take into account the prismatic slip. The relative CRSS of these systems are set to be $\tau_{basal}:\tau_{prism}:\tau_{<c+a>}:\tau_{tw}=1:3:X:2$. All other parameters are set to be the same than the previous simulation. The predicted results of Agnew et al. (2001) are presented in Fig. 6-10. By reducing X from 12 to 4, the basal poles can still be spread but not as evident as the case without prismatic slip.

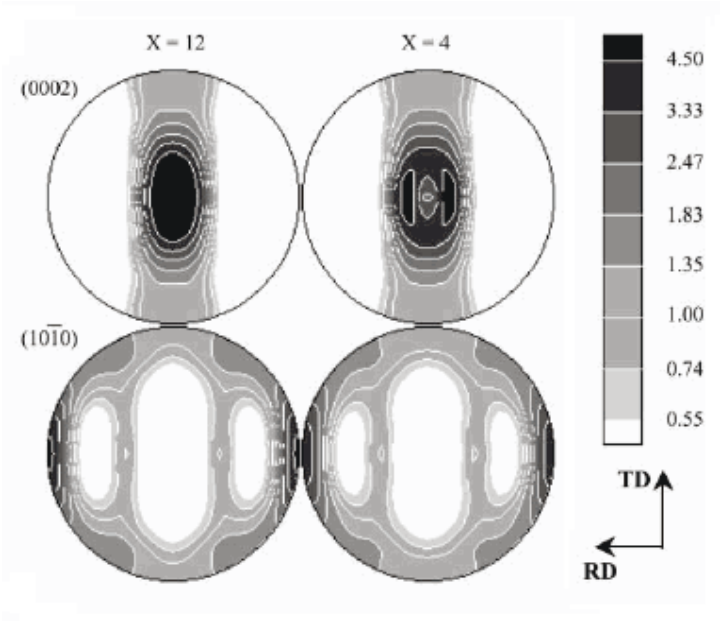

Fig. 6-10. Predicted rolling texture by Agnew et al. (2001). (0002) and $(10\bar{1}0)$ pole figures for X=12 and 4 ($\tau_{basal}:\tau_{prism}:\tau_{<c+a>}:\tau_{tw}=1:3:X:2$), $\varepsilon_{eq}=34\%$.

✓ **Simulations with the ϕ-model**

Similar simulation is carried out by using the ϕ-model and the predicted textures are shown in Fig. 6-11 and Fig. 6-12. A strong spread of basal poles can still be found for low ϕ values or low X values. Results of high ϕ values fit well the textures predicted by Agnew et al. (2001).

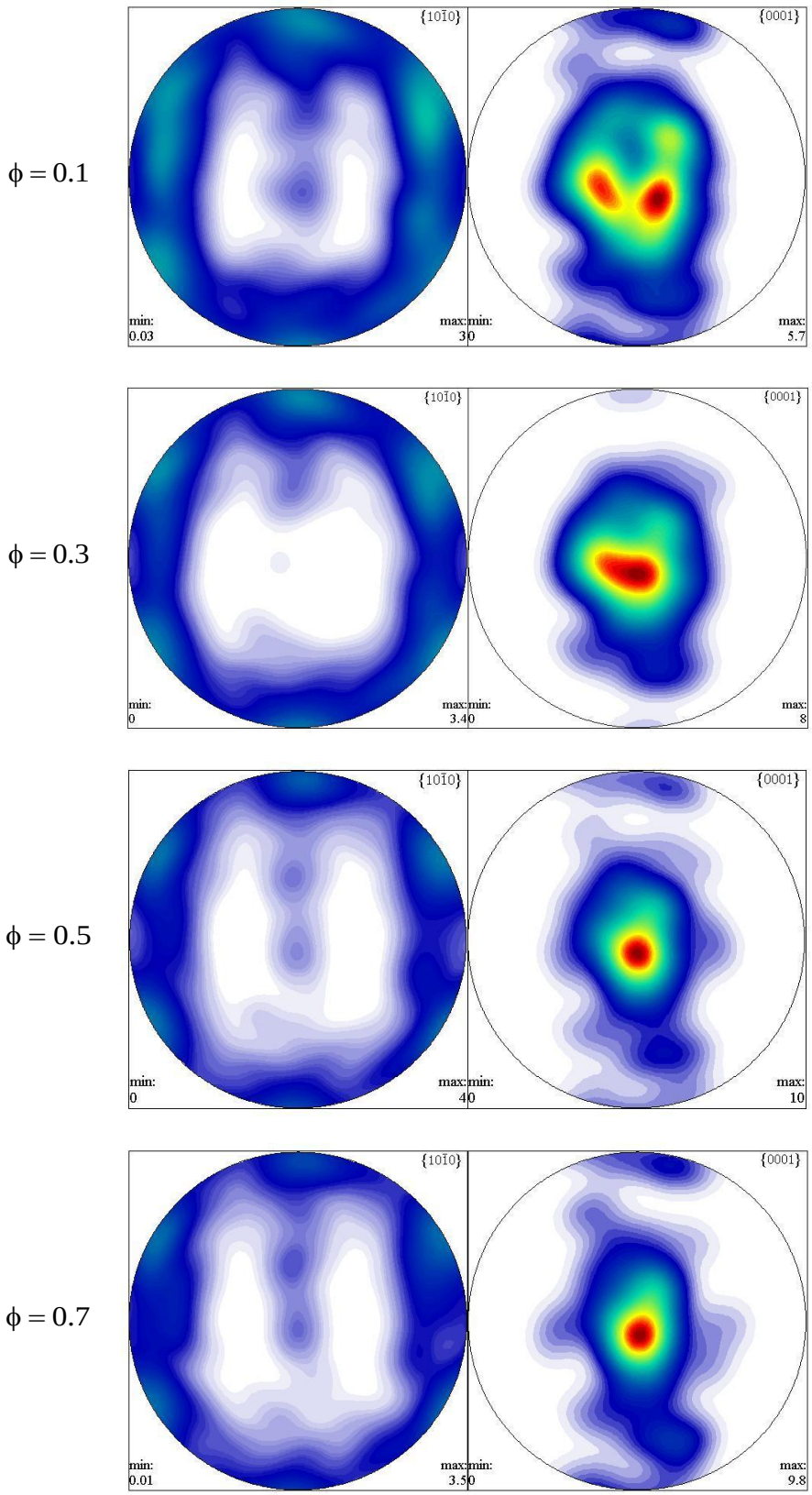

Fig. 6-11. Predicted rolling texture for X=12 ($\tau_{basal} : \tau_{prism} : \tau_{<c+a>} : \tau_{tw} = 1 : 3 : X : 2$). (0002) and $(10\bar{1}0)$ pole figures using the ϕ-model, $\varepsilon_{eq} = 34\%$.

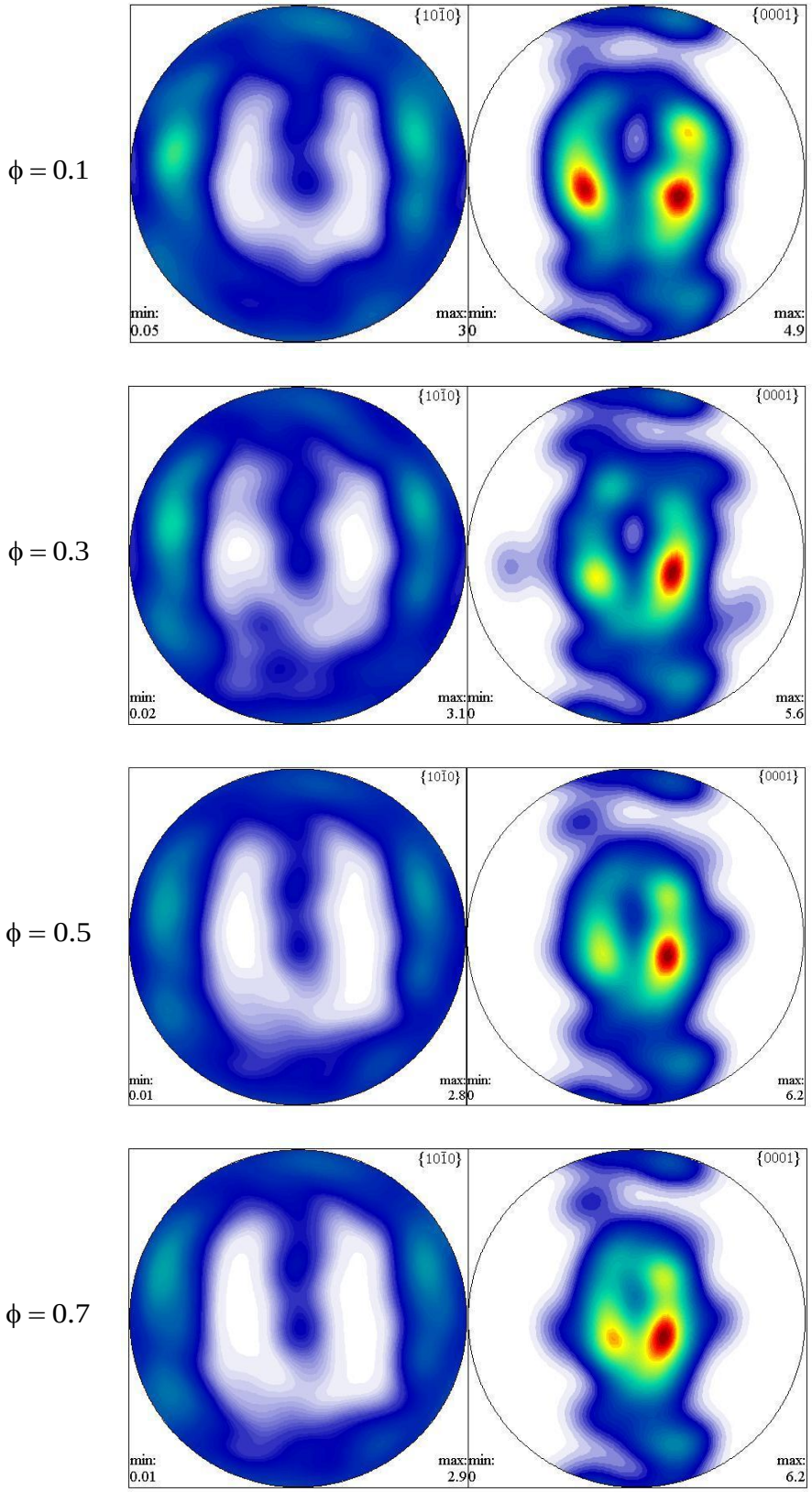

Fig. 6-12. Predicted rolling texture for X=4 ($\tau_{basal} : \tau_{prism} : \tau_{<c+a>} : \tau_{tw} = 1:3:X:2$). (0002) and $(10\bar{1}0)$ pole figures using the ϕ-model, $\varepsilon_{eq} = 34\%$.

The relative activities of the slip and twinning systems are presented in Fig.6-13a and Fig. 6-13b. The effects of X and ϕ on the activities of basal slip, pyramidal slip and tensile twinning are similar to the previous simulations. The activity of prismatic slip is weaker than other two slip systems, and it can be reduced by higher X values or by higher ϕ values.

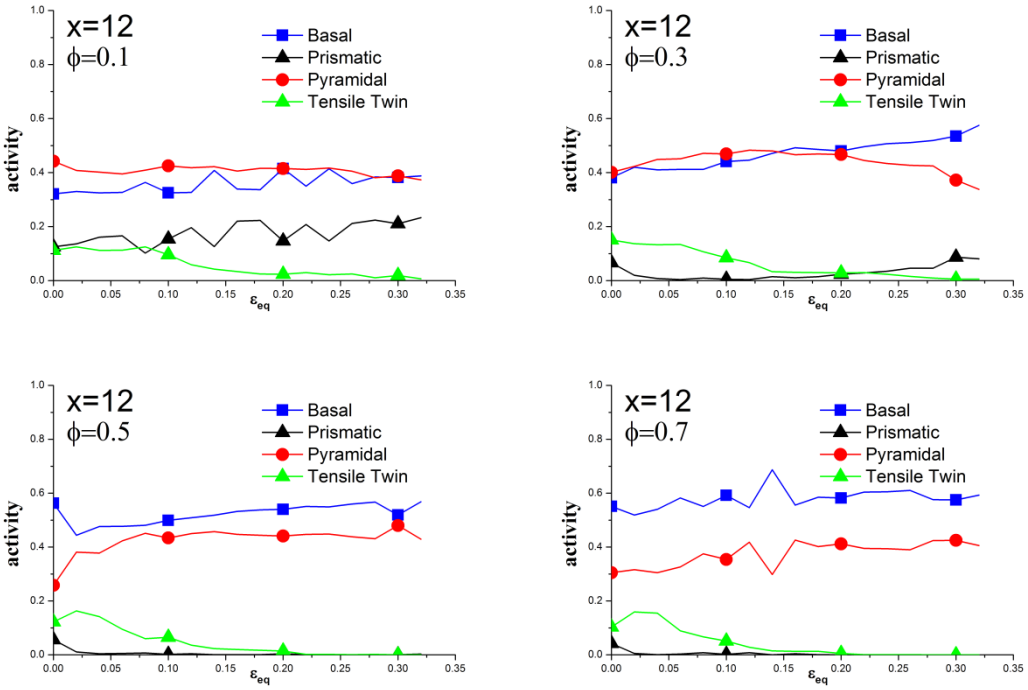

Fig. 6-13a. Effect of ϕ value on the slip and twinning activities for X=12 ($\tau_{basal} : \tau_{prism} : \tau_{<c+a>} : \tau_{tw} = 1:3:X:2$).

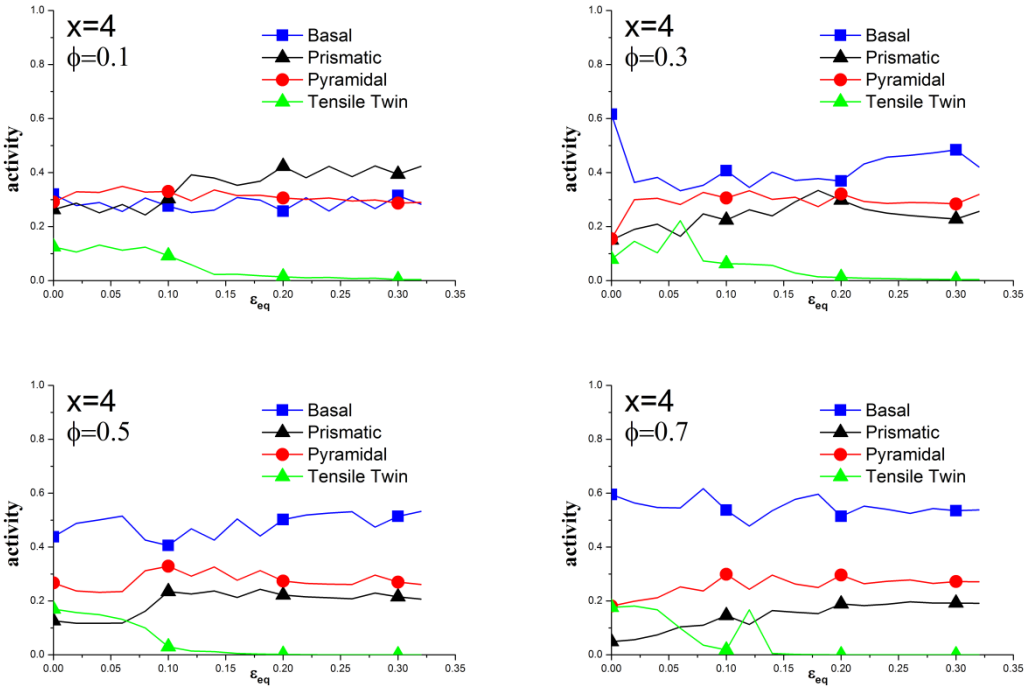

Fig. 6-13b. Effect of ϕ value on the slip and twinning activities for X=4 $(\tau_{basal}:\tau_{prism}:\tau_{<c+a>}:\tau_{tw}=1:3:X:2)$.

VI.2.2 Application of ϕ-model on magnesium alloy AZ31

VI.2.2.1 Input parameters

The material studied here is magnesium alloy AZ31, a hexagonal material with parameter ratio c/a=1.624. The intermediate ϕ-model was applied to simulate the deformation behavior of AZ31 and validated with experimental results from the literature (Jain and Agnew, 2007; Styczynski et al., 2004; Ulacia et al., 2010a, b; Wang et al., 2010).

Two series of tests were carried out in this study. First, we simulated cold rolling of heat treated AZ31 sheet with initial random texture. Second, we conducted simulations of compression and tension tests, of rolled AZ31, in different directions. The plastic deformation mechanisms in AZ31 is assumed to be composed of three

kinds of slip systems : (0001)<11$\bar{2}$0> basal slip, (1000)<11$\bar{2}$0> prismatic slip, (11$\bar{2}$2)<11$\bar{2}$3> pyramidal slip and tensile twinning (10$\bar{1}$2)<10$\bar{1}$1>. In all the numerical simulation, the reference shear rate and rate sensitivity parameters (see Eq. (1)) are assumed to be the same for all the considered systems: $\dot{\gamma}_0$=0.001s^{-1} and n=19. The other voce hardening parameters are listed in Tab. 6-1. Here, the first-order $\langle c+a \rangle$ pyramidal slip system has a much higher critical resolved shear stress than that of basal slip and prismatic slip systems.

Mode	τ_0 (MPa)	τ_1 (MPa)	θ_0 (MPa)	θ_1 (MPa)
basal	16	4	2300	110
prismatic	70	11	450	77
pyramidal	110	23	7350	54
twin	30	0.	0.	0.

Tab. 6-1. Model parameters describing critical resolved shear stress and hardening parameters.

The hardening parameters used in Tab. 6-1 are obtained by backfitting the experimental mechanical behavior for the case of high interaction with the parameter $\phi = 0.1$. Fig. 6-14 shows the stress strain curve of rolled magnesium sheet under uniaxial tension along rolling direction (RD). The initial texture for these simulations is that of rolled sheet. Experimental data are obtained from Jain and Agnew's work (2007).

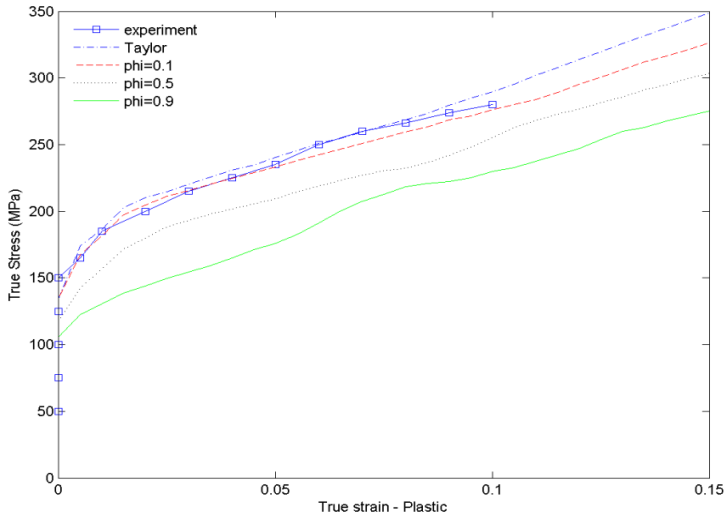

Fig. 6-14. Simulated and experimental stress strain curves of rolled AZ31 sheet under uniaxial tension along rolling direction (data after Jain and Agnew, 2007).

Using parameters in Tab. 6-1, simulation results from Taylor model and intermediate model with $\phi = 0.1$ agrees well with the experimental results. With the increase of interaction parameter ϕ, stress strain curves drop down and deviate from experimental data. It is possible to fit the curves for all cases of interaction parameters by changing the hardening law parameters, just like it is possible to simulate the stress-strain response by different models by changing the parameters. However, we will not fit the experimental data under different interaction parameters. Instead, a parametric study will be performed to investigate the influence of the interaction parameters on deformation systems activities and texture evolution. The goal of this paper is to validate the intermediate model in simulating mechanical behavior and texture evolution of hexagonal magnesium alloys.

VI.2.2.2 Rolling tests

In the first test set, rolling of initially random AZ31 polycrystals was simulated. Texture evolution results are listed in Fig. 6-15. The experimental (0001) and $(11\bar{2}0)$

pole figures of rolled sheet are shown in Fig. 6-15a (Styczynski et al., 2004). The simulated polycrystalline aggregate is composed of 100 single crystals with initial random texture as shown by pole figures in Fig. 6-15b. After rolling, experimental texture (Styczynski et al., 2004) has a strong component with c-axis aligned around the normal direction (ND) (Fig. 6-15c). Texture evolution and mechanical behavior have been simulated up to 20% equivalent strain and using $\phi \to 0$, 0.1, 0.2, 0.5, 0.7, 0.9. The results for $\phi \to 0$ is the same as that from Taylor model (not reported here). Although we observed a large difference in the simulated stress-strain curves for different values of ϕ, the corresponding textures simulated are close. There is only small movement of the split of the basal texture components as shown by the (0001) poles figures. For these reasons, we are showing only the simulated results for $\phi = 0.1$ (see Fig. 6-15d) and $\phi = 0.9$ (see Fig. 6-15e).

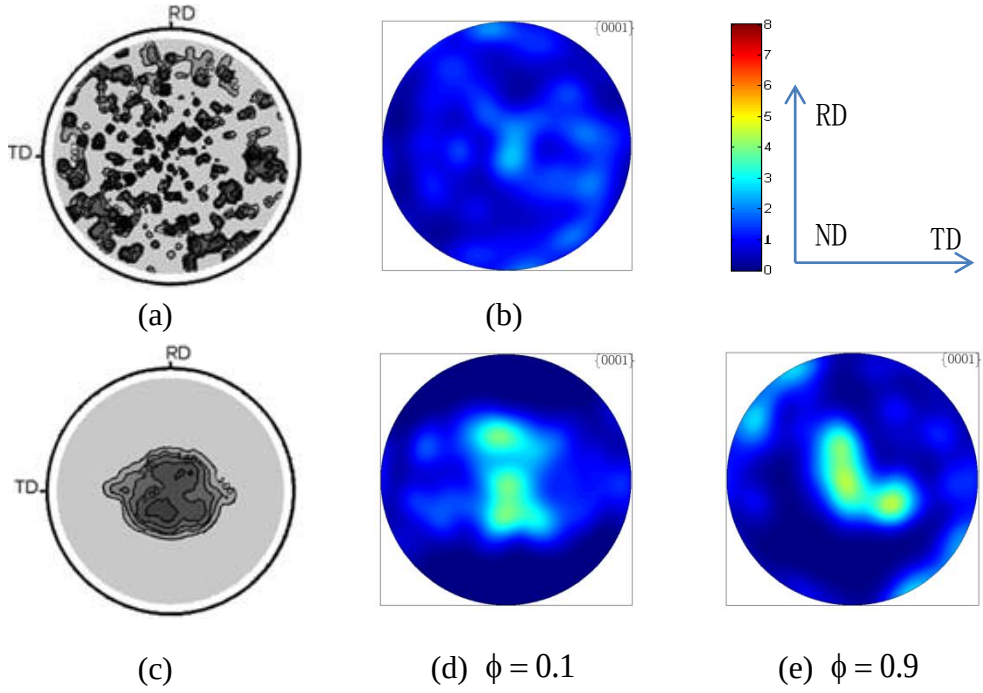

Fig. 6-15. (0001) pole figures of squeeze cast AZ31 sheet with random texture (a), simulated AZ31 with random texture (b), cold rolled AZ31 sheet (c), simulated rolled texture using the ϕ-model ($\varepsilon_{eq} = 20\%$) with $\phi = 0.1$ (d), $\phi = 0.9$ (e). (experimental data after Styczynski et al., 2004).

The large difference in predicted stress-strain curve using different ϕ, not reported here, is attributed to the predicted activities of different deformation mechanisms. As shown in Fig. 6-16, contribution from twinning activity is smaller in all cases. Texture evolution is therefore dominated by slip. In the case of low ϕ, shown in Fig. 6-16a and Fig. 6-16b, activities of the three slip families are similar and there are no much changes during rolling. The pyramidal slip is strongly activated for low ϕ values and remains at a constant level throughout the deformation process. With the increase of ϕ, the activity of pyramidal slip are smaller at the beginning of deformation and increases with increasing deformation, as seen in Fig. 6-16c and 5-16d. For $\phi = 0.9$, the basal slip is very active whereas the activity of prismatic slip is weak at low strain. During the deformation, the basal slip is weakened and the prismatic is strengthened.

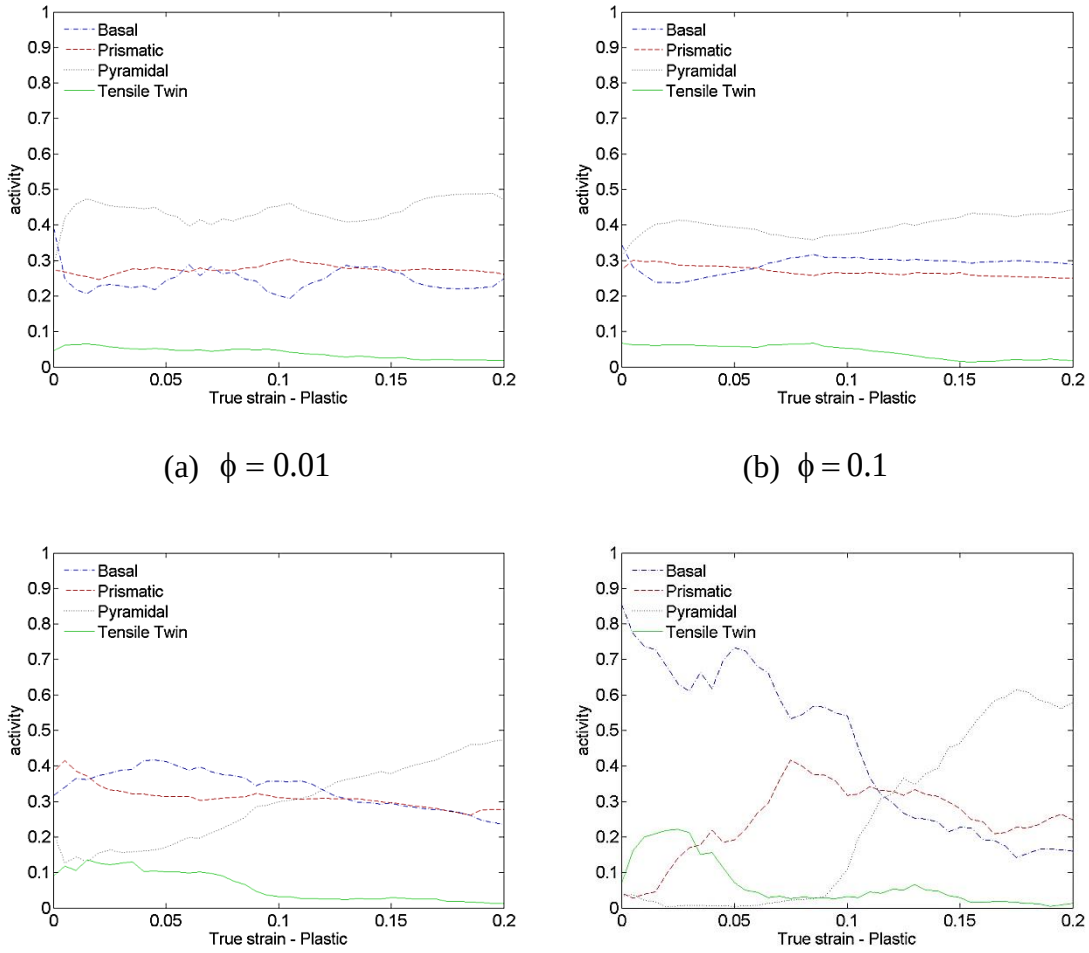

(a) $\phi = 0.01$ (b) $\phi = 0.1$

(c) $\phi = 0.5$ (d) $\phi = 0.9$

Fig. 6-16. Predicted activities of different deformation mechanisms in Mg sheet during rolling using the intermediate ϕ-model, $\phi = 0.01$ (a), $\phi = 0.1$ (b), $\phi = 0.5$ (c) and $\phi = 0.9$ (d).

VI.2.2.3 Tension and compression tests on rolled Mg sheet

✓ **Tensile tests along RD**

In the second set of test, tension and compression of rolled magnesium sheets along different directions were investigated. For the simulation of tensile deformation test up to 20% strain, we used the rolling texture in Fig. 6-15d as initial texture. Tensile tests were performed along RD. The predicted textures for different values of ϕ are plotted in Fig. 6-17 in comparison with the experimental results (Ulacia et al., 2010a,

b). Fig. 6-17a shows the experimental (0001) and $(10\bar{1}0)$ pole figures of rolled Mg sheet uniaxially stretched along RD at room temperature (Ulacia et al., 2010a, b). The deformation texture has a strong texture component with c-axis aligned along ND. $(10\bar{1}0)$ axis distributed along the plane of RD (also tension direction here) and transverse direction (TD). Pole figures simulated using the intermediate ϕ-model with $\phi = 0.01$, 0.1 and 0.9 are presented in Figs. 6-17b, 6-17c and 6-17d, respectively.

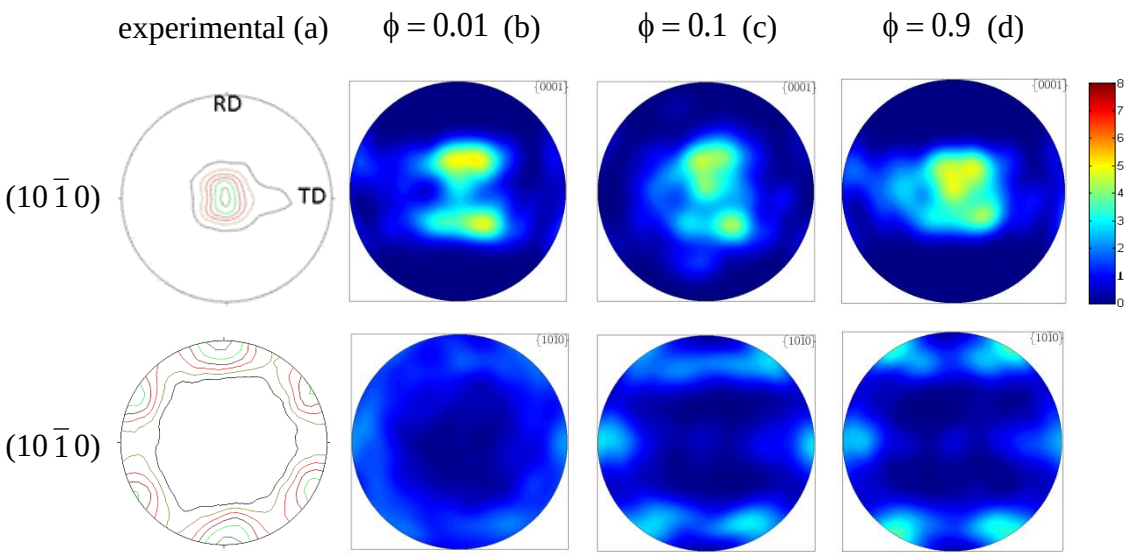

Fig. 6-17. Experimental (a) and simulated (0001) and $(10\bar{1}0)$ pole figures of Mg sheet uniaxially stretched along RD using the ϕ-model with different interaction parameter ϕ (b, c, d) (experimental data after Ulacia et al., 2010a, b)

Again, simulated pole figures from the intermediate ϕ-model agree well with the experimental results, no matter what interaction parameters used here. For low interaction (high ϕ value), the crystal are less constrained and thus the activity of hard modes (pyramidal) is not required for the accommodation of plastic deformation. However, as deformation proceeds, the polycrystal becomes highly textured with the soft modes becoming less favorable for activation and therefore, hard mode start to be more activated. As shown in Fig. 6-16d, the best correlation with the experimental texture evolution is obtained for high value of ϕ and low interaction strength.

The predicted activities of different deformation mechanism in the case of tension along RD are presented in Fig. 6-18. Similar to the rolling case, contribution from twinning is small. This is an accord with the results of Wang et al. (2010), who showed that the activity of tensile twinning is relatively low and decreases with increasing strain. In addition, there is no much change in the activities during deformation for high interaction strength (low ϕ, see Figs. 6-18a, b). The activities of basal and prismatic modes are strain independent for $\phi = 0.01$ and $\phi = 0.1$. In the case of intermediate and low interaction strength ($\phi = 0.5$ in Fig. 6-18c and $\phi = 0.9$ in Fig. 6-18d), the activity of basal slip decreases while that of prismatic slip increases during tension. Higher ϕ value leads to lower activity of pyramidal slip.

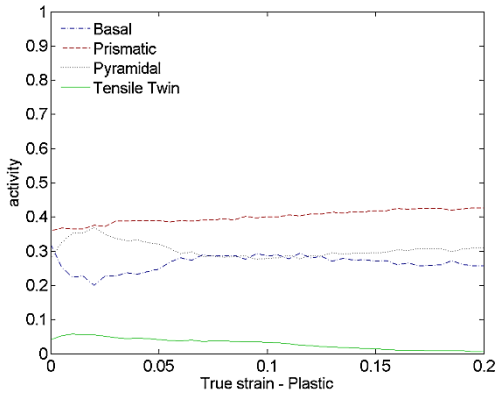

(a) $\phi = 0.01$

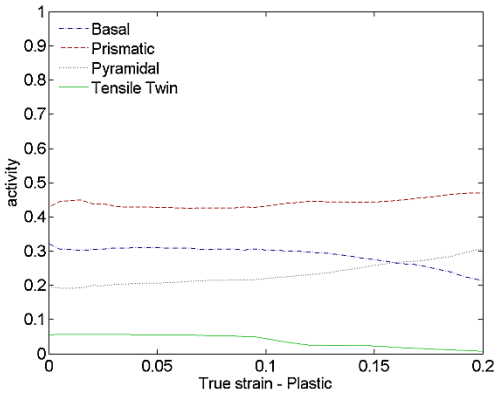

(b) $\phi = 0.1$

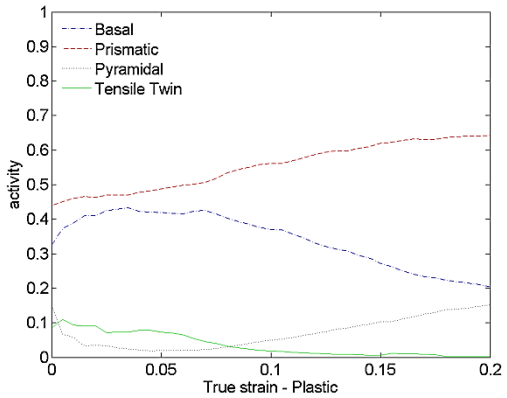

(c) $\phi = 0.5$

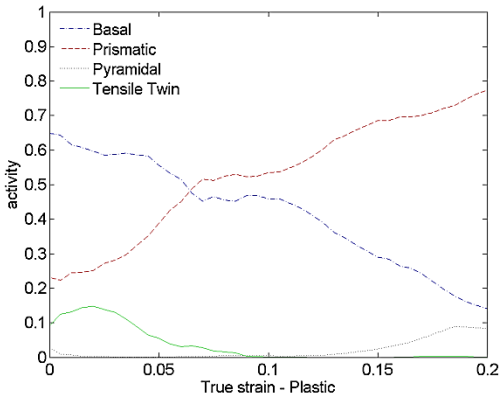

(d) $\phi = 0.9$

Fig. 6-18. Predicted activities of different deformation mechanisms in Mg sheet during uniaxial tension along RD using the intermediate ϕ-model, $\phi = 0.01$ (a), $\phi = 0.1$ (b), $\phi = 0.5$ (c) and $\phi = 0.9$ (d).

✓ **Compression tests along TD**

For the uniaxial compression of the rolled sheet, different loading directions were investigated. First simulated texture evolution during uniaxial compression along TD was compared with Jain and Agnew's experimental results (Jain and Agnew, 2007), as shown in Fig. 6-19. The experimental results demonstrate a strong texture component with c-axis aligned close to the uniaxial compression direction (parallel to TD). The simulated results reveal a strong dependence on the used ϕ value. The best

correlation with the experimental texture is obtained for low interaction strength ($\phi = 0.9$) where the most grains reorient their c-axes along the loading direction (TD). For the very high interaction strength ($\phi = 0.01$), we obtained results which agree less the experimental results. We note that the case with $\phi \to 0.$ is a case equivalent to the upper-bound Taylor model.

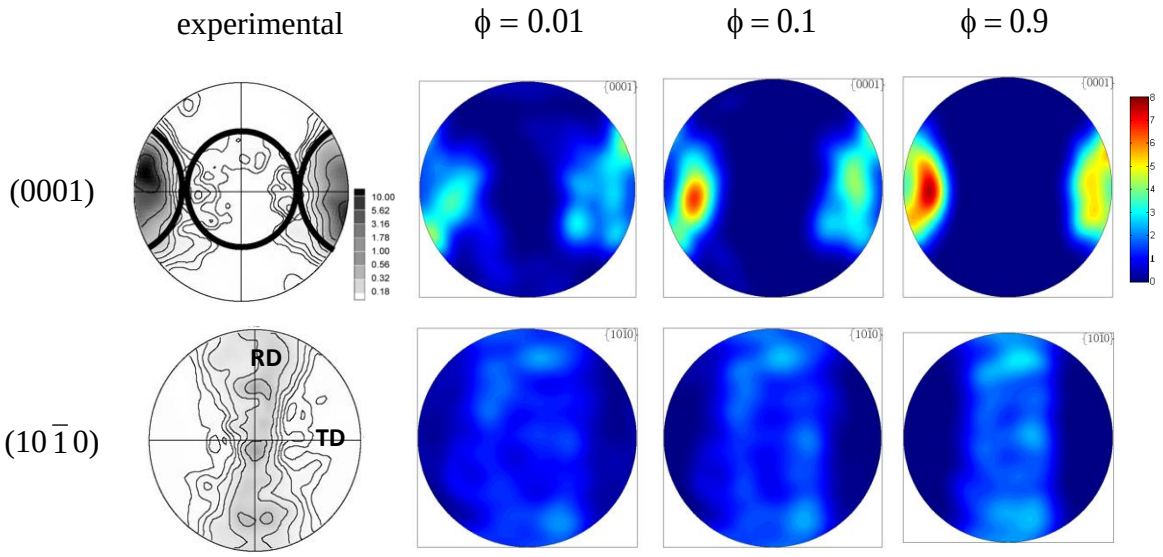

Fig. 6-19. Experimental and simulated (0001) and (10$\bar{1}$0) pole figures of Mg sheet uniaxially compressed along TD using the intermediate ϕ-model with different ϕ. (experimental data after Jain and Agnew, 2007).

Activities of different deformation mechanisms in Mg sheet during compression along TD explains the large difference in texture simulation using different ϕ. As shown in Fig. 6-20, the difference between different systems activities during compression predicted by low ϕ values is smaller than those predicted from the other simulations for larger ϕ. The activity of twinning increases with increasing ϕ, particularly for low strains. However, this activity decreases drastically for larger strains and for intermediate and large ϕ values.

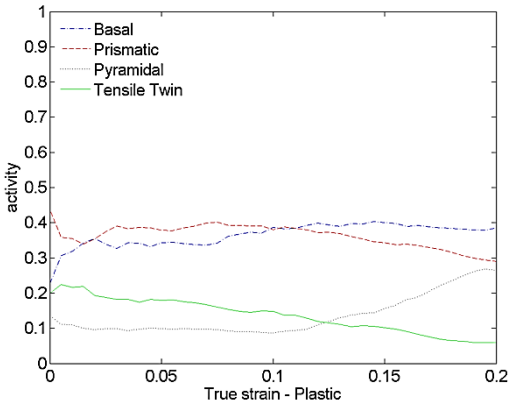

(a) $\phi = 0.01$

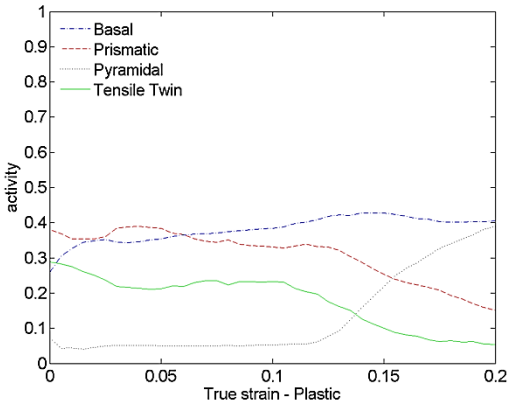

(b) $\phi = 0.1$

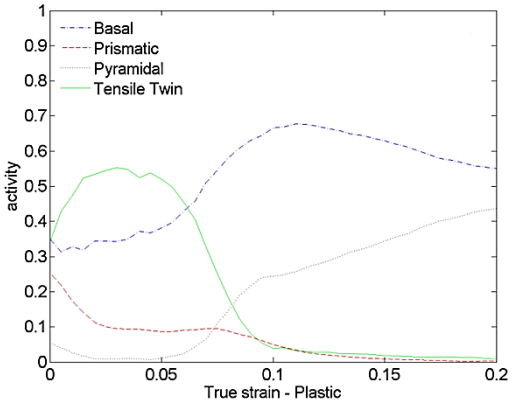

(c) $\phi = 0.5$

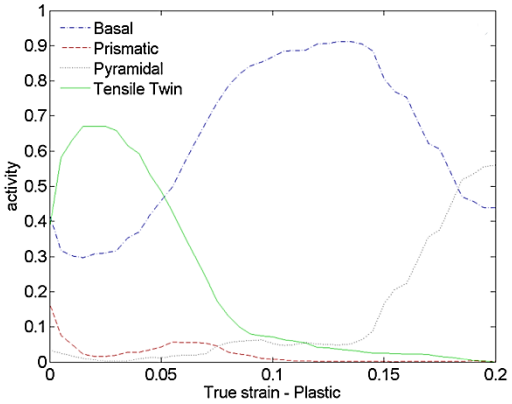

(d) $\phi = 0.9$

Fig. 6-20. Predicted activities of different deformation mechanisms in Mg sheet during uniaxial compression along TD using the intermediate ϕ-model, $\phi = 0.01$ (a), $\phi = 0.1$ (b), $\phi = 0.5$ (c) and $\phi = 0.9$ (d).

✓ **<u>Compression tests along RD</u>**

Compression of rolled Mg sheet along RD is also simulated. Fig. 6-21 shows the predicted texture at 20% strain for various ϕ values. These predictions are compared to the experimental results of Jain and Agnew (2007). Experimental data show that the c-axis is aligned with the RD, which is also the loading direction in this case. Using $\phi = 0.01$, simulated results presents a basal texture component with c-axis aligned between RD and ND; with about 30° tilt away from RD. With the increase of ϕ, the

basal texture component moves closer to the RD (loading direction). However, the best correlation between experimental and predicted textures, in terms of both intensity and alignment, is obtained for low interaction strength ($\phi = 0.9$). Predicted systems activities for compression along RD have a similar tendency to those obtained for compression along TD, and thus not reported here.

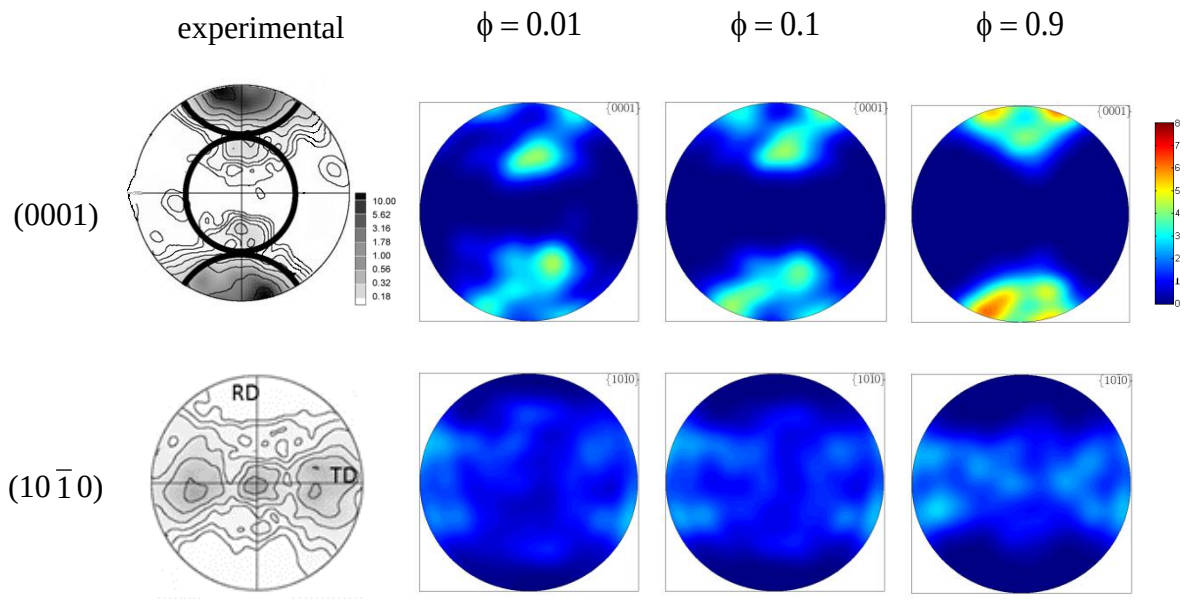

Fig. 6-21. Experimental and simulated (0001) and $(10\bar{1}0)$ pole figures of Mg sheet uniaxially compressed along RD using the intermediate ϕ-model with different ϕ (experimental data after Jain and Agnew, 2007).

✓ **Compression tests along ND**

The compression test along the ND of the Mg sheet is also studied in this work. Fig. 6-22 shows the predicted slip/twinning activities. For low ϕ values ($\phi \to 0$ and $\phi = 0.1$), the plastic deformation is mostly accommodated by pyramidal slip, and then by the basal and prismatic slip. For intermediate and high ϕ values ($\phi = 0.5$ and $\phi = 0.9$), the deformation is dominated by basal slip. For strains $\varepsilon > 0.1$, the basal slip activity decreases whereas the pyramidal slip activity increases with strain. The activity of the tensile twinning is relatively weak at lower strain and nearly

disappeared for $\varepsilon > 0.1$. The corresponding predicted textures are presented in Fig. 6-23. Higher ϕ value leads to sharper textures where c-axes align almost parallel to ND with a slight tendency to tilt around ND.

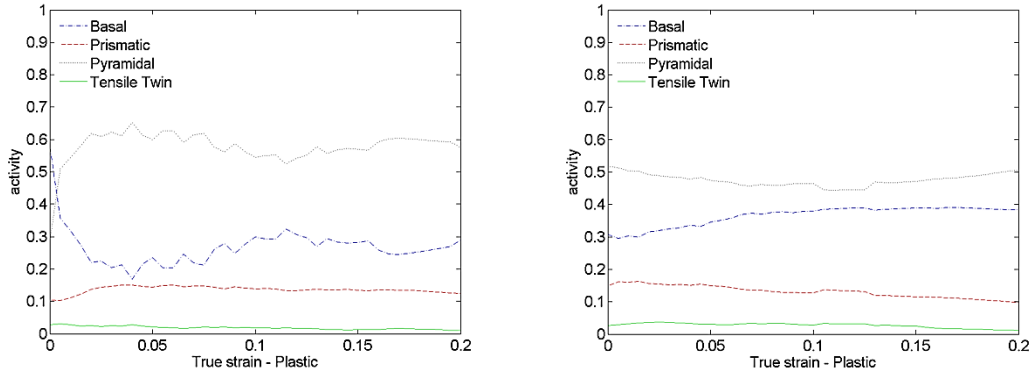

(a) $\phi = 0.01$ (b) $\phi = 0.1$

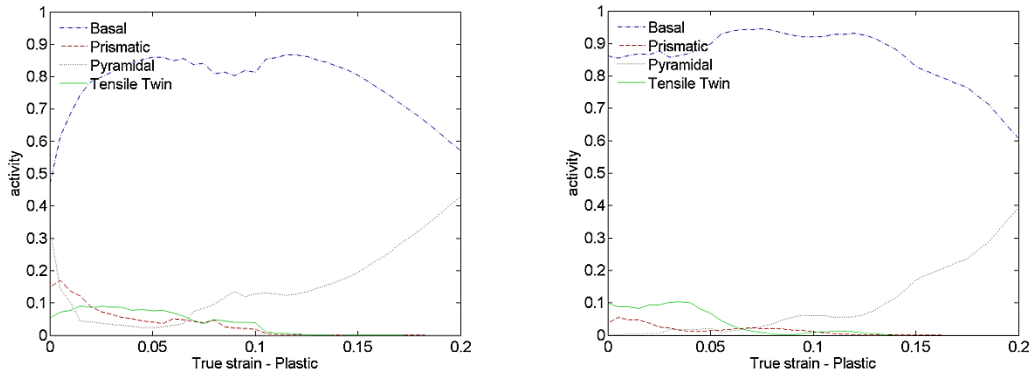

(c) $\phi = 0.5$ (d) $\phi = 0.9$

Fig. 6-22. Predicted activities of different deformation mechanisms in Mg sheet during uniaxial compression along ND using the intermediate ϕ-model, $\phi = 0.01$ (a), $\phi = 0.1$ (b), $\phi = 0.5$ (c) and $\phi = 0.9$ (d).

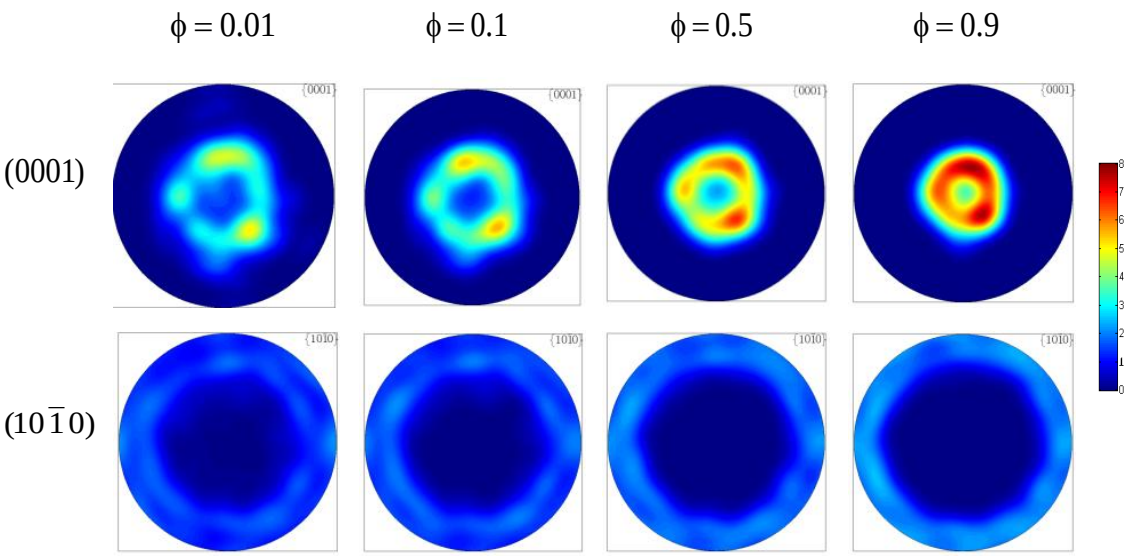

Fig. 6-23. Effect of parameter ϕ on the predicted textures under uniaxial compression along ND.

VI.3 Conclusion

In the first part of this chapter, we studied the effects of the interaction strength and the relative activities of slip and twinning systems on the texture evolution using the visco-plastic intermediate ϕ-model. We compared our results with the predicted ones for Mg alloys under rolling tests from literature. The results show that the activation of basal slip can be promoted when the activity of pyramidal slip is depressed (high X value) or when the interaction strength is low (high ϕ value). The highly activated basal slip can reduce the spread of basal poles towards RD and lead to the formation of the typical basal texture.

In the second part, the ϕ-model was applied to simulate the deformation behavior and texture evolution in magnesium alloys AZ31. Different cases, including rolling of initially random textured magnesium, tension as well as compression of rolled magnesium sheets along different directions were investigated. Our predicted texture results were validated by comparing to experimental results taken from literature. The

influence of different intergranular interaction strengths on the predicted results (texture evolution and deformation systems activity) was studied.

In simulating rolling of initially random textured Mg sheet, the effect of ϕ on texture development up to 20% strain is not significant. However, for both uniaxial tension and compression of rolled sheet, the simulated texture results are highly dependent on the value of ϕ. Predicted deformation mechanism activities provide good explanation for the texture development. For rolling, the twinning activity is very fairly low for all ϕ values, which affects slightly the texture development as observed by the tilt of the basal texture. For tension and compression of rolled sheet, slip/twinning activity is highly depending on the value of ϕ. As expected, tensile twinning contributes significantly to plasticity under compression and negligibly under tension. For the uniaxial compression, high values of ϕ induce high activity of the hard modes (twinning or pyramidal). In this case, twinning is highly activated at the lower strains and decreases at large strains where it becomes compensated by a higher activity of the pyramidal slip. Based on our predicted textures, particularly for uniaxial tension and compression, it is concluded that the best correlation with the experimental results was found for low interaction strength (high value of ϕ).

References:

Agnew, S.R., Duygulu, Ö., 2005. Plastic anisotropy and the role of non-basal slip in magnesium alloy AZ31B. Int. J. Plasticity 21, 1161-1193.

Agnew, S.R., Yoo, M.H., Tomé, C.N., 2001. Application of texture simulation to understanding mechanical behavior of Mg and solid solution alloys containing Li or Y. Acta Mater. 49, 4277-4289.

Brown, D.W., Agnew, S.R., Bourke, M.A.M., Holden, T.M., Vogel, S.C., Tomé, C.N., 2005. Internal strain and texture evolution during deformation twinning in magnesium. Mater. Sci. Eng. A 399, 1-12.

Francillette, H., Bacroix, B., Gasperini, M., Bechade J.L., 1998. Grain orientation effects in Zr702α polycrystalline samples deformed in channel die compression at room temperature. Acta Mater. 46, 4131-4142.

Fundenberger, J.J., Philippe, M.J., Wagner, F., Esling, C., 1997. Modelling and prediction of mechanical properties for materials with hexagonal symmetry (Zinc, Titanium and Zirconium alloys). Acta Mater. 45, 4041-4055.

Jain, A., Agnew, S.R., 2007. Modeling the temperature dependent effect of twinning on the behavior of magnesium alloy AZ31B sheet. Mater. Sci. Eng. A 462, 29-36.

Kocks, U.F., 1970. The relation between polycrystalline deformation and single crystal deformation. Metall. Mater. Trans. 1, 1121-1143.

Kocks, U.F., Westlake, D.G., 1967. The importance of twinning for the ductility of CPH polycrystals, Trans. TMS-AIME 239, 1107-1109.

Lebensohn, R.A., Tomé, C.N., 1993. A self-consistent anisotropic approach for the

simulation of plastic deformation and texture development of polycrystals: application to zirconium alloys. Acta Metall. Mater. 41, 2611-2624.

Lebensohn, R.A., Canova, G.R., 1997. A self-consistent approach for modelling texture development of two-phase polycrystals: Application to titanium alloys. Acta Mater. 45, 3687-3694.

Mayama, T., Aizawa, K., Tadano, Y., Kuroda, M., 2009. Influence of twinning deformation and lattice rotation on strength differential effect in polycrystalline pure magnesium with rolling texture. Comp. Mater. Sci. 47, 448-455.

Molinari, A., Canova, G.R., Ahzi, S., 1987. A self consistent approach of the large deformation polycrystal viscoplasticity. Acta Metall. 35, 2983-2994.

M'Guil, S., Ahzi, S. Garmestani, H., 2006. Modelling of texture evolution for HCP materials. Third International Conference: Multiscale Materials Modeling, Freiburg, Germany, Edited by P. Gumbsch, p. 515-517. 18-22 September 2006.

M'Guil, S., Ahzi, S., Gracio, J.J., 2009. Analysis of texture evolution in hcp polycrystals using a viscoplastic intermediate approach. Int. J. Mater. Form. 2, 57-60.

Parks, D.M., Ahzi, S., 1990. Polycrystalline plastic deformation and texture evolution for crystals lacking five independent slip systems. J. Mech. Phys. Solids 38, 701-724.

Plunkett, B., Lebensohn, R.A., Cazacu, O., Barlat, F., 2006. Anisotropic yield function of hexagonal materials taking into account texture development and anisotropic hardening. Acta Mater. 54, 4159-4169.

Prantil, V.C., Jenkins, J.T., Dawson, P.R., 1995. Modeling deformation induced textures in titanium using analytical solutions for constrained single crystal response. J. Mech. Phys. Solids 43, 1283-1302.

Proust, G., Tomé, C.N., Jain, A., Agnew, S.R., 2009. Modeling the effect of twinning and detwinning during strain-path changes of magnesium alloy AZ31. Int. J. Plasticity 25, 861-880.

Schoenfeld, S.E., Ahzi, S., Asaro, R.J., 1995. Elastic-plastic crystal mechanics for low symmetry crystals. J. Mech. Phys. Solids 43, 415-446.

Styczynski, A., Hartig, Ch., Bohlen, J., Letzig, D., 2004. Cold rolling textures in AZ31 wrought magnesium alloy. Scr. Mater. 50, 943-947.

Suwas, S., Beausir, B., L.S., Tóth, L.S., Fundenberger, J.-J., G., Gottstein, G., 2011. Texture evolution in commercially pure titanium after warm equal channel angular extrusion. Acta Materialia 59, 1121-1133.

Tomé, C.N. Canova, G., Ahzi, S., Molinari, A., 1987. Simulation of texture development in hexagonal materials using a self-consistent approach, Proceedings of ICOTOM-8, Eds J. Kallend and G. Gottstein, pp.395-400, Santa Fe.

Ulacia, I., Dudamell, N., Gálvez, F., Yi, S., Pérez-Prado, M., Hurtado, I., 2010a. Mechanical behavior and microstructural evolution of a Mg AZ31 sheet at dynamic strain rates. Acta Materialia 58, 2988-2998.

Ulacia, I., Yi, S., Perez Prado, M., Dudamell, N., Galvez Diaz-Rubio, F., Letzig, D., Hurtado, I., 2010b. Texture evolution of AZ31 magnesium alloy sheet at high strain rates. 4th International Conference on High Speed Forming, Columbus, Ohio, EEUU

Wang, H., Raeisinia, B., Wu, P.D., Agnew, S.R., Tomé, C.N., 2010. Evaluation of self-consistent polycrystal plasticity models for magnesium alloy AZ31B sheet. Int. J. Solids Struct. 47, 2905-2917.

Yi, S.B., Davies, C.H.J., Brokmeier, H.-G., Bolmaro, R.E., Kainer, K.U., Homeyer, J., 2006. Deformation and texture evolution in AZ31 magnesium alloy during uniaxial loading. Acta Mater. 54, 549-562.

Conclusions & Perspectives

The visco-plastic ϕ-model is a novel model for simulating the texture evolution and other mechanical behaviors in polycrystals materials during large deformation process. This model provides the novelty on the formulation and is able to predict large scale results from a stiff interaction to a more compliant interaction by varying the interaction strength parameter ϕ.

In this work, the ϕ-model has been applied on metals with different lattice structures and under different loading conditions. The mechanical twinning has been implemented into the ϕ-model. The coupled effect of the mechanical twinning and the interaction strength (controlled by the interaction strength parameter ϕ) has been deeply studied. We also used this model to predict the mechanical behaviors including the texture evolution on BCC and HCP metals and compared the predicted results with the experiments. The results show that the ϕ-model is well suitable to predict the large deformation response of metals with different properties.

The possible links between the interaction strength parameter ϕ and the microstructural features such as the grain size and the stacking fault energy (SFE) of the polycrystals are briefly mentioned. However, additional work is needed to clarify and quantify this link.

With the advantage of the high computation speed, the intermediate ϕ-model will play an important role in integrated computational materials engineering (ICME) to provide guidance on processing optimization.

The future work should focus on the development and application of the ϕ-model. It might include the following:

1. The modeling of other deformation mechanisms in polycrystals, beside crystallographic slip and twinning, is an active topic of research. The ϕ-model

may be adopted to take into account those mechanisms such as the twin barrier effect and shear banding. Such a work will optimize the simulation capability of ϕ-model

2. In this thesis, the possible physics background of the ϕ-model has been briefly mentioned. We suggest that the ϕ parameter should be linked with the SFE and grain size. However, such a suggestion needs to be quantitatively validated. Some experimental work should be carried out on this point.

3. The ϕ-model may be extended and applied on the multi-phase metals such as the dual-phase steel and the silver-copper cast eutectic nanocomposite. We suggest carrying out some experimental works on multi-phase metals in order to investigate the effect of the high densities of the interfaces on the microstructure evolutions. The predicted results of the ϕ-model should be compared with the experimental ones. This work may lead to a better understanding of the physics background of the ϕ-model.

4. In the previous works, only the velocity gradient can be imposed in the ϕ-model as the boundary condition. We suggest that the stress imposed boundary condition should be implemented into the ϕ-model. This work will enable the ϕ-model to predict the Lankford value.

5. The ϕ-model can be embedded into a FEM code to simulate complex metal forming processes which naturally involve non-homogeneous boundary conditions. The texture evolution will be known at each deformation step which will help to optimize the mechanical processes.

Appendix. Texture representation: pole figure, inverse pole figure and orientation distribution function (ODF)

✓ Pole figure

The pole figures are normally stereographic projections of the crystallographic directions present in the grains. The axes of the sample are aligned with the axes of the projection sphere. For example in rolling tests, the sample normal direction is the center of the projection and the rolling and traverse directions are chosen to be the vertical and horizontal directions of the projection, respectively. See Fig. A-1a. For each grain, the normal of the crystallographic plane {hkl} pierces the half sphere in P1. The point P2 is the intersection of SP1 and the rolling plane. If the P2 points obtained from all the grains are considered, we can plot a pole figure. In addition, the density (with the consideration of the volume fraction of each grain) of the points on the pole figure can be distinguished by colors or contour lines, which is more legible and precise way to present the crystallographic texture. The examples of the (111) and (110) rolling textures for FCC metals are shown in Fig. A-1b.

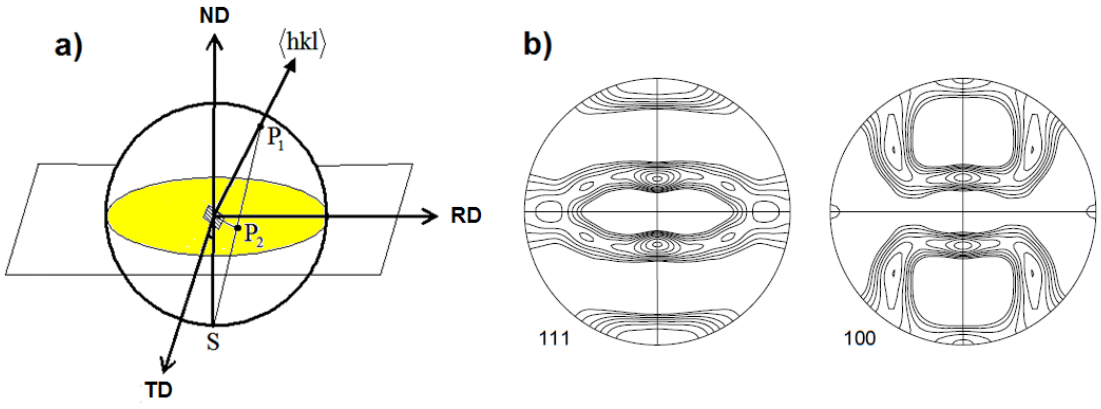

Fig. A-1. a) Description of pole figure; b) Examples of the FCC rolling texture pole figures

✓ Inverse pole figures

The inverse pole figure, as it is named, can be considered as an opposite method to pole figure to represent the texture. It is usually used for the axially symmetric texture such as the tensile and compression texture for cubic metals. Firstly, we need to identify a plane in a unit cell whose normal direction is parallel to a specified plane of the sample. Then, by using the same manner of pole figure, a corresponding point for the specific plane on the projection plane can be found. When all grains are considered, a complete inverse pole figure will be obtained. If the crystal structure is symmetry, the complete inverse pole figure can be separated into several parts containing the same texture information. Each of those parts is defined as the inverse pole figure. For the cubic systems, the inverse pole figure is represented by a triangle figure as shown in Fig. A-2.

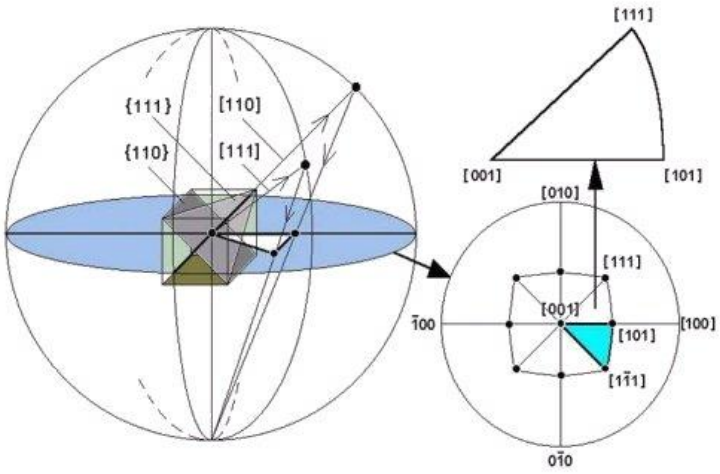

Fig. A-2. Description of inverse pole figure for cubic systems.

✓ Orientation distribution function (ODF)

The full 3-Dimension description of crystallographic texture can be given by the orientation distribution function (ODF) which is defined as the volume fraction of

grains in a certain orientation g.

$$\frac{\Delta V / V}{dg} = f(g) = f(\varphi_1, \Phi, \varphi_2) \qquad \text{(A-1)}$$

If we consider the three Euler angles as the three axes of Cartesian coordinates, a specific area of space can be obtained which is called the Euler orientation, see Fig. A-3a. Each point in this space represents a specific orientation of a single crystal. The orientation distribution function f(g) can be represented as a three-dimensional function in this space Euler such that each point in this space is indicated by the value of f(g).

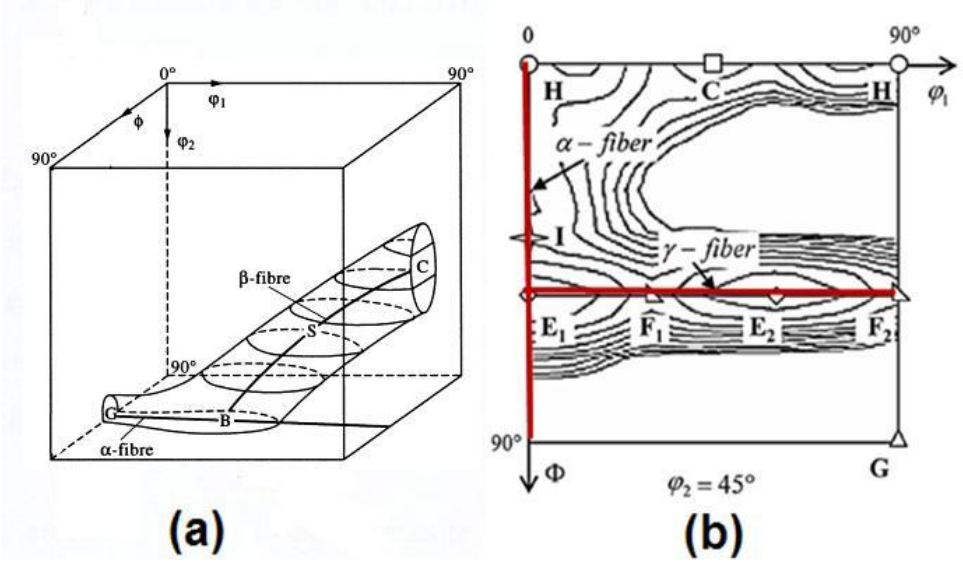

Fig. A-3. a) example of Euler space, b) example of the ODF section with texture components and fibers.

The Fig. A-3a shows an example of a texture described in terms of Euler space. The textures are normally presented by the sections of the Euler space (Fig. A-3b). The intensity on certain points and lines in the ODF section may contain important information of the texture. They are called texture components and fibers respectively (see Fig. A-3b).